

Public reporting burden for this collection of information is estimated to average 1 hour per response, including the time for reviewing instructions, searching existing data sources, gathering and maintaining the data needed, and completing and reviewing the collection of information. Send comments regarding this burden estimate or any other aspect of this collection of information, including suggestions for reducing this burden to Washington Headquarters Services, Directorate for Information Operations and Reports, 1215 Jefferson Davis Highway, Suite 1204, Arlington, VA 22202-4302, and to the Office of Management and Budget, Paperwork Reduction Project (0704-0188), Washington, DC 20503.

1. AGENCY USE ONLY (Leave blank)		2. REPORT DATE 1 December 1998	3. REPORT TYPE AND DATES COVERED Conference Proceedings	
4. TITLE AND SUBTITLE XXIII International Conference on Phenomena in Ionized Gases, VOL 3			5. FUNDING NUMBERS F6170897W0048	
6. AUTHOR(S) Conference Committee				
7. PERFORMING ORGANIZATION NAME(S) AND ADDRESS(ES) Universite Paul Sabatier 118 Route de Narbonne Toulouse Cedex 31062 France			8. PERFORMING ORGANIZATION REPORT NUMBER N/A	
9. SPONSORING/MONITORING AGENCY NAME(S) AND ADDRESS(ES) EOARD PSC 802 BOX 14 FPO 09499-0200			10. SPONSORING/MONITORING AGENCY REPORT NUMBER CSP 97-1013	
11. SUPPLEMENTARY NOTES One book of Invited Papers and five volumes of Proceedings and Contributed Papers				
12a. DISTRIBUTION/AVAILABILITY STATEMENT Approved for public release; distribution is unlimited.			12b. DISTRIBUTION CODE A	
13. ABSTRACT (Maximum 200 words)  The Final Proceedings for XXIII International Conference on Phenomena in Ionized Gases, 17 July 1997 - 22 July 1997  kinetic, thermodynamics, and transport phenomena; elementary processes; low pressure glows; coronas, sparks, surface discharges, and high pressure glows; arcs; high frequency discharges; ionospheric magnetospheric, and astrophysical plasmas; plasma diagnostic methods; plasma surface effects; plasma processing; plasma flows; non ideal plasmas; waves and instabilities; non-linear phenomena; particle and laser beam interactions with plasmas; plasma sources of radiation; modeling; plasma for environmental issues; plasma thrusters; surface treatment; high pressure, non-thermal plasmas.				
14. SUBJECT TERMS  EOARD, Space Environment, Pulsed Power, Astrodynamics, Coatings, Fluids & Lubrication, Electromagnetics, High Power Generation, Lasers			15. NUMBER OF PAGES Too Many to Count	
			16. PRICE CODE N/A	
17. SECURITY CLASSIFICATION OF REPORT UNCLASSIFIED	18. SECURITY CLASSIFICATION OF THIS PAGE UNCLASSIFIED	19. SECURITY CLASSIFICATION OF ABSTRACT UNCLASSIFIED	20. LIMITATION OF ABSTRACT UL	

NSN 7540-01-280-5500

Standard Form 298 (Rev. 2-89)  
Prescribed by ANSI Std. Z39-18  
298-102

Reproduced From  
Best Available Copy

**XXIII**

FGI 708-97-W0048

CSP 97-1013

**I nternational  
C onference on  
P henomena in  
I onized  
G ases**

**Editors:** M.C. Bordage and A. Gleizes

19981216 004



**Proceedings**

**Contributed Papers**

**Vol. III**

**Saturday, July 19**

AQF99-03-0347

### **Organizers :**

Centre de Physique des Plasmas et leurs Applications de Toulouse (CPAT)  
Laboratoire de Génie Electrique de Toulouse (LGET)  
From the Université Paul Sabatier, Toulouse France.

### **International Scientific Committee**

R. d'Agostino	Italy
J. Allen	Great Britain
A. Bouchoule (Chairman)	France
E. Desoppere	Belgium
H. Kikuchi	Japan
E.E. Kunhardt	USA
J. Mentel	Germany
B. Milic	Yugoslavia
D. Morrow	Australia
A.H. Oien	Norway
A.A. Rukhadze	Russia
M. Sicha	Czech. Republic

### **Local Organizing Committee**

J.P. Bœuf	M.C. Bordage (Sec.)
H. Brunet (co-Chair.)	J.P. Couderc
B. Despax	M. Dziadowiec
A. Gleizes	B. Held
F. Massines	L.C. Pitchford (co-Chair.)
Y. Segui	S. Vacquie
M. Yousfi	G. Zissis

### **Sponsors**

Association pour le Développement de la Physique Atomique (ADPA)  
International Union of Pure and Applied Physics (IUPAP)  
Centre National de la Recherche Scientifique (CNRS)  
Université Paul Sabatier (UPS) of Toulouse  
Direction de la Recherche et Technologie (DRET)  
Commissariat à l'Energie Atomique (CEA), Cycle de Combustible  
Electricité de France through :  
    Club Arc Electrique, Club Chimie des Hautes Températures and Novelect  
Conseil Régional de la Région Midi-Pyrénées  
Conseil Général du Département de la Haute-Garonne  
Mairie de Toulouse  
CRT Plasma-Laser  
Union Radio Scientifique Internationale (URSI)  
US Department of Energy, US BMDO  
US Air Force through the EOARD

*The Local Organizing Committee wishes to express appreciation to the following corporations for their support :*

AGA S.A.	Thomson Tubes Electroniques
Motorola Semiconducteurs S.A.	Schneider Electric
Osram-Sylvania Inc.	Philips Lighting (for the Penning Award)

## FOREWORD

This volume is the third of five volumes which contain contributed papers that were accepted by the Local Organizing Committee of the XXIII ICPIG for presentation in poster sessions. These papers are to be listed in the INSPEC data base.

The contributions were submitted in camera-ready form by the authors. Therefore, the responsibility for the contents and the form of the papers rests entirely with the authors.

The first four volumes have been arranged by topics, the sequence of which corresponds to that of the respective poster sessions. The fifth volume is comprised of 'late' papers, those for which the authors registered after the deadline for printing of their papers.

The texts of the invited talks are to be published shortly after the conference in a special issue of Journal de Physique.

The editors would like to acknowledge the contributions of Mrs L. Fourmeaux, Mr J.M. Barachet and Mr J.P. Chauchepat in the preparation of these volumes. The computer file of contributed papers and authors was prepared by C. de Peco, and her careful execution of this task is gratefully acknowledged.

April 1997

The Editors

For additional copies of this publication, please contact :

M.C. Bordage, CPAT, Université Paul Sabatier, 118 Route de Narbonne, 31062  
Toulouse cedex 4 France

Printed in France, in the Université Paul Sabatier of Toulouse , 1997



Topic number	SCHEDULE FOR POSTERS	
<b>VOLUME 1</b> THURSDAY, JULY 17		
MORNING		
1	Kinetics, thermodynamics and transport phenomena (Part A)	
2	Elementary processes (Part A)	
6	High frequency discharges (Part A)	
13	Waves and instabilities, including shock waves (Part A)	
AFTERNOON		
1	Kinetics, thermodynamics and transport phenomena (Part B)	
2	Elementary processes (Part B)	
6	High frequency discharges (Part B)	
12	Non-ideal plasmas. Clusters and dusty plasmas	
13	Waves and instabilities, including shock waves (Part B)	
18	Plasmas for environmental issues	
<b>VOLUME 2</b> FRIDAY, JULY 18		
MORNING		
3	Low pressure glows (Part A)	
5	Arcs (Part A)	
17	Numerical modeling (Part A)	
AFTERNOON		
3	Low pressure glows (Part B)	
5	Arcs (Part B)	
11	Generation and dynamics of plasma flows	
14	Non-linear phenomena and self-organization processes	
17	Numerical modeling (Part B)	
<b>VOLUME 3</b> SATURDAY, JULY 19		
7	Ionospheric, magnetospheric, and astrophysical plasmas	
16	Plasma sources of radiation	
19a	Highly ionized, low pressure plasmas	
19b	High pressure, non-thermal plasmas	
<b>VOLUME 4</b> MONDAY, JULY 21		
MORNING		
4	Coronas, sparks, surface discharges and high pressure glows (Part A)	
8	Plasma diagnostic methods (Part A)	
10	Physical aspects of plasma chemistry, plasma processing of surface and thin film technology (Part A)	
AFTERNOON		
4	Coronas, sparks, surface discharges and high pressure glows (Part B)	
8	Plasma diagnostic methods (Part B)	
9	Plasma wall interactions, electrode and surface effects	
10	Physical aspects of plasma chemistry, plasma processing of surface and thin film technology (Part B)	
15	Particle and laser beam interaction with plasmas	
<b>VOLUME 5</b> LATE PAPERS		

## CONTENTS

### Topic 7 : Ionospheric, magnetospheric, and astrophysical plasmas.

MODELLING OF PULSE FLUCTUATION REFLECTOMETRY IN FUSION AND SPACE PLASMAS Heuraux S., Hacquin S., Leclert G., Boucher I., Fanack C.	III-2
A STUDY OF SUB TO SUPERSONIC OUTFLOW OF HELIUM FROM POLAR REGIONS Jacobsen L., M., Oien A.H.	III-4
NONLINEAR WHISTLER WAVE SCATTERING IN SPACE PLASMAS Yukhimuk V., Roussel-Dupre R.T.	III-6
GENERATION OF ELVES BY SPRITES AND JETS Taranenko Y., Roussel-Dupre R.T., Yukhimuk V., Symbalisty E.	III-8
HF ECHOES FROM IONIZATION POTENTIALLY PRODUCED BY HIGH ALTITUDE DISCHARGES Roussel-Dupre R.T., Fitzgerald T.J., Symbalisty E., Blanc E.	III-10
HIGH ALTITUDE ATMOSPHERIC DISCHARGES ACCORDING TO THE RUNAWAY AIR BREAKDOWN MECHANISM Symbalisty E., Roussel-Dupre R.T., Yukhimuk V., Taranenko Y.	III-12
COMPUTER AND PHYSICAL SIMULATIONS OF ELECTRODISCHARGE PHENOMENA NEAR THE NEUTRON STARS Skvortsov V.A., Vogel N.I.	III-14

### Topic 16 : Plasmas sources of radiation.

OPTIMIZATION OF THE RADIATIVE FLUX COMPUTATION FOR HIGH PRESSURE DISCHARGES Simonet F., Aubes M., Damelincourt J.J.	III-16
ROLE OF ATOMIC OXYGEN IN SELF-REGENERATION OF CO <sub>2</sub> LASER MIXTURES Cenian A., Chernukho A., Borodin V.	III-18
A COUPLED NEGATIVE GLOW-THERMIONIC CATHODE MODEL FOR LOW PRESSURE FLUORESCENT LAMP DISCHARGE Li Y.M.	III-20
MODELING AND DIAGNOSTICS OF RADIATION TRANSPORT IN HIGH PRESSURE DISCHARGES FOR LIGHTING Adler H.G., Lister G.G.	III-22
PARTICULES DENSITIES DETERMINATION IN HIGH PRESSURE MERCURY DISCHARGES Asselman A., Damelincourt J.J., Mouadili A., Sarroukh H.	III-24
VUV FLUORESCENCE OF TRIATOMIC IONIC EXCIMERS Delaporte Ph.C., Voitik M., Fontaine B., Sentis M., Uteza O.	III-26

HOLLOW CATHODE EFFECTS IN A PULSED CAPILLARY DISCHARGE Favre M., Choi P., Moreno J., Dumitrescu-Zoita C., Zambra M., Chuaqui H., Wyndham E.	III-28
HIGH ENERGY PHOTONS EMITTED FROM A HIGH VOLTAGE FAST DISCHARGE IN VACUUM AND IN LOW PRESSURE GASES Khacef A., Cachoncinlle C., Viladrosa R., Robert E., Pouvesle J.M.	III-30
FROM THE « THIRD CONTINUUM » TO THE « MOLECULAR ION CONTINUA » OF RARE GASES Robert E., Cachoncinlle C., Khacef A., Viladrosa R., Pouvesle J.M.	III-32
TEMPORAL AND RADIAL BEHAVIOUR OF THE METASTABLE DENSITY IN A PULSED XENON DISCHARGE AT MEDIUM PRESSURE Kindel E., Schimke C., Loffhagen D.	III-34
EXPERIMENTAL INVESTIGATIONS OF MICRODISCHARGES IN EXCIMER BARRIER DISCHARGE LAMPS Kling R., Gasteiger S., Neiger M.	III-36
EXPERIMENTAL STUDY AND MODELLING OF A DC-EXCITED SLAB CO <sub>2</sub> LASER DISCHARGE Van Egmond C., Leys C., Poppe F., Desoppere E	III-38
VUV EMISSION GENERATION AT HELIUM PLASMA RECOMBINATION Ivanov V.V., Klopovskiy K.S., Kopytin A.A., Lopaev D.V., Rakhimov A.T., Rakhimova T.V.	III-40
CROSS-TALK IN AN AC MATRIX PLASMA DISPLAY CELL : 2D INTERACTIVE SIMULATION Punset C., Bœuf J.P., Pitchford L.C.	III-42
PRODUCTION OF CAPILLARY DISCHARGES FOR THE STUDY OF DISCHARGE PUMPED SOFT X-RAY LASER Rosenfeld W., Dussart R., Hong D., Cachoncinlle C., Hure L., Viladrosa R., Pouvesle J.M., Fleurier C.	III-44
GENERATION OF HIGH-POWER MICROWAVES DUE TO PROPAGATION OF A RELATIVISTIC ELECTRON BEAM IN PLASMA Birau M., Buzzi J.M., Caillez Y., Wiolland R., Saulle C., Krasilnikov M.A., Kuzelev M.V., Loza O.T., Rukhadze A.A., Strelkov P.S., Shkvarunets A.G., Ulyanov D.K.	III-46
IMPROVEMENT OF THE METAL VAPOUR DISTRIBUTION IN CCRF EXCITED METAL VAPOUR LASERS BY CATAPHORESIS Teuner D., Schulze J., Schmidt E., Mentel J.	III-48
THE MEAN ELECTRON ENERGY IN RF AND HC DISCHARGES Kocik M., Grabowski D., Mizeraczyk J., Heldt J., Schulze J., Mentel J.	III-50
OPTICAL, RADIO AND X-RAY RADIATION OF RED SPRITES PRODUCED BY RUNAWAY AIR BREAKDOWN Yukhimuk V., Roussel-Dupre R.T., Symbalisty E., Taranenko Y.	III-52
FULLERENE AS THE NEW EMITTING ADDITIVE FOR A LOW PRESSURE GAS DISCHARGE LIGHT SOURCE Milenin V.M., Timofeev N.A., Kidalov S.V., Kozyrev S.V., Vul A.Ya.	III-54

THE EFFECTIVE LOW PRESSURE GAS DISCHARGE SOURCE OF OPTICAL RADIATION BASED ON HYDROXYL OH Milenin V.M., Timofeev N.A., Kidalov S.V., Kozyrev S.V., Vul A.Ya.	III-56
SPATIALLY ONE-DIMENSIONAL MODELLING OF A STABILIZED DISCHARGE PUMPED XECL* LASER Gortchakov S., Loffhagen D., Winkler R.	III-58
EXPLORING THE INFLUENCE OF AMBIPOLAR DIFFUSION MECHANISM IN A HG-AR LOW PRESSURE POSITIVE COLUMN UNDER AC OPERATING CONDITIONS BY A SELF-CONSISTENT TIME-DEPENDENT COLLISIONAL-RADIATIVE CODE Porras D., Zissis G.	III-60
POWER INTERRUPTION EXPERIMENTS ON A HIGH PRESSURE SULPHUR DISCHARGE Johnston C., Jonkers J., Van der Mullen J.A.M., Schram D.C.	III-62
MEASUREMENTS ON A HIGH CURRENT CONVENTIONAL FLUORESCENT LAMP AND COMPARISON WITH THE NUMERICAL MODEL Jonkers J., Herben P.G.J.M., Van Dijk J., Schram D.C., Van der Mullen J.A.M.	III-63

**Topic 19a :**  
**Highly ionized, low pressure plasmas**  
**(plasma thrusters, ion sources and surface treatment).**

A DIFFUSION MODEL FOR NEAR WALL CONDUCTIVITY IN PLASMA THRUSTERS Degond P., Latocha V.	III-64
OPTICAL AND ELECTRICAL INVESTIGATIONS ON PLASMA OSCILLATIONS OF SPT THRUSTERS Darnon F., Lyszyk M., Bouchoule A.	III-66
SPT AS GAS-DISCHARGE DEVICE Bugrova A.I., Morozov A.I.	III-68
ONE DIMENSIONAL MODELS OF STATIONARY PLASMA THRUSTER Garrigues L., Bœuf J.P., Pitchford L.C.	III-70
ARGON METASTABLE DENSITY IN AR-O <sub>2</sub> AND AR-TEOS HELICON PLASMAS Le Brizoual L., Granier A., Briaud Ph.	III-72
EMISSION SPECTRA OF O <sub>2</sub> /TEOS PLASMAS USED FOR SiO <sub>x</sub> C <sub>y</sub> H <sub>z</sub> DEPOSITION Granier A., Mage L., Nicolazo F., Raynaud P., Segui Y., Turban G., Vallee C., Vervloet M.	III-74
HELICON PLASMAS IN VARIOUS MAGNETIC FIELD CONFIGURATIONS Braginskiy O.V., Kovalev A.S., Lopaev D.V., Vasilieva A.N.	III-76
INVESTIGATION OF SMALL, CLOSED ELECTRON DRIFT, SPT-50 Guerrini G., Michaut C., Vesselovzorov A.N., Dudeck M., Bacal M.	III-78
PIC-MC MODELLING OF A RF MAGNETRON DISCHARGE Minea T.M., Bretagne J., Gousset G.	III-80

DISTRIBUTION OF SURFACE DISCHARGE FOR OZONE GENERATION Murata T., Okita Y., Terai K.	III-82
COMPARATIVE BEHAVIOUR OF DC POSITIVE POINT-TO-PLANE DISCHARGES IN NITROGEN AND DRY AIR FOR PRESSURES AROUND 50 TORR Ercilbengo A.E., Loiseau J.F., Peyrous R., Spyrou N., Soulem N., Held B.	III-84
EFFECT OF SAMPLE-CATHODE SHAPE IN DC GLOW DISCHARGE ION SOURCE FOR MASS SPECTROMETRIC ANALYSIS Baude S., Lorthioir S., Blaise G., Fiala A., Pitchford L.C.	III-86
CHARACTERISTICS OF LOW POWER HF 10-CM TECHNOLOGICAL ION SOURCE Kondranin S.G., Kralkina E.A., Koh S.K., Jang H.G., Choi W.K., Jung H.J., Antonova T.B., Bougrov G.E., Pavlov V.B., Rukhadze A.A., Alexandrov A.F.	III-88
MASS SPECTROMETRIC STUDY OF SF <sub>6</sub> PLASMA BEAM EXTRACTED FROM AN ECR ION SOURCE Chevolleau T., Tessier P.Y., Cardinaud C., Turban G.	III-90

### Topic 19b : High pressure, non-thermal plasmas.

DETERMINATION OF ELECTRON DENSITY AND TEMPERATURE OF AN ECR PLASMA BY VUV SPECTROSCOPY Berreby R., Hitz D., Druetta M.	III-92
EFFECT OF PARTIAL DISCHARGES ON SULFUR HEXAFLUORIDE(SF <sub>6</sub> ) BY PRODUCTS Clavreul R., Hoang T., G., Essolbi R.	III-94
THE EXPERIMENTAL STUDY OF THE RELAXATION PROCESSES IN HE WITH ADMIXTURE OF O <sub>2</sub> Glosik J., Bano G., Zakouril P.	III-96
OZONE PRODUCTION IN CYLINDER-TO-CYLINDER PROXIMITY BARRIER DISCHARGES IN OXYGEN Veis P., Goldman M., Goldman A., Haug R., Petit L.	III-98
DIAGNOSTIC OF A PLASMA DISPLAY PANEL CELL : SPECTROSCOPIC AND KINETIC STUDY. ELECTRIC STUDY OF LIGHT EFFICIENCY Hirech A., Destombes V., Guillot Ph., Galy J., Brunet H.	III-100
THE ONE ATMOSPHERE GLOW DISCHARGE AS A STERILIZATION AGENT Laroussi M., Alexeff I., Gillispie K., Saylor G.S.	III-102
THEORETICAL AND EXPERIMENTAL INVESTIGATION OF A DISCHARGE WITH LIQUID NONMETALLIC ELECTRODES IN AIR AT ATMOSPHERIC PRESSURE Afanas'ev V.P., Andre P., Barinov Yu.A., Faure G., Kaplan V.B., Lefort A., Shkol'nik S.M.	III-104
ELECTRICAL BEHAVIOR OF A DIELECTRIC BARRIER CONTROLLED ATMOSPHERIC PRESSURE GLOW DISCHARGE Decomps P., Massines F., Mayoux C.	III-106

- THE INFLUENCE OF THE SURROUNDING ATMOSPHERE ON PLASMAS SUSTAINED BY THE  
« TORCHE À INJECTION AXIALE » III-108  
Jonkers J., Selen L.J.M., Hartgers A., Van der Mullen J.A.M., Schram D.C.
- THE ROLE OF  $\text{He}_2$  MOLECULES IN PLASMA KINETICS OF HIGH PRESSURE HELIUM FAST  
DISCHARGES III-110  
Treshchalov A., Korge H., Chizhik A., Vill A.

*Topic 7*

**Ionospheric, magnetospheric and  
astrophysical plasmas.**

# MODELLING OF PULSE FLUCTUATION REFLECTOMETRY IN FUSION AND SPACE PLASMAS

S. Heuraux, S. Hacquin, G. Leclert, I. Boucher and C. Fanack

Laboratoire de Physique des Milieux Ionisés (Unité de Recherche Associée au CNRS 835), Faculté des Sciences, Université de Nancy I, B.P.239, 54506 Vandoeuvre Cedex (FRANCE) e-mail: heuraux@lpmi.u-nancy.fr

## 1. Introduction

The reflectometry is widely used in plasma fusion and in space plasmas as a tool. For fusion plasmas, it is wellknown that density fluctuations induce errors on the density profile reconstruction which may lead in some cases to unrealistic profiles[1]. In space plasma physics, the backscattered pulse due to artificial irregularities (PAI) are used to evaluate some plasma parameters. The present work has two aims. First, it studies some effects of coherent density fluctuations on the profile reconstruction; specifically, it focuses on the role of resonant Bragg backscattering (i.e. there is a resonant condition  $k_f = 2 \cdot k(x)$  between the local incident wavenumber  $k(x)$  and the fluctuation wavenumber  $k_f$ ) in pulse reflectometry. Second, it gives a quantitative model of the behaviour of the wave backscattered in the ionospheric E region in the PAI experiment[2]. We have implemented a code which solves the wave propagation equation in one space dimension (particular cases with 2 space dimensions can be treated). This code describes either the O-mode in a magnetized plasma or the electromagnetic wave in an isotropic plasma. For each case, we discuss briefly about the choice of the inputs and the limitations of the simulation. Then, we conclude by a discussion on what the 1D code can do or cannot describe.

## 2. Basic equation and numerical method

The one-dimensional wave equation can be written:

$$\partial_t^2 E_z - c^2 \partial_x^2 E_z + \omega_{pe}^2 E_z = 0 \quad (1)$$

where  $E_z$  is a function of  $x$  and  $t$  and  $\omega_{pe}$  depends on  $x$  only (i.e. the plasma is in a steady-state). Absorbing boundary conditions (no reflection at the boundaries)[3] are imposed on the edges of the numerical grid. The numerical method uses a centered finite difference scheme with a second-order accuracy for the D'Alembertian and splits the  $\omega_{pe}^2 E_z$  in terms  $E_z$  taken at different times. The space step  $\Delta x = c \Delta t$  (where  $\Delta t$  is the time step) satisfies the stability criterion for this scheme and permits to determine easily the initial conditions for a right-going pulse launched in vacuum. The numerical accuracy is consistent with the order of the numerical error. Under the assumptions mentioned before, the explicit scheme writes

$$E_{ij+1} = \frac{1}{1 + \omega_{pe}^2(i)/4} \left\{ -\frac{\omega_{pe}^2(i)}{2} E_{ij} + E_{i+1,j} + E_{i-1,j} \right\} - E_{i,j-1}$$

where the  $i$  and  $j$  indices represent space and time respectively. The initial conditions require that  $E_{i,0}$  and  $E_{i,1}$  be specified; for instance, in vacuum  $E_{i,1} = E_{i,0}$ . The outgoing conditions can be found in the reference [3].

## 3. Profile reconstruction with density fluctuations

Two distinct situations have been simulated with the use of appropriate initial conditions and diagnostics: (i) classical (CW) reflectometer, and (ii) pulsed radar reflectometer. For simplicity, to test the influence of density fluctuations on these systems, a linear density profile was chosen, although the results can easily be extended. Modulated (carrier wavenumber  $k_f$ ) Gaussian density perturbations are used. The phase shift or time delay is computed for different frequencies, and an Abel inversion is performed to reconstruct the density profile.

For the classical reflectometer, the initial pulse  $L_p$  is long enough ( $L_p > 4(x_c - x_0)$ , ( $x_c$  and  $x_0$  are the plasma cut-off and edge positions) so that the ingoing and outgoing parts of the pulse coexist all over the plasma. This long pulse propagative code has been compared to the (steady-state) Helmholtz code. We obtain the same results for the phase shift with or without density fluctuations. As in the Helmholtz case[4], spectral effects due to the width of the density perturbation are observed. The phase shift due to Bragg backscattering is either the image of the density perturbation itself (spatial regime) or the image of its Fourier transform (spectral regime). In the spatial regime, the phase shift varies like  $L_g^{1/2}$ , where  $L_g$  is the gradient length. For  $L_g \sim 50\lambda_0$ , density fluctuations begin to modify the profile reconstruction if their level is greater than  $\sim 10\%$ .

For the pulsed radar reflectometer, there is an optimal pulse length  $\tau_{opt}$  which minimizes the reflected pulse length (this minimal length is twice the incident pulse length). This optimal length allows to determine the density gradient length at the cut-off position. For a linear density profile  $\tau_{opt} = \sqrt{8 \ln 2 k_0 L} / \omega_{pe}$ . Spectral effects are also found in this case. Usually, in space plasma physics, the pulse width is greater than the optimal length, the reflected pulse is the image of the incident pulse (spatial case). The incident wavenumber spectrum is narrow so the Bragg backscattering process is sharply localized and only a narrow frequency band leads to perturbations of the reconstructed profile. Typically, if one assumes that the time delay is defined by the maximal amplitude of the reflected pulse, the reconstructed profile is modified by the density



fluctuations when their level is  $\sim 10\%$ . Figures 1 and 2 show respectively the pulse shape and the profile obtained in such a case. A lower threshold would lead to a greater influence of the fluctuations. Long wavelength perturbations near the cutoff do not backscatter the wave, but they can also induce large modifications of the time delay.

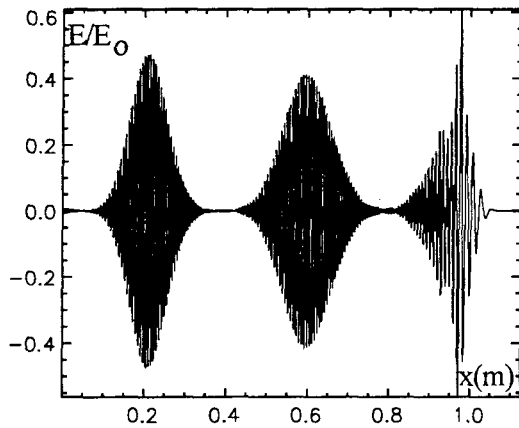


Fig1. Shape of the reflected pulse with  $\Delta n/n \approx 10\%$ . Backscattering corresponds to the leftmost pulse.

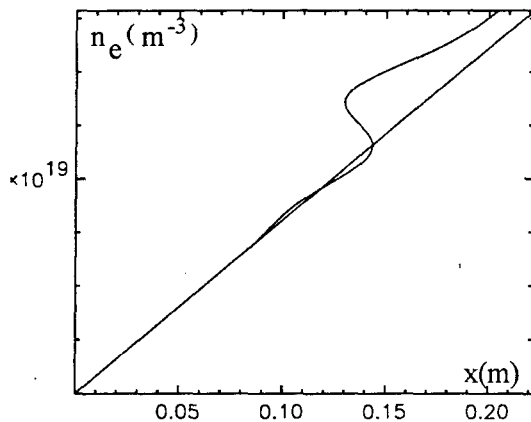


Fig 2. Comparison of the reconstructed profiles with and without fluctuation

#### 4. Modelling of the PAI experiment

In this experiment the ionosphere is heated by a large amplitude quasicontinuous (.1 s to 3 mn) HF wave that produces a nonlinear density perturbation. This perturbation is then analyzed by a radar pulse (50  $\mu$ s, spatial regime above mentioned). Assuming that

electrons behave adiabatically in the ponderomotive potential, the nonlinear density perturbation is proportional to  $E_z^2/(T_e(x)+T_i(x))$ . It can be obtained by solving iteratively the 1D Helmholtz equation, where the first iteration starts with the day-time density and temperature profiles of the ionosphere. The resulting perturbed profile is then introduced in the 1D propagative wave equation that models the probing wave. The iterated Helmholtz equation shows that the nonlinear density perturbation is larger in the E-layer, since the temperature is lower in this region. Accordingly the propagative wave equation gives a significant backscattered pulse coming mainly from the E-region, since the nonlinear density perturbation satisfies the Bragg rule everywhere. Figure 3 gives the behaviour of the received pulse. Furthermore, at large fluctuation amplitude, there is a nonlinear broadening of the Bragg rule  $k_f = 2k(x)$ , that is, the probing frequency can be slightly different from the heating frequency.

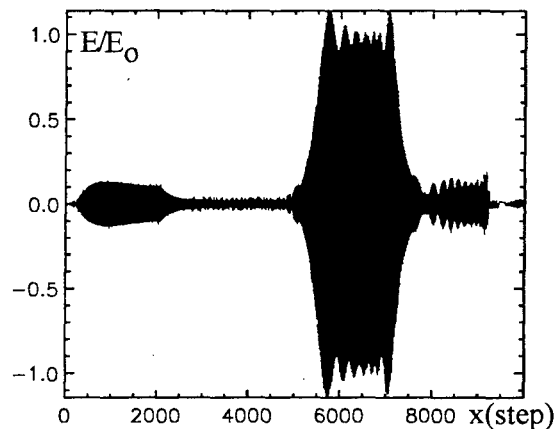


Fig 3. Backscattered pulse shape versus time in simulated PAI experiment

However the iterative method of solution of the nonlinear Helmholtz equation can be used only for moderate nonlinearity. This 1D analysis can be extended to the spherically symmetrical case. The  $1/r$  decay of the field amplitude shifts the maximal nonlinearity towards lower altitudes, hence the Bragg backscattering from the E-region is even more pronounced.

#### References:

- [1] C Laviron, A.J.H. Donné, M.E. Manso and J. Sanchez " Reflectometry techniques for density profile measurements on fusion plasmas" *Plasma Phys Cont Fusion*, **38** (1996) 905.
- [2] G.I. Terina "Characteristics of signals scattered by artificial ionospheric turbulence" *J. Atmos. Teresr Phys.* **57** (1995) 273.
- [3] R. L. Higdon "Absorbing boundary conditions for difference approximations to the multi-dimensional wave equation" *Math. Computation* **47** (1986) 437.
- [4] C. Fanack, I. Boucher, F. Clairet, S.Heuraux, G. Leclert and X.L. Zou "Ordinary-mode reflectometry : modification of the scattering and cut-off responses due to the shape of localized density fluctuations" *Plasma Phys Control. Fusion* **38** (1996) 1915.

# A study of sub- to supersonic outflow of helium from polar regions

Liv M. Jacobsen and Alf H. Øien

Nansen Environmental and Remote Sensing Center, Edv. Griegsv. 3A, 5037 Bergen, Norway,  
Department of Applied Mathematics, University of Bergen, Allégt. 55, 5007 Bergen, Norway

## 1. Introduction

In polar regions where magnetic field lines are open a continuous outflow of light ions takes place (polar wind, [1], [2]). In particular, helium released from radioactive decay in the Earth crust eventually, when ionized, may be transported away in this way from the Earth atmosphere. The acceleration force upwards is the ambipolar electric field set up by electrons and heavy ions (in particular oxygen) in the upper atmosphere, and counteracting this force both the gravitation and the friction force from the background gas, together with pressure, play an important role. In the model presented we use a special method to show how helium ions are accelerated to supersonic velocity upwards. In particular we study the relative influence of the different forces and the position of the sonic point with varying parameter values.

## 2. Model

The model equations for the helium fluid are obtained by taking velocity moments of the kinetic equation. We use a Fokker-Planck collision term for light helium ions of mass  $m$  interacting with heavy oxygen ions (subscript '2'). Other collisional interactions are neglected in this model. The collision term is simplified assuming a large mass ratio  $m_2/m$ , and hence energy exchange between light and heavy ions is neglected.

### 2.1 Conservation equations

We further limit the set of equations for the helium fluid to equations only for number density  $n$ , fluid velocity  $u$  in the  $z$ -direction and temperature  $T$ , i.e. a 5(3) moment approximation. Thus we obtain the continuity equation,

$$u \frac{dn}{dz} + n \frac{du}{dz} = 0,$$

the momentum equation

$$\kappa T \frac{dn}{dz} + nmu \frac{du}{dz} + \kappa n \frac{dT}{dz} = \frac{T_e}{(T_e + T_2)} \frac{GMm_2 n}{(R + z_0 + z)^2} - \frac{MGm}{(R + z_0 + z)^2} - K \exp\left\{-\frac{GMm_2}{\kappa(T_e + T_2)(R + z_0)}\left(1 - \frac{R + z_0}{R + z_0 + z}\right)\right\} \frac{nu}{(T^{3/2} + \frac{m}{2\kappa} T^{1/2} u^2)}$$

where  $K = \frac{4\pi}{3} \Gamma m (\frac{m}{2\pi\kappa})^{3/2} n_{20}$ , and the (reduced) energy equation,

$$mu \frac{du}{dz} + \frac{5}{2} \kappa \frac{dT}{dz} = \frac{T_e}{(T_e + T_2)} \frac{GMm_2}{(R + z_0 + z)^2} - \frac{GMm}{(R + z_0 + z)^2}$$

$R$  is Earth radius,  $z_0$  the lower edge or baseheight (subscript '0') of the region in the ionosphere we study, and  $z$  the height above this level.  $T_2$  and  $T_e$  are the oxygen and electron temperatures (both assumed

constant), and  $n_{20}$  the oxygen density at the lower edge.  $G$ ,  $M$ ,  $\Gamma$  and  $\kappa$  are respectively the Gravitational constant, the Earth mass, the Coulomb logarithm and the Boltzmann constant. The terms on the right hand side of the momentum equation are respectively the ambipolar electric force field set up by electrons and heavy ions, the gravitation force and the friction force due to helium-oxygen interactions. The energy equation shows the interplay between directional- and thermal-energy and electric- and gravitational energy of helium ions.

### 2.2 Integrating through the singularity

Non-dimensional variables  $\xi = \frac{z}{z_0}$ ,  $\rho = \frac{n}{n_0}$ ,  $\omega = \frac{u}{u_s}$  and  $\tau = \frac{T}{T_0}$  are introduced where  $u_s = \sqrt{\frac{\kappa T_0}{m}}$  is a sonic speed of helium. The set of equations may be put on the non-dimensional form,  $A \cdot \frac{d\sigma}{d\xi} = \mathbf{b}$ , or

$$\begin{pmatrix} \omega & \rho & 0 \\ \tau & \rho\omega & \rho \\ 0 & \omega & \frac{5}{2} \end{pmatrix} \cdot \frac{d}{d\xi} \begin{pmatrix} \rho \\ \omega \\ \tau \end{pmatrix} = \begin{pmatrix} 0 \\ \frac{A\rho}{(r+1+\xi)^2} - \frac{B\rho}{(r+1+\xi)^2} - C \exp\{-D(1 - \frac{r+1}{r+1+\xi})\} \frac{\rho\omega}{\tau^{3/2} + \frac{1}{2}\tau^{1/2}\omega^2} \\ \frac{A}{(r+1+\xi)^2} - \frac{B}{(r+1+\xi)^2} \end{pmatrix}$$

On the right hand side the constants  $A$ ,  $B$ ,  $C$  and  $D$ ,

$$A = \frac{T_e}{T_e + T_2} \frac{GMm_2}{\kappa_0 T_0}, \quad B = \frac{GMm}{\kappa_0 T_0}, \quad C = \frac{\Gamma m^2 2^{1/2} n_{20} z_0}{\pi^{1/2} \kappa^2 3 T_0^2}, \quad D = \frac{GMm_2}{\kappa_0 (T_e + T_2)}$$

express the order of magnitude of the forces acting on the helium ions, and  $r = \frac{R}{z_0}$ . From Cramer's rule,

$$\frac{d\sigma_i}{d\xi} = \frac{N_i(\xi, \sigma)}{\Delta(\sigma)}, \quad i = 1..3, \text{ where } \Delta(\sigma) = \det(\mathbf{A})$$

and  $N_i(\xi, \sigma)$  are similar determinants except that vector  $\mathbf{b}$  replaces the  $i$ 'th column. The system of equations is singular when  $\Delta = \frac{\rho}{2}(3\omega^2 - 5\tau)$  equals zero, i.e. when  $\omega = \omega_s = (\frac{5}{3}\tau)^{1/2}$ , the sonic speed of helium ions. For a solution to exist at the sonic velocity also the  $N_i(z, \sigma)$ ,  $i = 1..3$ , must be equal zero there. A remarkable property of the system of equation is that when  $\Delta(\sigma) = 0$  and  $N_i(z, \sigma) = 0$  for one of  $i = 1..3$ , then all the other  $N_i(z, \sigma)$  equal zero also, [3].

The equations are transformed into an autonomous form of 4 equations of 4 unknowns ( $z, \sigma$ ) by setting, [3],

$$\frac{dz}{dt} = \Delta(\sigma), \quad \frac{d\sigma_i}{dt} = \frac{d\sigma_i}{dz} \frac{dz}{dt} = N_i(z, \sigma), \quad i = 1..3$$

thus formally transforming the singularity into an equilibrium point in the  $(z, \sigma)$ -space. A closer study of solutions of the 4 equations in the neighborhood of the singularity in the  $(z, \sigma)$ -space reveals the equilibrium point is a saddle point in a two-dimensional subset of the 4 dimensional  $(z, \sigma)$ -space. Two solutions pass exactly through the singularity, one from sub- to supersonic velocity, and one from super- to subsonic velocity. The position of the singular (sonic) point (subscript 's') is given for instance by  $N_1(z, \sigma) = 0$ , i.e. by the zero of the function

$$\varphi(\xi_s) = \frac{3}{2} \frac{A}{(r+1+\xi_s)^2} - \frac{3}{2} \frac{B}{(r+1+\xi_s)^2} - C \exp\left\{-D\left(1 - \frac{r+1}{r+1+\xi_s}\right)\right\}^{\frac{2\sqrt{15}}{11}} \frac{1}{\tau_s}$$

### 3. Solutions

We seek solutions passing through the singularity, and let  $z_0 = 250\text{km}$ . This is approximately the position of maximal ion density.  $n_{2,0}$ , the oxygen ion and electron density, is set to  $10^{10}/\text{m}^3$ , the electron and oxygen ion temperatures to  $T_e = 3000\text{K}$  and  $T_2 = 1000\text{K}$ , respectively. For the helium ion fluid we use the following boundary conditions at the lower edge  $\xi = 0$ :  $\rho(0) = 1$ ,  $T(0) = T_0 = 1000\text{K}$ ,  $\rho(0)\omega(0) = \omega(0) = F$ , the constant flux, and  $\tau(0) = 1$ . The position of the singular point is found from  $\varphi(\xi_s) = 0$  and a value of  $\tau_s$  in this equation that matches the boundary condition  $\tau(0) = 1$  when integrating from the singularity to  $\xi = 0$ . The direction of the solutions through the singularity is found from solving a linearized version of the fluid equations in a neighborhood of the singularity. When  $\tau_s$  is determined, and hence  $\omega_s$ , using  $\omega(0)$  and the flux  $F$ , the helium density at  $\xi_s$  becomes  $\rho(\xi_s) = \frac{\omega(0)}{\omega(\xi_s)}$ .

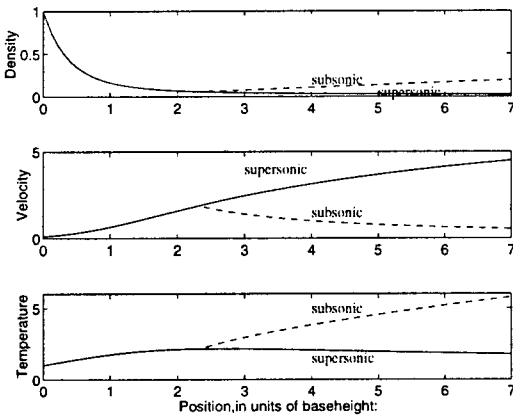


Fig.1: Non-dimensional density, velocity and temperature of vertically flowing helium with parameter values as given in text.

Fig. 1 shows typical results from calculations, and Fig. 2 depicts the corresponding sum of accelerating forces. Both physical solutions that pass smoothly through the singularity (full line), and non-physical solutions (dashed) are shown. The singularity is at  $\xi_s = 2.3$ .

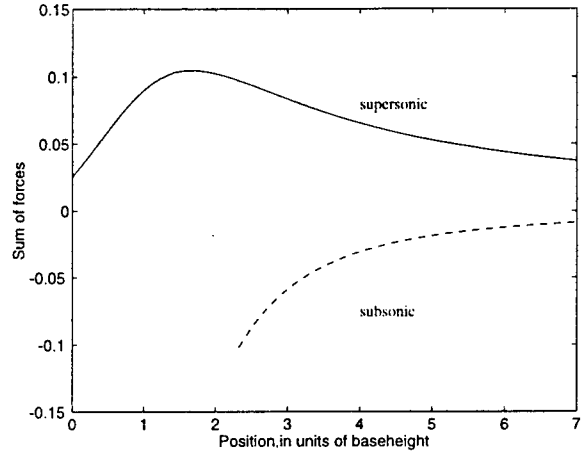


Fig.2. Sum of non-dimensional forces per unit volume. Parameter values as given in text.

We study how the position of the singularity varies with parameters  $n_{2,0}$ ,  $T_e$ ,  $T_2$  and  $T_0$  in A, B, C and D related to the different forces:

- (i) Varying  $n_{2,0}$  from  $5 \cdot 10^9/\text{m}^3$  to  $10^{11}/\text{m}^3$ ,  $\xi_s$  grows from 1.5 to 4.4: As oxygen density rises friction increases, and the helium ions have to accelerate over longer distance to reach the sonic point.
- (ii) Varying  $T_e$  from 1000K to 5000K: As  $T_e$  increases, the diffusion of electrons increases relative to ions, and the ambipolar electric field increases. However, the oxygen density will decrease more slowly with height. Hence up to  $T_e \approx 1400\text{K}$   $\xi_s$  falls from approximately 1.75 to 1.65. Here the growth of the electric field dominates the acceleration. From 1400K upwards  $\xi_s$  grows to 2.65. Here the increased oxygen density, and hence friction, dominates.
- (iii) Varying  $T_2$  from 1000K to 2800K, the value of  $\xi_s$  rises steadily from approximately 2 to 5.75. This is because the diffusion of oxygen ions rises and reduces the ambipolar field and also leads to a slower decrease of the oxygen density with height.
- (iv) Varying  $T_0$  from 500K to 2000K, the value of  $\xi_s$  decreases in a monotonic way: The decrease is due to lower collision frequency  $\nu = \frac{\Gamma n_2}{v}$  with increasing temperature, and hence lower friction, and the helium accelerates to the sonic velocity over shorter and shorter distances.

### 4. References

- [1] W.I. Axford: J.Geophys.Res., **73** (1968), 6855.
- [2] E. Leer, Ø. Lie-Svendsen, E. Lyngdal Olsen, V.H. Hansteen: J.Geophys.Res., **101** (1996) 17,207.
- [3] Z. Bilicki, C.Dafermos, J. Kestin, G. Majda, D.L. Zeng: Int. J. Multiphase Flow, **13** (1987) 511.

# Nonlinear whistler wave scattering in space plasmas

Vyacheslav Yukhimuk and Robert Roussel-Dupre

(Space and Atmospheric Sciences Group, MS D466, Los Alamos National Laboratory, Los Alamos, NM)

## 1. Introduction

In this paper the evolution of nonlinear scattering of whistler mode waves by kinetic Alfvén waves (KAW) in time and two spatial dimensions is studied analytically. We suggest this nonlinear process as a mechanism of kinetic Alfvén wave generation in space plasmas. This mechanism can explain the dependence of Alfvén wave generation on whistler waves observed in magnetospheric and ionospheric plasmas. The observational data [1,2] show a dependence for the generation of long periodic pulsations Pc5 on whistler wave excitation in the auroral and subauroral zone of the magnetosphere. This dependence was first observed by Ondoh T. I. [1]. For 79 cases of VLF wave excitation registered by Ondoh at College Observatory (L=64.6 N), 52 of them were followed by Pc5 geomagnetic pulsation generation. Similar results were obtained at the Loparskaia Observatory (L=64 N) [2] for auroral and subauroral zone of the magnetosphere. Thus, in 95% of the cases when VLF wave excitation occurred the generation of long periodic geomagnetic pulsations Pc5 were observed. The observations also show that geomagnetic pulsations Pc5 are excited simultaneously or insignificantly later than VLF waves [2]. In fact these two phenomena are associated genetically: the excitation of VLF waves leads to the generation of geomagnetic pulsations Pc5 [2]. The observations [3] show intensive generation of geomagnetic pulsations during thunderstorms. Using an electromagnetic noise monitoring system covering the ULF range (0.01-10 Hz) A.S. Fraser-Smith observed intensive ULF electromagnetic wave during a large thunderstorm near the San-Francisco Bay area on September 23, 1990. According to this data the most significant amplification in ULF wave activity was observed for waves with a frequency of 0.01 Hz and it is entirely possible that stronger enhancements would have been measured at lower frequencies.

## 2. Theoretical results

We use two-fluid magnetohydrodynamics and kinetic plasma theory to describe three wave interactions. We consider the parametric decay of a whistler wave WW into a KAW and another whistler wave:

$$WW \rightarrow WW + KAW$$

We assume that the process takes place in a locally uniform plasma with a uniform magnetic field because the wave length of the interacting waves is less than the scale size of the background ionospheric plasma inhomogeneity by about three order of magnitude. We select the direction of magnetic field line to be parallel to the z-axis of a Cartesian system of coordinates. The conservation of energy and momentum in this process is reflected in the frequency and wave vector matching conditions:

$$\begin{aligned}\omega_0 &= \omega_1 + \omega_A \\ \vec{k}_0 &= \vec{k}_1 + \vec{k}_A\end{aligned}\quad (1)$$

Where  $\omega_0, k_0$  are the frequency and wave vector of whistler pump wave;  $\omega_1, k_1$  are the frequency and wave vector of scattered WW;  $\omega_A, k_A$  are the frequency and wave vector of the KAW. For the case when the plasma parameter  $\beta \ll 1$ , the electric field of the KAW can be written:

$$\vec{E}_A = -\vec{\nabla}\varphi_A - \frac{1}{c}\frac{\partial}{\partial t}A_z\vec{e}_z\quad (2)$$

By using the set of two - fluid MHD equations we obtain the dispersion equation for KAW coupling with whistler waves:

$$\eta_A \varphi_A = \mu_A E_0 E_1^* \quad (3)$$

Where  $E_0$  is the electric field of whistler pump wave;  $\eta_A = \omega_A^2 - k_{Az}^2 V_A^2 (1 + k_{Ax}^2 \rho_s^2)$

From the set of two - fluid MHD equations we obtain dispersion equation for WW coupling with KAW and whistler pump wave:

$$\eta_1 \varphi_1 = \mu_1 E_0 \varphi_A^* \quad (4)$$

Where  $\eta_1 = \omega_1^2 - c^4 k_1^2 k_{1z}^2 \omega_{Be}^2 / \omega_{pe}^2$

and  $\mu_A, \mu_1$  are the coupling coefficients.

We solved this system of nonlinear dispersion relations (3,4) numerically taking into account

the frequency and wave vector matching conditions (1), and attenuation factors for KAWs and WWs known from kinetic plasma theory, and assuming an amplitude for the whistler pump wave of  $E=1$  mV/m, for the typical ionospheric plasma parameters at an altitude of 300 km. The dependence of the instability growth rate on the angle between the whistler pump wave vector and the geomagnetic field line is shown in Fig. 1.

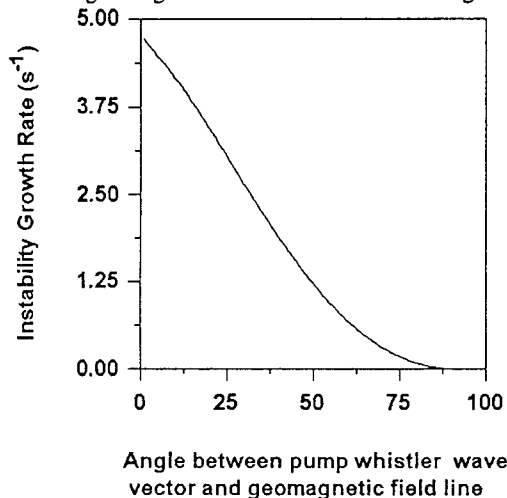


Fig. 1

Figure 2 shows the dependence of the instability growth rate on the angle between the scattered whistler wave vector and the geomagnetic field line.

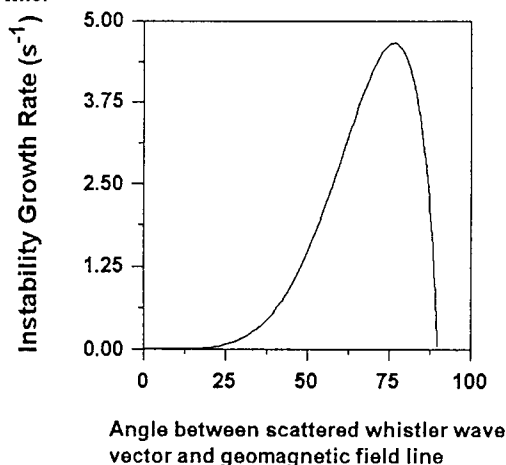


Fig. 2

### 3. Discussion and conclusion

Using a two-fluid MHD approach to study three wave interactions of whistler mode waves with

KAWs (which can interact with other types of waves much more efficiently than MHD Alfvén waves because of the presence of a longitudinal electric field component for the KAW [4,5]) we conclude that VLF whistler waves can be scattered by ULF kinetic Alfvén waves, and that the latter will be enhanced in such cases. The amplification of ULF waves is indeed observed during thunderstorms, simultaneously with excitation of VLF electromagnetic radiation[3]. Some recent satellite observations also show the presence of KAWs in the magnetosphere and in the topside of the ionosphere [6,7]. In the magnetosphere the long-periodical geomagnetic pulsation generation dependence on whistler waves is observed as well. This dependence was first noted in [1]. Similar results were obtained for the subauroral zone in [2]. In the auroral zone the geomagnetic pulsation generation was observed simultaneously or later than whistler excitation. It can be concluded that whistler excitation in the magnetosphere leads to long-periodical geomagnetic pulsation generation. The mechanism discussed in this paper can be applied for the case of whistler wave propagation in the magnetosphere as well.

### 4. References

- [1] Ondoh T.I: Geomag. and Geoelect. **16** (1968) 86
- [2] N.G. Kleimenova: Natural electromagnetic field of the Earth. Nauka, Moscow, 1977, p.53
- [3] Fraser-Smith, A. C: Geophys. Res. Lett., **20** (1993) 467
- [4] V. Yukhimuk: Ph. D. thesis, Kiev University, (1995)
- [5] V.A. Yukhimuk, A.K. Yukhimuk, V.P. Kucherenko: Annales Geophysical., **13** (1995) c698
- [6] J. E. Wahlund, et al.: Geophys. Res. Lett., **21** (1994) 1831
- [7] P. Louarn, et al.: Geophys. Res. Lett., **21** (1994) 1847

## Generation of Elves by Sprites and Jets

Yuri Taranenko, Robert Roussel-Dupre, Vyacheslav Yukhimuk, and Eugene Symbalisky  
(MS F645, Los Alamos National Laboratory, Los Alamos, NM 87545, USA; yuri@lanl.gov)

### 1. Introduction

Recent years of observations of the upper atmosphere and the lower ionosphere brought a fascinating collection of new phenomena including optical, radio, and gamma-ray emissions originating in the 20 to 90 km altitude range. Up to now, the most diverse phenomenology has emerged from the optical observations which have led to the identification of red sprites, blue jets, blue starters, e.g. [1-4], and elves, e.g. [5], [6]. Most of the studies have concentrated on relating such phenomena in the upper atmosphere to regular lightning discharges in the troposphere. For example, sprites and jets are believed to be optical manifestations of electrical discharges in the upper atmosphere caused by quasi-electrostatic fields penetrating to high altitudes during a regular lightning discharge. The sprite/jet discharge itself can be caused by the runaway air breakdown [8]. The standard theory [9] for optical airglow transients [5] in the lower ionosphere above the thunderstorms also known as elves [6] suggests that they are produced during interaction of electromagnetic pulses (EMP) from lightning with the lower ionosphere. Heating of the ambient electrons by the EMP in the D region can result in excitation of optical emissions once the optical excitation thresholds are reached. In this paper we suggest that in addition to this mechanism [9] elves can be caused by an EMP generated by sprites and jets. If sprites and jets are indeed accompanied by electrical discharges then some energy of their EMPs reaches to the ionosphere and heats ambient electrons there that in turn stimulates optical emissions similar to EMPs from regular lightning.

### 2. Model

In our description of the model we will refer to Figure 1. Let us start from the moment when a regular cloud to ground discharge occurs. At this time an EMP from lightning (L-EMP) is generated followed by quasi-electrostatic (QE) fields that are established in the upper

atmosphere. When a L-EMP reaches to the ionosphere it can generate optical emissions in that region known as elves [6]. In the model that we consider sprites and jets are produced by the runaway discharge mechanism, e.g. [7] and other papers at this conference from our group, that is developed from cosmic ray seed MeV electrons in the presence of QE-fields. Such sprite/jet discharges generate their own EMP (SJ-EMP) that reaches the ionosphere and can generate optical emission in the same manner as a L-EMP does.

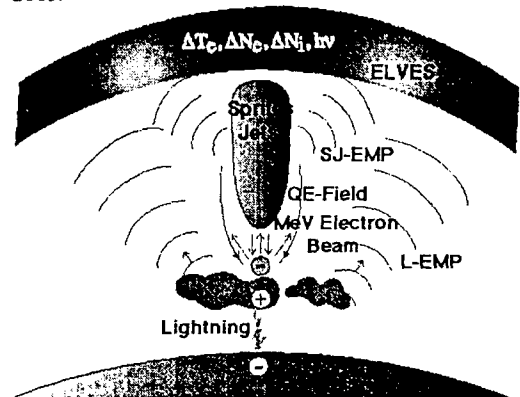


Figure 1. Comparison of lightning and sprite/jet mechanisms of elves generation.

The proximity of sprites/jets to the lower ionosphere means that in their case the power of an EMP could be several times lower than the power of a L-EMP and still cause generation of elves comparable in brightness to the ones generated by a L-EMP.

### 3. Results

The results of our computations indicate that the typical time duration of a SJ-EMP is 100 to 200  $\mu$ s, for figure see Yukhimuk et al. at this conference. Such duration is comparable to duration of a L-EMP. Figure 2 shows dependence of the maximum electric field of a SJ-EMP at the altitude of 80 km versus radius. Duration of the stimulating lightning discharge was 5 ms. To draw conclusions concerning the generation of optical emissions by an EMP with such electric field at the bottom of the ionosphere we refer to paper [9] where it is shown that an

EMP with about 100  $\mu$ s duration and an electric field amplitude larger than 20 V/m is sufficiently potent to produce optical emissions with intensities twice that of the nighttime background. From the radial distribution of electric field in Figure 2 we conclude that the emissions are generated in the region between two radii where the condition  $E > 20$  V/m is satisfied.

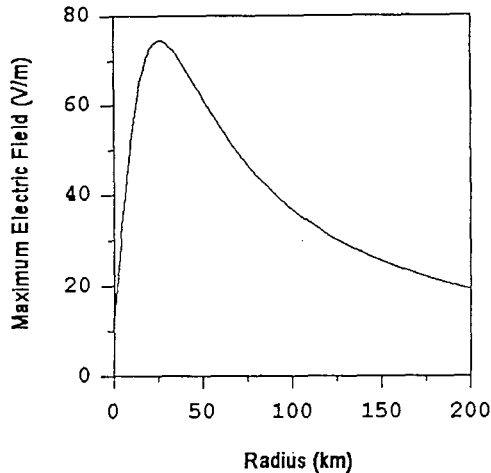


Figure 2. Distribution of maximum electric field of SJ-EMP versus radius. Duration of the driving lightning discharge is 3 ms.

Figure 3 summarizes results on the maximum electric field of a SJ-EMP and the radius of elves generated by such an EMP as a function of lightning duration. At this point we give rough estimates of these parameters. When the driving lightning discharge is slow ( $> 7$  ms) a SJ-EMP becomes weak and we do not expect generation of elves for such cases.

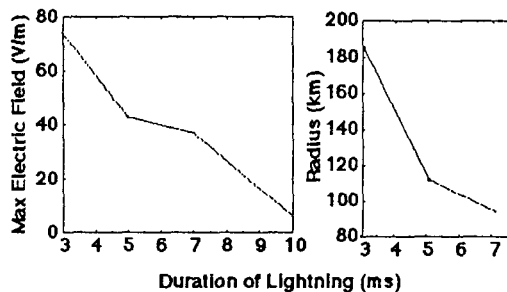


Figure 3. Maximum electric field of sprite/jet EMP at the altitude of 80 km and the expected radius of elves.

#### 4. Conclusions

Our simulations demonstrate that sprites/jets driven by the runaway air breakdown mechanism

can generate a powerful EMP that can stimulate transient airglow brightenings in the lower ionosphere also termed elves [6]. The sequence of events involved in this process is the following: *i*) an atmospheric cloud to ground or intracloud discharge occurs that leads to *ii*) establishment of strong QE fields in the upper atmosphere, *iii*) where runaway air breakdown [7] is stimulated by ambient cosmic rays, *iv*) such a discharge can produce a strong EMP with duration of 100 to 200  $\mu$ s that is predominantly upward directed due to the relativistic nature of the source [10], *v*) the EMP in turn can produce optical emissions, perturbations of electron density and chemical perturbations in the lower ionosphere [9]. We find that parameters of a SJ-EMP are similar to those produced by regular lightning which makes it difficult in observations to distinguish an EMP produced by two different sources: lightning and sprites/jets. This fact makes the picture of electromagnetic interactions in the atmosphere more rich and fascinating.

#### 5. References

- [1] D. D. Sentman, and E. M. Wescott, *Physics of Plasmas*, **2** (1995) 2514.
- [2] J. R. Winckler, W. A. Lyons, T. E. Nelson, and R. J. Nemzek: *J. Geophys. Res.* **101** (1996) 6997.
- [3] W. A. Lyons: *J. Geophys. Res.*, **101** (1996) 29,641.
- [4] E. M. Wescott, D. D. Sentman, M. J. Heavner, D. L. Hampton, D. L. Osborne, O. H., Vaughan, Jr., *Geophys. Res. Lett.*, **23** (1996) 2153
- [5] W. L. Boeck, O.H. Vaughan, Jr., Blakeslee, B. Vonnegut, and M. Brook, *Geophys. Res. Lett.*, **19** (1992) 99.
- [6] Fukunishi, H., Y. Takahashi, M. Kubota, K. Sakanoi, U.S. Inan, and W. A. Lyons, *Geophys. Res. Lett.*, **23** (1996) 2157.
- [7] Y. N. Taranenko and R. A. Roussel-Dupre, *Geophys. Res. Lett.*, **23** (1996) 571.
- [8] V. P. Pasko, U. S. Inan, Y. N. Taranenko, and T. F. Bell, *Geophys. Res. Lett.*, **22** (1995) 365.
- [9] Y. N. Taranenko, U. S. Inan, and T. F. Bell, *Geophys. Res. Lett.*, **20** (1993) 2675.
- [10] R. A. Roussel-Dupre and A. V. Gurevich, *J. Geophys. Res.*, **101** A2 (1996) 2297.

# HF Echoes from Ionization Potentially Produced by High-Altitude Discharges

R. Roussel-Dupré, T.J. Fitzgerald, E. Symbalisty

(Space and Atmospheric Sciences Group, MS D466, Los Alamos National Laboratory, Los Alamos, NM)

Elisabeth Blanc

(Laboratoire de Détection et de Géophysique, Commissariat à l'Énergie Atomique, 91680 Bruyères-le-Chatel, France)

## 1. Introduction

In this paper we report on recent radar measurements taken during the month of October 1994 with the LDG HF radar in the Ivory Coast, Africa as part of the International Equatorial Electrojet Year. The purpose of this experimental effort in part was to study the effects of thunderstorms on the ionosphere. At the same time, we decided to carry out a set of experiments of an exploratory nature to look for echoes that could potentially arise from ionization produced in the mesosphere. The two leading candidates for producing transient ionization in the mesosphere are meteors and high-altitude discharges. Each is discussed in the context of our measurements.

## 2. Experimental Setup

The R4FEL HF radar used in our experiments was developed at the Laboratoire de Détection et de Géophysique (LDG) of the Commissariat à l'Énergie Atomique (CEA). It was conceived by *Herbeteau* [1] and was installed at Korhogo, Ivory Coast (9°24'62" N, 5°39'38" W), for the International Equatorial Electrojet Year. This location is particularly well suited for studies of the equatorial ionosphere and lightning. The frequency of stormy days per month ranges from 20-25 during the April-October period [2], [3]. The LDG radar [4] operates in the frequency range from 1-30 MHz and is composed of two spiral antennas (each 100 m in diameter) for transmission and reception. At the frequencies used in these experiments the antenna lobe, full-width at half-maximum power is approximately 50°. However, the combination of antenna sensitivity, transmitted power, and low noise background in the Ivory Coast permits the

recording of echoes over a cone of approximately 140°. Two pulses separated by 50  $\mu$ s are transmitted at two different frequencies every 5-10 ms. This procedure permits management of two parallel elementary sounding cycles. The pulses have a Gaussian envelope with a selectable full-width at half-maximum of 10 - 20  $\mu$ s or 40  $\mu$ s and a peak power of 5 kW.

The large number of possible parameter- and task- combinations permits performance of a wide variety of investigations [4]. The experiments described in this paper used a specific 'lightning' mode that consists of envelope detection at one sounding frequency over a range of 1000 km. The time and range resolutions were 70 ms and 1.67 km, respectively.

Goniometer measurements of spherics were used to determine the location of thunderstorms. Sensors composed of two crossed-loop antennas with bandwidths of 1 kHz-8 MHz were used to detect lightning signals and to determine their angle-of-arrival. Data taken at two or more widely separated sites permitted identification of the source location. One sensor was placed at the main station D: Korhogo. Two additional stations B and C were located at 17 and 19 km from D with azimuthal directions BD and CD relative to magnetic north of 159° and 211°, respectively. The transmission of time-of-arrival and azimuthal data from stations B and C to the main station was performed using unidirectional radio links. If an event was detected by two or three stations, the location was determined. This system yields maps of storm positions within about 400 km of the main station.

## 3. Measurements

Experiments designed specifically to look for echoes from high-altitude discharges were



performed on five occasions over a period of ~10-15 minutes each. Two additional control experiments were performed after the thunderstorm season. Despite the measurements of Rumi [5] at high frequencies (28 MHz), we decided in this initial set of experiments to operate only at frequencies below 3 MHz in order to maximize our chances of obtaining an echo. One nighttime and two daytime cases clearly showed signatures that could be associated with ionization produced by lightning discharges. One additional daytime experiment showed evidence for oblique reflections originating at large ranges (several hundred kilometers). The remaining daytime experiments showed no evidence of isolated transient events or were contaminated by sporadic-E which made it difficult to identify such events.

In all cases, the radar was operated at 2.2, 2.5, and/or 2.8 MHz. The echoes turned on in several interpulse times of 70 ms and were generally correlated with strong lightning activity prior to onset. Returns lasted several hundred ms at night and 1 - >10 s during the day. The angles of arrival of spherics detected at three goniometer stations were used to determine the distance to thunderstorms.

Detailed range-time plots of the echoes will be presented for all cases along with goniometer maps showing the locations of lightning spherics as a function of time.

#### 4. Interpretation

Two potential sources of transient ionization in the upper atmosphere are meteors and high-altitude discharges associated with thunderstorms. In the case of meteors, there are some basic inconsistencies between the characteristics of meteor echoes and our observations. At the most probable altitudes for meteor intercepts, ambipolar diffusion dominates the density decay and yet the data show a much longer event duration during the day than at night. Reflection virtual heights (of 82 km) that are much lower than the most probable heights were measured on occasion. Finally, the echoes identified in our measurements are correlated with lightning activity. High-altitude discharges termed sprites can produce significant transient ionization of the mesosphere according to theoretical calculations based on runaway air breakdown [6], [7], [see also, companion papers presented at this meeting]. A plot showing the computed electron

density profile along the symmetry axis of a sprite simulation is shown in Figure 1.

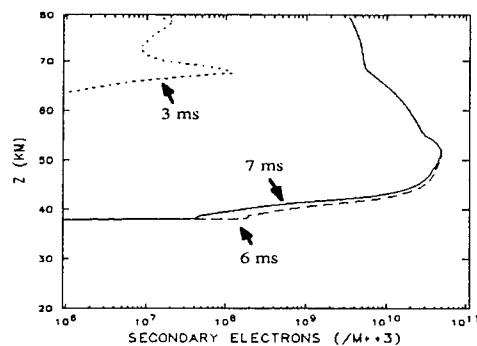


Fig. 1

The data are consistent with specular reflections from an ionization layer produced by a sprite like event at 55-65 km altitude and having minimum electron densities of  $6 \times 10^4$ - $10^5 \text{ cm}^{-3}$ . The duration of the ionization is consistent with attachment, detachment, and recombination times in the nighttime and daytime mesosphere at these altitudes.

Detailed comparisons between theory and experiment will be presented along with ray-tracing calculations showing the detailed reflection geometry for a range of frequencies. The self-consistent temporal evolution of the full 2-d electron density profile is included in these calculations.

#### 5. References

- [1] Herbreteau, L., Ph.D. thesis, University of Paris, (1979).
- [2] communicated by l'Agence Nationale de l'Aviation Civile et de la Météorologie, (1992).
- [3] Despiau, S. and Laroche, P., *Journal de Recherches Atmospheriques* 16, No. 1, 1, (1982).
- [4] Blanc, E., Mercandalli, B., and Houngninon, E., *Geophys. Res. Lett.* 6, No. 23, 645, (1996).
- [5] Rumi, G.C., *J. Geophys. Res.* 62, No. 4, 547, (1957).
- [6] Roussel-Dupré, R.A. and Gurevich, A.V., *J. Geophys. Res.* 101, No. A2, 2297, (1996).
- [7] Taranenko, Y.N., and Roussel-Dupré, R., *Geophys. Res. Lett.* 23, No. 5, 571, (1996).

## High Altitude Atmospheric Discharges According to the Runaway Air Breakdown Mechanism

Eugene Symbalisty, Robert Roussel-Dupré, Vyacheslav Yukhimuk, and Yuri Taranenko  
(Space and Atmospheric Sciences Group, MS D466, Los Alamos National Laboratory, Los Alamos, NM)

### 1. Introduction

High altitude optical transients (see e.g. [1]) - red sprites, blue jets, and elves - are modeled in the context of the relativistic electron runaway air breakdown mechanism. These emissions are usually associated with large mesoscale convective systems (hereafter MCS). In thunderstorms cloud electrification proceeds over a time scale long enough to permit the conducting atmosphere above the cloud to polarize and short out the thunderstorm electric field. When a lightning strike rapidly neutralizes a cloud charge layer runaway driving fields can develop in the stratosphere and mesosphere. According to our simulations of the full runaway process the variety of observed optical emissions are due to the nature of the normal lightning event in the MCS that kick starts the runaway avalanche. In this paper we describe some details of the model, present the results of the evolution of the primary electron population, and summarize the initial conditions necessary for different types of discharges. Two companion papers present (a) the predicted optical, gamma ray, and radio emissions caused by these electrical discharges, and (b) the time evolution of the secondary electron population and its implications in terms of observables.

### 2. Theoretical results

In our simulations a quasi-electrostatic, multifluid approach similar to that of Taranenko and Roussel-Dupré [2] is used to model the relativistic (primary) electrons, secondary electrons and the positive and negative ions. The work includes, for the first time, the full time evolution of the runaway discharge. This evolution starts by resolving the initiating cloud-to-ground or intracloud discharge and continues to late times when the discharge itself or the background conductivity eliminates the driving electric fields. The present formulation, contrary to [2], includes the contributions of the positive and negative ions, produced as a result of ionization and attachment, to the total electrical

current density and hence the evolution of the self-consistent fields. Because of their large densities at low altitude, the ion contribution to the net current is significant for slow discharges and in particular blue jet simulations. The electrostatic equations are solved in a different way, providing significant savings in computational time.

Polynomials are fit to the numerical results from detailed kinetic calculations [3] to obtain the primary electron energy, velocity, and production rate as a function of the total electric field ( $E$ ) and the atmospheric pressure ( $p$ ). At an altitude of about 55 km, the mean free path of the primary electrons becomes large. A simple prescription is used, for the first time, to allow the primary electrons to smoothly transition between the collision dominated regime and the free streaming limit.

The secondary (low energy) electrons produced in the avalanche process are collision dominated and establish equilibrium distributions in time scales much shorter than the time for runaway breakdown. Their mean properties are also defined by  $E$  and  $p$  and are derived from the standard swarm parameters [4,5].

### 3. Discussion and conclusion

We have been able to find reasonable parameters for intracloud and positive cloud-to-ground lightning strokes that produce the observables for red sprites, blue jets, and elves. Since we have just begun to explore the morphology of the observable emissions we do not claim that the cases we describe next are the only possible scenarios. The MCS, and the annihilation of charge by discharges in the MCS are modeled by the creation of charge of opposite polarity in free air. The highly complex thunderstorm complex is thereby eliminated, and we can only look at atmospheric evolution well above the discharge location. The charge is allowed to build with an

exponential time scale or with a constant current source (i.e. a linear time scale).

Four simulations that produced red sprites were initiated by a positive cloud to ground stroke. They discharged 200 C at an altitude of 11 km with an exponential time scale of 3, 5, 7, and 10 ms respectively. The computational grid extended from 20 to 80 km in altitude and 50 km in radius. The peak primary electron concentrations were 1.1, 0.75, 0.5, and 0.15 per cc respectively. In each case there were two large scale and very bright atmospheric discharges. However, when observed with a video camera and thereby integrated over 17 ms, to the observer there would only be one flash. For example, in the 7 ms case, the first discharge occurred between 6.7 and 8.0 ms after the start of the positive cloud-to-ground stroke. The second discharge occurred between 12 and 14 ms. The kinetic energy of the primary electron population in each discharge reached 100 kJ. The peak current to the ionosphere reached 6 kA.

In each of these four red sprite simulations, the electric field first broke threshold, for the runaway mechanism to start, at high altitude and the location for breaking threshold moved downward in time. By the time the threshold was broken at 30 km there were enough avalanche lengths traversed by the upward propagating electron beam to produce large concentrations responsible for the first discharge. This also had the effect of quickly shorting out the field in the region of the discharge. However, the external driving field was still growing around the high conductivity region eventually resulting in the second discharge. The external driving field was complete by this time and the runaway process was ended. The fastest case produced the highest peak primary electron concentrations and also the highest electric radiation fields - reaching nearly 40 V/m in the lower ionosphere. As a result this case also provides the electromagnetic environment required for elves.

For discharges that occur at lower altitudes within the MCS, more charge would have to be annihilated and conversely less charge for higher altitude discharges. The fact that the runaway mechanism produces red sprites with a wide range of time scales is a notable result. Red sprites are now observed quite routinely which suggests a

mechanism that is not too sensitive to normal lightning discharge parameters.

A blue jet was modeled with a constant current intracloud discharge of reverse polarity. Computationally this is simulated by the creation of a dipole. The location of the dipole was at 17 and 14 km. A current of 1 kA for 200 ms (or a total charge of 200 C) produced a blue jet that moved from the bottom of the grid (19 km) to 35 km with an average speed of about 70 km/s. In this case the electric field first breaks threshold near the cloud top and moves upward in time. The reverse polarity of the discharge means the primary electron beam is moving down. When the primary electron beam reaches 40 km in altitude the ambient electrical conductivity has had enough time to eliminate the driving electric field. Obviously the termination altitude is quite sensitive to the ambient conductivity profile. We have chosen a nighttime profile from [6]. The blue jet simulations are computationally more intensive because of their long time duration and because the avalanche process must still be resolved in space and with the same time resolution. Also, the peak electric fields during the evolution are less than a factor of two over the threshold value. Therefore the simulation is strongly dependent on the runaway process parameters near threshold electric field values.

We are continuing to explore the parameter space of the initiating lightning strokes and are also beginning to look at aspects of normal lightning in the context of the runaway mechanism.

#### 4. References

- [1] D. D. Sentman, E. M. Wescott, D. L. Osborne, D. L. Hampton, and M. J. Heavner: *Geophys. Res. Let.*, **22** (1995) 1205.
- [2] Y. N. Taranenko and R. Roussel-Dupré, *Geophys. Res. Let.*, **23** (1996) 571.
- [3] R. A. Roussel-Dupré, A. V. Gurevich, T. Tunnell, G. M. Milikh: *Phys. Rev.*, **49** (1994) 2257.
- [4] L.G. H. Huxley and R. W. Crompton, *The Diffusion and Drift of Electrons in Gases*, John Wiley & Sons, New York, 1974.
- [5] A. W. Ali, Naval Research Laboratory Memorandum Report, 5815, 1986.
- [6] Geophysics Study Committee, *The Earth's Electrical Environment*, National Academy Press, Washington, D. C. 1986.

# COMPUTER AND PHYSICAL SIMULATIONS OF ELECTRODISCHARGE PHENOMENA NEAR THE NEUTRON STARS

V.A.Skvortsov, N.I.Vogel (\*)

High Energy Density Research Center, Russian Academy of Sciences,  
127412, Moscow, Izhorskaya, 13/19, IVTAN, Russia

(\*) University of Technology Chemnitz-Zwickau, Department of Physics, D-09107, Chemnitz, Germany

## 1. Introduction

A principal new physical effects of current self-focusing (and defocusing) as well as the "shooting solitons" (SS)-generation were observed in our physical and computer experiments [1-3]. Based on considered nonlinear phenomena a new mechanism of charge particle generation from nucleus of quasi stellar radio sources (QSS), pulsars have been proposed in [3-5]. This paper deals with a continuation of our work in area of physical and computer simulations of electrodischarge processes near the neutron stars (NS). We consider a question of "working" pulsars (including X-ray pulsars) and represent a new interpretation of "strange" behavior of QSS 3C273. As well as in [6] we will regard that a source of super high power jet is a black hole. But in contrast with a considered there 4 models of jet generation, which are based on an assumption about giant mass of black holes (about of  $10^{11}$  of sun mass  $M_{\odot}$ ), our model is based on an Oppenheimer-Snyder's prediction that the mass of typical black hole (NS) is about of  $3M_{\odot}$ . For explanation of an anomalous light brightness and strong microwave radiation from 3C273 we took into account a possibilities of self-channeling of directed energy flows (including relativistic electron and ion jets, as well as an electromagnetic radiation). It occurs in result of density concentration in electric discharge induced plasma corona near the NS as well as in its magneto-sphere. Under this we regard that the represented in [6] estimations of extremely high ( $10^7 M_{\odot}c^2$ ) energy of magnetic field and kinetic energy of particles is not correct. This estimation was produced for an increased volume of emitted sources and considers only a mechanism of synchrotron radiation without taking into account a possibility of formation of strongly directed energy flows, as well as possible radiation from beam plasma [7,8] and a reflection of electromagnetic waves of Space (with its amplitudes and frequencies multiplication) from the moving with relativistic velocity a large front of jet (see, for example, [9]). For our opinion the disregarding this important phenomena is not correct. For example also it is not correct to speak about extremely high temperatures of low intensity He-Ne-laser on the base of its extremely high brightens temperatures (which may be, for example, up to  $10^{15}$  K under intensity 10 mW). By the way as it was notified in [10] the most of QSS can not be observed because of its jets generation occurs under big

angle to observer! Note also that earlier in [11] a physical simulation of astrophysical jet generation (in a case of an accretion disk) had been considered using laser plasma as well as 2-D MHD computer simulation on the base of the pinch effect at an uncontrived plasma configurations, in which an azimuthal field occurs. In contrast to [11] in our modeling the mentioned above nonlinear phenomena are very important. They appear in essentially strongly coupled plasma in micro volume of cathode torch or in macro volume of plasma corona of electrical discharges near NS. We emphasize that picosecond Nd-YAG laser in our physical simulation was used as "shoot trigger" and as a diagnostic instrument for visualization of jets produced due to electro-discharge nonlinear phenomena after a few nanosecond after ignition.

## 2. Electrohydrodynamic jets

For simplicity we disregarded a peculiarities of space-time near the NS calculations which was produced by Oppenheimer and Snyder, Zel'dovich and his group [6]. At the first approximation we also disregarded a magnetic field (remarkably that in computer experiments it was easy to "switch off" its influence). We used a 2D-mathematical model [12,13], which is based on the electrodynamics, hydrodynamic and heat-transfer equations. It is very important that thermal and electrical conductivity were calculated including effects of strongly coupled plasma. Now we represent some results of direct computer simulation of such exotic electrical discharge (see Fig.1 as well as an additional figures in [4]). We assumed that at the surface of NS there exist a thermoemission processes with an initial temperature in some spot (with a radius of 20 m) of the order of 20 eV and work function about of 200 eV [14]. The tension of electric fields near the surface of neutron stars may be 100 MV/cm in accordance with an estimations in [14]. In this simulation we proposed that the distance between the surface of neutron star crust (with a density of iron about of  $10^5$  g/cc) and its magnetosphere equals to 100 m as in [15]. In Fig 1, a spatial distribution of current density in plasma torch of such exotic discharge is represented. We can see, that in the vicinity of central region of plasma torch the self-focusing of electric current and volumetric generation of SS take place similar to laboratory plasma [1-5]. High density electron beams are generated (its density does not show in figure) and accelerated in strong electric fields up to relativistic energies. Due to rotation of NS the shooting

of jets occurs strongly in one direction like as from gyro-stabilized platforms due to the rotation of NS. By the way, the particle beams which generated during NS-storms can be a large lasers (free electron lasers - for generation an electromagnetic radiation as well as a free ion lasers - for gravitational radiation). The temporal behavior of the total current of such "electrical generator" was represented in [4]. In accordance with our calculations we can conclude that an intensity of relativistic electron beam riches a values of order of  $10^{20}$ - $10^{22}$  W/cm<sup>2</sup> with a pulse duration of about 0.5-1 msec. These pulses can recur with a cycle time of a few msec. It is obvious that during such electrical discharges the generation of high power electromagnetic radiation (including X-ray due to overheating instability in plasma corona [3,5]) take place. The main plasma parameters at some intermediate time are represented in Fig.1 b, c). Naturally we can see only fragment of plasma and jet formation in the calculation frame with  $R \times Z = 80 \times 120$  m (in the depth  $0 \leq Z \leq 20$  m from crust of NS. A strong shock wave (with  $V_s \sim 10$ -20 km/s) is generated and a crater is formed. A mass velocities of plasma corona is about of 3-150 km/s. In considered example we have only one jet. In reality during NS-storm a few jets like as in our physical simulations may be generated simultaneously. It had been demonstrated in experimental investigations of laser-induced discharges in vacuum [1-3], as well as of laser produced plasmas in air near the Al-target [16], which presents an additional interesting possibilities for astrophysical applications (for example, the production a large relativistic mirror for reflection and enhancement of electromagnetic radiation from ambient stars [9]). Finally note that 2-D - MHD simulation confirms this result and in comparison to an electrohydrodynamic simulation we have only an additional compression of current densities due to an influence of magnetic field [17].

### 3. References

1. N.I.Vogel, V.A. Skvortsov : Proc. ICPIG-XXII, Hoboken, USA, 5 (1995).
2. N.Vogel, V.Skvortsov : Proc. XVII-th ISDEIV. Berkeley, 1 (1996), 89.
3. V.A.Skvortsov, N.I.Vogel: Proc.: International Conference on Physics of Strongly Coupled Plasmas. Binz. (1995) 343.
4. V.A.Skvortsov, N.I.Vogel: Proc. 11-th Int. Conf. Beams'96. Prague, 1 (1996) 513.
5. V.A.Skvortsov, N.I.Vogel: In book of Abstracts. Conf. on Phys. of High Temperature Plasma and Confinement Fusion. Zvenigorod. (1997).
6. K.S.Torn: Black Holes and Time Wards: Einstein's Outrageous Legacy. N.Y., W.W.Norton Publ. (1994).
7. M.V.Kuzelev, A.A.Rukhadze: Electrodynamics of Dense Electron Beams in Plasma. M.: Nauka (1990).
8. K.G.Kato, G. Benford, D. Tzach: Phys. Fluids, 26 (1983) 3636.
9. V.A.Skvortsov, N.I.Vogel: Proc. of this Conf.
10. I.S.Shklovskii: Problems of Modern Astrophysics M.: Nauka (1982) 117-131.
11. A.R.Bell: Phys. Plasmas, 38 (1994) 1643.
12. V.A.Skvortsov: Proc. 40 th IEEE Holm Conference on Electrical Contacts, Chicago, (1994) 43.
13. V.A.Skvortsov: Reports of High Energy Density Research Centre of the RAC, Moscow, (1997), ch.3.
14. A.I. Tsygan, : Priroda, No.8 (1994) 82.
15. M.A. Ruderman, P.G. Sutherland P.G.: The Astrophysical Journal, 196 (1975) 51.
16. N.I.Vogel: Proc. 7 th Workshop Advanced Acc. Concepts, Oct.12-18, 1996, Lake Tahoe, CA, USA.
17. V.Skvortsov, A.Otochin, A.Krukovsky, S.Zakharov: Proc. XVII-th ISDEIV. Berkeley, 2 (1996) 823.

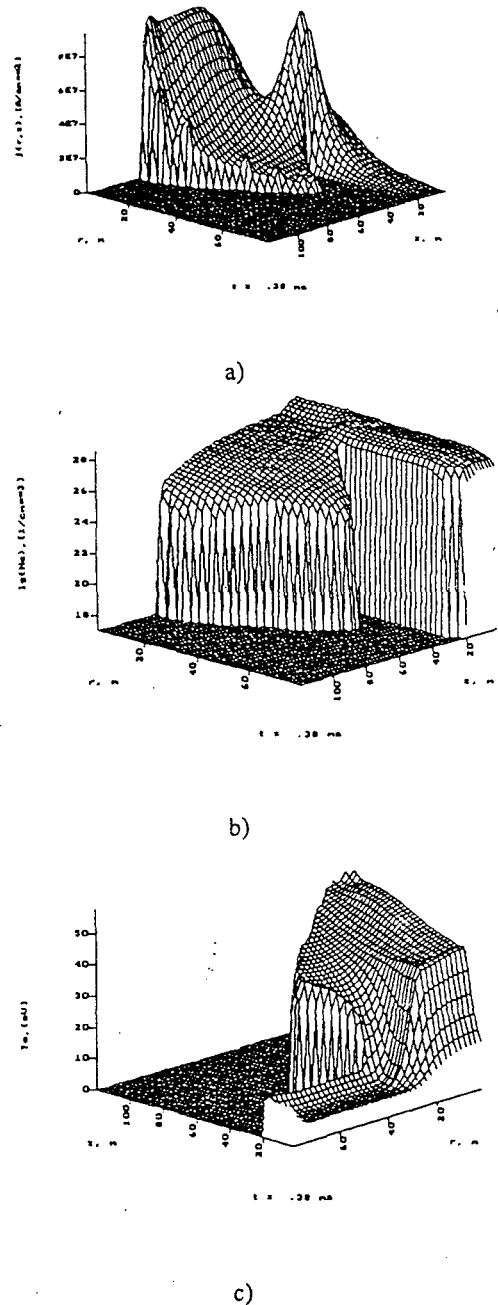


Fig.1. Spatial distribution of current density (a), plasma density (b) temperature (c) at  $t=0.38$  ms in torch of NS.

*Topic 16*

**Plasma sources of radiation.**

## Optimization of the radiative flux computation for high pressure discharges.

F. Simonet, M. Aubès and J.J. Damelin court

Centre de Physique des Plasmas et de leurs Applications (ESA 5002)

Université Paul Sabatier

118, Route de Narbonne, 31062 Toulouse Cedex, France

### 1. Introduction

The energy balance of discharge lamps strongly depends on radiation, for this reason, the radiative flux is a fundamental quantity in radiation source research and development. Phenomena that generate radiation and formalism that ensues are well known for several decades<sup>(1)</sup> but the full calculation of the radiation flux density makes heavy demands on computer resources (see Eq.1). Hence, prohibitive time computation prompts the use of approximate methods<sup>(2,3)</sup>. In this paper, we propose a different method which enables to reduce strongly the time computation of the spectral flux density defined by the following four-fold integral

$$F_{\lambda}(r) = -4 \int_0^{\pi/2} \int_0^{\pi/2} \int_0^{\pi/2} \int_0^{\pi/2} \varepsilon_{\lambda}(s) \times \left\{ \int_0^{\pi/2} \sin(\Theta) \exp \left[ -\int_0^s \kappa(\lambda, s') / \sin(\Theta) ds' \right] d\Theta_2 \right\} \cos(\Phi) ds_3 d\Phi_4 \quad (1^*)$$

for cylindrical and high-pressure discharges (assumed to be in local thermodynamic equilibrium<sup>(4)</sup>). Beside this, only energy transfers due to spectral lines will be treated.

It is shown that the application field can be characterized by a synthetic parameter called the equivalent optical depth (EOD) denoted  $\tau_e$  and defined as

$$\tau_e = K_{T_c}(\lambda_0) R \quad (2)$$

where  $K_{T_c}(\lambda_0)$  represents the absorption coefficient at the center of the discharge and at the center of the line whereas  $R$  is the radius.

This quantity, already used by Irons and Lowke<sup>(3,5)</sup>, gives an estimation of the maximum optical depth relative to the considered discharge in a very simple way. Furthermore, it enables to describe the application field of the code. It has been verified that the model can be used for values of  $\tau_e$  lying between  $10^{-5}$  and  $10^{+10}$ . Moreover, these values probably do not constitute absolute limits. Such a large scope is some of interest in so far as it allows to consider resonance as well as non-resonance transitions.

### 2. The model.

The first part is concerned with the angular variations of the relative contributions of the planes within the framework defined in the introduction (integral n°4). This study presents a double interest. On the one hand, it

leads to a semi-empirical relation (see Eq.3) which allows to define an effective integration interval  $\Delta\Phi_{\text{eff}}$ .

$$\Delta\Phi_{\text{eff}} = \text{Arcsin} \left[ \left( \frac{T_c - T_{\text{lim}}}{T_c - T_w} \right)^{1/h} \frac{1}{r/R} \right] \quad (3)$$

On the other hand, it brings forward the geometrical parameters which characterize a cylindrical discharge, the 'main plane' and the 'hot point' (see Fig.1). Concerning the radiative transfer along a plane (integral n°3), a reduced quantity called 'the efficient emission' is introduced in order to homogenize the results.

It is seen that this function (the efficient emission) passes through a maximum and may present strong gradients. Thus, it can be integrated more efficiently by adjusting the integration step around the maximum which will be in the first place approximated by a semi-empirical formula (see Eq.4a).

$$s_c(\Delta\lambda_r) = \frac{|r/R \cos(\Phi)|}{\left[ 1 - (r/R \sin(\Phi))^2 \right]^{1/2} - \cos(\Phi)} \times [1 - 0.0648 \ln(10\tau_e) \exp(-0.59\Delta\lambda_r)] \quad (4a)$$

Taking into account the variations of the efficient emission around this point, it becomes obvious that it is necessary to introduce a decreasing integration step within  $[0; s_c(\Delta\lambda_r)]$  and an increasing one within  $[s_c(\Delta\lambda_r); 1]$ .

The introduction of these adaptative steps consists in characterizing at best the variations of the efficient emission by gaining time computation. In this way, the following formulae are introduced

$$1) s(n) = s_c(\Delta\lambda_r) (1 - 0.258^n) \text{ within } [0; s_c(\Delta\lambda_r)] \quad (4b)$$

$$2) s(n) = s_c(\Delta\lambda_r) (1 - n/10) \text{ within } [s_c(\Delta\lambda_r); 1] \quad (4c)$$

Afterwards, the calculation of the absorption factor (integral n°2) that occurs in the efficient emission expression is treated. This term is defined by a double integration.

As far as the integration of the absorption coefficient is concerned (integral n°1), the proposed approximation consists in integrating the absorption coefficient and the efficient emission (integral n°3) by using the same integration steps. From a numerical point of view, this approximation means that the spectral flux density can be treated as a three-fold integral although its expression is given by a four-fold integral.

\* The successive integrals are numbered by the subscripts 1,2,3,4 which appear under the variables.

Concerning the second integration (integral n°2) which gives the absorption factor, the provided solution is the same as the one used for the planes in so far as it is based on a decrease of the interval which needs to be considered.

### 3. Results.

This section is devoted to a presentation of the spectral flux density relative to the main sodium and mercury lines. Firstly, a comparison with the results of Lowke<sup>(6)</sup> concerning the D lines is given in order to validate the model (see Fig.2).

Secondly, results relative to a typical mercury discharge will be compared with a personal basic model due to the lack of references in literature. Taking into account the calculation hypothesis quoted in the introduction, this model exactly computes the equation (1) and uses precise integration methods given by the numerical library NAG<sup>(7)</sup> (yielding the so called 'exact solutions').

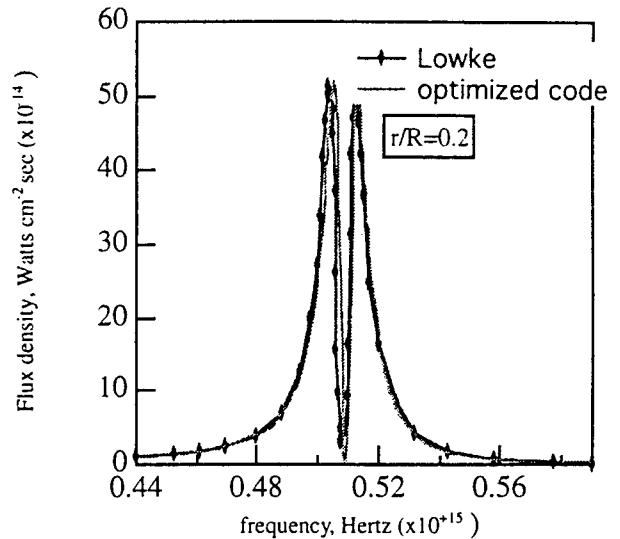


Fig.2. Comparison with the results of Lowke.

### 4. Conclusion.

The flux density which appears in the energy balance equation is defined by a five-fold integral. This quantity can be written as the integration over the wavelength (or the frequency) of the spectral flux density which has been especially studied in this paper.

This method is based on a physical analysis of the functions involved in the calculation. It turns out that a discharge can be described owing to a minimum number of spectral and geometrical characteristics. From these characteristics, the relative contribution of the planes and the efficient emission have been introduced in order to 'normalize' the behaviour of the discharge. The decrease of computation time is based on a localization of the effective contribution areas thanks to semi empirical formulae.

It is found that the numerical code predicts spectral flux density values which agree to better than 5% with 'exact solution' whereas time computation is more than two orders of magnitude less. Moreover, it can be used for EOD lying between  $10^{-5}$  and  $10^{+10}$  (for the typical cases that has been studied,  $\tau_e$  varies from  $10^{-1}$  to  $10^{+4}$ ). The next step of the computation procedure will consist in optimizing the integration of the spectral flux density in order to calculate the flux density.

### 5. References.

- [1]. C.H. CHURCH, R.G. SCHLECHT, I. LIBERMAN and B.W. SWANSON, AIAA 4. 1947 (1966).
- [2]. J.J. LOWKE and E.R. CAPRIOTTI, JQSRT 9. 207 (1969).
- [3]. F.E. IRONS, JQSRT 22, 21 (1979).
- [4]. H.P. STORMBERG and R. SCHÄFER, JQSRT 33, 27 (1983).
- [5]. J.J. LOWKE, JQSRT 14, 111 (1973).
- [6]. J.J. LOWKE, JQSRT 9, 839 (1968).
- [7]. NAG Fortran Library Manual, Mark 15, Vol 1.

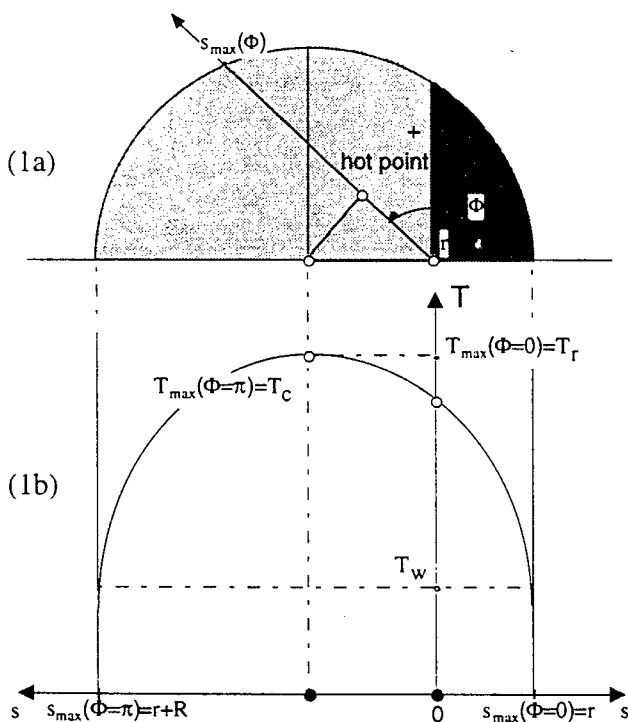


Fig.1a. Transverse cutaway of the discharge: position of the hot point within positive and negative areas. 1b. Justification from the temperature profile for planes corresponding to  $\Phi=0$  and  $\Phi=\pi$  ( $\Phi=\pi$  represents the main plane).



## Role of atomic oxygen in self-regeneration of CO<sub>2</sub> laser mixtures.

A. Cenian, A. Chernukho\* and V. Borodin\*

Polish Academy of Sci., Institute of Fluid-Flow Machines,  
80-952 Gdansk, 14, Fiszerka Str., Poland,  
e-mail: cenian@imppan.imp.pg.gda.pl.

\*) Belarus Academy of Sci., A.V. Luikov Heat & Mass Transfer Institute,  
220072 Minsk, 15 p. Brovka Str., Belarus,  
e-mail: chern@itmo.by

### 1. Introduction.

The CO<sub>2</sub> decomposition due to collisions with electrons is responsible for mixture degradation and declining performance of CO<sub>2</sub> lasers. It has been shown in our previous papers [1-3] that atomic oxygen produced mainly in reactions with electronically excited N<sub>2</sub> molecules can substantially influence the level of CO<sub>2</sub> conversion described by so called "equilibrium CO<sub>2</sub> conversion, X<sub>e</sub>". In this report we show that the atomic oxygen content influences the pressure dependence of X<sub>e</sub> i.e. it can change its monotonous character into the one with a minimum.

### 2. Model Description

The model described in detail in ref. 1 is used here. The following plasma chemical processes of 54 species are considered: reactions initiated by electron collision, reactions of neutral atoms, molecules and their basic electron states, reactions with positive and negative ions, heterogeneous as well as homogeneous recombination and energy relaxation of electron levels.

The rate constants of reactions initiated by electron collision as a function of reduced electric field E/N and laser mixture composition were calculated, based on the electron energy distribution function (EEDF) and the relevant cross sections. In the Boltzmann equation, we took into account the processes of elastic collisions, electron excitation, ionization and dissociative attachment. Moreover, due to the importance of superelastic electron collisions, the effect of the CO<sub>2</sub> and N<sub>2</sub> vibrational excitation on EEDF was taken into account. The kinetic equations for chemical processes in a positive column of the DC plasma were solved under conditions of constant gas temperature, pressure and electron density.

### 3. Results and Discussion

Figure 1 presents the pressure dependencies of equilibrium CO<sub>2</sub> conversion X<sub>e</sub> for different CO<sub>2</sub>:N<sub>2</sub>:He gas mixtures calculated for DC discharge chamber of MLT 1.2 kW laser [4] - solid lines. In contrast to these curves, the dashed line - representing equilibrium CO<sub>2</sub> conversion in small diameter discharge tube [5] - monotonously decreases to null with pressure growth. As discussed in our previous works [1,3] this is related to the role of ambipolar diffusion in this systems and the

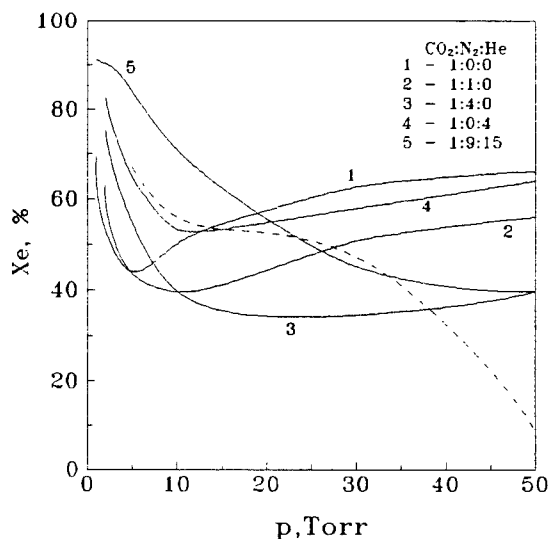


Fig. 1. Equilibrium CO<sub>2</sub> conversion as a function of pressure.

resulting pressure dependence of reduced field E/N. In large diameter discharge as in MLT 1200, pressure dependence of X<sub>e</sub> can preserve monotonous character, e.g. curve (5) for the standard laser gas mixture CO<sub>2</sub>:N<sub>2</sub>:He = 1:9:15, but saturational plateau appears in this case. However, X<sub>e</sub>(p) can change its monotonous character for the one with a minimum, which is most pronounce in the case of pure CO<sub>2</sub> gas discharge. As the dissociation rate (as well as E/N value) does not depend on the pressure discharge chambers, the character of X<sub>e</sub>(p) is most probably determined by CO<sub>2</sub> recombination processes. In our previous works [1-3] already, we have reported that in MLT 1200 laser recombination takes place mainly in afterglow region and almost completely results from homogeneous and heterogeneous CO recombination on atomic oxygen i.e.



Therefore, Fig. 2 shows the relative recombination rates of atomic oxygen and equilibrium CO<sub>2</sub> conversion values (dashed lines) at the beginning of the afterglow region. Curve 1 represents the rate for these processes leading to CO<sub>2</sub> recombination, i.e. reactions (1) and (2), and curve 2 the rate of all the other processes. In the case of pure CO<sub>2</sub> gas

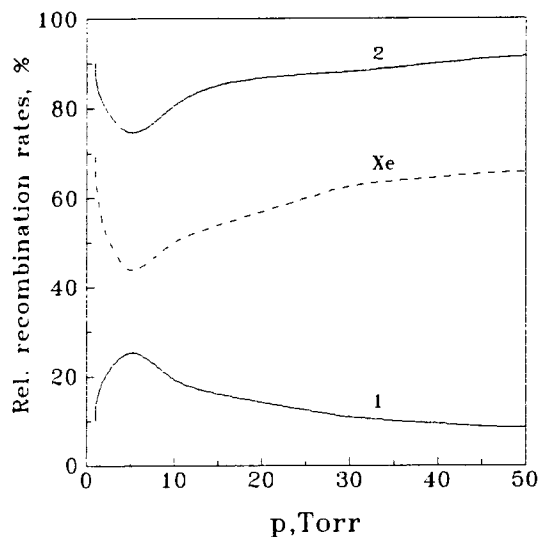
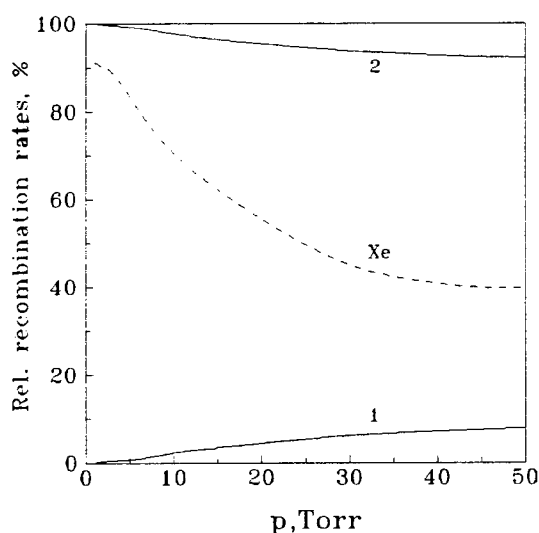
(a) discharge in pure CO<sub>2</sub> gas;(b) discharge in gas mixture CO<sub>2</sub>:N<sub>2</sub>:He = 1:9:15.

Fig. 2. Relative recombination rates of atomic oxygen as a function of pressure.

discharge (Fig.2.a), these processes are: heterogeneous recombination of O on wall



in low pressure range and homogeneous recombination reactions



in high pressure region. In interim region, CO<sub>2</sub> reversion processes (1-2) reach their maximum

(curve 1) as the result of competition with reactions (3-6). This explains unmonotonous character of the  $X_e(p)$  dependence.

When adding nitrogen to CO<sub>2</sub>, the competition for CO<sub>2</sub> reversion processes increases by the presence of additional channels



in the low pressure range and besides,



is added in high pressure. However, nitrogen plays a positive role in CO<sub>2</sub> reversion process. As we see from curves 1-3 in Fig.1 the minimum of equilibrium conversion decreases, moves to higher pressure and widens up with N<sub>2</sub> content increase. It is related to the positive role of electronically excited nitrogen (especially N<sub>2</sub>(A<sup>3</sup>Σ)) in production of atomic oxygen. In the case of the standard MLT 1200 laser gas mixture (Fig.2.b), reaction (7) and (3) significantly reduce the rates for CO<sub>2</sub> reversion in interim pressure range (no maximum of CO<sub>2</sub> reversion appears in this case (curve 1 in Fig.2.b). This determines the monotonous character of dependence  $X_e(p)$  for CO<sub>2</sub>:N<sub>2</sub>:He = 1:9:15 mixture.

On the contrary, helium increases CO<sub>2</sub> conversion level as follows from comparison of curves 1, 3 and 4.

#### 4. Conclusion

The pressure dependence of  $X_e$  can lose its monotonous character as we go from small diameter discharges to higher diameter one. It allows to find the pressure range where the laser mixture degradation will be minimal for given gas composition. The high content of nitrogen promotes the decrease of the mixture degradation but helium can intensify the CO<sub>2</sub> conversion.

#### 5. References

- [1] Cenian A., Chernukho A., Borodin V. and Sliwinski G, Contrib. Plasma Phys. 34 (1994) 1, 25, 35 (1995) 3, 273.
- [2] Cenian A., Chernukho A. and Borodin V., Contributed Papers of III International School-Seminar "Nonequilibrium Processes and their Applications", (Minsk, September 8-13,1996), (1996) 69.
- [3] Cenian A., Chernukho A., Kukiello P., Zarembo R., Borodin V. and Sliwinski G., J.Phys. D: Appl. Phys. (1997) in print.
- [4] Kukiello P. and Rabczuk G., Laser and Particle Beams 10 (1992) 865.
- [5] Tanaka K. and Gao D.W., Int. Conf. "ISPC-8", Conf. Proc., Tokyo (1987) 874.

# A Coupled Negative Glow-Thermionic Cathode Model for Low Pressure Fluorescent Lamp Discharge

Yan-Ming Li

Lighting Research Center, OSRAM SYLVANIA INC., 71 Cherry Hill Dr., Beverly, MA 01915, USA

## 1. Introduction

The conventional fluorescent lamp is a low pressure mercury discharge with a buffer gas, typically argon, to maintain the charged particle balance. The life determining component of the lamp is the oxide coated thermionic cathode, so understanding its operation is of great interest within the lighting community. The basic parameters for the operating thermionic cathode and its interaction with the negative glow plasma have been described by J. Waymouth [1]. Briefly, the thermionically emitted electrons accelerate through the high field cathode fall region and undergo excitations and ionizations in the low field negative glow region. The negative glow plasma ions drift and diffuse back to the cathode, forming the cathode fall and providing the power to maintain cathode temperature. Although the basic theory and measurements of the important parameters such as cathode fall voltage, ratio of ion to electron current density at the cathode surface etc., are discussed in [1], only recently has a more quantitative ambipolar diffusion theory of hot-cathode negative glow discharge been developed [2]. The aim of this work is to couple both the cathode thermal model and the negative glow model so that all the important parameters such as the cathode spot temperature, cathode fall voltage, and negative glow discharge characteristics are calculated self-consistently for a wide range of parameters.

## 2. Details of the Model

The overall model is the synthesis of the following components: (1) negative glow model, (2) collisionless ion sheath model, (3) cathode emission and power balance models.

### 2.1 Negative Glow Model

The negative glow is assumed to be a quasineutral plasma governed by ambipolar diffusion equations for the electron and mercury ion ( $n_p$ ). In addition, a third equation accounts for the relaxation of the fast electrons originating from the cathode (beam electrons,  $n_b$ ):

$$\begin{aligned} \frac{d}{dx} [\mu_e (-\theta_e \frac{dn_p}{dx} - n_p E)] &= (1 + f_{ih}) v_h n_b - (\frac{D_a}{\Lambda^2} - v_{ip}) n_p \\ \frac{d}{dx} [\mu_i (-\theta_i \frac{dn_p}{dx} + n_p E)] &= f_{ih} v_h n_b - (\frac{D_a}{\Lambda^2} - v_{ip}) n_p \\ D_b \frac{d^2 n_b}{dx^2} + v_h n_b &= 0 \end{aligned}$$

The definitions for various quantities are given in Ref. [2]. For a given thermionic electron beam current and cathode fall, these equations determine the negative glow plasma density, the electric field distribution, and the ion current back to the cathode (based on the Bohm criteria).

### 2.2 Collisionless Ion Sheath Model

The beam electron space charge is neglected in comparison with the ion space charge in the Poisson Equation. No double sheath formation is considered. Assuming collisionless ions, the Langmuir sheath equations relating ion current density ( $J_i$ ), cathode fall ( $V_k$ ), and cathode fall thickness ( $d_k$ ) are applicable:

$$\begin{aligned} E_k &= \frac{4}{3} \frac{V_k^{1/4} J_i^{1/2}}{(4\epsilon_0/9 \sqrt{2e})^{1/2} \sqrt{M_i}} \\ d_k &= (\frac{4\epsilon_0}{9 \sqrt{2e}})^{1/2} \frac{V_k^{3/4}}{J_i^{1/2}} \end{aligned}$$

where  $M_i$  is the ion mass. For a given  $J_i$  and  $V_k$ , the  $E_k$  and  $d_k$  are computed and  $E_k$  is in turn utilized by the cathode emission model.

### 2.3 Cathode Emission and Cathode Power Balance Models

For a given  $E_k$  and cathode temperature,  $T_k$ , the fully general thermal field emission model (Dyke and Dolan [3]) is implemented, including both the "evaporation" of electrons over the work function potential barrier lowered by  $E_k$  and the "quantum tunneling" of electrons due to "thinning" of the barrier. Such a model can be applied to cathode emission models for both low and high pressure discharges. For relatively low fields and low current density, the general formula for cathode emission reduces to the Richardson equation with the Schottky correction.

A simplified Cathode Power Balance equation is used, i.e. ion current power input is balanced by thermionic and radiative cooling:

$$I_i (V_k + U_i - \phi_w) = I_e \phi_w + \epsilon_m \sigma S T_k^4$$

where  $U_i$ ,  $\phi_w$  is the ionization potential and work function, and  $\sigma$ ,  $\epsilon_m$ ,  $S$  and  $T_k$  are the Stefan-Boltzmann constant, thermal emissivity, surface area and temperature of the cathode spot respectively. A more

detailed cathode model including thermal conduction reveals that conduction power loss is small in comparison with thermionic and radiative cooling.

### 3 Results and Discussions

The basic variables are  $T_k$ ,  $V_k$  and  $J_i$ , and the model is implemented as a set of nonlinear equations for the discharge current balance, ion current balance, and cathode power balance. The constant cathode spot area is an input parameter, and is assumed to be  $0.02 \text{ cm}^2$ , based upon an experimentally observed value. Some important features of the parametric dependence are given below:

(1) As shown in Figure 1,  $V_k$  decreases and  $T_k$  increases with increasing current. Large increases in  $V_k$  are seen at low currents.

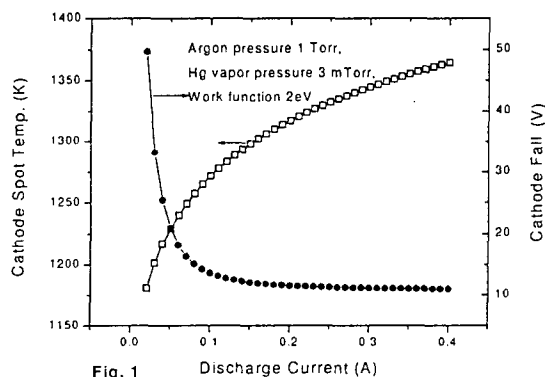


Fig. 1

(2) For a constant discharge current,  $I$ ,  $V_k$  decreases slightly with increasing pressure as given in Figure 2. The effect of pressure on  $V_k$  is more pronounced for higher work functions.

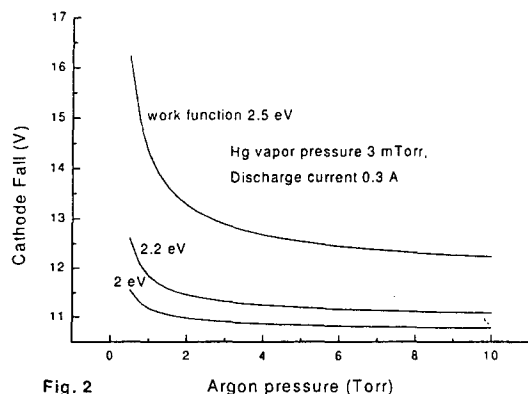


Fig. 2

Extensive measurements of the cathode fall using a Langmuir probe agree reasonably well with model predictions. Further details are given in [4].

(3) Non-monotonic variation of the ion current to electron current ratio at the cathode surface,  $J_i/J_e$ , with  $\phi_w$  is shown in Figure 3.

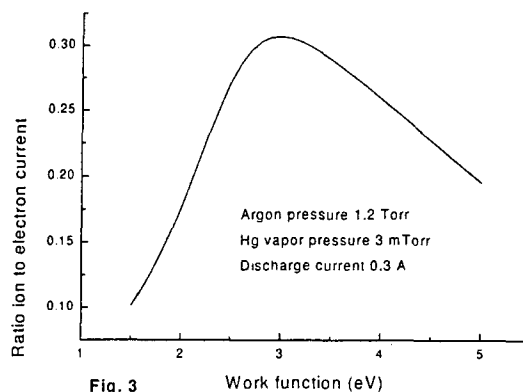


Fig. 3

The collisionless ion sheath is justified posteriori. With 1 Torr argon,  $d_k$  is  $10^{-3} \text{ cm}$  over a range of discharge current. The ion mean free path for  $\text{Hg}^+$  is estimated to be  $6 \cdot 10^{-3} \text{ cm}$ . However, at sufficient high cathode fall voltage, excitation and ionization by electrons in the cathode sheath may be possible, and the non-ionizing Langmuir sheath equations are not valid.

Small increases in the hot spot area with increasing discharge current  $I_d$  were observed experimentally. This effect can be simulated by assuming the hot spot size varies as  $S = 0.01 \cdot (1 + I_d/0.4)$ . The result is given in Figure 4:

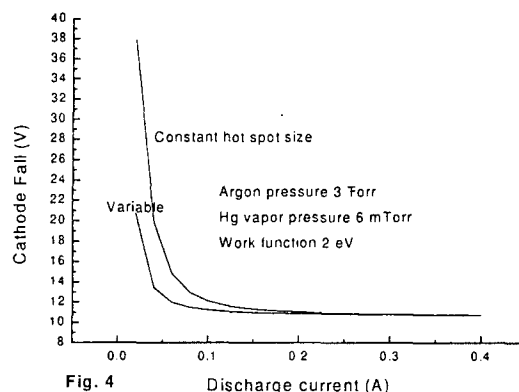


Fig. 4

To eliminate the assumption of constant hot spot size, the solution of a multidimensional cathode power balance with an appropriate negative glow plasma description is necessary. Some work in this direction has begun.

### 4 References

- [1] John F. Waymouth: ELECTRIC DISCHARGE LAMPS, chapter 4, p.71 (1971), MIT Press
- [2] J. H. Ingold: Phys. Rev. A, **43** (1991) 3093
- [3] W. P. Dyke and W. W. Dolan: Advances in Electronics and Electron Physics, **8** (1956) 90
- [4] R. C. Garner and Y. M. Li: IEEE International Conference on Plasma Science, poster (1997)

# Modeling and Diagnostics of Radiation Transport in High Pressure Discharges for Lighting

H G Adler and G G Lister

OSRAM SYLVANIA INC., Beverly, MA 01915, USA

## Introduction

High pressure metal halide lamps are proving successful in providing high quality and efficient lighting for a number of applications. The gas discharges which provide the light source for these lamps are extremely complex systems, and the use of numerical models to assist in lamp development is limited by a lack of data for some fundamental processes. A particular example is radiation transport and the broadening of spectral lines.

Spectral line broadening plays two important roles in metal halide lamp operation. Firstly, the absorption in the wings of broadened lines is often different from that at the line centers, and this energy redistribution (radiation transport) can have a significant effect on the power balance of the lamp. Secondly, line broadening affects the spectrum emitted from the lamp and consequently the quality of the light source.

The major component of conventional metal halide lamps is mercury vapor at a pressure of several bar, the value depending on the lamp operating characteristics. The pressure of the dissociated metal vapors is typically 0.1 bar. Radiation and broadening of mercury lines can therefore be expected to make a significant contribution to the power balance of these lamps.

The classic experimental measurements for pressure broadening in high pressure mercury lamps are by Stormberg and Schäfer [1]. The inferred line broadening parameters differ in many cases by more than an order of magnitude from theoretical calculations. Further, the results relate to a particular set of discharge parameters and are based on assumptions regarding inter-atomic potentials which are themselves open to question. It has thus proved difficult to extrapolate the values obtained in [1] to discharge parameters relevant to other applications, such as metal halide lamps.

The purpose of the present paper is to quantitatively address differences between theory and experiment for high pressure discharges in mercury and to discuss the implications for numerical modeling of these discharges.

## Theory

The principal mechanisms for broadening of spectral lines in high pressure metal halide lamps are van der Waals broadening and resonance broadening. Stark broadening can be important at high temperatures at the arc center and near the electrodes, but is not considered in the present discussion.

### Van der Waals Broadening

Using the quasi-static approximation London [2] showed that the first order perturbation in an atomic energy level due to a perturbing atom vanishes unless both atoms are in identical states, and the second order term is [3]

$$\delta E_{mj}^{AB} = c_{6,mj} / R^6 \quad (1)$$

$$c_{6,mj} = \frac{3e^4 \hbar^4}{2(4\pi\epsilon_0 m_e)^2} \sum_{j' n'} \sum_{m' m} \frac{f_{jj'}^A f_{mm'}^B}{\Delta E_{jj'}^A \Delta E_{m'm}^B (\Delta E_{jj'}^A + \Delta E_{m'm}^B)} \quad (2)$$

where  $\delta E_{mj}^{AB}$  Joule is the perturbation of the state  $m$  (energy  $E_m^A$ ) of an atom of species  $A$  due to the presence of an atom of species  $B$  in state  $j$ ,  $f_{jk}^X$  is the oscillator strength for transition  $j \rightarrow k$  in species  $X$ ,  $\Delta E_{jk}^X = E_j^X - E_k^X$  and  $R$  is the inter-atomic distance.

The van der Waals broadening "half width" due to a local density of perturbers  $N \text{ m}^{-3}$ , expressed in wave numbers, is  $\bar{w}_{mn}^v \text{ m}^{-1}$ , where [4]

$$\bar{w}_{mn}^v = \frac{2\pi^2}{9c\hbar} \left| \sum (c_{6,mj} - c_{6,nj}) \right| N^2 \quad (3)$$

The quasi-static line profile for van der Waals broadening for the transition  $m \rightarrow n$  about the line center  $\bar{\nu}_{mn} \text{ m}^{-1}$  is [4]

$$\bar{L}_{mn}(\bar{\nu}) = \left( \frac{\bar{w}_{mn}^v}{\pi(\Delta\bar{\nu}_{mn})^3} \right)^{1/2} \exp(-\bar{w}_{mn}^v / \Delta\bar{\nu}_{mn}) \quad (4)$$

for  $\Delta\bar{\nu}_{mn} > 0$  and  $\bar{L}_{mn}(\bar{\nu}) = 0$  if  $\Delta\bar{\nu}_{mn} < 0$ , where  $\Delta\bar{\nu}_{mn} = \bar{\nu}_{mn} - \bar{\nu}$ , i.e. the line is only broadened on the "red" side and the maximum of the line profile is shifted by  $\bar{\nu}_{mn}^v = 2\bar{w}_{mn}^v / 3$ .

### Resonance Broadening

Liebermann and Lowke [5] adapted the impact broadening theory of Griem [6] to include transitions from multiplet states. The resulting width for resonant transitions  $m \rightarrow g$ ,  $\bar{w}_{mg}^r \text{ m}^{-1}$  is

$$\bar{w}_{mg}^r = \frac{3r_e}{4\pi} \left( \frac{G_1}{G_M} \right)^{1/2} \left\langle \frac{f}{\Delta\nu} \right\rangle_M N \quad (5)$$

where  $r_e$  is the classical electron radius,  $G_M$  is the statistical weight of the multiplet  $M$ ,  $G_I$  is the statistical weight of the groundstate multiplet and

$$\left\langle \frac{f}{\Delta \bar{\nu}} \right\rangle_M = \frac{1}{G_I} \sum_{k,g} \frac{(2J_k + 1)f_{gk}}{\bar{\nu}_{kg}} \quad (6)$$

where the sum is over all groundstates  $g$  and all states  $k$  in multiplet  $M$ . The width of transitions  $m \rightarrow n$ , where  $m$  and/or  $n$  has a groundstate transition is

$$\bar{w}_{mn}^r = \max(\bar{w}_{mg}^r, \bar{w}_{ng}^r) \quad (7)$$

satisfying a Lorentzian profile

$$L_{mn}(\bar{\nu}) = \frac{1}{\pi \bar{w}_{mn}^r} \left( \frac{1}{(\Delta \bar{\nu}_{mn})^2 + 1} \right) \quad (8)$$

The line broadened profiles of spectral lines are thus a convolution of the profiles (4) and (8) [1].

### Comparison with Experiment

We have previously reported [7] comparisons between experimental measurements of gas temperatures and spectral line broadening in mercury discharges and predictions using numerical models [8]. In the numerical programs, the gas temperature was determined self consistently by including a 1D model of the radiation transport in the energy balance equation. In the computations, the larger of the Stormberg [1] and theoretical values for the van der Waals broadening were used, while resonance broadening was computed by multiplying (5) by a factor 2/3 for agreement with the Stormberg [1] value for the 185 nm line.

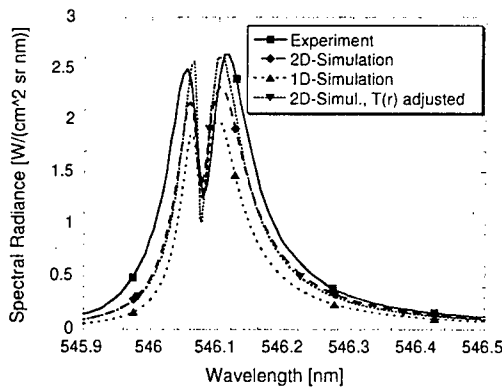


Figure 1: Comparison of theory and experiment for the Hg 546 nm line

Figure 1 shows a comparison between the experimentally observed line profile of the Hg 546 nm line with those computed using the temperature profile obtained from the 1D and 2D arc models. The discharge had a radius of 6.5 mm and a gas pressure of 3.5 bar. The measured gas temperature on axis was 6100 K and that computed was 5900 K.

The comparison between arc model results and experiment is poor. However, closer agreement was obtained by repeating the calculation using the experimentally measured temperature profile, suitably extrapolated in the outer mantle.

In pure Hg discharges, UV radiation at 185nm and 254 nm may represent 30% of the available radiation energy in the arc. Some of the discrepancy between experimentally observed and computed temperatures may be attributed to uncertainties in the profiles of these lines.

We are currently conducting a series of experiments in Hg discharges at pressures between 2 and 8 bar, in order to clarify some of the issues raised above.

### Conclusions

The mechanisms for broadening of spectral lines in high pressure Hg lamps is still not well understood. A continuing experimental and theoretical research program is necessary if the radiation processes in metal halide lamps are to be well understood.

### References

- [1] Stormberg H-P, Schäfer R; *J. Appl. Phys.* 54 (1983) 4338
- [2] London F; *Z. Phys.* 63 (1930) 245
- [3] Hindmarsh W R, Farr J M; *Progress in Quantum Electronics* (eds. J H Sanders and S Stenholm; Oxford Pergamon Press) 2 (1972) 141
- [4] Peach G; *Adv. Phys.* 30 (1981) 367
- [5] Liebermann R W, Lowke J J; *J. Quant. Spectr. Radiat. Transp.* 17 (1976) 253
- [6] Griem H R; *Plasma Spectroscopy* (McGraw Hill, 1964)
- [7] Adler H G, Liebermann R W, Speer R; *Proc. 7<sup>th</sup> Int. Symp. On the Science and Technology of Light Sources, Kyoto, Japan* (1995) 203
- [8] Lowke J J, Zollweg R J, Liebermann R W; *J. Appl. Phys.* 46 (1975) 650; Lowke J J; *J. Appl. Phys.* 50 (1979) 147

# Particules densites determination in high pressure mercury discharges

A. Asselman, J. J. Damelincourt\*, A. Mouadili and H. Sarroukh

Université Abdelmalek Essaadi, Faculté des sciences de Tétouan, B.P. 2121 M'Hanech, 93002 Tétouan Maroc

\*Centre de Physique des Plasmas et Applications de Toulouse (CPAT), Université Paul Sabatier, 118 route de Narbonne, 31062 Toulouse FRANCE.

## 1. Introduction

In high pressure mercury discharges or in metal halide discharges containing mercury as a buffer gas the profile of the 690.7 and 491.6 nm mercury lines (figure 1) is proposed to be used for electron and neutral densities determination, these two lines suffering no or little absorption: Particularly for the studied discharges, the transmission of the two lines is within 0.95-0.99. Because of this low absorption the shape of the line profile as emitted along a chord of the discharge is mainly due to broadening processes [1]. Therefore it can be expected that broadening of these lines would provide an easily used diagnostic tool. In this paper we report on the study of 690.7 and 491.6 nm mercury line broadening processes for diagnosis purposes.

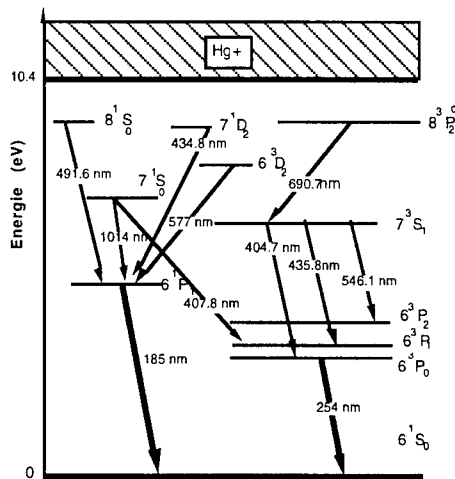


Figure 1: Energy levels in mercury

## 2. Line shape Modeling

Line profiles are computed by solving the integral form of the radiative transfer equation with the usual assumption of local thermodynamic equilibrium (L.T.E.). For local line profile we take into account Doppler

broadening and pressure broadening by neutral and charged particles. For this purpose we need plasma composition of the species which can be deduced from temperature profiles. Broadening constants are introduced as parameters which have been determined by comparing computed profiles with experimental ones.

We have estimate neutral and charged particles effects by performing time resolved measurements for several discharges operated on ac power. Computational details and fitted broadening constant values are given in our recents works [2], [3]. Broadening constante are resumed in table 1. With this set of values we find a good agreement between our computed and mesured profiles.

	491.6 nm line	690.7 nm line
$2\delta_n$	$2\delta_r (1 - B \cdot n_0)$	$2\delta_6$
$\Delta_n$	$-0.13 \times 2\delta_r$	$\Delta_6 = 0.36 \times 2\delta_6$
$2\delta_{ei}$ and $\Delta_{ei}$	Griem's formula	Griem's formula
rapport $2\delta_{ei}/\Delta_{ei}$	1.16	2.3
$k_r$	$(2.7 \pm 0.15)$ [2] 2.72 [4] 1.73 [5]	-----
$C_4$ (rad.cm <sup>4</sup> .s <sup>-1</sup> )	$1.8 \cdot 10^{-13}$ a	$3.5 \cdot 10^{-12}$
$A_{ea} \times 10^{-6}$ s <sup>-1</sup>	4.8	3.2
$C_6$ (rad. cm. <sup>6</sup> .s <sup>-1</sup> )	-----	$4.65 \cdot 10^{-29}$ a

Table 1: used formulas and broadening constantes

$2\delta_{ei}$ ,  $2\delta_n$ ,  $2\delta_r$ ,  $2\delta_6$ , are the full width at half-maximum for charged particles, neutral particles, resonance and van der waals

broadening respectively.  $\Delta_{ei}$  and  $\Delta_6$  are the charged particles and van der Waals shift respectively.  $C_4$  and  $C_6$  are the broadening constant for Stark and van der Waals effect.  $B$  is a parameter and  $A_{ea}$  the transition probability.

### 3- Results

Due to the fact that the 690.7 nm and 491.6 nm lines profiles depend essentially on electron and neutral densities respectively, we expect that we can evaluate  $n_e$  and  $n_0$  in L.T.E. conditions using iterative method. For practical use of the obtained results, we study the influence of the electron and neutral densities on the line broadening. We use a temperature profile whose analytic form is given by:

$$T(\rho) = T_c - (T_c - T_w) \rho^\beta \quad (1)$$

where  $\rho$  is the reduced radius,  $T_w$  the wall temperature ( $T_w = 1000$  °K),  $T_c$  the axial temperature and  $\beta$  a parameter.

Results of figure 2 and 3 show that  $2\delta$  depends essentially on  $n_e$  and  $\beta$  for the red line and on  $n_0$  for the blue one. Thus, by comparing experimental line widths with calculated ones we can estimate axial electron density  $n_e$  and evaluate axial neutral density  $n_0$  value from the 690.7 nm and 491.6 nm line broadening respectively. With these two parameters one can characterize the discharge.

These curves lead to the following fitted analytical formula which gives  $2\delta$  as a function of  $n_e$ ,  $\beta$  and  $n_0$ :

$$2\delta_r(nm) = (-5.3 \cdot 10^{-3} + 8.7 \cdot 10^{-21} \cdot n_0) + (1.9 \cdot 10^{-17} + 0.3 \cdot 10^{-17} \cdot \beta - 3.1 \cdot 10^{-19} \cdot \beta^2) \cdot n_e \quad (2)$$

$$2\delta_b(nm) = -1.1 \cdot 10^{-40} \cdot n_0^2 + (0.374 - 5.3 \cdot 10^{-18} \cdot n_e + 1.12 \cdot 10^{-33} \cdot n_e^2) \times 10^{-19} \cdot n_0 \quad (3)$$

$2\delta_r$  and  $2\delta_b$  are the FWHM of the 690.7 nm and 491.6 nm mercury lines respectively.  $n_e$  and  $n_0$  are in  $\text{cm}^{-3}$ .

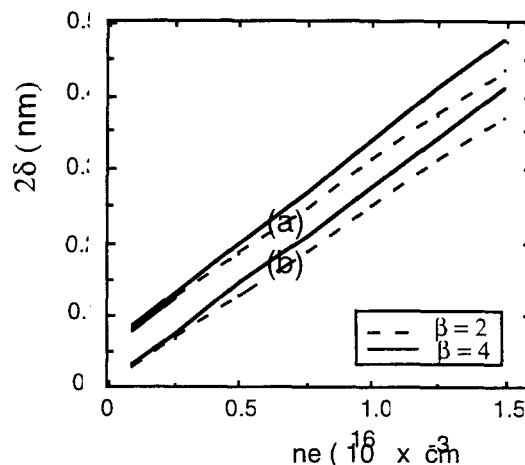


**Figure 2:** Calculated value of the 690.7 nm FWHM as a function of axial value of  $n_e$  and  $n_0$ , with  $\beta$  as a parameter. (a):  $n_0 = 7.3 \cdot 10^{18} \text{ cm}^{-3}$  and (b):  $n_0 = 1.5 \cdot 10^{18} \text{ cm}^{-3}$

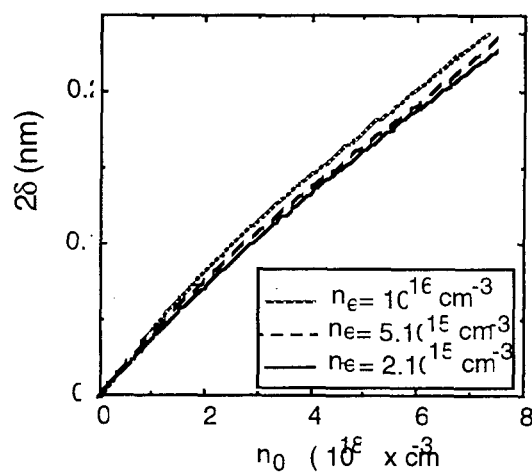


**Figure 3:** Calculated value of the 491.6 nm FWHM as a function of axial value of  $n_e$  and  $n_0$ .

### References

- [1] Griem H.R., Plasma Spectroscopie. Mac Graw Hill Company, New-York (1974).
- [2] Asselman, A., M. Aubes, J.J. Damelincourt and J. Salon, J. Appl. Phys., Vol 71, 10 (1992) 4739
- [3] Asselman, A., M. Aubes, S. Couris and J. Salon, J. Appl. Phys., Vol 72, 8 (1992) 1
- [4] Rompe R., Schulz P., Zs. Phys. 118 (1941) 269
- [5] Stormberg H.P. and Schafer R., J. Appl. Phys. 54 (1983) 4338



## VUV fluorescence of triatomic ionic excimers

Ph. Delaporte, M. Voitik, B. Fontaine, M. Sentis, O. Uteza

Institut de Recherche sur les Phénomènes Hors Equilibres

U.M.R. 6594 C.N.R.S. - Universités Aix - Marseille I et II

163 Av. de Luminy, 13288 Marseille cedex 9

France

e-mail : delaporte@mfmcalas.univ-mrs.fr

### 1. Introduction

Ionic excimer molecules have previously been investigated to extend the gas laser performances towards the shorter wavelengths. Particularly, experimental studies [1-3] allowed one to observe several VUV fluorescence lines of diatomic alkali (A) rare-gas (Rg) excimer from 63.8 nm ( $\text{He}^+\text{K}$ ) [4] to 189.9 nm ( $\text{Xe}^+\text{Li}$ ) [1]. Unfortunately, the strong photoabsorption by alkali atoms in the VUV region as well as some kinetic processes prevented the demonstration of such a VUV laser.

We report now the observation of alkali rare-gas triatomic ionic excimers, such as  $\text{Rg}_2^+\text{A}$ . We carried out experiments on  $\text{Kr}_2^+\text{Cs}$  (158 nm),  $\text{Kr}_2^+\text{Rb}$  (160 nm),  $\text{Xe}_2^+\text{Cs}$  (190 nm),  $\text{Ar}_2^+\text{Cs}$  (135 nm) by electron beam excitation of alkali rare-gas mixtures. The observation of the VUV emission spectra of these ionic molecules provided information about the electronic structure and the formation kinetic processes of these excimers.

### 2. Experimental setup

A cold cathode electron gun was used to excite transversally the gas mixtures [5]. This electron gun, energized by a 300 kV- 1500 J Marx generator (MX 31 from Physics International Company), is separated from the cell (active volume of  $1.7 \times 1.7 \times 15 \text{ cm}^3$ ) by a 25  $\mu\text{m}$  thick titanium foil. The current density was about 1  $\text{A}/\text{cm}^2$  for 800 ns. Under these conditions, an energy deposition of a few hundred  $\mu\text{J}/\text{cm}^2$  has been produced in one bar of argon. In order to obtain sufficient alkali vapor density inside the cell one must heat the gas to 400°C.

The gas inside the cell is separated from the detection apparatus by a magnesium-fluoride window. The spectra emitted from the excited volume are observed with a 0.2 m Seya-Namioka vacuum ultraviolet monochromator (VM 502 Acton Research Corporation) with a 1200 lines/mm grating. The fluorescence emissions are either time integrated by an optical multichannel analyser (IVUV 700 Princeton Instruments) with a spectral resolution of 0.4 nm or time resolved by a fast solar-blind photomultiplier (Thorn Emi VUV C640).

### 3. Experimental results

Experiments were performed by electron-beam excitation of alkali rare-gas mixtures with and without argon as a buffer gas. Fig. 1 presents spectra observed

for three different argon/krypton/cesium mixtures. Before the introduction of cesium, the spectra recorded in the 120 nm - 180 nm region after the excitation of pure krypton or argon-krypton mixture consists only of the fluorescence of the broad second continuum of krypton ( $\text{Kr}_2^+$ ) centred at 144 nm ( $T \sim 350^\circ\text{C}$ ). In the presence of alkali vapor, the  $\text{Kr}_2^+$  signal intensity is greatly reduced and two other emission bands appear. As it is shown in Fig. 1, the spectra exhibit a narrow band (FWHM  $\approx 1.5 \text{ nm}$ ) at 132 nm, the  $\text{Kr}_2^+$  emission, and a new broad continuum centred around 160 nm. The 132 nm emission has been extensively studied [6] and is generally attributed to the ionic excimer  $\text{Kr}^+\text{Cs}$ . The other emission, which appears only in the presence of cesium, and only for krypton pressure higher than 80 mbar, is attributed to the triatomic ionic excimer  $\text{Kr}_2^+\text{Cs}$ . As for the diatomic ionic excimer, this new transition will occur between the emitting state combining a  $\text{Kr}_2^+$  ion and a Cs atom and the lower state  $\text{Kr}-\text{KrCs}^+$ .

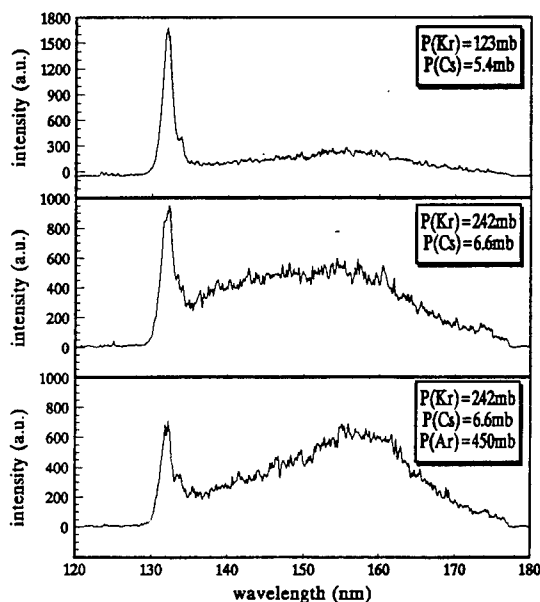


Figure 1. Emission spectra of  $\text{Kr}_2^+$ ,  $\text{Kr}^+\text{Cs}$  and  $\text{Kr}_2^+\text{Cs}$  excimers at three different mixtures.

Figure 2 presents the emission spectra recorded between 120 nm and 180 nm when three different alkali rare-gas mixtures are excited by an electron beam. In figure 2.a (resp 2.b), one can observe an intense emission of  $\text{Kr}^+\text{Rb}$  at 134 nm (resp.  $\text{Xe}^+\text{Cs}$  at 160 nm) and a weak and broad emission at 160 nm (resp. 190 nm). This last

continuum is due to the radiative decay of the triatomic ionic excimer  $Kr_2^+Rb$  (resp.  $Xe_2^+Cs$ ). Curve (A) of the figure 2.c was obtained by electron beam excitation of pure argon, and only the second continuum of argon  $Ar_2^+$  is visible (126 nm). Then, 6.6 mbarr of Cs has been added to this argon and the excitation of this mixture allowed one to record the spectrum of the curve (B). The  $Ar_2^+$  emission completely disappeared and a new broad continuum, due to  $Ar_2^+Cs$ , is now visible at 135 nm. The emission of the corresponding diatomic excimer  $Ar^+Cs$ , which emits at 114 nm, is not observable because of the absorption of the  $MgF_2$  window.

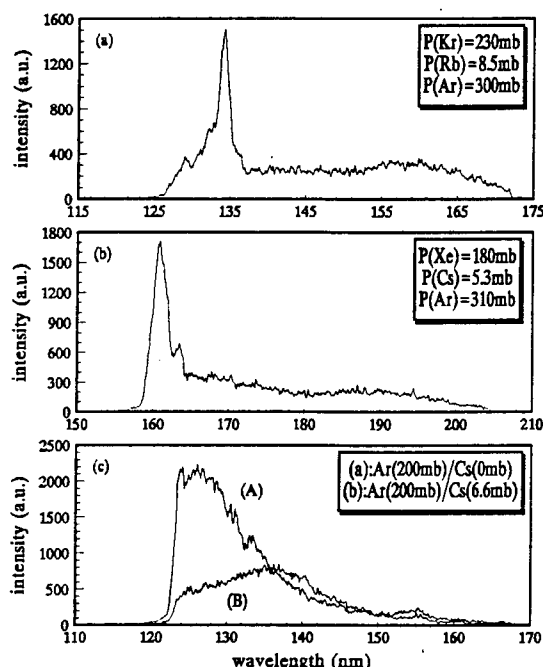


Figure 2 : emission spectra recorded between 120nm and 180nm after excitation of three different alkali rare-gas mixtures.

## 4. Discussion

### 4.1. Spectroscopy

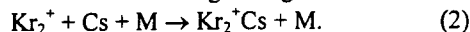
The  $Kr_2^+Cs$  continuum is centred at 159 nm with 16 nm width (FWHM). We estimated the energy  $E$  of the radiative transition as:

$$E = [I_p(Kr) - D_0(Kr_2^+Cs) - D_0(Kr_2^+)] - [I_p(Cs) - D_0(Kr^+Cs)] - \delta \quad (1)$$

where  $\delta$  is the repulsive energy of the ground level and estimated to be 1 eV by comparison with  $Kr_2^+$  excimer. The  $Kr_2^+Cs$  and  $Kr_2^+$  molecules both exhibit the repulsive ground level leading to broad fluorescence emission spectra. The  $Kr_2^+$  binding energy is 1.15 eV [7], and thus,  $D_0(Kr_2^+Cs)$  was estimated to be 0.9 eV, which is close to the value measured for the  $Kr^+Cs$  molecule (0.8 eV) [1]. In contrast to the alkali rare gas diatomic ionic excimers, the very broad, structureless character of the  $Kr_2^+Cs$  fluorescence spectra indicates repulsive behavior for the ground state.

### 4.2. Kinetics

We propose two channels for populating the upper fluorescence state of  $Kr_2^+Cs$ . By analogy with the  $Kr^+Cs$  kinetics, the first one is similar to the three body association processes clearly identified as the main production channel for forming the  $Rg^+A$  molecule



The second is a recombination of the diatomic ionic excimer with a krypton atom



From an analysis of the relative intensity ratios of the  $Kr_2^+Cs$ ,  $Kr^+Cs$  and  $Kr_2^+$  emissions as a function of the different gas pressures, we estimated the rate coefficients of the formation processes of this triatomic ionic excimer of  $k_2 \approx 10^{-30} \text{ cm}^6/\text{s}$  for reaction (2) and  $k_3 \approx 5.10^{-30} \text{ cm}^6/\text{s}$  for reaction (3).

## 5. Conclusion

The production of triatomic ionic excimers by electron beam excitation of alkali rare gas mixture was observed. The emission spectrum of  $Kr_2^+Cs$  is peaked at 159 nm and with 16 nm width. In spite of the high emission intensity obtained for the  $Kr_2^+Cs$  fluorescence, it is impossible to consider these molecules as suitable candidates for lasing because of a strong photoionization of alkalis in the VUV region and the competitive processes of the formation reactions.

The authors like to thank the French DRET for the financial support of this work.

## References

- [1] J. Fiedler et al, Z. Phys D - Atoms, molecules and clusters **11**, 141 (1989).
- [2] P. Millar, G. Warwar, P. J. Wisoff, R. Sauerbrey, and K. Balasubramanian, Appl. Phys. Lett. **55**, 2176, (1989).
- [3] H. M. J. Bastiaens, F. T. J. L. Lankhorst, P. J. M. Peters, and W. J. Witteman, Appl. Phys. Lett. **60**, 2834, (1992).
- [4] K. Petkau, J. W. Hammer, G. Herre, M. Mantel, H. Langhoff, J. Chem. Phys. **94**, 7769 (1991).
- [5] H. Tischler, Ph. Delaporte, B. Fontaine, B. Forestier, M. Sentis, Rev. Sci. Instrum. **67** (7), 2453, (1996).
- [6] H. Tischler, Ph. Delaporte, B. Fontaine, M. Sentis, IEEE J. Selected Topics Quantum Electron **1**, 877, (1995).
- [7] C. Ng, D. Trevor, B. Mahan, Y. Lee, Journ. Chem. Phys., **66**, 446, (1977).

# Hollow Cathode Effects in a Pulsed Capillary Discharge

M. Favre, P. Choi\*, J. Moreno, C. Dumitrescu-Zoita\*, M. Zambra\*\*, H. Chuaqui, and E. Wyndham

Facultad de Física, Pontificia Universidad Católica de Chile

Casilla 306, Santiago 22, Chile

\*LPMI, Ecole Polytechnique, Palaiseau 91128, France

\*\*Comision Chilena de Energia Nuclear, Casilla 188-D, Santiago, Chile

## 1. Introduction

The capillary discharge (CD) is known as a high brightness source in the VUV and soft X-ray region<sup>1</sup>, which is also a suitable medium for discharge based X-ray laser studies<sup>2</sup>. The successful operation of a CD as a high temperature plasma radiation source depends strongly on the initial formation of a conducting plasma column away from the wall. In this paper we report on time resolved studies of a fast CD which operates in the nanosecond regime with current in the kA region into a sub-millimetre diameter capillary. We present experimental evidence which indicates that electric breakdown inside the capillary is assisted by the hollow cathode effect (HCE)<sup>3</sup>. This is inferred from time resolved observations of axial electron beams, which are time correlated with measurements of discharge current and voltage, together with visible and VUV light emission. Time resolved XUV spectroscopic observations of the pulsed capillary discharge are presented in a companion paper<sup>4</sup>.

## 2. Experimental Apparatus.

The discharge chamber is arranged on the axis of a pair of parallel plate electrodes, separated by a thin dielectric to form a local energy storage capacitor which is pulse charged throughout a primary capacitor using a triggered switch. A pair of 90 mm diameter brass electrodes form the anode and cathode of the discharge, as well as the parallel plate capacitor. An alumina capillary, 0.8 mm diameter, 15 mm long, is located on axis between the two electrodes. On the cathode side, an additional plate is used to provide the optimum geometry of the aperture for the operation of the transient hollow cathode assisted ionization. A primary DC charged capacitor of 5 nF is used to pulse charge the storage capacitor within 100 ns. At a charging voltage of 25 kV, current above 10 kA is produced through the capillary, with a 10-90% current rise time of below 5 ns. The discharge is triggered by means of an auxiliary discharge from a small cable plasma gun, located a few mm behind the cathode aperture, with a delay of 80 to 120 ns. The cathode region is pumped through the capillary, thus allowing a higher pressure in the hollow cathode region, while maintaining a lower pressure in the capillary. The experiments have been performed in Argon at pressures

between 100 and 300 mTorr in the hollow cathode region (HCR) and a few mTorr at the Anode region. Apart from the voltage and current measurements, the plasma emission is studied in the visible with PIN diodes and photomultipliers, in the VUV region with filtered PIN diodes and XRD. Electron beams are measured using a Faraday cup and a scintillator-photomultiplier assembly.

## 3. Experimental Results

Figure 1 shows characteristic single shot signals for a triggered discharge at 12 kV, 160 mTorr. A cable delay of 110 ns is used for the auxiliary triggering discharge. The voltage rises to its maximum value in around 100 ns, and collapses in less than 10 ns at breakdown. At voltage collapse, a fast current pulse is observed, which is time correlated with an electron beam pulse. After the initial current pulse, the voltage recovers and grows up to ~1 kV. Additional electron beam pulses after breakdown are driven by the residual high voltage. The visible light emission is monitored axially, from behind the cathode. The first step observed in the visible corresponds to the auxiliary discharge. The second step coincides with the onset of the main discharge across the capillary. At later times the visible emission follows the oscillation of the external discharge current, through the primary circuit, as inferred from a software integration of  $dI/dt$ . The main feature of the triggered discharge are highly reproducible over the pressure range investigated. Figure 2 shows characteristic signals for a self breakdown, untriggered discharge, at the same conditions than in Fig. 1. When compared with the triggered discharge, the characteristic delay to breakdown in this particular shot increases by around 500 ns. An initial low current electron beam pulse is observed prior to electric breakdown. A fast current pulse is also observed at voltage collapse, which again coincides with the fast rise in visible light emission. At both triggering conditions, XRD and PIN diode observations show an initial fast, less than 10 ns width, VUV pulse which coincides with the main discharge current pulse. A high energy component, above 5 keV, in the electron beams has not been detected, presumably due to the relatively low applied voltage. The positive excursion in the electron beam signals is probably due to discharge plasma reaching the Faraday

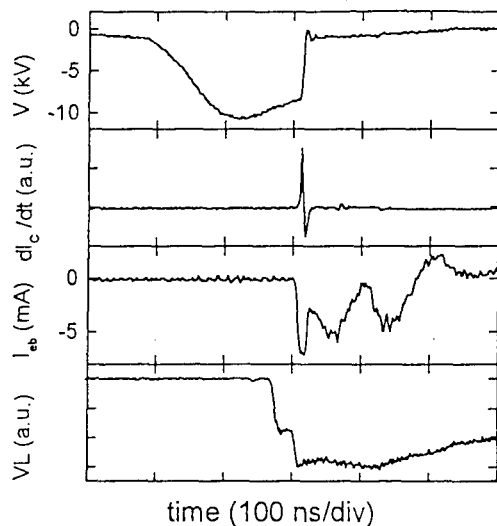


Figure 1: from top to bottom, applied voltage, time derivative of discharge current, electron beam current, and visible light emission for a triggered discharge.

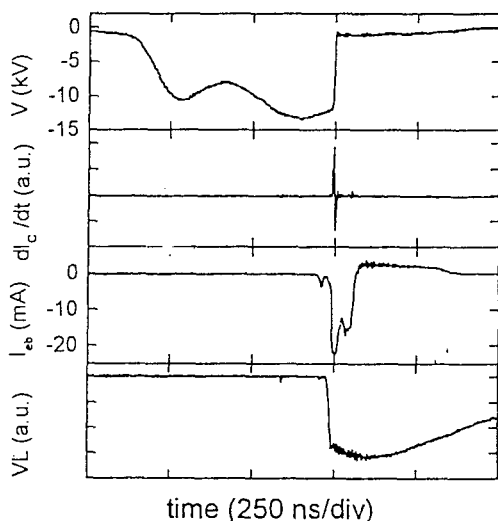


Figure 2: same signals as in figure 1 for an untriggered discharge.

cup collector plate. In general, the time delay to breakdown is not reproducible in the untriggered discharge, and an appreciable jitter is observed

#### 4. Discussion

Transient hollow cathode discharges (THCD) are characterized by a rapid voltage collapse accompanied by the growth of an intense electron beam leading to the formation of an on-axis ionization channel, which develops throughout a moving virtual anode<sup>5</sup>. The electron beams originate in a plasma region inside the hollow cathode region, which develops spontaneously following the application of the high voltage across the

electrodes. Initially the electron beams are of high energy, of the order of the external potential, and low characteristic current. At later times, just before electric breakdown, the electron beams are of lower energy but much higher current. Apart from the high energy component, these features are clearly identified in the sequence of events leading to electric breakdown in the pulsed capillary discharge. Auxiliary triggering inside the HCR provides an additional source of plasma to enhance the electron beam emission. A single electron beam pulse is observed to start just before electric breakdown and fall after breakdown has completed. The trigger plasma also continues to supply electrons for extraction and is seen as the long duration e-beam signal detected after breakdown. This is quite different from the conventional THCD development. In the late case, the formation of the electron beam relies purely on self sustained ionization processes inside the HCR, and the two periods observed, before and at the time of electric breakdown, are characteristic of a self breakdown THCD operating on a much lower aspect ratio<sup>6</sup>. The partial voltage recovery after the fast current pulse is a good indication that the initial discharge channel has been initiated along the capillary axis, away from the wall. Expansion of the plasma channel results in material being ablated from the capillary wall, thus leading to a fast cooling, with a subsequent increase in plasma resistivity.

#### 5. Conclusion

Our results show that the HCE is present in hollow cathode discharge geometries with a much higher aspect ratio than those previously investigated<sup>6</sup>. The pulsed capillary discharge can be initiated successfully with the assistance of the hollow cathode effect. The resulting discharge is characterized by a short, less than 5 ns half width current pulse, with an associated XUV light pulse<sup>4</sup>. The enhanced HCE due to the auxiliary discharge allows the XUV light pulse to be synchronized to external events.

#### 6. Acknowledgments

This investigation has been funded by FONDECYT project 1950798 and a CNRS-CONICYT collaboration program. J. Moreno holds a postgraduate scholarship from CONICYT.

#### 7. References

- <sup>1</sup>R.A. McCorkle, Appl. Phys. A, **A26**, 261 (1981)
- <sup>2</sup>J.J. Rocca et al., Phys. Rev. Lett. **73**, 2192 (1994)
- <sup>3</sup>P. Choi et al., IEEE Trans. Plasma Sci. **15**, 428 (1987)
- <sup>4</sup>P. Choi et al., these Proceedings.
- <sup>5</sup>M. Favre et al., IEEE Trans. Plasma Sci. **23**, 212 (1995)
- <sup>6</sup>M. Favre et al., Appl. Phys. Lett. **60**, 32 (1992)

# High energy photons emitted from a high voltage fast discharge in vacuum and in low pressure gases

A. Khacef, C. Cachoncinlle, R. Viladrosa, E. Robert, and J.M. Pouvesle  
GREMI, CNRS/Université d'Orléans, B.P. 6759, 45067 Orléans Cedex 2, FRANCE

## 1. Introduction

Pulsed electrical discharge in vacuum are currently founding an increasing number of applications in various field concerning both research and industry, including vacuum switches, circuit breakers, high power X-ray sources, etc...

In this work we report on the production and the analysis of the high energy photon emission from high voltage fast discharge in vacuum and in low pressure gases.

## 2. Experimental set-up

The experimental set-up is shown in Figure 1. The discharge cell made of quartz has a cylindrical shape (3 mm wall thickness, 35 mm outside diameter, and 130 mm length) on the axis of which are placed a hollow-cathode and a sharp anode. Experiments with different electrode material and geometry were performed. The results presented here were obtained with a 8 mm Cu hollow-cathode and 8 mm diameter W rod with 60° conical shaped tip.

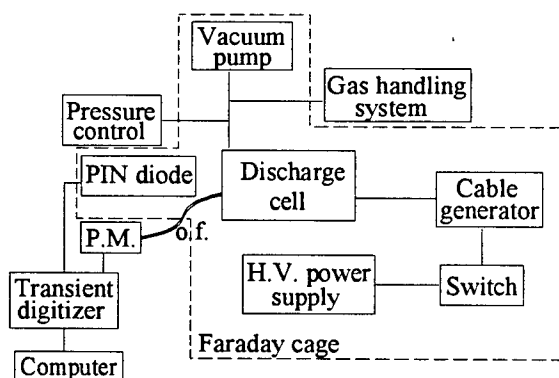


Figure 1: Block diagram of the experimental set-up (o.f. = optical fiber).

The high voltage pulses were delivered by a cable transformer which is powered by ceramic capacitors disposed in a Blumlein-like configuration and switched by a dielectric barrier discharge (DBD) triggered spark gap. Open circuit peak voltage in excess of 400 kV in typically 60 ns duration (FWHM) can be achieved while commutation occur at low voltage (< 20 kV). The maximum electrical energy stored in the system was about 7.2 J.

Extensive measurements have been made to study the characteristics of the emission of the radiation as a function of a wide range of experimental conditions (nature of gas, pressure, charging voltage, electrode material and shape, electrode gap) and the discharge was characterized by both electrical and spectroscopic means.

## 3. Results

When breakdown occurs, the radiation emitted from the plasma cover the large spectral band extended from the visible to hard X-rays.

Figure 2 shows the dependence of the X-ray dose per pulse and the duration in time (fwhm) of the output pulse, respectively, as functions of the residual air pressure in the discharge cell. The X-ray emission appears below threshold pressure (TP) of about 0.4 mbar for most of electrode spacings having some practical utility. Below the characteristic pressure (CP) of about 0.05 mbar, the X-ray production efficiency is high and the X-ray output remains constant exhibiting a plateau. The X-ray pulse duration exhibits the same behavior as the X-ray dose versus the residual pressure.

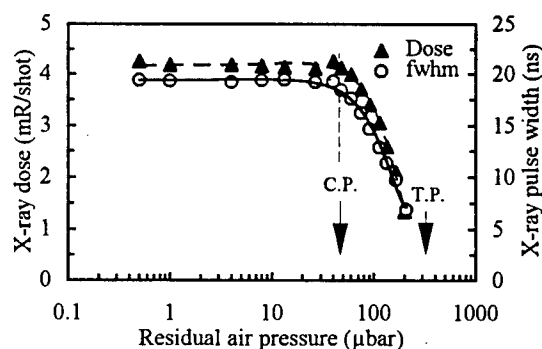


Figure 2: Effect of the residual pressure in the discharge cell on the X-ray dose per shot and on the X-ray pulse width measured at 25 cm from the source. (C.P. and T.P. represent the characteristic and the threshold pressures respectively).

These results indicates, that in such experimental conditions a high vacuum is not necessary as indicated in previous studies [1, 2]. One can note that when the residual pressure varies from 0.4 mbar to 0.05 mbar, the duration (fwhm) of the X-ray emission increases by nearly one order of magnitude. This behavior gives the possibility to adjust the pulse length from 4 ns to 20 ns

but at the expense of the emitted dose for the shorter pulse durations. This makes this high energy photon source applicable to specific fields of research such as, for example, photo-excitation of gaseous matter [3] and observation of ultra-short phenomena.

Discharge operation is also possible in gases (He, Ne, Ar, Kr, Xe, H<sub>2</sub>, N<sub>2</sub>) at pressures varying from 10<sup>-3</sup> mbar for xenon to about 1 mbar for helium without changing the emitted dose. In these cases the characteristic pressure (CP) seems strongly correlated to the ionization potential of the considered gases. The higher values of ionization potential correspond to the higher CP's except in the case of hydrogen [4].

A typical record of the X-ray power output in the forward direction as a function of time is shown in figure 3 for one of the lowest pressure of figure 2.

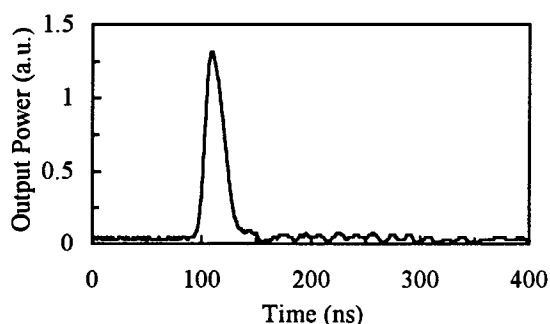


Figure 3: Typical recording of the X-ray output power as a function of time in the case of 15 kV charging voltage.

The spectral distribution emitted by the high flux X-ray source was estimated from attenuation measurements with foils of known thickness. X-rays of energy up to 400 keV can be generated and detected through a mylar window which limit the detection of the low energy part of the spectrum to around 5 keV.

An example of experimental data obtained in the case of the use of aluminum foils is shown in figure 4. These results are compared to the results of the theoretical simulation including the fact that the X-ray emission is polychromatic. In that case, the absorption cross section  $\sigma(E)$  strongly depends on the incident photon energy  $E$ . The fraction of the transmitted intensity, integrated all over the energy spectrum (from  $E_1$  to  $E_2$ ), is related to incident intensity  $I(E)$  by the following relation:

$$T = \frac{\int_{E_1}^{E_2} I(E) \exp(-\sigma(E) n x) dE}{\int_{E_1}^{E_2} I(E) dE}$$

where  $n$ , and  $x$  represents the absorber density, and the absorber thickness, respectively.

Comparison between experimental and theoretical data shows that around 90% of the total X-ray energy is radiated in characteristic lines of the anode material (K and L lines). The 10% remaining are distributed over a large bremsstrahlung continuum with an endpoint energy corresponding to the voltage across the electrodes.

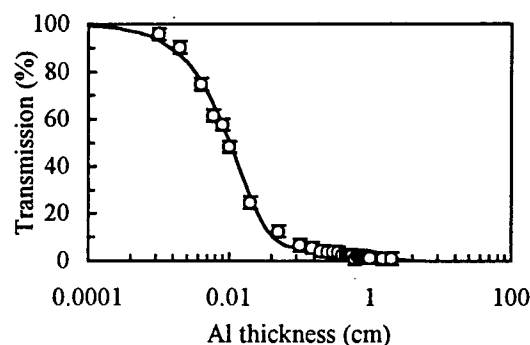


Figure 4: Experimental (dots) and calculated (line) transmission through different Al thickness. (Charging voltage = 14 kV, Anode W and cathode Cu).

The endpoint energy of the spectrum was confirmed by using SILENA detector calibrated by <sup>132</sup>Cs radioactive source coupled to a multi-canal analyzer. At 14 kV charging voltage the continuum spectrum has a maximum intensity at about 50 keV. In this case, and for 1 R ( $1R = 2.58 \times 10^{-4}$  C/Kg) X-ray dose, the number of photon integrated all over the spectrum was about  $4 \times 10^{12}$  per shot.

This work was supported by ANVAR grant N° A9309100F00.

#### 4. References

- [1] E. Sato, S. Kimura, S. Kawasaki, K. Takahashi, Y. Tamakawa, and T. Yanagisawa: Rev. Sci. Instrum., 61 (1990) 2343.
- [2] A. Ikhlef, and M. Skowronek: IEEE Trans. plasma Sci., 21 (1993) 669.
- [3] E. Robert, A. Khacef, C. Cachoncinlle, and J.M. Pouvesle: Opt. Comm., 117 (1995) 179.
- [4] A. Khacef, E. Robert, C. Cachoncinlle, R. Viladrosa, et J.M. Pouvesle: Journal de physique IV, 6 (1996) 747.

## From the "third continuum" to the "molecular ion continua" of rare gases

E. Robert, C. Cachoncinlle, A. Khacef, R. Viladrosa and J.M. Pouvesle

GREMI, CNRS/Université d'Orléans, B.P. 6759, 45067 Orléans Cedex 02, FRANCE

### 1. Introduction

Over the past decades, the fluorescence of rare gases (Rg) in the UV-VUV domain has been the subject of a large number of publications. Two major points have to be particularly enlightened: first the use of a great variety of excitation means: synchrotron, alpha particles, electron beams, charged particle beams, dielectric barrier discharges, X-rays,... and second the diversity of excited media: Rg at pressures between a few mbars up to several tens of bars, gas jets, clusters, solid targets,...

Besides the well known first and second continua of  $Rg_2$ , arising from transitions of the two lowest excited states of the neutral dimer ( $Rg_2$ )<sup>\*</sup> to the repulsive ground state, another broad spectral feature has been reported for all Rg at higher wavelengths than these two first continua. This emission was labelled as the "third continuum" [1] of Rg in the continuation of the denomination of the two first continua. Interest in this fluorescence relies both in the determination of the species at its origin and in the possibility to develop new efficient or even coherent UV-VUV sources. The manifold of experimental and theoretical works dedicated to the "third continua" of Rg has unfortunately led to a rather controversial situation concerning the origin of the fluorescence except for the ionic and molecular character of the emission.

In the course of this research, the flash X-ray excitation of both pure and binary mixtures of Rg at pressures ranging from a few mbars up to 30 bars allowed us to constitute the more complete database on the fluorescence of Rg. The possibility to study the Rg fluorescence with a single excitation source on a large pressure domain and especially with the availability of time resolved spectroscopy from 110 nm up to 800 nm enables us to produce almost all the spectra published in the literature for about thirty years.

This detailed spectroscopic study of Rg fluorescence leads us to propose a new and more adapted denomination of the so-called "third continuum". We showed that "third continuum" is composed of different spectral components with different origins [2], as also suggested by Langhoff [3]. The denomination "molecular ion continua" appears more precise to clearly describe the whole fluorescence emitted by the Rg on the UV-VUV domain.

In the following, argon will be chosen as an archetypical case of Rg as regard to the particularly pronounced evolution of the shape of its fluorescence spectra with pressure or versus time after pulse excitation. Then, the peculiar interest of the flash X-

ray excitation for kinetic studies of excitation transfer mechanisms or heteronuclear ion production, both at very high pressures, will be presented.

### 2. Results and discussion

The deposition of large doses, about one rad, of X-ray photons with energy of about 8 keV in Rg induces intense fluorescence on the UV-VUV domain. The X-ray doses were delivered by a home developed powerful flash X-ray facility able to produce X-ray pulses, with typical fwhm of 20 ns, at high repetition rate, up to 50 Hz and with an exceptional time stability for period of hours. The fluorescence was detected and analysed with fast photomultiplier tubes and a fast digitizer (with an overall time resolution of about 2 ns).

For argon, krypton and xenon the fluorescence of both second and "third" continua were efficiently produced. In the case of argon, five different spectral components, respectively centered around 160, 185, 200, 225 and 245 nm, were evidenced as depicted by the figure 1. These five spectral features are proposed to be labelled as third, fourth, fifth, sixth and seventh continua of argon. Figure 1a) presents the time integrated spectrum of argon fluorescence at a pressure of 0.5 bar. For this pressure, the third and fifth continuum can be clearly seen. For higher pressures, e.g. 17 bars, the figure 1b) exhibits the fourth, sixth and seventh continuum fluorescence of argon over the fifth continuum.

The apparition of these five continua depends on the pressure as shown in figure 1. At a given pressure, for which all of these continua are emitted, i.e. above atmospheric pressure in our experimental conditions, it has been shown that these continua does not appear at the same time in the plasma relaxation. These two features, dependence versus pressure and versus time, enable to understand the problem encountered by authors working on restricted range of experimental parameters (cw excitation, small pressure range,...). Another particularity of these Rg continua relies in their relative large broadness. The fifth continuum presents a spectral fwhm of about 50 nm while all the others have spectral fwhm of about 20 nm. This induces a strong overlap of these different continua and consequently the difficulty in their detailed analysis.

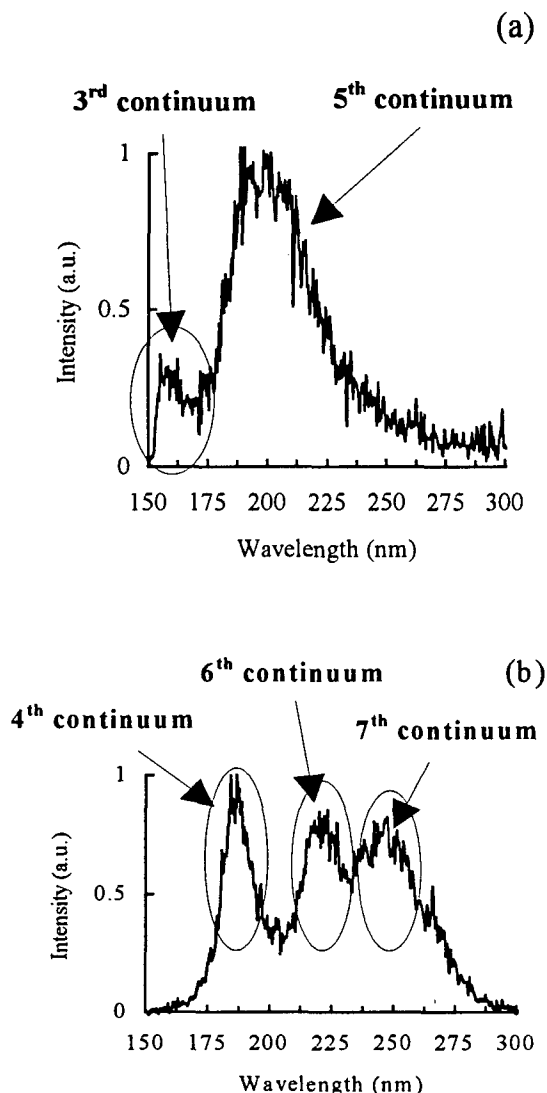


**Figure 1:** Time integrated spectra of the fluorescence spectrum of argon excited by a flash X-ray source at: (a) 0.5 bar and (b) 17 bars.

The existence of five different continua of argon between 150 nm and 300 nm was confirmed by gas mixtures fluorescence study. The figure 2 presents the time integrated spectrum of a mixture (Ar:N<sub>2</sub>/100:1) at a pressure of 5 bars. Two main results were deduced from this spectrum. First, nitrogen was shown to be an efficient quencher of the 4<sup>th</sup>, 6<sup>th</sup> and 7<sup>th</sup> continua of argon while having less effect on the 3<sup>rd</sup> and 5<sup>th</sup>. The spectra of the mixture of argon with nitrogen at high pressure, e.g. 5 bars see figure 2, appears quite similar with that of pure argon for low pressure (below atmospheric pressure). Intense production of the fluorescence of the second positive system of nitrogen, N<sub>2</sub><sup>+</sup>(C) states, were measured at 298, 316, 337 and

380 nm. The rate coefficient for the reaction of argon metastable levels, Ar<sup>+</sup>(4s), with N<sub>2</sub> has been measured on the whole pressure domain ranging up to 30 bars.

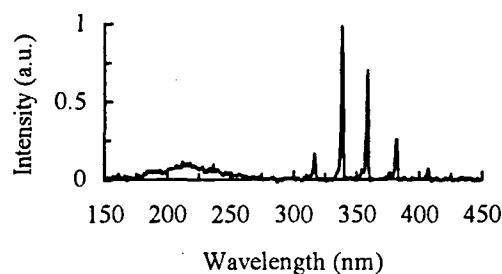


**Figure 2:** Time integrated spectrum of a mixture of argon and nitrogen (Ar:N<sub>2</sub>/100:1) at a pressure of 5 bars excited by flash X-ray source.

The flash X-ray excitation of binary mixtures also leads to the production of heteronuclear ions, (ArNe<sup>+</sup>) at 216, 224 nm and (Ar<sup>+</sup>Xe) at 328, 509 nm. In this case, flash X-ray excitation appeared as a unique source to study these fluorescences both for pressures for which, to our knowledge, they have not been reported, and especially with time resolved spectroscopy. For argon-neon mixtures, long-lived emission was measured. For example, at a pressure of 1.3 bar in the mixture (Ar:Ne/100:0.7), the 216 nm and 224 nm fluorescence signal exhibits a time fwhm of about 100 ns. The fluorescence of (ArNe)<sup>+</sup> originates from a transition between ArNe<sup>+</sup> and Ar<sup>+</sup>Ne ions. Thus, the long-lived fluorescence of this ionic species indicates the presence of long-lived high energy levels in our experimental conditions.

### 3. Conclusion

The whole fluorescence emitted by argon from 150 nm to 300 nm was shown to be the result of the superposition of five different continua labelled as 3<sup>rd</sup>, 4<sup>th</sup>, 5<sup>th</sup>, 6<sup>th</sup> and 7<sup>th</sup> centered respectively around 160, 185, 200, 220 and 245 nm. Same denomination appeared unavoidable for krypton and xenon. The possibility to study heteronuclear ion fluorescence and excitation transfer mechanisms at high pressure (up to 30 bars) with flash X-ray excitation was demonstrated.

### 4. References

- [1] G. Klein and M.J. Carvalho: J. Phys. B: At. Mol. Phys., 14 (1980) 1283.
- [2] E. Robert, A. Khacef, C. Cachoncinlle and J.M. Pouvesle: Opt. Comm., 117 (1995) 179.
- [3] H. Langhoff: J. Phys. B: At. Mol. Phys., 27(1994) L709.

This work was supported by the Conseil Régional du Centre



# Temporal and Radial Behaviour of the Metastable Density in a Pulsed Xenon Discharge at Medium Pressure

E. Kindel, C. Schimke, D. Loffhagen

Institut für Niedertemperatur-Plasmaphysik, 17489 Greifswald, Germany

## 1. Introduction

The temporal evolution of the rare-gas plasma at medium pressure is controlled by the interplay of various electron and heavy particle collision processes. For the understanding of the discharge plasma the population of the metastable  $1s_5$  level of the rare-gas atoms is of great interest. These excited atoms play an important role for the electrical behaviour and are precursors for the first and second excimer continuum radiation. In this paper experimental and theoretical results obtained for the constricted positive column plasma of a pulsed xenon discharge are presented.

## 2. Experimental Set-up

The absolute densities of the metastable xenon atoms have been determined by the hook method, which was introduced first by Rozhdestvenski in 1912 [1]. This classical interferometrical method uses the anomalous dispersion in the vicinity of an absorption line, where rapid changes of the index of refraction occur. The experimental set-up is shown in Fig. 1.

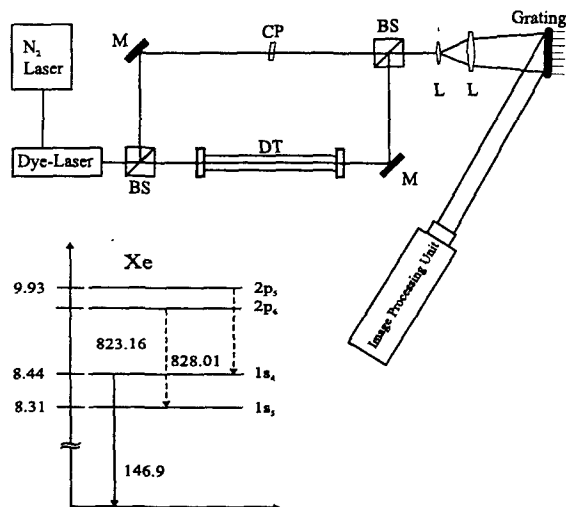


Fig. 1: Hook method. BS: beam splitter, CP: compensating plates, DT: discharge tube, L: lens, M: mirror.

A Mach-Zehnder interferometer has been used to measure the wavelength distance  $\Delta$  between the minimum and maximum in the interference pattern. The background light source is a dye laser with

a beam diameter of 0.3 mm. This laser has been pumped by a  $N_2$  pulse laser with a pulse duration of about 10 ns. Instead of a conventional spectrometer a combination of a beam expander, a grating with 1200 lines/mm and a CCD camera has been employed. The interference patterns are stored and analysed by a PC. For the analysis the hook vernier method has been used [2].

The density  $N$  of the lower xenon level of the transition  $2p_6-1s_5$  at the wavelength  $\lambda_0 = 823.16$  nm is given by

$$N = \frac{\pi K \Delta^2}{r_0 f l \lambda_0^3} \quad (1)$$

Here  $K$ ,  $r_0$ ,  $f$  and  $l$  are the hook constant as determined from an undistorted fringe pattern, the classical electron radius, the oscillator strength of the transition and the absorption length, i.e. in this case the length of the positive column plasma. A special gate circuit allows to measure the particle density at any time of the discharge period. The measurements have been performed in a discharge tube with an inner diameter of 6.5 mm and a column length of about 70 cm. Flat windows at both ends of the tube has been used to allow the laser beam to pass axially through the positive column. To determine the radial density distribution the tube has been shifted with respect to the laser beam.

## 3. Results and Discussion

Studies of the pulsed xenon glow discharge at gas pressures between 10 and 40 Torr and peak currents of 100 to 300 mA have been performed. The discharge was powered by a rectangular voltage pulse at a repetition frequency of 6 kHz with duty cycle of 1:1. The rise and decay time of the voltage pulses were about 200 ns. The purity of the xenon gas was 99.99 per cent.

In Fig. 2 the temporal behaviour of the discharge current and of the particle number density of the metastable atoms at a peak current of 130 mA and a pressure of 40 Torr are shown. The sustaining voltage was switched off at the moments  $t = 20 \mu s$  and  $184 \mu s$  and switched on at about  $t = 100 \mu s$ . In the early off-phase of the discharge (afterglow) the metastable density increases by about two orders of magnitude, followed by a continuous decrease of the population density. The rise of the density is mainly caused by collision processes between  $Xe(2p)$  and ground state atoms and by radiation transitions

from the 2p levels. In the reignition phase of the discharge, a further slight increase is observed. A similar temporal behaviour of the discharge current and the metastable density has been obtained for the entire peak current and pressure range considered.

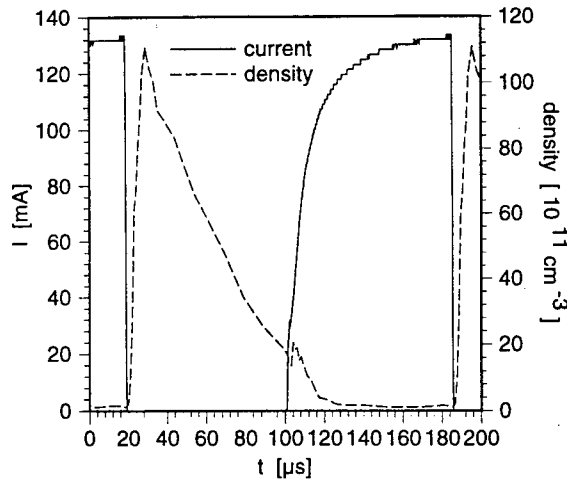


Fig. 2: Temporal behaviour of the discharge current and the Xe(1s<sub>5</sub>) density.

In Fig. 3 the radial profile of the absolute metastable density at  $t = 40 \mu\text{s}$  is presented. The profile can be approximated by a Gaussian distribution around the centre of the column plasma  $N(r) \propto \exp[-(r/r_w)^2]$  with a width  $r_w$  of 1.2 mm.

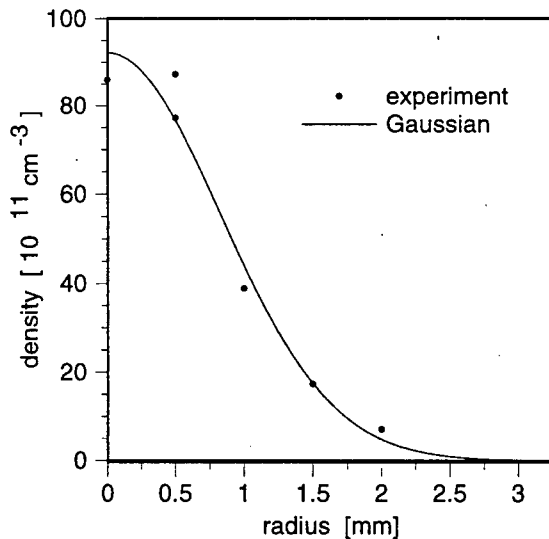


Fig. 3: Radial profile of the Xe(1s<sub>5</sub>) density.

The experimental results for the temporal behaviour of the constricted positive column plasma have been compared with the results obtained by model calculations. The self-consistent treatment of the discharge plasma has been obtained by the sim-

ultaneous solution of the time-dependent electron Boltzmann equation, the rate equation system for the relevant heavy particles and the current balance equation for the determination of the axial electric field. A radial averaged treatment of the plasma column has been employed. In accordance with Fig. 3 a Gaussian distribution has been adopted for the radial profile of the electrons, ions and excited atoms and molecules. Fig. 4 shows the measured and calculated temporal behaviour of the axial electric field strength and the density of the metastable atoms. For the electric field a good agreement between experiment and model is obtained. In the afterglow of the discharge the measured and calculated results for the densities agree qualitatively with certain differences in the decay. However, discrepancies between experimental and theoretical results are found in the reignition phase of the discharge. The measured densities are much lower than the calculated ones. In the on-phase of the discharge the course of the latter is very similar to temporal behaviour of the electric field. Although the observed increase of the metastable density during the reignition of the discharge is expected to be accompanied with a rise of the first and second VUV continuum and the near-infrared radiation, no such increase has been measured for the VUV radiation.

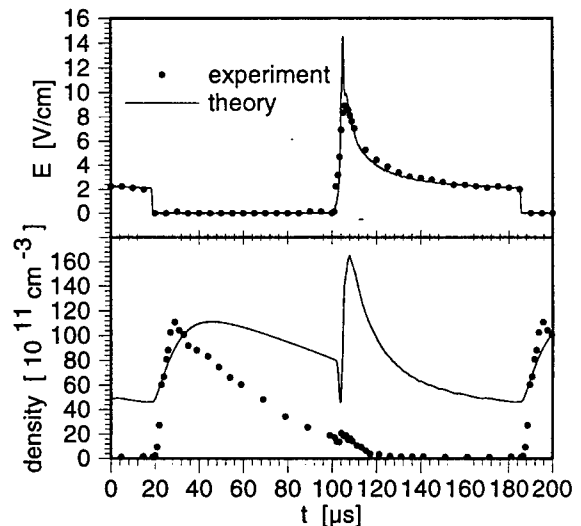


Fig. 4: Measured and calculated temporal behaviour of the electric field and the Xe(1s<sub>5</sub>) density.

#### 4. References

- [1] D. S. Rozhdestvenski: Ann. Phys., **39** (1912) 307
- [2] R. J. Sandemann: Appl. Opt., **18** (1979) 3873

## Experimental Investigations of Microdischarges in Excimer Barrier Discharge Lamps

R. Kling, S. Gasteiger and M. Neiger

LTI (Lighting Technology Institute), University of Karlsruhe, PO Box 6920 12, D-761281 Karlsruhe, Germany

### 1. Introduction

Dielectric barrier discharges (DBE) in rare gases and rare gas/halogen mixtures are selective incoherent excimer radiation sources with a narrow bandwidth in the vuv and uv spectral range [1,2,3,4,5]. Our investigations deal with the temporal and spatial development of microdischarges in the gas by high speed photography in the ns- and  $\mu$ s- range. A classification system for microdischarges between large area electrodes is proposed. Interactions between microdischarges are caused both by radiation and by remanent charges on the dielectric and in the gas. Proper interpretation of these results and a corresponding change in operation conditions lead to substantially increased radiation efficiency.

### 2. Experiment

The measurements are carried out using Xenon ( $\text{Xe}_2^*$ :  $\lambda = 172$  nm), Krypton ( $\text{Kr}_2^*$ :  $\lambda = 146$  nm) and a rare gas/halogen mixture  $\text{Kr}/\text{Cl}_2$  ( $\text{KrCl}^*$ :  $\lambda = 222$  nm) in the pressure range from 100 mbar to 1 bar. We apply sinusoidal voltages with frequencies from 1 kHz to 250 kHz or square wave voltages in the frequency range from 1 - 50 kHz. For the measurements we use both coaxial lamps and flat lamps. A gated, intensified CCD- array camera is used for high speed photography with exposure times from 5 ns up to several microseconds. Both electrical input power and radiation power are measured with high accuracy.

### 3. Results and discussion

The appearance of the plasma in excimer lamps with large electrodes varies from homogeneous to quasihomogeneous modes to strongly filamented modes with a large number of microdischarges. High speed

rising  $p \cdot d$  product causes a transition from type 1 to type 6 microdischarges.

The following single frame with 100 ns exposure time shows a homogenous  $\text{KrCl}_2$  discharge (Fig.2). This type of microdischarge has highest radiation efficiency.

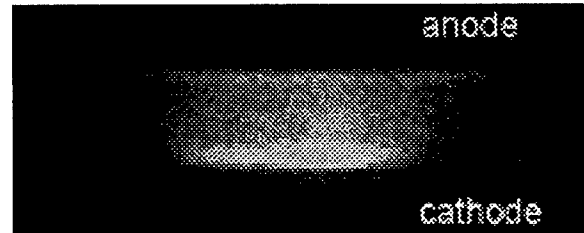


Figure 2: Homogenous discharge: ( $\text{Ne}/\text{Kr}/\text{He}-\text{Cl}_2 = 700/273/27$ ,  $p = 1000$  mbar,  $f = 30$  kHz, gap = 5 mm, diameter = 30 mm,  $t_b = 100$  ns)

A typical conical microdischarge is shown in Fig.3. This Xenon microdischarge has a channel diameter of about 3 mm.

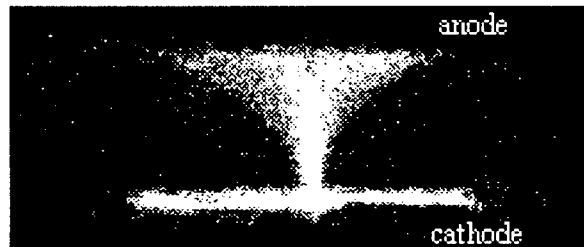


Figure 3: Xenon conical microdischarge ( $p = 100$  mbar,  $f = 8$  kHz, gap = 5 mm,  $t_b = 12$   $\mu$ s)

Figure 4 is a single frame with 10  $\mu$ s exposure time, showing spatial radiation intensities with a "thin filament" microdischarge according to Fig.1. The

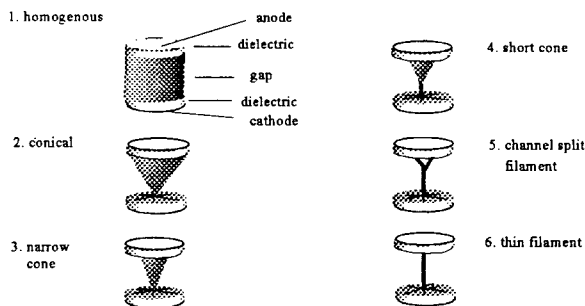


Figure 1: Fundamental types of microdischarges

photography shows a variety of shapes of such microdischarges which can be separated into 6 fundamental types (Fig.1). Rising voltage amplitude or

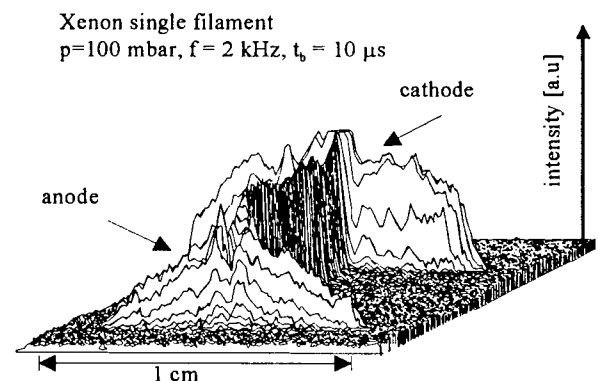


Figure 4: Xenon thin filament microdischarge (gap: 5 mm,  $\hat{U} = 3$  kV)

channel diameter between anode and cathode has a width of about 200  $\mu\text{m}$ .

Our measurements show that in the pressure region from 50 mbar to 200 mbar the microdischarges are strongly influenced by preionisation from neighbouring microdischarges. This occurs only if times between microdischarges are less than several tens of ns. Another strong influence is caused by remaining charges on the dielectric barrier. Increasing amplitude or frequency of the applied voltage leads to increasing remaining conductivity also in the gap itself.

By applying different types of driving voltages, it is possible to influence the appearance of the microdischarges, too. There is a homogenizing tendency if square wave voltage drives the lamp. This is only true for lower voltage amplitudes. High voltage amplitudes of the square wave lead to highly contracted and fewer filaments with considerable lower radiation efficiency. Figure 5 shows a comparison of internal radiation efficiencies for a coaxial Xenon lamp for sinusoidal voltage and square wave operating voltage. For the square wave mode the efficiency can be increased at

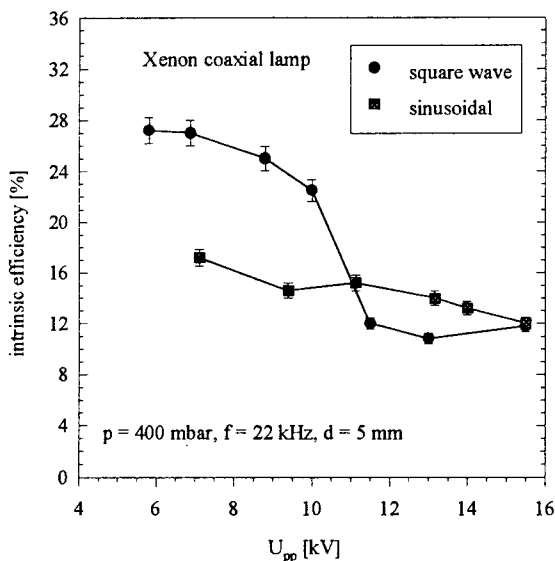


Figure 5: Xenon coaxial lamp: internal radiation efficiency ( $\lambda = 172 \text{ nm}$ ) for sinusoidal and square wave driving voltages

voltage amplitudes below 10 kVpp. This is due to the existence of "cone shaped" microdischarges in this range. For sinusoidal driving voltages, the discharge consists of either "short cone" (low voltages) or "thin filament" (high voltages) microdischarges.

#### 4. Summary

A classification system for excimer barrier discharge lamps is presented by high speed photographic measurements. Several types of microdischarges can be distinguished. One method of generating conical microdischarges in Xenon is shown by applying other voltage shapes than sinusoidal ones. Homogenous discharge modes and conical microdischarges show highest radiation efficiency.

#### 5. References

- [1] Eliasson, B.; Kogelschatz, U.: "UV Excimer Radiation from Dielectric Barrier Discharges", Appl. Phys. B 46 (1988), p.299-303
- [2] Schorpp, V.: Doctoral thesis, University of Karlsruhe, 1991
- [3] Stockwald, K.: Doctoral thesis, University of Karlsruhe, 1991
- [4] Müller, H.: Doctoral thesis, University of Karlsruhe, 1991
- [5] Neiger, M.; Kling, R. et al.: "Plasmatechnische Untersuchungen zur Realisierung inkohärenter Hochleistungslampen", BMFT- Abschlußbericht FKZ 13 N 5990, 1994

# Experimental study and modelling of a DC-excited slab CO<sub>2</sub> laser discharge

C van Egmond, C Leys, F Poppe and E Desoppere

University of Ghent, Department of Applied Physics,  
Rozier 44, 9000 Gent, Belgium

## 1. Introduction

The use of DC-excitation in slab geometries represents an economic route to compact high power CO<sub>2</sub> lasers. In designing these lasers one might take benefit from the predictive capabilities of numerical models of the discharge properties. First, a one-dimensional plasma-chemical model is constructed that computes the charged and neutral particle densities and the self-sustaining reduced electrical field  $E/N$  ( $N$ : density) in a self-consistent way. Next, the set of diffusion equations for the dominant positive and negative ion species is solved along with the heat equation to yield the charged particle density, gas temperature and  $E/N$  profiles across the discharge gap. These then serve as input for a vibrational kinetics code based on a three temperature model. The results of the plasma-chemical and vibrational kinetics model are compared with experimental data as derived from mass spectrometry and emission spectroscopy respectively.

## 2. Plasma-chemistry

The first step is to develop a numerical model for the plasma-chemical processes that occur in a slow-flowing CO<sub>2</sub> laser plasma that is uniform in the direction perpendicular to the flow. The model includes reactions [1] such as recombination, attachment, detachment, dissociation and ion-neutral reactions between the different species (neutrals, negative ions, positive ions and electrons). The set of non-linear differential equations, describing the build-up of the particle densities in the discharge and in the flowing afterglow, are solved using the Bader-Deuflhard method for stiff sets of equations [2]. The rate coefficients for electron impact reactions are depending on  $E/N$ , which in itself is a function of the gas mixture composition. Therefore, for the model to be self-consistent, electrical field and particle densities are to be obtained simultaneously. To this

aim, the continuity equation is added to the set of rate equations. In a flowing plasma the continuity equation takes the form  $dj/dt = 0$  where  $j = n_e e v_{dr}(E/N)$  is the current density and  $d/dt$  is a convective derivative in the direction of the flow. Assuming a flat current profile, the inlet electron density  $n_e$  can be derived from the total discharge current  $I$  and the drift velocity  $v_{dr}$  at the inlet value of  $E/N$  which equals the self-sustaining reduced field of the undissociated gas mixture [3]. The functional dependencies of the drift velocity and the reaction rate coefficients on  $E/N$  are evaluated from the convolution of the corresponding cross sections with the electron energy distribution function (EEDF), which is obtained by solving the Boltzmann equation with ELENDIF [4].

The relative abundancies of the negative and positive ions in the slab discharge are studied experimentally by means of a differentially pumped quadrupole mass spectrometer.

As a next step we calculate the profiles of the dominant charged particle densities and the reduced electrical field across the discharge gap, i.e. perpendicular to the flow. First, the set of diffusion equations is solved for a uniform  $E/N$ . From the resulting electron density profile the electrical power density  $jE(x)$  is computed which serves as the source term in the heat equation. Solving the latter yields the gas temperature profile which is used to calculate a corrected  $E/N$  profile. This procedure is repeated until convergence is reached.

## 3. Vibrational kinetics

A three temperature model is used to calculate the energy densities in the vibrational modes. As the input electron density and  $E/N$  is spatially resolved, the model outputs the vibrational temperature and small signal gain profiles across the discharge gap. To validate the model, the (spatially averaged) nitrogen vibrational temperature is

measured with an emission spectroscopy technique: from the measurement of the relative intensities of the vibrational bands of the nitrogen second positive system ( $C^3\pi_u - B^3\pi_g$ ) the non-equilibrium vibrational temperature  $T_4^*$  of the  $C^3\pi_u$ -state is derived [5]. The data in fig.1. reveal the decrease of the relative densities of vibrationally excited  $N_2$  molecules with pressure due to the collisional relaxation of the  $CO_2$  ( $00^0_1$ ) level. Assuming that the  $C^3\pi_u$ -levels are populated by direct electron impact, the vibrational temperatures  $T_4^0$  of the  $N_2$  electronic ground state can be calculated using Franck-Condon factors [5]. The latter are found to be about 1000 K lower than the corresponding  $T_4^*$  values. It follows that in the homogeneous glow regime 7-16 % of the ground state  $N_2$  molecules is vibrationally excited ( $v \geq 1$ ) and contribute to the population of the upper laser level. Ground state vibrational temperatures in fast-axial-flow lasers are typically higher [6]. However, it should be noted that the use of an uncooled pyrex plate on one side of the slab (for diagnostic purposes) limited the range of accessible power loadings. In fact, the data at 30 Torr suggest a thermal saturation effect.

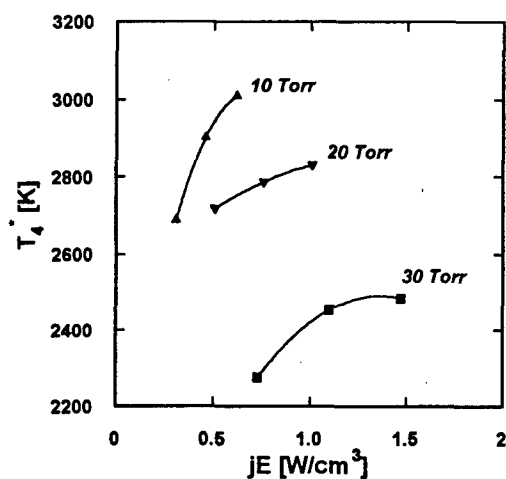


Fig.1. Vibrational temperature of the  $C^3\pi_u$ -state of  $N_2$  vs input power density at different gas pressures.

The small signal gain, as derived from the amplification of a probe laser beam, is shown in Fig.2. At a pressure of 20 Torr the recorded values range between  $0.45 \text{ m}^{-1}$  and  $0.65 \text{ m}^{-1}$ . The measured gain values are in fair agreement with the results of the three temperature model [7] (full curve). The relatively steep decrease in gain at higher power

loadings should again be attributed to the asymmetrical cooling of the gas. The three temperature model calculations indeed show that substantially higher values of the gain are to be expected if proper cooling is applied (dashed curve).

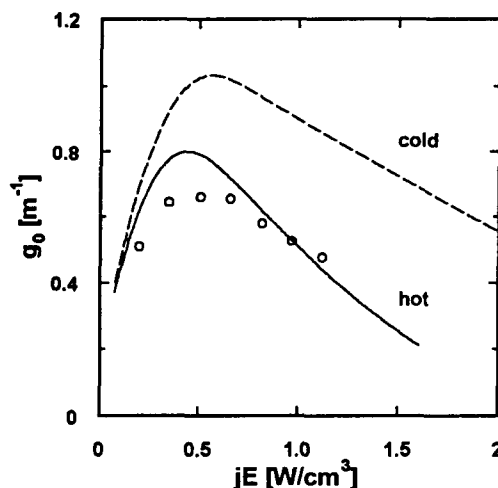


Fig.2. Small signal gain: experimental (O) – three temperature model calculation with pyrex plate (full curve) and with cooling plate (dashed);  $p = 20$  Torr.

#### 4. References

- [1] Leys C, van Egmond C and Desoppere E 1995 *J. Appl. Phys.* **78** 2265-2269
- [2] Legrand J-C, Damiy AM, Hrach R and Hrachova V 1995 *Proceedings 12th International Symposium on Plasma Chemistry*
- [3] Leys C, van Egmond C and Desoppere E 1997 *J.Phys.D: Appl. Phys* to be published
- [4] Morgan W L and Penetrante B M 1990 *Comp. Phys. Commun.* **58** 127
- [5] Novgorodov M Z, Ochkin V N, Sobolev N N 1970 *Sov.Phys.-Tech.Phys.* **15**(6) 977-982
- [6] Spiridonov M, Leys C, Toebaert D, Sazhin S, Desoppere E, Wild P, McKenna-Lawlor S M P 1994 *J.Phys.D: Appl. Phys.* **27** 962-969
- [7] Sazhin S, Wild P, Leys C, Toebaert D 1993 *J.Phys.D: Appl. Phys.* **26** 1872-1883

## VUV emission generation at helium plasma recombination.

V.V. Ivanov, K.S. Klopovskiy, A.A. Kopytin, D.V. Lopaev, A.T. Rakhimov, T.V. Rakhimova  
119899, Nuclear Physics Institute, Moscow State University, Moscow, Russia

### Introduction

At present time there is uncreasing interest to mercury-free luminescent sources having comparable efficiency as the current mercury-based ones. The choice for the rare gas is explained by a number of factors - available emitting transitions, requirements of efficiency, ecology, safety, reliability and etc. The existing devices use as rule one of the self-sustained discharge schemes that limits the emission generation efficiency at definitive and often not enough high level.

The reduction of rediced field in plasma permits significantly to increase the discharge system efficiency, therefore the transition to non-selfsustained discharge system when gas ionization is provided by an external ionizator could be one of the most effective approaches to VUV emission generation problem. Besides, under these conditions a plasma recombination itself can notiably contribute into emitting state excitation.

We have attempted to realize and investigate this approach for xenon-helium mixture by using the open discharge system. Here we present the main results of the experiments on VUV emission generation in pure helium open discharge plasma.

### Experiment

The discharge was controlled by three electrodes: copper cathode with a diameter of 20 mm, grounded grid with the cell of 0.04 mm and the transparency of 52%, placed at distance of  $d=0.2$  mm from cathode so that a work range of pd parameter (where p is pressure) was on a left side of Paschen curve. The grid anode with the cell of 0.5 mm and the transparency of 80% was placed in 8 mm from the first grid. Either the pulsed or the constant negative voltage  $U_c$  up to 1 kV was fed to the cathode, with anode being under the constant positive voltage  $U_a$  from 0 to 100 V. Discharge camera was connected with VUV monochromator trough the  $MgF_2$  window. The monochromator was pumped during the experiment and controlled by the programmable step drive. The open discharge emission in a spectral range of 120-250 nm was detected by solar-blind pfotomultiplier with  $MgF_2$  window. The pfotomultiplier anode current was fed either to a digital stored oscilloscope or to an electrometric amplifier and then to an analog-digital converter, which were connected with IBM PC by GPIB interface. Currents of all electrodes were measured by the same way.

### Results and discussion

A typical emission spectrum of open discharge in pure helium is represented in Fig. 1.

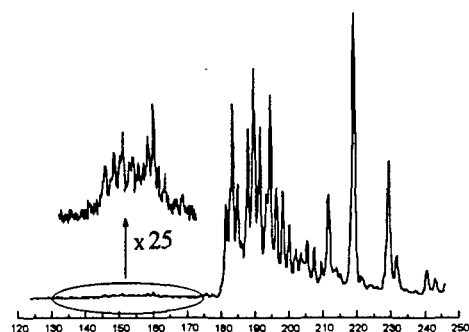


Fig. 1

A typical emission spectrum of open discharge in pure helium,  $P_{He}=30$  Torr,  $U_c=-800$  V,  $U_a=100$  V.

Two spectral features - the first in  $\sim 136-168$  nm and the second in  $\sim 180-250$  nm - are well-pronounced. The spectroscopic analysis have revealed the main feature in 180-250 nm is due to the transitions between two bounded exited states of  $He_2$  dimer. The pulsed measurements have shown that the observed emission is determined by plasma recombination processes so that one can consider the upper emitting states of  $He_2$  molecule as the autoionized states ultimately bounded up with corresponding vibrational states of  $He_2^+$  molecular ion. The obtained vibrational constants of both the upper and the lower states forming the spectrum as the photon energy have enabled accurately to identify these states. An approximate scheme of the observed transitions is represented in Fig. 2.

Energy, eV

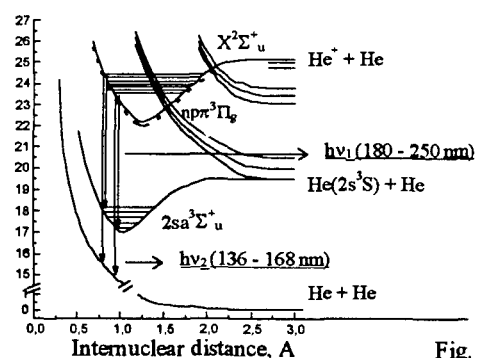
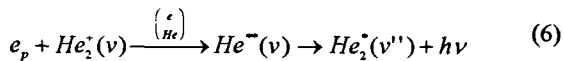
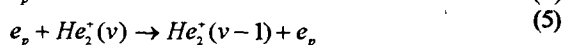
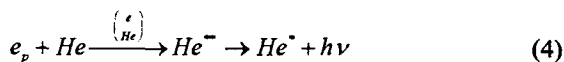
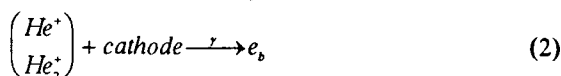


Fig. 2

Scheme of  $He_2$  molecule transitions corresponding to the spectrum shown in Fig. 1

The analysis of spectroscopic data has indicated that VUV recombination emission of  $He_2^+(v)$  ion occurs from upper vibrational levels with  $v > 10$ . In order to provide the observed intensity of recombination spectrum, the population in this vibrational states of  $He_2^+(v)$  has to be enough high that can be explained by a relative arrangement of  $He_2^+$  and  $He_2^*$  potential curves. Just the mutual position of  $He_2^+$  and  $He_2^*$  molecular terms is responsible for the branching of  $He_2^+$  recombination stream on the different channels. Like in light ions of  $H_2^+$  and  $H_2^*$  the potential curves arrangement in  $He_2^+ - He_2^*$  system is so that there is some group of  $He_2^+$  molecule high vibrational levels placed far from the intersection points with  $He_2^+$  repulsive states. The probability of fast dissociative recombination for this levels is low enough so that the VT-relaxation and impact-radiative recombination by slow electrons are the main channels of the losses of the level population [1].

Thus the basic processes of VUV emission generation in helium open discharge can be represented by the next kinetic scheme:



.....  $\rightarrow He^+ + He$

( $v \sim 4 \div 6, v > 16$ )

The (1) and (2) processes describe the electron beam formation in cathode-grid space [2]. Beam electrons rapidly run through this space, accelerating up to the energy equal to a cathode potential. This fast electrons have a wide energetic distribution function in a range of hundreds of electronvolts, i.e. in energy range close to maximum of helium ionization cross-section. It leads to an effective ionization of gas in grid-anode space. Atomic ions as well as formed molecular ions of helium in grid-anode space drift to the grid and then fall in the strong field of grid-cathode gap where they are accelerated to high energies. Accelerated ions effectively strike the cathode and knock  $\gamma$ -electrons which in turn take high energy in grid-cathode electric field, produce the following gas ionization and increase the plasma concentration thereby leading to the process development. Therefore concentration of recombining plasma in grid-anode space can reach a

significant value up to  $10^{12}-10^{13} \text{ cm}^{-3}$ , that at lowered pressures about 10-40 Torr when  $He^+$  are the main ions causes the intensive recombination stream to the  $He_2^{++}(v)$  formation.

Simplified analysis of (1)-(7) kinetic scheme by using the "steady-state" approach and experimental data for the various pressures, currents, cathode and anode voltages enables to estimate a scaling factor for the branch ratio  $\frac{\beta_r^R}{K_r^e}$  in dependence on  $v$  - quantum number of  $He_2^+(v)$  vibrational state (where  $\beta_r^R$  - is a "general" rate constant of  $He_2^+(v)$  recombination and  $K_r^e$  is a rate constant of VT relaxation by slow electrons). This dependence is shown in Fig. 3.

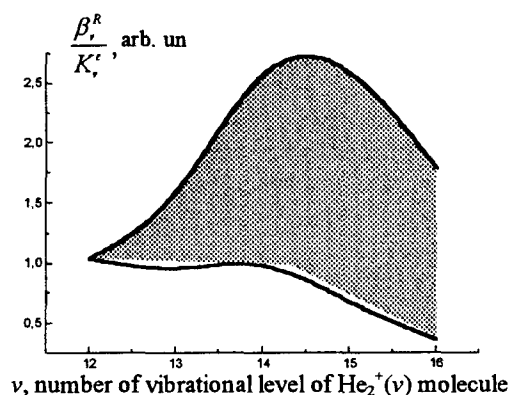


Fig. 3

Scaling dependence (in arb. un.) of  $He_2^+(v)$  quenching branch ratio between the channels of recombination and VT relaxation by electrons.

The shaded region between the curves indicates on possible positions of  $\frac{\beta_r^R}{K_r^e}$  dependence. The estimate of the branch ratio scaling confirms our considerations.

A growth of  $\frac{\beta_r^R}{K_r^e}$  with the vibrational level number is

possible only if these vibrational states are placed far from the intersection with  $He_2^+$  terms. In turn the decrease of this ratio at  $v > 15$  can be explained by the proximity of similar intersection and a noticeable contribution of dissociative recombination in  $He_2^+(v)$  quenching.

This research was supported by grant 96-02-18770 of Russian Fund of Fundamental Investigations.

#### References

- [1] V.A. Ivanov, Y.E. Skoblo: JETP (Russian), 106 (1994) 1704
- [2] A.S. Kovalev, Y.A. Mankelevich, E.A. Muratov, A.T. Rakhimov, N.V. Suetin: Sov. J. Plasma Phys. (Russian), 18 (1992) 1076



# Cross-talk in an AC Matrix Plasma Display Cell: 2D Interactive Simulation

C. Punset, J.P. Boeuf and L.C. Pitchford

Centre de Physique des Plasmas et Applications de Toulouse (E.S.A. 5002), UPS,  
118 route de Narbonne, 31062 Toulouse Cedex, France

## 1. Introduction

Plasma display panels (PDP's) occupy now a central position in the competition for the market of large diagonal (more than 40 in.) flat panel displays for television applications. Japanese manufacturers have announced mass production of such displays in 1996. However some of the characteristics of PDP's still need to be improved (e.g. the efficiency of PDP's is still rather low, on the order of 1 lm/W; also cross-talk problems, i.e. optical or electrical interaction between cells can appear for high resolution). In this abstract we present results from the modeling of AC plasma displays in a matrix electrode configuration. The typical geometry of a simulated PDP domain including one discharge cell and two half cells appears in Fig. 1. In this matrix electrode geometry, the two parallel plates are separated by a typically 100  $\mu\text{m}$  gas gap filled with a UV emitting rare gas mixture (e.g. Xe-Ne) at a pressure on the order of 600 torr. The electrodes on each plate are parallel (with a distance between electrodes on the order of 300  $\mu\text{m}$ ) and the two sets of electrodes are perpendicular, forming the lines and columns of a matrix. A discharge can be fired at the intersection of each line and column. The electrodes are covered with a dielectric layer and dielectric barriers are deposited along the electrodes on the back plate, in order to better confine optically and electrically the discharge cells. Phosphors are used to convert the UV light from the discharge cells into visible light. A MgO layer (large secondary emission coefficient by ion impact) is deposited on the dielectric layer above the electrodes. Other geometries, where the discharges occur between coplanar electrodes, the electrodes on the other plate being used for addressing, are also being developed.

In AC PDP's a square wave (typically 50 kHz) voltage is constantly applied between lines and columns. The amplitude of this 'sustaining' voltage is below the breakdown voltage of the mixture. A cell can be turned on by applying, across the electrodes defining this cell and during a short time, a 'firing' voltage above the breakdown voltage. Breakdown occurs and a transient glow discharge forms. This discharge is quenched by the charging of the dielectric surface.

When the sustaining voltage changes sign, another discharge is initiated because the induced voltage due to the charge stored on the dielectric surface adds to the sustaining voltage. The 'ON' state of the cell is therefore a succession of current pulses whose typical duration is on the order of 100 ns. The cell can be turned off by

applying a smaller voltage across the cell, in order to cancel the memory charges.

We present here results from a 2D user-friendly model which can simulate the discharge evolution in one or several adjacent cells.

## 2. Description of the model

The physical basis of the model is similar to those of the 1D models described in [1] and [2] where charged particle transport equations (continuity and momentum transfer equations) for electrons and ions are coupled with Poisson's equation for the electric field. The system of transport equations is closed with the local field approximation whose validity has been checked by comparisons between 1D fluid and hybrid models. The excited species kinetics is supposed to be decoupled from the discharge model, and this is reasonable for these relatively low current transient discharges. This has been checked by comparisons with the model of [2] where the excited species kinetics were included.

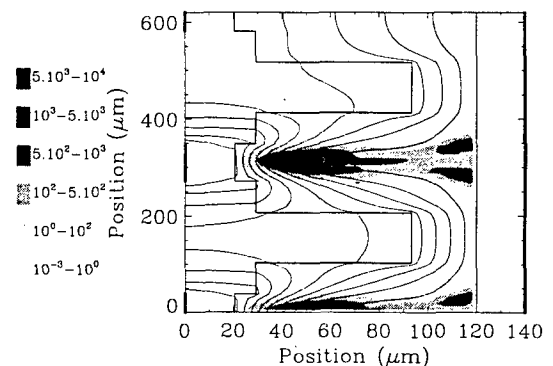


*Figure 1: Potential distribution (lines) and power dissipated ( $\text{W/cm}^3$ ) in xenon excitation (gray) at the time of maximum current. The increment between potential contours is 28.4 V. Xe(10%)-Ne(90%) at 560 torr; secondary emission coefficients 0.5 and 0.05 for neon and xenon ions on MgO, respectively.*

The present model is identical to the one used in [3] and assumes a Cartesian 2D geometry with symmetry imposed in the transverse direction. The electrode configuration, dielectric geometry, gas mixture etc... can be changed interactively by the user and the results can be visualized in the form of movies as the program is running (one discharge pulse can be simulated in about 30 minutes on a PC pentium).

### 3. Results

The 2D model is used to study the interaction (cross-talk) between adjacent cells. We simulate the behavior of three adjacent cells when two of them are fired and study the effect of the dielectric barriers and cell dimensions on the electrical interaction between the cells.

The gas mixture is Xe(10%)-Ne(90%) at 560 torr. At  $t=0$ , the voltage of the two bottom left electrodes is set to zero, the voltage of the right electrode is set to 284 V, and the voltage of the upper left electrode is set to 142 V. Since 284 is above the breakdown voltage and 142 V is below, a discharge is initiated in the two bottom cells and the third cell stays in the OFF state. Figure 1 shows the potential distribution and the dissipated power density in xenon excitation at the time (162 ns after the voltage is applied) of maximum current. The current pulse is displayed in Fig. 2. The spreading of the discharge on the right dielectric surface (anode side) is due to the charging of the dielectric surface, as described in [3]. The simulation of the subsequent sustaining pulses shows no evidence of interaction between adjacent cells in these conditions..

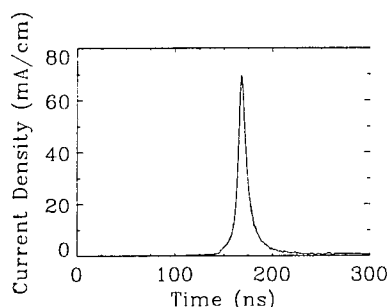


**Figure 2:** Time variation of the current density collected by the right electrode in the conditions of Fig. 1.

Figure 3 shows the potential and power dissipated in xenon excitation for the same gas mixture and gap length, but without dielectric barriers. We see that the discharge is less confined electrically and its transverse extension is much larger. The presence of the dielectric barrier in Fig. 1 leads to a larger axial field next to the dielectric surface which controls the spreading of the electrons along the dielectric surface. It appears from the simulation of the subsequent sustaining pulses in the case of Fig. 3 that the adjacent cells strongly interact electrically and that it becomes impossible to control separately the adjacent cells.

Figure 4 shows the potential and power dissipation in xenon at the time of maximum current for the 11<sup>th</sup> sustaining pulse after the writing pulse for a geometry where the gap length is increased to 160  $\mu\text{m}$ , everything else being kept the same as in the geometry of Fig. 1. The height of the dielectric barriers is therefore relatively smaller in this case. One can see clearly the

effect of the electrical interaction between adjacent cells in this figure.

### 4. Conclusion

A two-dimensional model has been used to quantify the electrical interaction between adjacent cells in a matrix PDP. The height of the dielectric barrier is an important parameter and should be large enough to prevent electric interaction between the cells.

### 5. Acknowledgments

This work has been supported by Thomson Tubes Electroniques. The calculations have been performed with SIPDP-2D, a Kinema Software product.

### 6. References

- [1] C. Lanza, O. Sahni: IBM J. Res. Develop., **22** (6) (1978) 641
- [2] J. Meunier, Ph Belenguer, J.P. Boeuf: J. Appl. Phys., **78** (1995)
- [3] J.P. Boeuf, L.C. Pitchford, IEEE Trans. Sci. **24**, (1996) 95-96.

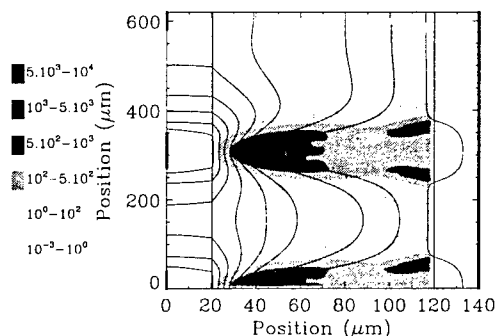


**Figure 3:** potential and power in xenon excitation at the time of maximum current in a geometry without ribs and phosphors.

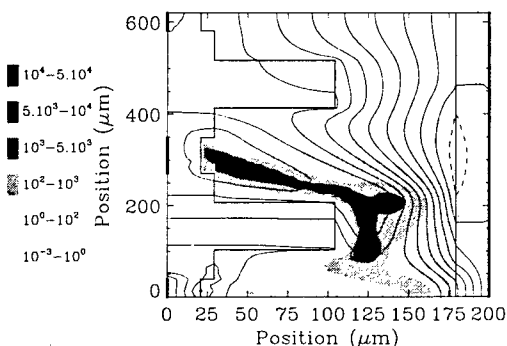


**Figure 4:** potential contours (lines, increment 31 V) and power dissipated in xenon excitation (gray) at the maximum of current time in a geometry similar to that of Fig. 1, but with a gas gap of 160  $\mu\text{m}$ , during the 11<sup>th</sup> sustaining pulse. The height of the dielectric barriers is not large enough in these conditions, and the discharges in adjacent cells obviously interact in this example.

## Production of capillary discharges for the study of discharge pumped soft X-ray laser

W. Rosenfeld, R. Dussart, D. Hong, C. Cachoncinlle, L. Huré, R. Viladrosa,  
J.M. Pouvesle, C. Fleurier

GREMI CNRS UMR 6606 / Université d'Orléans - B.P. 6759 45067 ORLEANS Cedex 2

### 1. Introduction

Since 1984, when for the first time a high gain has been observed on a soft X-ray transition [1], a run to short wavelengths laser began. Hence, during the last ten years, several laboratories around the world developed what is currently called "soft X-ray laser", exhibiting transitions from 100 nm down to the water-window range. A laser emitting in X wavelength range can be of practical use for many domains such as physics (atomic physics, solid-state physics,...), biology (studies of biological cells, radiography,...), micro-electronic and micro-technology.... Probably many applications have not been yet identified.

Up to date, most of demonstrated X-ray lasers are laser pumped by very powerful laser. For example, the LLNL group obtained unique performances with X-ray laser peak power up to 32 MW and extracted laser energy of 7 mJ at 15.5 nm in Ne-like Y plasma using the largest laser facility by the world [2]. This way of pumping gives excellent results but also shows several inconvenients as very low wall-plug efficiency and repetition rate. Moreover access to these very large devices is rather difficult and then can limits potential applications. Several groups turned towards the development of new pumping methods and promising results have been obtained by reducing the size of pumping lasers with energy as low as 70 mJ [3] but evidently at the expense of the extracted laser energy. A very interesting way came from capillary discharges-created plasmas in vacuum with wall ablation or at low gas pressure. A hot and dense plasma contained within capillary walls is formed by magnetic compression (pinch effect) on capillary axis.

Different kinds of discharges were used as switch triggered discharges, discharges triggered by gas injection or uncontrolled discharges. Hence most of groups used straight capacitors discharges which is definitively the easiest approach to get energy transfer to the amplifying medium. In these cases, discharge voltage is limited by electrical breakdown voltage which imposes constraints on storage capacitance that directly affect the current pulse length, and then the obtention of a skin effect near the tube walls. To get suitable current pulse and good energy coupling, a special care must be taken to adapt the electrical circuit impedance to plasma impedance.

After all, very interesting and encouraging results have been obtained in recombination pumping scheme. For example Shin et al. [4] as well as Steden et al. [5] obtained soft X-ray amplification in the CVI Balmer- $\alpha$  line at 18.2 nm using different types of direct discharges. Impressive results in collisional pumping scheme in Ar-plasma have been obtained by Rocca's group at Colorado State University (USA). They report the first demonstration of saturated operation of a discharge-pumped soft X-ray laser and the generation of laser pulse energies up to 30  $\mu$ J at 46.9 nm on the 3p-3s J=0-1 transition in a Ne-like Ar plasma in double pass amplification experiments [6]. Such significant results have thus imposed a completely different approach for discharges structures. The production of the plasma in a low pressure medium (700 mTorr of pure Ar) makes use of a small transfer capacitor charged by a Marx generator under a high voltage ( $\approx$ 100-400 kV) then avoiding the increase of the FWHM current pulse.

### 2. Experimental set-up and results

In a first stage experiment, we studied and developed capillary discharges structures to get ASE (Amplified Spontaneous Emission) quite similarly to what have been recently performed by Shin et al. The experimental set-up is shown in figure 1.

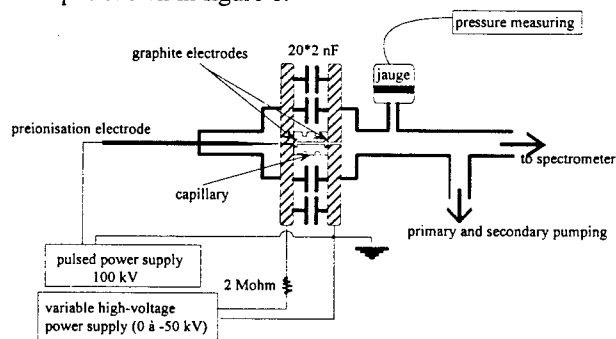


figure 1 : diagram of the experimental set-up.

The capillary is on the axis of a circular flat plates that hold 20x2 nF-knob capacitors mounted in parallel. This geometry provides a low inductance circuit which is favourable to get a high power density. Capacitors are charged by a 50 kV power supply and discharges through a 1 mm-diameter and 19 mm-length capillary. Two different materials containing carbon, polypropylene and polytetrafluorethylene, were used for

capillaries. A preionization electrode connected to a 100 kV pulsed power supply is used to trig the main discharge. Measured current reached 27 kA at 32 kV applied voltage (corresponding to 21 J stored energy) with a pseudo-period of around 230 ns. Strong ablation of walls was effective and led to transient pressure rise that could be measured in the vacuum chamber connected to the X-UV spectrometer. The detection system consists of a Spartuvix-type spectrometer [7] equipped with rapid photodiodes or MCP array detector coupled to a high-resolution ICCD camera. Spectroscopic studies in the visible domain has been performed allowing to follow time evolution of CIII lines. Detailed X-ray spectroscopy of the carbon plasma is under progress. Special care has been put on protection of X-ray optics that can be damaged by particles ejection from capillaries. The system is presently being equipped with a synchronised fast shutter that will prevent debris damage of X-ray mirrors and gratings. To overcome difficulties link with straight capacitor discharge systems, especially pre-breakdown, we are presently studying discharge devices using a new type of pulse forming line (PFL) based on a Blumlein-like PFL. The two main advantages of this type of devices are that, first, they give the possibility to get energetic and very short rise time pulses which are necessary to obtain effective plasma compression and, second, the two electrodes of the capillary are initially at ground potential which prevents pre-breakdown. These systems can be operated at moderate voltage. They are well-adapted for operation in repetitive mode. Objectives to be reach are the following:

- $U=40$  kV
- impedance:  $Z = \sqrt{L/C} \leq 1 \Omega$
- $I_{\max}=100$  kA
- $dI/dt \approx 10^{12}$  A/s
- $E_{\text{stored}}=100$  J

Main differences with the Rocca's experiment lie in the value of the used high-voltage and, probably, in the value of the circuit impedance of the system. A special care must be taken to determine the geometry of Blumlein line as it plays a significant role on impedance adaptation. Hence, we conducted studies on different geometries in which we tried to decrease as low as possible the impedance  $Z$ -value down to the matching plasma impedance at pinch moment of about  $0.3 \Omega$ . These first studies revealed that circular plates line geometry might be of great interest as inductance increases only with the radius logarithm whereas capacitance increases with the squared radius of plates then providing a small impedance value and a large stored energy.

We report here experimental and theoretical studies on electrical parameters of this original pulse forming line. Preliminary experiments on different lines have recently been made to better understand the geometry influence on voltage and current evolution, and compare circuit behaviours between circular plate Blumlein and conventional ones. Measured voltage and current time

evolutions has been compared with the ones obtained from the resolution of the set of differential equations derived from the analysis of the equivalent electrical circuit. This was necessary to conduct Z-pinch numerical simulations. As shown on figure 2, there is a rather good agreement between experimental results and model.

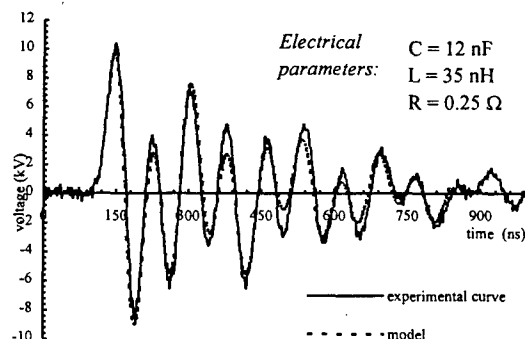


figure 2 : Comparison between experimental and theoretical voltage evolution with time.

Then the calculated current was coupled to Miyamoto's model [8] to study the Z-pinch effect by varying different parameters. Proceeding in this way, we have access to the time-evolution of the plasma radius and then estimate the corresponding temperature, density and ionisation degree. This is important to optimise the energy coupling considering the pinch effect efficiency.

### 3. Conclusion

In this work, both ablative capillary discharges in vacuum and Z-pinch capillary discharges in low pressure gas have been investigated. Blumlein PFL appear as convenient means for production of capillary discharges dedicated to the study of discharge pumped soft X-ray lasers. They allow a good control of discharge ignition and main discharge parameters. They are particularly well suited to repetitive mode and compact size systems.

This work was supported by DRET, CNRS and the Region Centre.

### References

- [1] D.L. Matthews et al.: Phys. Rev.Lett., **54** (1985) 110
- [2] L.B. DaSilva et al.: Opt. Lett., **18** (1993) 1174
- [3] B.E. Lemoff et al.: Phys. Rev. Lett., **74** (1995) 1574
- [4] H.J. Shin et al.: Phys. Rev. E, **50** (1994) 1376
- [5] C. Steden et al.: Int. Colloquium on X-ray lasers, Schliersee (1992)
- [6] J.J. Rocca et al.: Proceed. of the 5th Int. Conf. on X-ray lasers, Lund (1996)
- [7] J.L. Bourgade et al.: Rev. Sci. Instrum., **59** (1988) 1840
- [8] T. Miyamoto: Nuclear Fusion, **24** (1984) 337
- [9] J.J. Rocca et al.: Phys. Plasmas, **2** (1995) 2547

# Generation of High-Power Microwaves due to propagation of a relativistic electron beam in plasma

M. Birau, J-M. Buzzi

*Laboratoire de Physique des Milieux Ionisés, Laboratoire du C.N.R.S  
Ecole Polytechnique, 91128 Palaiseau Cedex, France*

Y. Caillez, R. Wiolland, C. Saulle  
*Centre d'Etudes de Geamat, 46500 Gramat France*

M. A. Krasilnikov, M. V. Kuzelev  
*Moscow State University of Press, Moscow, Russia*

O. T. Loza, A. A. Rukhadze, P. S. Strelkov, A. G. Shkvarunets, D. K. Ulyanov  
*General Physics Institute of Russian Academy of Sciences,  
Vavilova 38, Moscow, Russia*

## I. INTRODUCTION

In this paper, we present the last results concerning the interaction of a high-current relativistic electron beam (REB) with a spatially - confined plasma. This interaction is fundamental in the plasma Cerenkov oscillator (P.C.O) or plasma Cerenkov maser, experimental device which consists in transferring the kinetic energy of a relativistic electron beam into electromagnetic radiation. It was shown earlier [1] that single-particle stimulated Cerenkov radiation takes place, microwave power of 100-300 MW was achieved with an efficiency of 10-15 % in power [2]. In our latest work, microwave spectra were measured [3] and calculated [4]. It was shown that the mean frequency and spectrum width could be changed by variation of plasma frequency and transverse structure of electron beam and plasma. All these investigations have been performed for a beam energy up to 650 keV and 3 kA. An other setup has been launched in Ecole Polytechnique permitting the increase of beam energy up to 1 MeV. We shall discuss here the behavior of the oscillator for both regimes of electron beam : 500 keV, 2 kA and 1 MeV, 5 kA.

## II. EXPERIMENTAL RESULTS

The setup used for our experimental investigations is displayed in Fig. 1. The hollow relativistic electron beam (1) is generated by the explosive cathode (2). The hollow plasma column (3) is created by a discharge obtained after the propagation of a low-energy electron beam flux from the heated cathode (4) in xenon. REB and plasma are immersed in a strong longitudinal magnetic field (5). An additional coil (6) permits tuning the plasma radius. Both REB and plasma are lost to the collector (7), that is simultaneously a part of the outlet coaxial horn (8).

The pulse shape of the microwave signal has been measured with a semiconductor crystal detector cooled by liquid nitrogen. The radiated energy by a calorimeter. The beam current oscillogram has a width

of 20 ns and the influence of the plasma density and of the beam - plasma radial gap on the radiation power spectrum is investigated for both beam regimes.

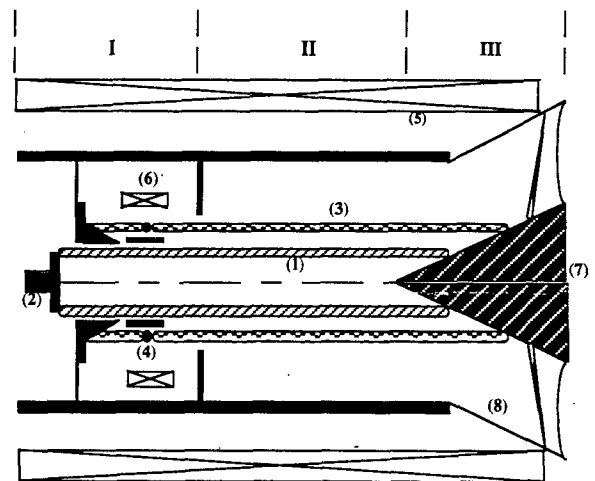


Figure 1. Experimental setup scheme of the Plasma Cerenkov Maser studied in Ecole Polytechnique (France) and General Physics Institute (Russia) : I: Plasma and beam creation zone. II: Interaction zone. III: Emission zone.

The results of the measurements are shown in Fig. 2a for  $E = 500$  keV,  $I = 2$  kA and in Fig. 2b for  $E = 1$  MeV,  $I = 5$  kA. These two series of shots have been obtained for a plasma column radius of 8.0 mm. The dependence of the radiated energy and power versus the discharge current is represented. In this range, this current has approximately a logarithmic growing with the plasma density. From the similar behavior of power and energy curves of Fig 2a, it is found that the pulse duration of microwave signal does not change significantly with increasing plasma density. The maximum efficiency in power is obtained for a plasma density slightly above the generation threshold and is about 15 % (150 MW of radiation for 1 GW of beam). Beyond this maximum, the efficiency slowly decreases. Fig. 2b shows the same characteristics. Note however

that the efficiency has diminished to 10 % (500 MW of radiation for 5 GW of beam). We have also studied the influence of the plasma column radius on the radiated power and energy. For a radius of 10.5 mm, we found the same behavior versus the plasma density. The differences between two series of shots corresponding to two different radii are comparable to the accuracy of our measurements.

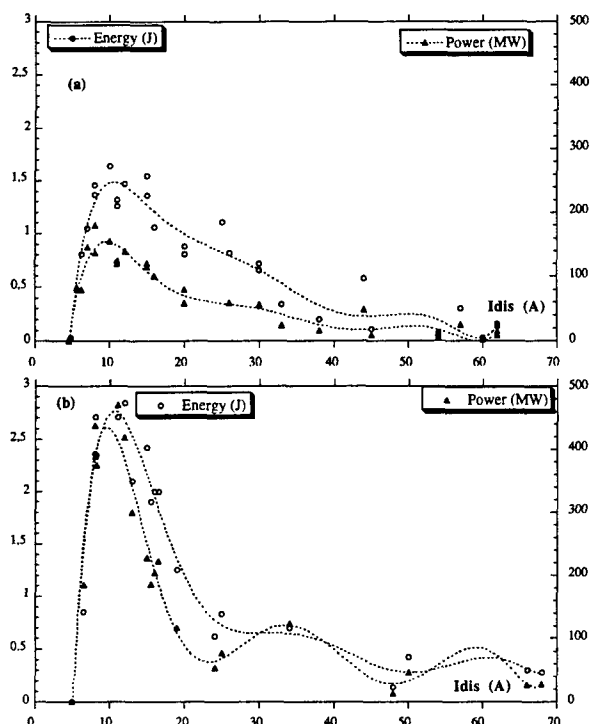


Figure 2. Measured microwave energy and power for  $E = 500$  KeV,  $I = 2$  kA (a), and  $E = 1$  MeV,  $I = 5$  kA (b) versus the discharge current.

### III. NUMERICAL RESULTS

We have created a numerical model to describe the interaction between the relativistic electron beam and the plasma waves. This code assumes an infinitely thin plasma and beam column in a strong longitudinal magnetic field, a linear behavior of plasma motion and a narrow band spectrum of emission. It takes into account the finite dimensions of the interaction region by reflecting at its longitudinal boundaries a certain part of the microwave signal, and considers the finite beam pulse shape. In this framework, we have studied the dependence of the interaction efficiency versus the plasma Langmuir frequency for the two experimental beam parameters. The result is displayed in Fig. 3. The dependence shows similar behavior to the experimental measurements: a sharp threshold in plasma density and a maximum located near this threshold. For the regime of 500 keV, the maximum efficiency (10 %) in energy corresponds to a power of 180 MW and describes correctly the experiment. When the energy of the beam

is increased from 500 keV up to 1 MeV, the threshold of plasma density shifts to a lower value and the maximum efficiency increases up to 14 %. These two phenomena have not been observed in the experiment.

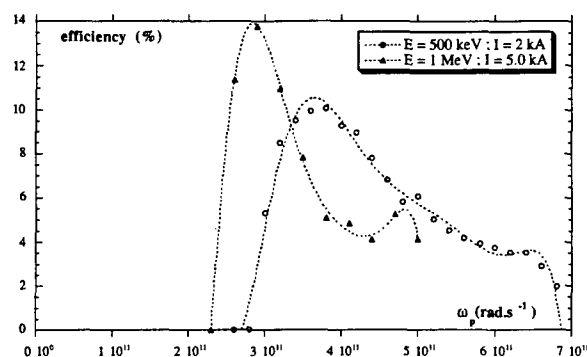


Figure 3. Calculated efficiency of the plasma oscillator for two regimes of relativistic electron beam versus plasma Langmuir frequency.

### IV. CONCLUSIONS

Radiation spectrum measurements have been performed using a wide - aperture calorimetric spectrometer in the frequency range 3 - 40 GHz for an electron energy of 500 keV [3]: it was shown that the mean frequency of radiation could be tuned by increasing the plasma density. Numerical simulations confirmed this main behavior. New results concerning the spectrum for the beam energy of 1 MeV will be presented at the conference and compared to the numerical predictions.

The efficiency and the tunability of the plasma Cerenkov oscillator are of interest for a wide range of applications. Also, the reported experiments are a prime necessity to validate the numerical treatments of the beam-plasma interaction.

**Acknowledgements.** We acknowledge the support of DGA-DRET, contract n° 40-95-007-00.

- [1] M. V. Kuzelev, O.T. Loza, A.V. Ponomarev et al., JETP **82** (6), 1102, (1996)
- [2] A. G. Shkvarunets, A.A. Rukhadze, P.S. Strelkov, Plasma Phys. Rep. **20**, 613, (1994)
- [3] M.V. Kuzelev, O.T. Loza et al. : 11th Int Conf. on High Power Particle Beams. Prague, Czech Republic, **1**, 225, (1996)
- [4] M. Birau, Phys. Rev. E, **54**, n° 5, 5599, (1996)

## Improvement of the metal vapour distribution in CCRF excited metal vapour lasers by cataphoresis

D. Teuner, J. Schulze, E. Schmidt, J. Mentel  
Ruhr-Universität Bochum, Lehrstuhl AEEO, Germany

### 1. Introduction

Three types of metal ion lasers were realized using a capacitively coupled radio frequency (CCRF) excited discharge as an active medium. Since many years He-Cu<sup>+</sup>, He-Cd<sup>+</sup> and He-Zn<sup>+</sup> laser are well known as hollow cathode lasers [1]. Due to the similar plasma properties, inversion on the same metal ion lines can be achieved in the CCRF excited discharge [2].

A homogenous metal vapour distribution along the discharge tube is of main importance for a stable and powerful laser operation. This is incompletely achieved if the metal vapour is only supplied from an external oven and distributed only by diffusion along the tube. With the intention to improve the metal vapour distribution by the effect of cataphoresis a DC current is superimposed on the discharge along the tube. For this purpose the tube is supplied by a DC anode and a DC cathode. The vapour is fed into the tube from an oven attached to the tube at the anodic side.

Measurements have clearly shown the dependence of the resonator power on different discharge parameters for the three metal ion lasers. To measure the metal vapour distribution the intensity of strong metal atom and ion lines were recorded along the discharge tubes. These spectroscopic measurements demonstrate that the cataphoretic effect improves considerably the metal vapour distribution.

As the investigated lasers have potential UV laser lines, i.e. 193.0 nm for zinc, 248.6 nm for copper and 325.0 for cadmium these investigations are useful to realize CCRF excited UV lasers in the next future.

### 2. Tube design

The measurements were performed using He-Cd<sup>+</sup>, He-Zn<sup>+</sup>, and He-Cu<sup>+</sup>(CuBr) lasers. The tube construction of the lasers is shown in Fig. 1. The tubes were made of fused silica with an Al<sub>2</sub>O<sub>3</sub> tube insert. The inner diameter of the ceramic tube was 4 mm the outer diameter 7 mm. The outer diameter of the fused silica tube was 9 mm. The RF electrodes were made of nickel plated copper with a length of 400 mm and a width of 4 mm. They had a curvature so that they fit on to the outer tube wall. The electrodes were connected via a symmetric matching circuit [3] to a 13.56 MHz RF power supply. The RF power was constantly 400 W during the measurements.

Connecting the anode and the cathode to a DC power supply ( $V_{\max} = 5$  kV,  $I_{\max} = 350$  mA) a DC dis-

charge could be ignited in addition to the RF discharge. To protect the DC power supply from RF interference an inductance of 5  $\mu$ H was placed in the cathode feeding.

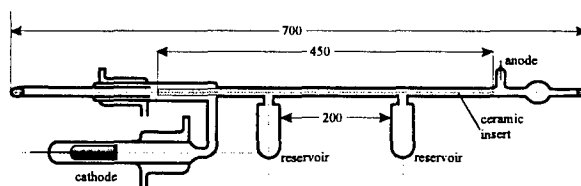


Fig. 1: Tube construction

The metal vapour was produced by two external ovens located equally spaced along the tube. They could be heated separately. So the metal vapour pressure could be controlled independently from the discharge conditions. The part of the tube in front of the cathode was water cooled to avoid that contaminations emitted from the cathode reach the discharge region.

### 3. Measurements

To investigate the effect of an additional DC discharge the output power of the laser was measured behind one of the high reflecting mirrors.

Fig. 2 shows the laser output power for different He pressures of the 441.6 nm line of the He-Cd<sup>+</sup> laser. The laser power, which was achieved using the pure RF discharge, was measured with optimized oven temperatures that were nearly the same for both ovens. When the DC discharge was operated additionally only the anode sided oven was heated with an insignificant higher temperature. The DC current was optimized for each pressure to get maximum laser power. It can be seen that the optimum DC current increases nearly linearly with the He pressure. The laser output power could be increased considerably using an additional DC discharge. Furthermore, the pressure optimum is shifted to higher pressures and laser operation is possible at higher pressures, respectively. This behaviour was also observed for the other lines of the He-Cd<sup>+</sup> laser in the visible and infrared spectral range.

Furthermore, it was observed that the laser output power was more stable when the laser was operated with the additional DC discharge.

The same measurements were performed at the He-Zn<sup>+</sup> and the He-Cu<sup>+</sup>(CuBr) laser showing a similar behaviour.

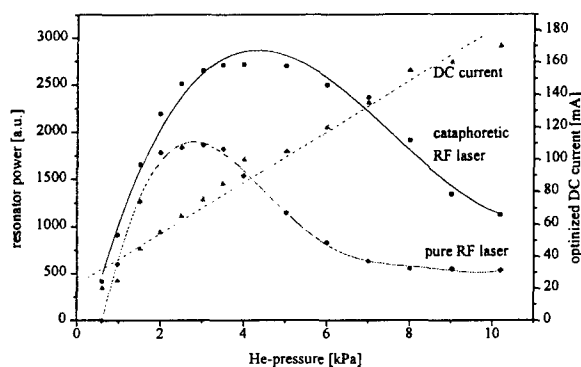


Fig. 2: Laser resonator power of the pure RF and the cataphoretic RF He-Cd<sup>+</sup> laser line ( $\lambda = 441.6$  nm) with the optimized DC current

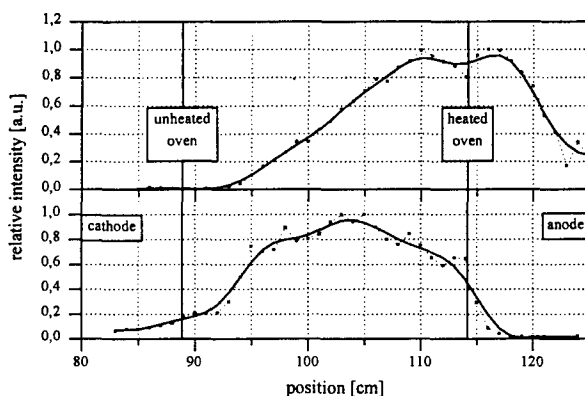


Fig. 3: Intensity distribution of the Cu I 521.8 nm line without and with an additional DC discharge

To determine the distribution of the metal vapour measurements of the side light of the discharge were performed. The side light was recorded along the tube using a 0.275 m spectrograph with a  $150 \text{ mm}^{-1}$  grating and an optical multichannel analyser. The intensity of a metal vapour atom line was divided by the intensity of an adjacent He atom line at the same position, since He as a gas is distributed homogeneously. So irregularities of the intensity due to deposits on the walls could be eliminated. Fig. 3 shows the results obtained using a He-Cu<sup>+</sup>(CuBr) discharge. The tube had two ovens as the above mentioned He-Cd<sup>+</sup> laser. The intensity of the 521.8 nm Cu I line was divided by the intensity of the 587.6 nm He I line. The upper part of Fig. 3 shows the Cu vapour distribution if the anodic sided oven is heated without an additional DC discharge. A maximum of the intensity can be observed at the position where the oven is located. The metal vapour density decreases monotonously to the left and to the right side. This distribution is reached by diffusion. The effect of igniting an additional DC discharge can be seen from the lower part of Fig. 3. The metal vapour moves in direction to the cathode. The distribution is more homogeneous. Atomic lines are not excited at the anodic side of the discharge. This demonstrates the effectiveness of the cataphoresis. Since the cathode

sided oven was not heated the metal vapour condenses there and a decay of the line intensity occurs at this position. When also this oven was heated to get a more homogeneous distribution using the additional DC discharge too much metal vapour was supplied to the discharge. So a really uniform distribution could not be reached using the tube construction with two ovens. Better results are achieved using cataphoresis with a tube supplied only with one oven located at the anodic end of the discharge tube.

#### 4. Conclusions

The metal vapour distribution in CCRF excited metal vapour ion lasers is rather inhomogeneous if the metal vapour is transported only by diffusion. The region of a uniform distribution is limited due to collisions between buffer gas atoms and metal vapour atoms. The higher the buffer gas pressure is, the more collisions occur and the smaller is the region of a uniform distribution. The distribution of the metal vapour is improved considerably if the metal vapour ions are accelerated by an additional DC field perpendicular to the RF field. A higher force is needed to transport the metal vapour ions through the discharge volume at higher pressures. So the positive effect of the additional DC discharge becomes more important at higher buffer gas pressure. Since the metal vapour ions are produced by the RF discharge the necessary DC current to move the ions, is rather low in comparison to positive column lasers.

It was shown that the laser power of CCRF excited metal vapour ion lasers can be increased if the metal vapour is distributed more homogeneously by an additional DC discharge.

Supported in parts by the Commission of the European Communities (CIPA-CT93-0219) and by the Deutsche Forschungsgemeinschaft (SFB 191, A10)

#### References

- [1] I.G. Ivanov, E.L. Latush, M.F. Sem, "Metal vapour ion lasers", John Wiley & Sons (1996)
- [2] J. Mentel, N. Reich, J. Mizeraczyk, M. Grozeva, N. Sabotinov, "Capacitively coupled RF excitation of CW gas lasers and its comparison with hollow cathode lasers", Proceedings of the NATO ARW on Gas Lasers – Recent Developments and Future Prospects, W.J. Witteman, V.N. Ochkin (Eds.), Kluwer Academic Publishers (1996)
- [3] N. Reich, "Transversale kapazitive Hochfrequenzanregung von Gasentladungslasern", Ph. D. dissertation, Ruhr-Universität Bochum, Germany (1994)



## The mean electron energy in RF and HC discharges

M. Kocik, D. Grabowski\*, J. Mizeraczyk, J. Heldt\*, J. Schulze\*\*, J. Mentel\*\*

Institute of Fluid Flow Machinery, Polish Academy of Sciences, Fiszer 14, 80-952 Gdańsk, Poland

\*Institute of Experimental Physics, University of Gdańsk, Wita Stwosza 57, 80-952 Gdańsk, Poland

\*\* Department of Electrotechnical Engineering, Ruhr-University, Universitätsstraße 150, D-44780 Bochum, Germany

### ABSTRACT

The similar laser capabilities of the radio-frequency (RF) and hollow-cathode (HC) discharges are believed to be a result of their similar electric properties. However, there are not many experimental evidences indicating that the plasmas of both discharges resemble each other.

This investigation was aimed at comparing the mean electron energy in the RF and HC discharges run in the same hollow electrode.

### 1. Introduction

The HC discharge-excited ion gas lasers are attractive because of their capability of generating in the UV spectral range [1]. However some technological difficulties made the HC discharge-excited lasers unpractical. On the other hand, there are some evidences that the capacitively coupled RF discharge is as effective in exciting the ion gas lasers as the HC discharge [2]. It seems that the similarity in laser characteristics of the RF and HC discharges is a result of their similar electrical properties [3]. However, there are few experimental evidences which show that the plasmas of both discharges are similar.

In this paper the results of measuring the mean electron energy in the RF and HC discharges typical of the ion gas lasers are presented.

### 2. Experimental set-up

The RF and HC discharges were run in He-Cu-sputtered and He-CuBr-based laser systems. The He-CuBr-based laser system is an alternative to the He-Cu-sputtered system in producing  $\text{Cu}^+$  ions capable of lasing. The discharge tube for the He-Cu-system is presented in Fig. 1.

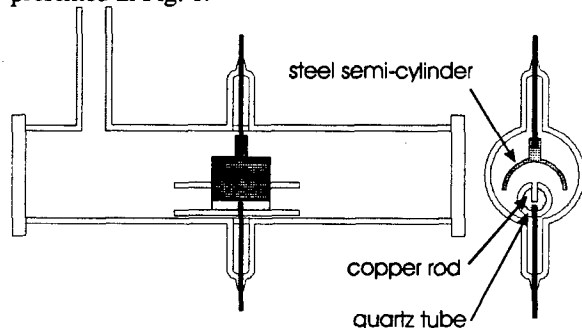


Fig.1 The scheme of the He-Cu-sputtered discharge tube.

In the He-Cu-sputtered system the sputtered part of the copper rod electrode was a slit  $3 \times 2$  mm made along the rod. The counter-electrode was a stainless-steel semi-cylinder. The copper rod was enveloped in a quartz tube having a slit along the copper slit.

The following power supplies were used to provide either the RF or HC discharge to the He-Cu-sputtered tube:

- for the RF discharge a 13.56 MHz pulsed or cw generator was used. The RF power was supplied to the discharge tube via a symmetric matching circuit [4],
- the HC discharge was supplied with 50 Hz half-wave rectified pulses. The stainless-steel semi-cylinder served as an anode. The slit in the copper rod electrode worked as a hollow-cathode.

The He-CuBr-based discharge tube is presented in Fig.2. The discharge tube was supplied from the RF generator (13.56 MHz) and a DC power supply. Both discharges, RF and DC, were simultaneously run inside the quartz-ceramic tube (40 cm long and 4 mm in diameter). CuBr vapour were delivered inside the tube from a heated CuBr reservoir. After dissociation of the CuBr molecules, Cu atoms were present in the discharge. Due to the DC discharge, cataphoresis effect was produced in the tube to provide a uniform  $\text{Cu}^+$  ions distribution in the tube. The Cu atoms were ionized and excited by charge transfer reactions with He ions.

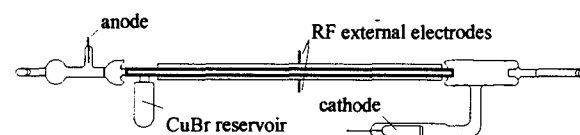


Fig.2 The scheme of the He-CuBr discharge tube.

### 3. Experimental method

A spectroscopic method based on a condition that the plasma is in local thermodynamic equilibrium (LTE) was used to determine the mean electron energy ( $E_T$ ). In this model the number of excited atoms in plasma is described by the Boltzmann distribution which depends on the mean electron energy. The mean electron energy can be determined by measuring the relative intensities (which are proportional to the appropriate number of excited atoms) of several lines emitted by the plasma [5].

In order to increase the accuracy of determined  $E_T$  and verify the LTE assumption it is necessary to

rearrange the Boltzmann distribution formula into the following equation:

$$\ln \left\{ \frac{\varepsilon_1 f_{mn}(2) g_n(2) \left( \frac{\lambda(1)}{\lambda(2)} \right)^3}{\varepsilon_2 f_{mn}(1) g_n(1)} \right\} = -\frac{1}{E_T} (E_m(1) - E_m(2)) \quad (1)$$

where: 1 and 2 denotes the measured lines,  $f_{mn}$  is the oscillator strength for the transition  $m \rightarrow n$ ,  $g_m$  and  $g_n$  are the statistical weights of the two levels,  $\varepsilon_1$  and  $\varepsilon_2$  are the intensities of the measured lines,  $\lambda(1)$  and  $\lambda(2)$  are the lines wavelengths,  $E_m$  is the energy of the upper level of the transition.

For the case of thermodynamic equilibrium the Boltzmann plot is a linear function of the energy difference  $[E_m(1) - E_m(2)]$ . The slope of the Boltzmann plot determines the mean electron energy.

For determining  $E_T$  the relative intensities of the following lines were used:

**He I-** 492.2 nm, 501.6 nm, 667.8 nm, 728.1 nm in the case of the He-CuBr laser system,

**He I-** 492.2 nm, 438.8 nm, 396.5 nm, 388.8 nm and **Cu I-** 578.2 nm, 521.8 nm, 515.3 nm, 510.6 nm in the case of He-Cu sputtered system. The oscillator strengths of He and Cu lines were taken from [6] and [7].

#### 4. Results and Conclusion

The obtained linear energy dependence of the Boltzmann plot suggests that the distribution of the He and Cu atoms over the energetic states has equilibrium character in the investigated discharges.

In every examined type of discharge,  $E_T$  almost did not change with changing electric power (see Fig.3).

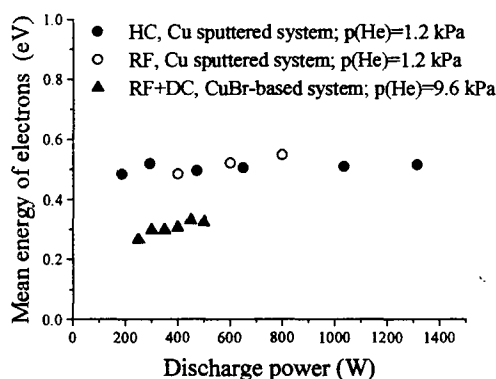


Fig.3 Mean electron energy as a function of delivered power.

On the other hand, the intensity of He and Cu lines increases with increasing input RF power in both laser systems. This means that the increase of atom excitation

with increasing electric power is caused by an increase of the number of electrons capable of exciting the atoms (since the energies of electrons cannot increase when increasing electric power because the operating voltage remains constant).

The mean electron energy in the He-CuBr plasma generated by a combined RF and DC discharge was lower than that in the Cu-sputtered system mainly due to higher He pressure (9.6 kPa).

In conclusion, the obtained results show that the mean electron energies in the RF and HC discharges are similar. In both discharges the bulk of the electrons consists of low-energy electrons characterised by a mean energy of about 0.5 eV. The similar mean electron energies in the RF and HC discharges found in this experiment is another evidence for similarity of both discharges.

#### Acknowledgment

This work was supported by the Commission of the European Community under Copernicus Program CIPA CT 93-0219.

#### 5. References

- [1] R.C. Tobin, K.A. Peard, G.H. Bode, K. Rozsa, Z. Donko, L. Szalai: High-Gain Hollow-Cathode Metal Ion Lasers for the UV and VUV, IEEE J. Quantum Electronics, Vol. I, No. 3, 805-809 (1995)
- [2] J. Mentel, N. Reich, J. Schulze, M. Grozeva, N. Sabotinov, J. Mizeraczyk: Radio frequency excited CW gas ion lasers, Trans. IEE of Japan, Vol. 116-A, No. 11, 964-969 (1996)
- [3] J. Mentel, N. Reich, J. Mizeraczyk, M. Grozeva, N. Sabotinov: Capacitively Coupled RF Excitation of CW Gas Lasers and its Comparison with Hollow Cathode Lasers, NATO Advanced Research Workshop ARW 950443, Gas Lasers-Recent Developments and Future Prospects, Moscow, Ed.: W. J. Witteman and V. N. Ochkin, Kluwer Academic Publishers, 55-67 (1995)
- [4] N. Reich: Transversale Kapazitive Hochfrequenzanregung von gasentladungslasern, Dissertation, Ruhr-Universität Bochum, Fakultät für Elektrotechnik, Elektrooptik und Elektrische Entladungen (1994)
- [5] Bekefi G: Principles of Laser Plasmas, New York, Chapter 13, 589-596 (1976)
- [6] Atomic Transition Probabilities, U.S. Department of Commerce, National Bureau of Standards, Vol I, Vol. II
- [7] M. Riemann: Measurement of Relative and Absolute Transition Probabilities of Cu I with a Wall-Stabilized Arc, Z. Phys., 179, 38 (1964)

# Optical, radio and X-ray radiation of Red Sprites produced by runaway air breakdown

Vyacheslav Yukhimuk, Robert Roussel-Dupré, Eugene Symbalisty, and Yuri Taranenko  
(Space and Atmospheric Sciences Group, MS D466, Los Alamos National Laboratory, Los Alamos, NM)

## 1. Introduction

We use the runaway air breakdown model of upward discharges to calculate optical, radio, and X-ray radiation generated by red sprites. Red sprites are high altitude (up to 90 km) lightning discharges. Aircraft based observations [1] show that sprites are predominantly red in color at altitudes above  $\sim 55$  km with faint blue tendrils, which extend downward to an altitude of 40 km; the duration of a single sprite is less than 17 ms, their maximum brightness is about 600 kR, and estimated total optical energy is about 1-5 kJ per event. The ground based observations show similar results, and provide some additional information on spatial and temporal structure of sprites [2], and on sprite locations [3]. One difference between aircraft and ground-based observations is that blue tendrils are rarely observed from the ground. Sprites usually occur above the anvils of large mesoscale convective systems and correlate with strong positive cloud to ground discharge [4]. Upward discharges are the most probable source of X-ray emission observed above large thunderstorm complexes by the Compton Gamma-ray Observatory [5]. To escape the atmosphere these  $\gamma$ -rays must originate above 25 km altitude. Red sprites are usually observed at altitudes higher than 50 km, and are therefore a likely source of this x-ray emission.

## 2. Theoretical results

We compute optical, radio and gamma-ray emissions caused by electrical discharges propagating upward in upper atmosphere. The results of the kinetic theory for runaway air breakdown [6] are used in our numerical calculations. We use the air fluorescence efficiencies measured by Davidson and O'Neil [7], and Mitchell [8] to calculate optical emissions. The spatial and temporal distribution of the number density and velocity of charged particles, from computer simulations, allow us to reproduce the corresponding distribution of

optical emissions in space and time. We use extinction coefficients measured by Guttman [9] to calculate the atmospheric attenuation of optical emissions. The maximum intensity of optical emission calculated over 17 ms (corresponding to one camera frame) is 647 kR. Red emission of 1P  $N_2$  predominates at altitudes higher than 55 km. At altitudes lower than 55 km blue emission of 2P  $N_2$  and 1N  $N_2^+$  predominates. We also calculate the radio emissions caused by the upward propagating discharge by using the distribution of electrical current density and charged particle number density in space and time, taken from the numerical simulations of runaway air breakdown.

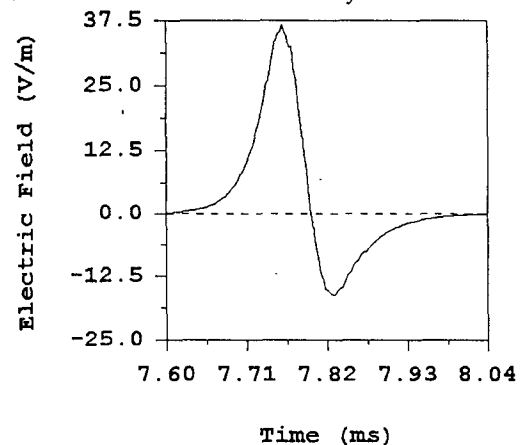


Fig. 1

The electric field of electromagnetic radiation as a function of time for an observer at altitude 80 km and 50 km from the center of the discharge is shown in Fig. 1. The maximum electric field amplitude is 37 V/m. Our results show that the radio emission of upward discharges is comparable with the radio emission of regular lightning. Therefore it is reasonable to conclude that ionospheric phenomena usually associated with radio emission of regular lightning such as ionospheric heating and glowing, lower-hybrid wave generation, explosive spread F and others can be caused by the radio emissions of upward discharges as well. Given the distribution of velocity and number density of relativistic

electrons in space and time we compute the spatial and temporal distribution of gamma-ray flux caused by the upward propagating discharge. In our calculations we use the emissivities calculated by Roussel-Dupré et al., [6] based on the Bethe-Heitler doubly differential cross section for bremsstrahlung emission by a relativistic electron. We take into account gamma-ray photons with energy  $E > 30$  keV.

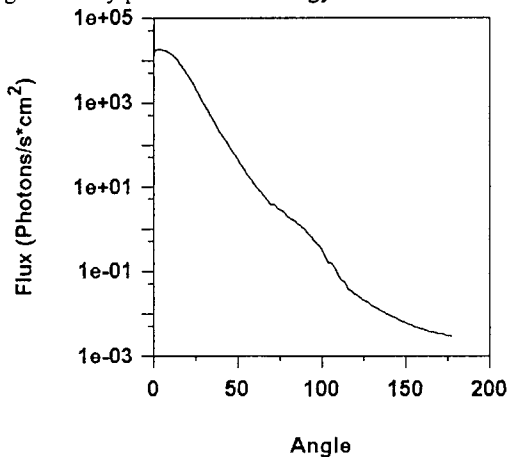


Fig. 2

The gamma-ray flux angular distribution at 1000 km from the discharge center is shown in Fig. 2.

### 3. Discussion and conclusion

We have compared our theoretical results for optical emissions with observations [1,2,3]. The computed intensity is in excellent agreement with the results of observations [1] measured from aircraft. The peak value measured by Sentman et al. [1], is about 600 kR, which is close to our computed peak value: 647 kR. Our calculations show the presence of visible blue emission at the bottom of the red sprite (blue tendril), which extends downward as low as 40 km. In this case, the blue tendril is visible only from high-altitude platforms ( $h \sim 11$  km), and becomes invisible from low-altitude because of Rayleigh scattering and scattering from aerosols. This result is in agreement with ground-based observations of red sprites which show no blue tendril for distant sprites.

The computed values of the gamma-ray flux are in agreement with observational results reported by Fishman et al., [5]. As one can see in Fig. 2, the gamma-ray flux depends significantly on the angle of observation. For an observation angle of  $90^\circ$  the computed flux value is about 0.8

photons/s\*cm<sup>2</sup>, for an angle near  $0^\circ$  the flux exceeds  $10^4$  photons/s\*cm<sup>2</sup>. The measured gamma ray flux [5] is about 100 photons/s\*cm<sup>2</sup>. We have calculated the gamma-ray flux without taking into account scattering by air. The scattering will lead to increasing the duration of the pulse and simultaneously decreasing the peak flux value. Our simulation shows that an upward discharge has a tendency to produce several short (with duration about 0.1-0.5 ms) gamma-ray pulses with time separation about 0.1-1 ms. These pulses could appear to an observer as one gamma-ray burst with duration 1-3 ms as a result of gamma-ray scattering. Indeed, such fine structure of the gamma-ray burst was observed by [5], and gamma-ray pulses with duration between 1-3 ms usually had multiple peaks.

In conclusion we note that the runaway air breakdown theory explains  $\gamma$ -ray emissions above thunderstorms and the blue tendrils of sprites; two phenomena that can not be explained by any other model of upward discharges.

### 4. References

- [1] D. D. Sentman, E. M. Wescott, D. L. Osborne, D. L. Hampton, and M. J. Heavner: *Geophys. Res. Lett.*, **22** (1995) 1205
- [2] J. R. Winckler, W. A. Lyons, T. E. Nelson, and R. J. Nemzek: *J. Geophys. Res.* **101** (1996) 6997
- [3] W. A. Lyons: *J. Geophys. Res.*, **101** (1996) 29641
- [4] Boccippio, D. J., E. R. Williams, S. J. Heckman, W. A. Lyons, I. T. Baker, and R. Boldi: *Science*, **269** (1995) 1088
- [5] Fishman, G. J., P. N. Bhat, R. Mallozzi, J. M. Horack, T. Koshut, C. Kouveliotou, G. N. Pendleton, C. A. Meegan, R. B. Wilson, W. S. Paciesas, S. J. Goodman, and H. J. Christian: *Science*, **264** (1994) 1313
- [6] R. A. Roussel-Dupré, A. V. Gurevich, T. Tunnell, G. M. Milikh: *Phys. Rev.*, **49** (1994) 2257
- [7] G. Davidson and R. O'Neil: *J. Chem. Phys.*, **41**, 12 (1964) 3946
- [8] K. B. Mitchell: *J. Chem. Phys.*, **53**, 5 (1970) 1795
- [9] A. Guttman: *Appl. Opt.* **7**, 12 (1968) 2377

# Fullerene as the new emitting additive for a low pressure gas discharge light source

V.M.Milenin, N.A.Timofeev, S.V.Kidalov\*, S.V.Kozyrev\*, A.Ya.Vul'\*

St.Petersburg State University, Ulianovskaya 1, St.Petersburg, 198904 Russia

\*Ioffe Physico-Technical Institute, Polytechnicheskaya 26, St.Petersburg, 194021 Russia

The search of new additives (atomic or molecular), which would be able to replace mercury in luminescent light sources, is continuously carried out by all leading lighting companies all over the world.

This paper deals with the possibility of using a recently discovered substance - a molecular cluster  $C_{60}$  which is referred to as fullerene - as an emitting additive of a gas discharge light source.

Several factors, concerning physical and chemical properties of fullerene molecules [1,2], lead to the hypothesis that fullerene can be a suitable additive for a low pressure gas discharge light source.

They are as follows:

- 1) a low ionization potential 7.6 eV;
- 2) theoretically predicted optical transitions between excited levels in a range 200-260 nm (see Fig.1 which presents the levels' structure of  $C_{60}$ );
- 3) molecules  $C_{60}$  do not dissociate during the collisions with fast electrons (up to energy 80-100 eV) or absorb UV photons (with energy up to 30 eV);
- 4) fullerene is stable to heating up to 900-950°C;
- 5) the pressure  $10^{-2}$ - $10^{-1}$  Torr of fullerene vapour is reached at 600-700°C;
- 6) fullerene molecules have practically no ecological effects;
- 7) it is not aggressive to other materials.

The points 1-3 make it possible to draw a conclusion that under some discharge conditions fullerene molecules, being added to a buffer gas (as mercury, being added to argon in luminescent lamps), can form emission properties, ionization balance in the plasma of a discharge and absorb the major part of applied electric power. Similar picture takes place in mercury luminescent lamps and ensures their high efficacy.

The possibility of using fullerene molecules as the emitting additive in a gas discharge light source was verified on electric discharges in noble gases He, Ne, Ar and Xe. The discharge chambers were made from transparent quartz glass allowing measurement in a spectral range 200-800 nm with the wall heating up to 700°C. Two types of discharge were studied: d.c. discharge and HF inductive discharge at 60 MHz. The noble gas pressure varied within 1-30 Torr and the discharge current density was about  $10^{-2}$  A/cm<sup>2</sup>; the HF discharge power was high enough for the optical emission to be observed by with the naked eye. Fullerenes were introduced into the discharge either as  $C_{60}$  powder or fullerene-containing soot.

The plasma emission spectrum was measured in the range 200-800 nm at various temperatures of the discharge chamber, various gas pressures and discharge current.

The measurements have shown that the heating in the presence of fullerene-containing material leads to

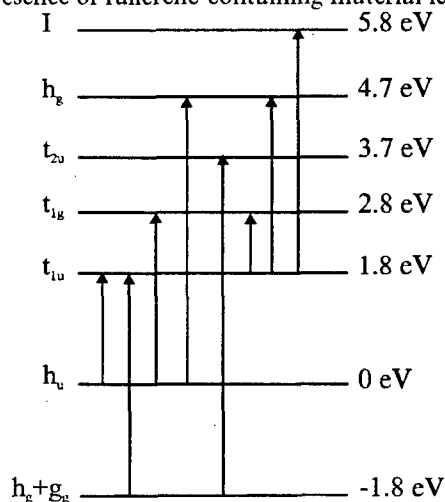


Fig. 1 Diagram of the electronic terms of the  $C_{60}$  molecule.

sweeping in the emission spectra for both d.c. discharge and HF discharge. At near-room temperature only noble gas atom lines are present.

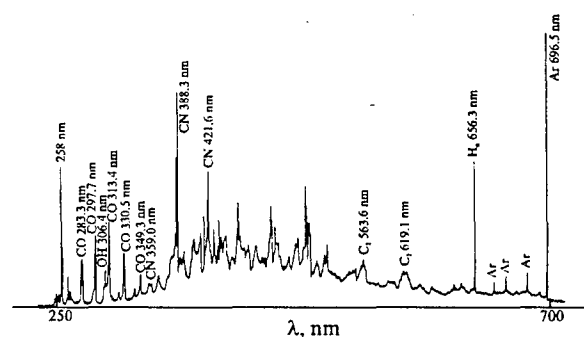


Fig. 2 Emission spectrum of an rf discharge in argon

Increasing temperature and appearance of fullerene vapour "inhibits" these and produces new lines (bands) in the blue-green and UV spectral regions (Fig.2). The lines observed can be identified as  $C_2$ , CN, CO and H lines. These dashes are presented in a fullerene sample and can hardly be eliminated by previous heating up to 150°C. The higher temperature is not used, because it is possible the pre-oxidation of  $C_{60}$  [3] and following destruction of the pre-oxyded fullerene. The band in the range 260 nm (see Fig.3) is due to the fullerene vapours in the plasma [4].

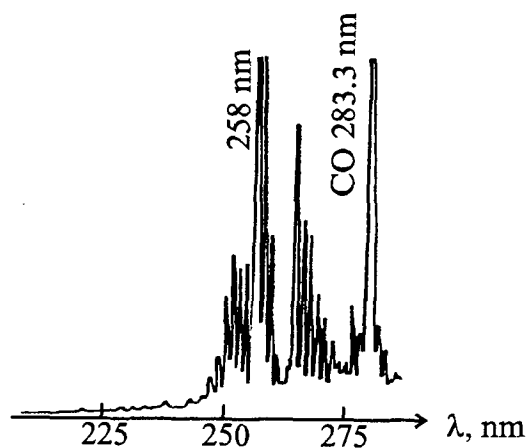


Fig.3 Emission spectrum (near 260 nm) of an rf discharge in argon in the presence of C<sub>60</sub> vapor in the gas phase.

The radiation at 260 nm is near the mercury resonance line 254 nm that makes it suitable to use this band instead of mercury line for the excitation of phosphors provided that the intensity at 260 nm is sufficiently high. The latter requires further investigation.

- [1] A.V.Eletskii, B.M.Smirnov: Usp. Fiz. Nauk, **163** (1993) 33 (in Russian).
- [2] S.V.Kozyrev, V.V.Rotkin: Sov. Phys. Semic., **27** (1993), 777.
- [3] H.Werner, M.Wohlers, D.Hrein, T.Schedel-Niedring, A.Bauer, R.Schlögl: Abstracts of Invited Lectures and Contributed Papers., Int. Workshop "Fullerenes and Atomic Clusters", St.Petersburg, Russia, June 19-24, (1995) 33.
- [4] N.L.Bashlov, V.M.Milenin, N.A.Timofeev, A.Ya.Vul', S.V.Kidalov, S.V.Kozyrev: JETP Lett. **63** (1996) 713.

## The effective low pressure gas discharge source of optical radiation based on hydroxyl OH

V.M.Milenin, N.A.Timofeev, S.V.Kidalov\*, S.V.Kozyrev\*, A.Ya.Vul'\*

St.Petersburg State University, Ulianovskaya 1, St.Petersburg, 198904 Russia

\*Ioffe Physico-Technical Institute, Polytechnicheskaya 26, St.Petersburg, 194021 Russia

Up-to-date low pressure gas discharge light sources are filled with mixtures of a buffer gas and an emitting additive having got, in comparison with buffer gas atoms, low excitation and ionization potentials. The most well-known examples of such light sources comprise mercury luminescent lamps and low pressure sodium lamps. As the capacity of emitting additives alkali metals (Na, K, Rb) and alkali-earth metals (Hg, Cd, Zn) are often used. However these light sources, being remarkable for their very high efficacy, have got some disadvantages the main of which is, in our opinion, their ecological effects.

The paper is devoted to the study of an opportunity of creating a new effective light source of optical radiation based on a practically harmless molecular additive - hydroxyl OH. Molecules OH have ionization potential 12.1 eV which is comparatively lower than that of the light noble gases (He, Ne, Ar), their resonance radiation gives the emission band 306.4 nm, and their preparation from water molecules in a gas discharge medium is not difficult.

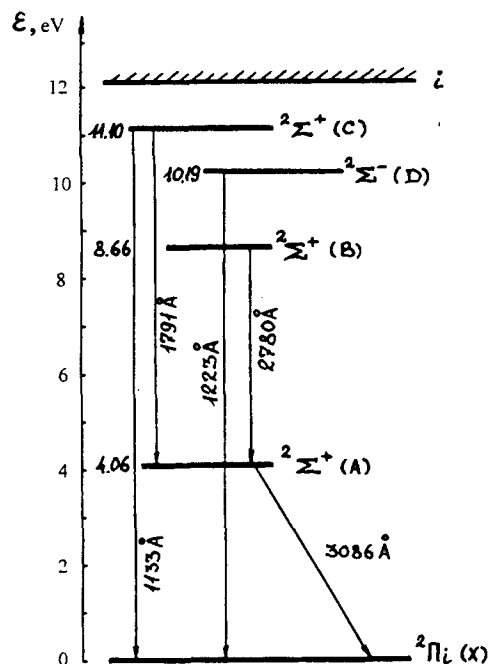


Fig.1 A simplified scheme of the molecule OH energy levels (only electron states are shown, vibrational and rotational structure are omitted).

Discharges in noble gases He, Ne, Ar, Xe were investigated when a molecular additive OH was present in a discharge tube. The pressure of the noble

gases varied in the range 3-30 Torr, the concentration of molecules OH was  $10^{13}$ - $10^{16}$  cm<sup>-3</sup> (it was derived from the quantity of water molecules filled in a discharge tube supposing that an electric discharge causes the dissociation of all water molecules H<sub>2</sub>O giving H and OH). Quartz discharge tubes 1 cm in diameter were used. Discharge current was 100-500 mA. Plasma emission spectrum in the range 200-800 nm and applied electric power were studied when discharge compositions and conditions were changed. Comparative experiments were also carried out to study the excitation of different phosphors by a mercury luminescent lamp and (OH + noble gas)-discharge plasma to estimate the light efficacy of the latter.

Fig.1 shows a simplified scheme of the molecule OH energy levels (only electron states are shown, vibrational and rotational structure are omitted).

The lower resonance state  $^2\Sigma^+(A)$  with excitation energy 4.06 eV gives the emission band 306.4 nm. This radiation can be used *per se*, because it coincides approximately with the maximum of the UV absorption band inherent in biological organisms, and this UV radiation can be also converted into visible range with the help of phosphors.

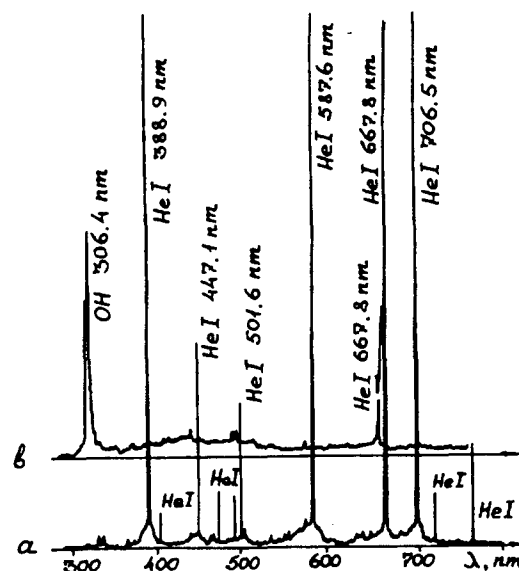


Fig.2 Optical emission spectra of the He-discharge plasma (a) and (He + OH)-discharge plasma (b).

The adding of the molecules OH into a noble gas discharge, as experiment shows, changes plasma

emission and electrical properties dramatically. Fig.2 presents optical emission spectra of the He-discharge plasma (a) and (He + OH)-discharge plasma (b). As one can see from the figure, the presence of the OH-additive in the discharge in question leads to the practically full suppression of the noble gas radiation in the spectral range under study. Instead of them there appeared an intensive emission band OH 306.4 nm. The high intensity of this radiation makes it possible to hope that the major part of the applied electric energy expends on the excitation of the OH-resonance radiation.

Similar results were obtained for the other mixtures of OH and the noble gases in question.

It will be noted that the radiation of atomic hydrogen is not appreciable (choosing discharge conditions the intensity of the hydrogen spectral line  $H\alpha$  can be decreased to  $10^{-2}$  of the 306.4 nm intensity) and the radiation of atomic or molecular oxygen which could arise from the dissociation of  $H_2O$  or OH is not registered at all.

The estimation of the plasma light efficacy of the discharge is under study, carried out with the help of phosphors excitation, shows good chances for the creation of a new effective source of optical radiation.



# Spatially One-Dimensional Modelling of a Stabilized Discharge Pumped XeCl\* Laser

S. Gortchakov\*, D. Loffhagen, R. Winkler

Institut für Niedertemperatur-Plasmaphysik, 17489 Greifswald, Germany

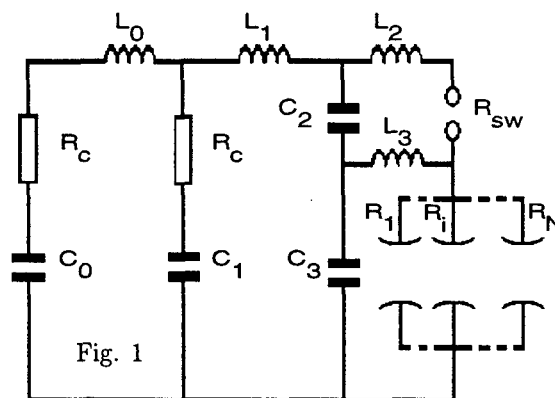
\* Institute of High Current Electronics, Russian Academy of Sciences, 634055 Tomsk, Russia

## 1. Introduction

To initiate and maintain a homogeneous laser discharge, recently a new arrangement for providing a stable, homogeneous discharge for the pumping of wide-aperture excimer lasers has been proposed in [1]. The suppression of the filamentation of the discharge plasma has been achieved by a special pumping technique which is based on the additional use of a low-current preliminary discharge ahead of the high-current discharge. In the present paper the impact of an inhomogeneous preionization on this excimer laser discharge is analysed. The studies have been performed with a self-consistent spatially one-dimensional model for a XeCl\* laser discharge.

## 2. Description of the Model

In the frame of the model a parallel resistor description [2] of the discharge plasma has been adapted. The total discharge region is divided into a number of spatially homogeneous discharges which are parallel to the discharge current and to the optical axis of the resonator cavity. Each discharge region  $i$  is characterized by its cross section area  $A_i$  and the initial electron density  $n_{ei}(t=0)$  according to the spatial distribution of the preionization. The laser discharge has been treated by self-consistently solving the equation system for the electrical circuit as well as, for each spatially homogeneous discharge region, the time-dependent electron Boltzmann equation including electron-electron interaction for the determination of the electron kinetic quantities and the rate equation system for the various heavy particles and photons occurring in the plasma. The present spatially one-dimensional model is an extension of the spatially homogeneous model described in [3]. Fig. 1 shows the equivalent electrical circuit used in the model calculations, where  $C_0 = C_1 = 200$  nF,  $C_2 = 1.8$  nF,  $C_3 = 0.85$  nF,  $L_0 = 2.2$   $\mu$ H,  $L_1 = L_2 = 40$  nH,  $L_3 = 0.5$  nH, and  $R_c = 0.01$   $\Omega$ . The resistance  $R_{sw}$  of a spark gap triggers the transition from the low-current to the high-current discharge phase. The resistance  $R_i$  of the discharge region  $i$  is determined by the solution of the electron Boltzmann equation for that region. The system of rate equations describes the temporal evolution of 22 heavy particle components and the laser photons and takes into account about 150 collision processes.



## 3. Results and Discussion

Results of model calculations for Ne/Xe/HCl mixtures with a standard composition of 1000/8/0.8 at a total pressure of 3 bar and a gas temperature of 293 K are presented. The parallel plate electrodes are separated by 8 cm, the discharge length is 60 cm and the width of the total discharge is 5 cm. The optical plane-plane resonator consists of a totally reflecting mirror and an output mirror with a reflectivity of 30 per cent and the cavity length has been chosen to be 80 cm. At the standard initial voltage of 39 kV a laser output energy of 1.4 J with an efficiency of about 1 per cent and a pulse duration of 400 ns was obtained when assuming a homogeneous discharge operation.

To study an inhomogeneous preionization, the total discharge has been divided into two regions, where the preionization electron density  $n_{e2}(t=0)$  in region 2 has been chosen to be higher than that in region 1. Thus, the discharge region 2 is assumed to represent the total number of filaments covering the area  $A_2$ . In Fig. 2 the temporal behaviour of the discharge voltage  $U_d$  (full line) and of the current density  $j_i$  in the discharge regions  $i = 1$  (short-dashed line) and  $i = 2$  (long-dashed line) are shown for the case with  $n_{e2}(t=0) = 1.05 \cdot n_{e1}(t=0)$  at  $n_{e1}(t=0) = 5 \cdot 10^8$  cm<sup>-3</sup> and  $A_1 = 4 \cdot A_2$ . After the charge of  $C_0$  is transferred to  $C_1$  and the capacitive divider  $C_2/C_3$  in a prephase of about 1.2  $\mu$ s, the low-current phase starts with the preionization of the discharge. In this phase the current density in both regions remains less than about 10 A/cm<sup>2</sup>. Typically after a low-current phase of about 400 ns the high-current phase is triggered. In contrast

with experiments [1] the results for the current densities obtained by the model calculations predict the development of an inhomogeneous high-current discharge. For times later than about 650 ns the voltage is insufficient to sustain the discharge in region 1 and the discharge contracts to region 2.

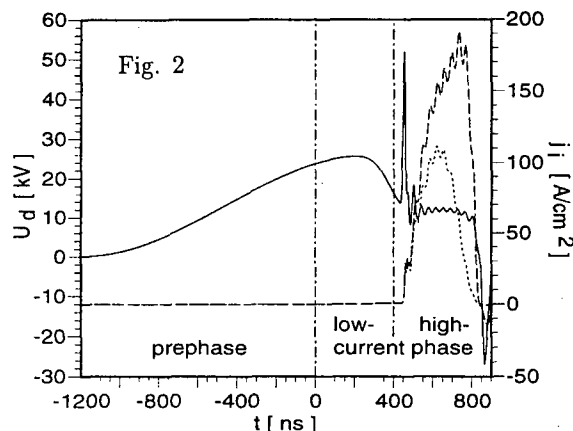
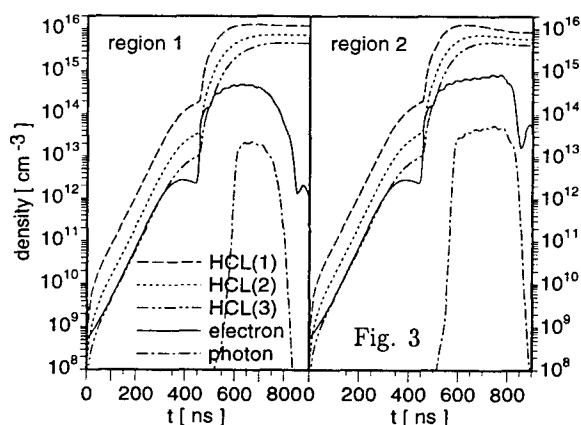
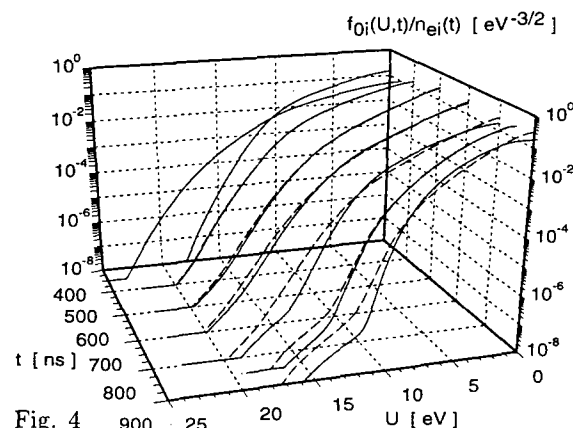


Fig. 3 presents the temporal evolution of the particle number densities of  $\text{HCl}(v)$  with  $v = 1, 2, 3$ , of the electrons and the photons in both discharge regions. During the low-current phase the densities of  $\text{HCl}(v)$  and the electrons increase nearly exponentially in both regions. The initially slight difference of 5 per cent between the electron densities increases continuously during the high-current phase up to more than one order of magnitude at the end of the discharge. For  $t > 600$  ns the enhanced electron density in region 2 causes a decrease of the  $\text{HCl}(v)$  densities in that region, while the densities of  $\text{HCl}(v)$  in region 1 remain nearly time-independent. As a consequence of the behaviour of the electron density, the photon density in region 2 reaches larger values and the photon pulse takes longer than in region 1.



In Fig. 4 the isotropic part  $f_{0i}(U, t)/n_{ei}(t)$  of the electron velocity distribution function normalized on the electron density  $n_{ei}(t)$  for the discharge re-

gions  $i = 1$  (full line) and  $i = 2$  (dashed line) is shown for several instants of the temporal evolution. During the low- and the early high-current phase the distribution functions in both regions almost coincide. Then the population of the distribution at higher energies diminishes in region 1 compared with the corresponding population in region 2. The behaviour of the distribution functions is accompanied by a different evolution of the corresponding electron transport coefficients and rate coefficients for electron-heavy particle collision processes in both discharge regions. Thus, the commonly used simplified treatment in the literature describing the reaction kinetics by transport and rate coefficients, which are tabulated as a function of the reduced electric field strength only and are related to hydrodynamic stages, may cause misleading results.



Similar results have been obtained for a variety of discharge parameters. In general it has been found by the parallel resistor calculations, that even small density perturbations of preionization electrons lead to the constriction of the discharge to the region with the initially higher electron density. The development of an inhomogeneous discharge plasma and laser output occurs faster, if the magnitude of the electron density perturbation and the  $\text{HCl}$  portion of the gas mixture are increased and the cross section area of the discharge region with higher initial electron density is decreased. On the other hand, the stabilizing effect of the low-current discharge phase for the discharge operation found in experiments was not explicable by the model.

#### 4. References

- [1] Yu. Bychkov, I. Kostyrya, M. Makarov, A. Suslov, A. Yastremsky: *Rev. Sci. Instrum.*, **65** (1994) 793
- [2] M. J. Kushner, A. L. Pindroh, C. H. Fischer, T. A. Znotins, J. J. Ewing: *J. Appl. Phys.*, **57** (1985) 2406
- [3] D. Loffhagen, R. Winkler: *J. Comput. Phys.*, **112** (1994) 91

# Exploring the influence of ambipolar diffusion mechanism in a Hg-Ar low pressure positive column under AC operating conditions by a self-consistent time-dependent collisional-radiative code

D. Porras, G. Zissis

Centre de Physique des Plasmas et de leurs Applications de Toulouse  
118 rte de Narbonne  
F-31062 Toulouse Cedex 4, France

## 1. Introduction

Lots of experimental and theoretical studies concerning low pressure mercury-argon discharge exist. The main application of such studies deals with lighting domain, in particular with the fluorescent tube that is a specific low pressure mercury-argon discharge. The last few years, important progresses, concerning not only the increase of light efficiency but more generally better knowledge about gas discharge behaviour, have been achieved. These researches mainly turn to more and more complete models which allow the prediction of optimal operating conditions of lamps. Thus, better understanding of important mechanisms taking place in the system is accomplished as well. The aim of modelling of Hg-rare-gas low pressure discharge lamps, which is a necessary complement to experimental investigations, is to predict the optimal operating conditions of these devices. Optimal operating conditions, in the case of certain applications, mean high luminous intensities at selected wavelengths and high efficacy for a large range of ambient temperatures. These operating conditions depend closely on several external parameters such as tube diameter and shape, discharge current and partial pressures of mercury and rare-gas in the positive column plasma.

This work deals with use of a collisional-radiative model concerning low pressure mercury-argon discharge operating under AC power supply in order to explore the positive column behaviour in a large domain of operating frequencies.

## 2. The model

This Self - Consistent Time - Dependent Collisional - Radiative model allows the determination of various characteristic quantities of the discharge solving the population and electronic energy conservation equations coupled to quasi-neutrality condition, perfect gas law and Ohm's law. In order to treat effectively this equation set we need the following simplifying assumptions: The positive column is assumed to be axisymmetric and therefore all calculations have been performed using cylindrical co-ordinates.

In this model, we consider for Hg atom a six level scheme ( $6^1S_0$ ,  $6^3P_{0,1,2}$ ,  $6^1P_1$ ,  $7^3S_1$ ) and the mercury ion. In this work we include also a very simplified 3 atomic level for argon ( $Ar$ ,  $Ar^*$ ,  $Ar^+$ ). As the average energy of

$Ar^*$  atomic levels is about 11.65 eV direct ionisation from the ground state is assumed negligible under the conditions considered in this study (the mean electron energy is about 1-2 eV). Interactions such as quenching, associative and Penning ionisation have been taken into account.

In the low pressure discharges, a diffusion controlled positive column is frequently assumed (Schottky's regime). The main ion-electron loss process is the diffusion of these pairs on the tube wall where recombination takes place, rather than the volume recombination. However, all classic models accounts for ambipolar diffusion mechanism, unfortunately this is valid if only one type of ion is present in the plasma. In our case where  $Hg^+$ ,  $Ar^+$  are existing we should use a more complete model to describe the charged particle diffusion as described by Rogoff [1].

The electronic temperature is assumed constant over the discharge tube radius. This assumption is justified experimentally by probe measurements [2]. We note that this hypothesis is rather restrictive and more especially in cases where total pressure increases or tube radius decreases.

## 3. Results

In this paper we focus our interest on the positive column behaviour of an almost classic fluorescent lamp a function of the applied frequency (AC power supply) and for two different buffer gas pressures. Thus calculations are performed for a discharge with the following characteristics:

Discharge internal radius  $R=14$  mm  
Hg pressure  $p_{Hg}=6.3$  mTorr  
Buffer gas pressure  $p_{Ar}$ : 3 and 5 Torr  
Arc current form  $I(t)=I_0\sin(2\pi ft)$   
Current amplitude  $I_0=400$  mA  
Frequency range  $f$ : 50 Hz up to 100 kHz

We note that the chosen mercury pressure correspond to a cold spot temperature of about 40°C which is very close to the maximum emission conditions for the 254 nm radiation.

Figure 1 illustrates the calculated electron temperature as function of frequency for two buffer gas pressures.

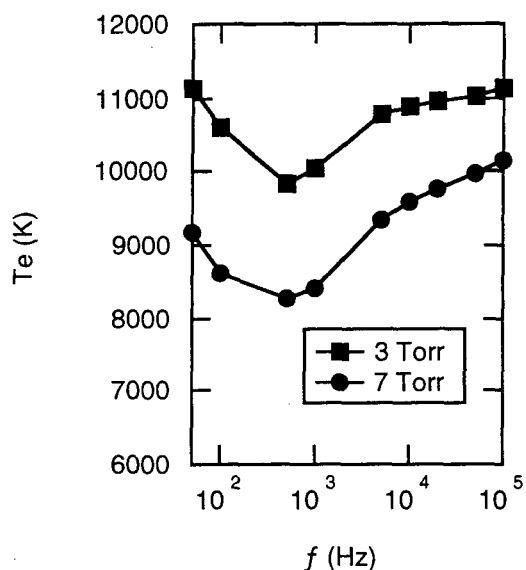


Figure 1

We observe that electron temperature presents a minimum (for both buffer gas pressures) in a frequency value of about 500 Hz. This minimum corresponds to a peculiar value linked to characteristic time of ambipolar diffusion in the positive column ( $\tau_{amb} \sim ms$ ). This limiting frequency value could be observed also in the figure 2 which presents the arc voltage wave form during a half operating AC period.

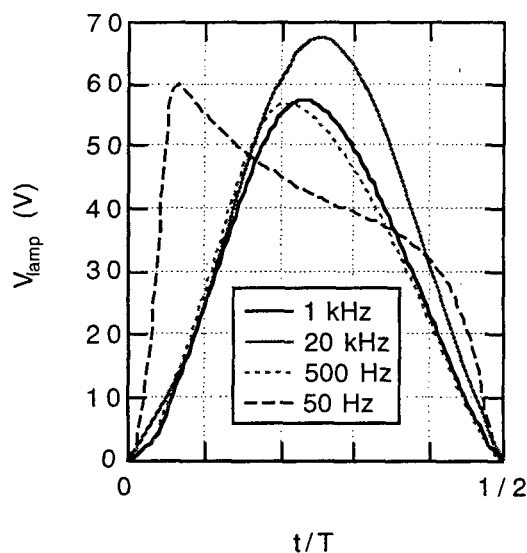


Figure 2

We observe that the wave form changes fundamentally in the region of 500 Hz. In fact, for frequencies larger than this limiting value the ratio of odd higher rang voltage harmonics (3, 5...) decreases very rapidly. An other important point is the following: Electron temperature is lower in the case of higher buffer gas

pressures for any frequency value. This behaviour could be explained by considering fact that when pressure increases, elastic collision energy loss increases too. Figure 3, confirms the previous explanation by illustrating the calculated electron density as function of ac frequency. As we observe, on the one hand, electron density increases when buffer pressure grows. On the other hand, electron density remains almost constant in the overall frequency range studied here.

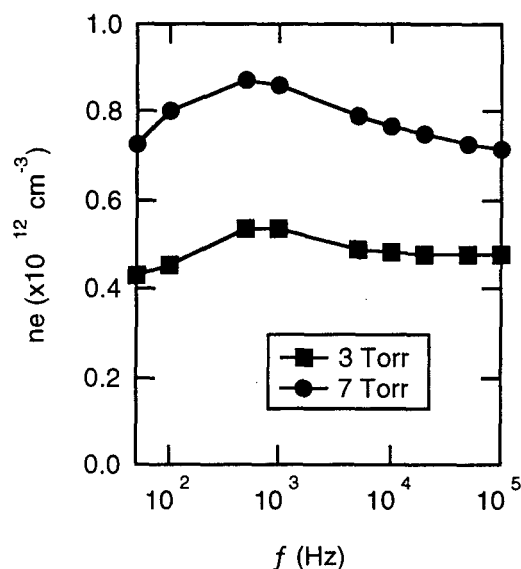


Figure 3

Finally, our calculation show that electric field values in the positive column pass through a minimum value in the same characteristic frequency. However, the overall UV efficiency remains almost constant (within  $\pm 2\%$ ) for a large frequency range within the studied domain.

#### 4. References

- [1] Rogoff, G.L., J. Phys. **D18**, 1533 (1985)
- [2] Verweij W., Philips Res. Rep. Suppl. **2**, 1 (1961)

# Power interruption experiments on a high pressure sulphur discharge

C. Johnston, J. Jonkers, J.A.M. van der Mullen and D.C. Schram

Department of Applied Physics, Eindhoven University of Technology,  
PO Box 513, 5600 MB Eindhoven, The Netherlands

## 1. Introduction

Power interruption experiments have been performed on a high pressure sulphur discharge sustained by microwaves. Such experiments involve the switching off of the power applied to the plasma and observing the responses in the spectrum. The spectrum of the discharge is continuous. The turn off time is typically 100 $\mu$ s at a repetition frequency of 40 Hz.

The plasma responds instantaneously to the removal of power indicating that it is not in LTE and that the electron temperature probably is significantly greater than the heavy particle temperature. It is expected that the difference in electron and heavy particle temperatures will be significantly greater than that normally observed in high pressure discharges. During the power off period a gradual response was observed.

## 2. Background

The spectrum of such a discharge is shown in figure 1. The plasma is very weakly ionised (ionisation degree ca.  $10^{-4}$ ) and no sulphur atomic lines have yet been observed. It is expected that this absence is due to inverse predissociation of sulphur and also to selective optical thickness of the molecular species to these lines. A backfill of argon is used as an aid to ignition but also its presence is essential to the processes that produce the spectrum.

As yet no argon lines have been search for.

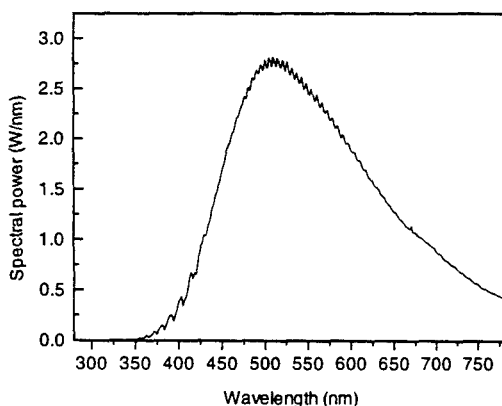


Figure 1: Spectrum of a microwave sulphur discharge

## 3. Processes

The spectrum depicted in figure 1 appears continuous however this due to the significant pressure broadening of vibrational lines. Any rotational transitions are 'washed' out of the spectrum. The potential curves of sulphur are described in figure 2.

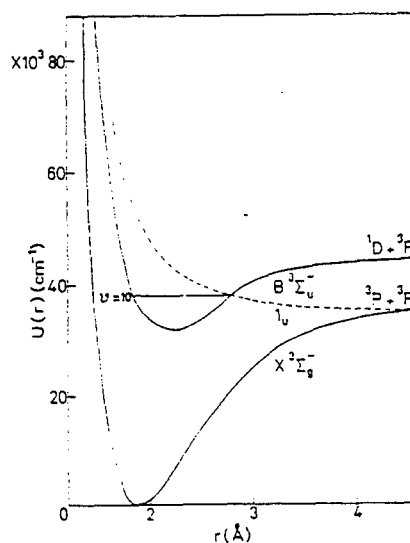
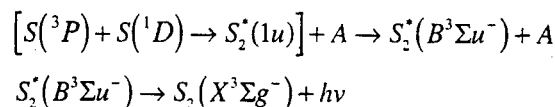


Figure 2: Potential energy curves of S<sub>2</sub>

The reaction that drives this process is believed to be



Where A is most likely an argon atom (the density of atomic sulphur is sufficiently smaller) which in the collision carries away such amounts of energy as to populate all the vibrational levels with  $v' \leq 9$  of the B state of S<sub>2</sub> which in turn will give rise to the observed spectrum.

With such a process atomic sulphur lines should be expected, however none have been observed, even in low pressure discharges. With knowledge, a priori, of some processes the structure of the plasma can be determined.

The beauty of the power interruption technique is that it allows investigation of the hierarchy of balances in the plasma.

## Measurements on a high current conventional fluorescent lamp and comparison with the numerical model

J. Jonkers, P.G.J.M. Herben, J. van Dijk, D.C. Schram and J.A.M. van der Mullen

Department of Applied Physics, Eindhoven University of Technology,  
PO Box 513, 5600 MB Eindhoven, The Netherlands

### 1. Introduction

There is an increasing interest in electrodeless lamps as, amongst other reasons, the life time is considerably longer than the conventional discharge lamps. Furthermore, reactions between the electrodes and the plasma are avoided, which makes the choice of the filling less restricted.

One special class of electrodeless lamps are the inductive fluorescent lamps. The first commercial lamps in this class have become available: the QL-lamp of Philips since 1992 (cf. Figure 1) and the Genura of General Electric since 1994 [1]. Recently Osram Sylvania announced the Endura. With respect to the mechanism of light generation these lamps are similar to the common mercury fluorescent lamp. Inside mainly UV radiation is created which is converted into visible light by a fluorescence powder situated at the wall of the bulb [2,3]. Besides the lack of electrodes, the other main difference between the electrodeless and the conventional fluorescent lamps is the plasma current. A typical current in a conventional fluorescent lamp is 400 mA, which is much lower than that in the inductively coupled lamp: 5 to 10 A.

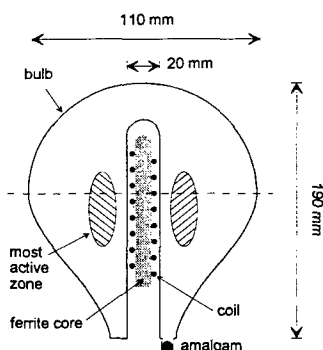


Figure 1: A schematic of the Philips' QL-lamp.

At the Eindhoven University of Technology a model is being developed which describes the QL-lamp. This two-dimensional model is also presented at this conference [4]. Based on the design parameters, like the driving current and gas pressures, macroscopic quantities as the production of light and heat are calculated. This model basically consists of two parts: one describing the gas discharge and an other describing the coupling between the coil and the plasma. The discharge physics differs from that used in models on the more conventional fluorescent lamp (as for instance [5]), since due to the much higher plasma current it is expected that the electron density is much

higher. This means that step-wise excitation has to be taken into account [6].

In this contribution measurements are presented which are used to verify the gas discharge model.

### 2. Experiments

In order to check the validity of the gas discharge model the voltage-current characteristics of several linear discharge lamps have been measured. The configuration is the same as the common fluorescent lamps, but the operating parameters are similar to those of the QL-lamp. Special electrodes are used in order to be able to operate at currents between 5 and 15 A. The radius is taken equal to the distance between the center of the most active zone and the inner wall of the bulb (see Figure 1), which is approximately 1 cm [7].

The voltage-current characteristics have been measured as function of the argon and mercury pressures, the kind of noble gas filling and the radius of the discharge tube.

### 3. References

1. D.O. Warmly and S.-A. El-Hamamsy: Proceedings of the 7th International Symposium on the Science and Technology of Light Sources, Kyoto Japan (1995) 27.
2. J.F. Waymouth: "Electrical Discharge Lamps", MIT Press, Cambridge MA (1971).
3. W. Elenbaas: "Light Sources", The MacMillan Press Ltd., London (1972).
4. J. van Dijk, M.A. Tas, J. Jonkers, P.G.J.M. Herben and J.A.M. van der Mullen: "Numerical Modelling of Low Pressure Argon/Mercury Discharges: an Application of PLASIMO", this conference.
5. T.P.C.M. Vos, F.A.S. Lighthart, P.A.P. Zeinstra, J. Jonkers and J.A.M. van der Mullen: "Dynamic Electrical Characteristics of Fluorescent Lamps", this conference.
6. J. van Dijk, A. Harigers, J. Jonkers, P.G.J.M. Herben and J.A.M. van der Mullen: "Towards a General Collisional Radiative Model", this conference.
7. J. Jonkers, M. Bakker and J.A.M. van der Mullen: "Absorption measurements on a low pressure, inductively coupled, argon/mercury discharge for lighting purposes. 1. Gas temperature and argon metastable density.", submitted to J. Phys. D: Appl. Phys.

*Topic 19a*

Special topic at the XXIII ICPIG :  
**Highly ionized, low pressure plasmas**  
**(plasma thrusters, ion sources**  
**and surface treatment).**

# A diffusion model for near wall conductivity in plasma thrusters

Pierre Degond and Vladimir Latocha

Mathématiques pour l'Industrie et la Physique-INSA  
Complexe Scientifique de Rangueil  
31077 TOULOUSE CEDEX

We propose a macroscopic diffusion model to describe the near wall electron conduction in plasma thrusters. For isotropic scattering, analytic diffusion and conductivity coefficients are obtained, which are inversely proportional to the square of the magnetic field, as experimentally observed.

## 1 The Stationary Plasma Thruster

Our model is aimed at describing the electron distribution function in an SPT 100 engine (see [2] for the operation principle of the SPT 100).

See figure 1 for a geometrical description.

## 2 Derivation of the Model

We start with the free transport equation on the electron distribution function in dimensionless variables:

$$\frac{\partial f}{\partial t} + v \cdot \nabla_x f + (E + v \times B) \cdot \nabla_v f = 0$$

$f(x, v, t)$  being the electron distribution function,  $E = E_z \vec{e}_z$  is an axial electric field,  $B = B_r \vec{e}_r$  is a radial magnetic field.

The boundary conditions are modelled by a splitting into specular and diffusive reflexions. The latter are then splitted into elastic and inelastic parts, given by integral operators. For the outer cylinder  $f_-(v) = f(v)|_{v_r < 0}$  is the part of  $f$  outgoing from the boundary, and  $f_+(v) = f(v)|_{v_r > 0}$  is the incoming part of  $f$  (for the inner cylinder the signs are

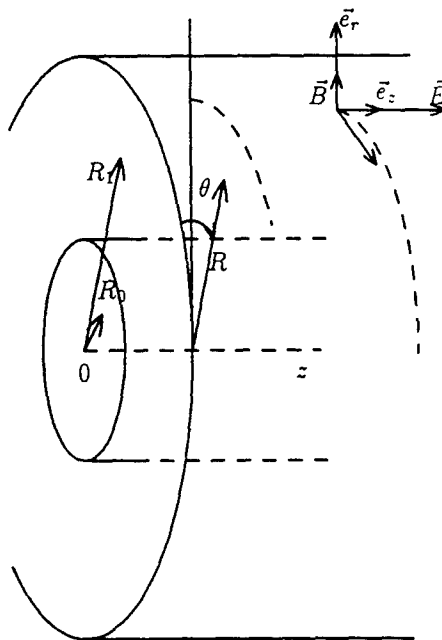


Figure 1: geometry and notations

reversed), and the reflexion operator reads:

$$\begin{cases} f_-(v) = \\ \alpha f_+(v^*) + (1 - \alpha)((1 - \beta)\mathcal{K}(f_+) + \beta\mathcal{H}(f_+)) \quad (2) \\ \text{with } v^* = (-v_r, v_\theta, v_z) \\ \mathcal{K}: \text{elastic part of the diffusive reflexions} \\ \mathcal{H}: \text{inelastic part of the diffusive reflexions} \end{cases}$$

$\mathcal{K}$  is given by an integral operator:

$$\mathcal{K} f_+(v) = \int_{\{\omega' \in S^2, \omega'_r < 0\}} K(z, |v|, \omega, \omega') f_+(|v|\omega') d\omega'.$$

$$\forall v \in \mathbb{R}^3, v_r > 0,$$



where the velocity direction  $\omega = v/|v|$  belongs to the unit sphere  $S^2$  and the kernel  $K$  satisfies some properties.

$\alpha \in [0, 1]$  is called the accommodation coefficient. It represents the probability of a specular reflexion,  $1 - \alpha$  is thus the probability of all other events, that is to say the diffusive reflexions.  $\beta \in [0, 1]$  is the probability of an elastic reflexion among diffusive reflexions,  $1 - \beta$  of the inelastic reflexions among diffusive reflexions.

The model is based on the assumption that the distance between the two cylinders  $R_1 - R_0$  is smaller than the radius of the cylinders  $R_0$ . We introduce a small parameter  $\eta = \frac{R_1 - R_0}{R_0} \ll 1$ .

The equations are then properly scaled.

When  $\eta$  is very small, under fairly general conditions on the elastic scattering operator, we get at leading order:

$$f_0(x, v) = N(z, \varepsilon = |v|^2/2, t) \quad (1)$$

where  $N$  satisfies a diffusion equation in the  $(z, \varepsilon = |v|^2/2)$  space, which reads:

$$\sqrt{2\varepsilon} \frac{\partial N}{\partial t} + \left( \frac{\partial}{\partial z} - \bar{E} \frac{\partial}{\partial \varepsilon} \right) \cdot \bar{J} = Q(N) \quad (2)$$

$$J = -D \left( \frac{\partial}{\partial z} - \bar{E} \frac{\partial}{\partial \varepsilon} \right) N \quad (3)$$

$Q(N)$  depending on the inelastic part of the reflexion operator.

The diffusion coefficient admits an analytical expression in the isotropic scattering case:

$$D(B, \varepsilon) = \frac{\varepsilon^2 \beta}{B^2} \int_0^1 G(B, \varepsilon, w) w (1 - w^2) dw$$

with  $\gamma$  and  $\beta$  constant terms and

$$G(B, \varepsilon, w) = \left( 1 - \cos \frac{B}{\sqrt{2\varepsilon} w} \right)^2 + \frac{\gamma}{\beta} \sin^2 \frac{B}{\sqrt{2\varepsilon} w}$$

### 3 Second order Boundary Conditions

To account for the electrons leaving the device at the cathode or absorbed by the anode, a Robin boundary conditions is set up:

$$f - \Lambda \cdot \eta \frac{\partial f}{\partial z} = f_0$$

where the extrapolation length  $\Lambda$  can be approximated in a first step by (the sign of  $\Lambda$  is positive for the anode and negative for the cathode):

$$\Lambda = \pm \frac{D(B, \varepsilon)}{2\Pi}$$

### 4 Scattering

The dominant scattering process is the collision with the boundary, modelled by (2). However Coulomb scattering against ions may be non negligible. An approximation for these scatterings will be included in the numerical computation.

### 5 Numerical Results

Numerical work is in progress. We will give a comparison with computations by a Monte Carlo method (see [3]).

### References

- [1] A.I. Morozov et A. P. Shubin, Electron kinetics in the wall-conductivity regime I and II: *Sov. J. Plasma Phys.* Vol. 10, No. 6, (1984), 728-735 and Analytic methods in the theory of near-wall conductivity I and II: *Sov. J. Plasma Phys.* Vol. 16, No. 10, (1990), 711-715.
- [2] P. Degond, A model of near-wall conductivity and its application to plasma thrusters: *preprint MIP-Toulouse* (1996) submitted
- [3] Laboratoire de physique des décharges, Centre de Physique des Plasmas et de leurs applications de Toulouse, *reports*, unpublished
- [4] Laurent Garrigues, Centre de Physique des Plasmas et de leurs applications de Toulouse. personal communications

# OPTICAL AND ELECTRICAL INVESTIGATIONS ON PLASMA OSCILLATIONS OF SPT THRUSTERS

## - ABSTRACT -

Franck DARNON<sup>†</sup>, Michel LYSZYK<sup>‡</sup> André BOUCHOULE<sup>\*</sup>

1

### INTRODUCTION

Oscillations in Stationary Plasma Thrusters (SPT) seem to play a major role in the good working of the thruster. However, these instabilities have to be controlled for the integration of the SPT on board and for Power Processing Unit (PPU) design. A better understanding of oscillations is essential for future improvement of SPT, PPU and FU (Filter Unit) designs. In this paper, we will describe oscillations of light intensity emitted by the plasma, corresponding to the local fluctuations of excited species densities. Then, we will analyse the electric behaviour of the system PPU / FU / SPT.

### SETUP

Measurements were performed on a SPT thruster, in the SEP test facility. The thruster worked in nominal conditions (4.5 A, 300 V, 5 mg Xe/s) in the 13 m<sup>3</sup> cryogenic pumping tank at a working pressure of 5 10<sup>-3</sup> mtorr of xenon. Data correspond to a thruster lifetime of 800 to 1300 hours.

The optical image of the exit plane of the thruster is realised with a spherical mirror (see figure 1). The light is collected by two optical fibres whose positions are moveable on X (horizontal) and Y (vertical) axis. The detection consists of two photo multipliers. The collected light come from a quasi cylinder of plasma (0.5 mm diameter). The 45 deg. angle between thruster axis and optical axis allows observations inside the channel.

Current and voltage probes have been inserted to measure electric signals at characteristic points of the electric circuit (figure 2). Different values of Rf, Cf and Cx have been tested.

This setup allows the characterisation in space, time and frequency of the light emission and give the evolution of electric oscillations as a function of FU parameters

### OPTICAL MEASUREMENTS

#### Description of oscillations

By a spectral analysis of the collected light, we can identify three groups of oscillations :

- A sharp peak at about 33 kHz, followed by 3 to 4 harmonics,
- A wide band, which shut down at about 200 kHz,
- A wide band, in the range of 200 - 500 kHz.

Oscillations at lower frequencies than 10 kHz are not available due to the spectrum analyser.

Oscillations at higher frequencies than 1 MHz imply only electrons, so they are not measurable with this method.

The optical signal, read on a time scale reveals a strong periodicity at a frequency of 33 kHz (about  $\pm 70\%$  of the total light intensity), a not symmetric signal (peak of intensity followed by a longer silent period) and the presence of an anomaly (little spike called "Vestnik" in Russia), decorrelated with the main oscillation.

#### Behaviour of the plasma

By measuring phase shift between two signals (corresponding to different points of observation), it can be concluded that the oscillation is propagating along the thruster axis, with a velocity of about 20 km/s. This result leads to the idea of a periodic ejection of ions at the frequency of 33 kHz. Moreover, observation of light emitted in the plume shows that we have a pulsed ejection (<10  $\mu$ s) of ions followed by a silent period (20  $\mu$ s).

Measurements of DC magnitude of light intensity and RMS level of oscillation as a function of the observed position can be interpreted in term of motion of the emissive zone. This have been checked with a simple numeric code. Making some assumptions, the model calculates the DC and RMS profiles of the light intensity which would be measured in our experimental conditions for different forms and different motions of the emissive zone.

The best similitude between measurements and calculations occurs for a pulsating plasma ring whose section is represented on figure 3 & 4). The calculation find a radial and axial motion. The minimum of light intensity corresponds to a thin emissive zone (figure 4). In opposition, the maximum corresponds to a wide luminous area (figure 3).

### ELECTRIC MEASUREMENTS

#### Oscillations in nominal working conditions

The discharge current (Id, figure 7) shape is about the same as the optical signal one. The magnitude of the 33 kHz oscillation is  $\pm 3$  A.

An oscillation of  $\pm 3$  V is measured on the discharge voltage (Vd). Based of Id and Vd signals, the impedance "seen" by the plasma has been calculated in the range 0 Hz - 1 MHz. The result fits very well with an impedance calculation of the complete electric circuit. We can identify the respective influence of each component as a function of an increasing frequency : Output impedance of PPU, Magnet coils, Cf, induction of wires. For the 33 kHz oscillation, the impedance of PPU + FU is reduced to the capacity Cf. That is why a parametric test on Cf has been performed.

A common mode current (difference between anode and cathode currents) has been detected. We find a wide band ( $\sim 10$  kHz - 1 MHz) and a 33 kHz component. This circulation of AC current, which can reach 200 mA RMS, is made possible through parasitic elements, looped by the vacuum chamber structure. This has been characterised by the addition of a capacity between the cathode and the tank structure (Cx).

#### Influence of FU parameter changes

- When Cf is lower than a critical value ( $\sim 0.5$   $\mu$ F), we can observe a decrease of the thruster efficiency, coupled with a slight decrease of Id oscillations and an increase of the common mode current. In this case, the impedance seen by the 33 kHz is not capacitive, but ruled by inductive elements.

- An increase of the capacity Cf leads to a decrease of discharge voltage oscillations, whereas current oscillation magnitude is not affected by this change. We can conclude that at the frequency of 33 kHz, the plasma is equivalent to a perfect current generator, which has to be loaded by a capacity.

By the study of common mode currents and cathode floating potential, it has been shown that the common mode current flows mainly through the parasitic capacity between the cathode and the tank structure (Cx). With a low value of Cx (10 nF), the common mode current can be strongly attenuated (< 50 mA RMS), although high frequency oscillations persist.

### CONCLUSION

Measurements of plasma luminosity has allowed a characterisation in time and space of the excited species density, which is equivalent to the plasma density.

\* Professor - Groupe de Recherches sur l'Energetique des Milieux Ionisés, University of Orleans, BP. 6744, 45067 Orléans Cedex 2, France

† Graduate student - Société Européenne de Propulsion, Aérodrome de Melun Villaroche, 77550 Moissy Cramayel, France

‡ Engineer - Société Européenne de Propulsion, Aérodrome de Melun Villaroche, 77550 Moissy Cramayel, France

The relative stability of the 33 kHz oscillation, a high harmonic content and the richness of the spectrum up to 500 kHz have been highlighted. The profiles of DC and oscillating levels have made possible a reconstruction of the emissive zone shape. Moreover, a pulsating mechanism of the plasma and a pulsed ejection of ions have been suggested. Electric measurements reveal that the plasma is equivalent to a current generator oscillating at the frequency of 33 kHz in a capacitive load. Anyway, the electric response of PPU + FU to this current stimulation can be understood only by a complete circuit analyse, including in particular parasitic elements, impedance of power supplies and capacitive effects with the chamber.

#### ACKNOWLEDGEMENTS

This work is supported by CNRS, SEP and Region Centre

#### REFERENCES

Esipchuk, Morozov, Tilinin, Trofimov, "Plasma oscillations in closed-drift accelerators with an extended acceleration zone", *Sov. Phys. Tech. Phys.* Vol. 18, 7 january 1974

Characterization of Oscillations in Closed Drift Thruster", AIAA-94-3013e, June 27-29, 1994, Indianapolis

Manzella, "Stationary Plasma Thruster plume emission", IEPC-93-097, September 13-16, 1993, Seattle

Hamley, Sankovic, Petrenko, Manzella, Cartier, "The effect of power supply output characteristics on the operation of the SPT-100 Thruster", IEPC 95-241, September 19-23, 1995, Moscow

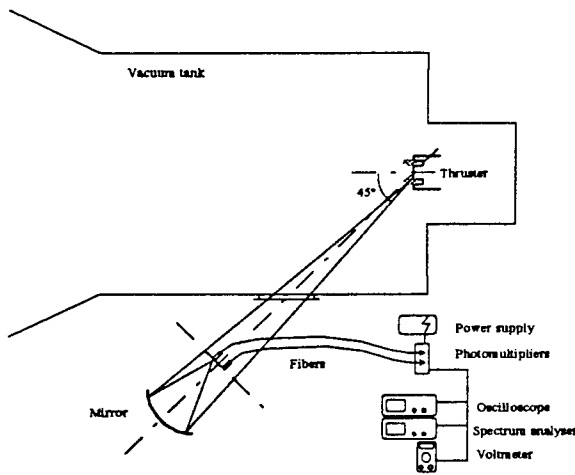


Fig. 1 : Schematic of the setup

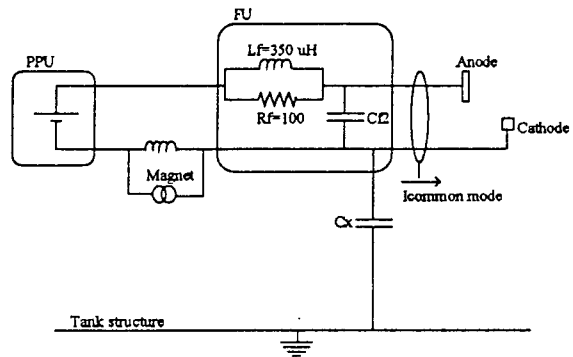


Fig. 2 : Simplified electric circuit

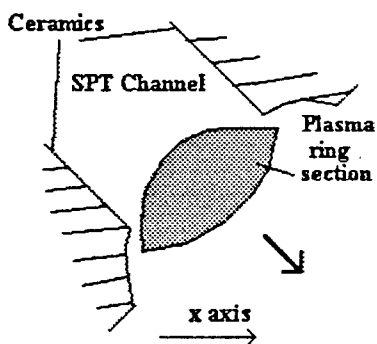


Fig. 3 : Plasma ring section (optical signal = max)

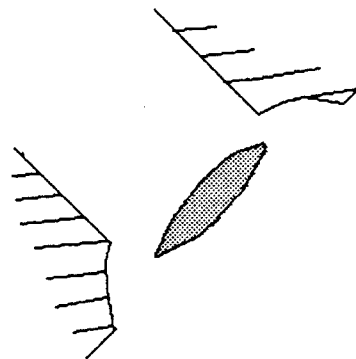


Fig. 4 : Plasma ring section (optical signal = min)

## SPT as gas-discharge device.

A.I. Bugrova, A.I. Morozov

Moscow State Institute of Radio Engineering, Electronics and Automation (MIREA), Moscow, Russia

It is known that classic discharges (arc, glow, etc.) was investigated during nearly 200 years in several countries. Physical processes in these discharges are studied sufficiently well and theory coincides with experiment. Their main features are well known: the presence anode and cathode (source of electrons) between which a voltage is applied, the main voltage drop taking place near a cathode and just here being the main ionization region, electric field in plasma column being less by several orders than in near-electrode zones and practically whole discharge current being transferred by electrons (positive ions only compensate spatial charge of electrons). Besides, plasma ionization degree is very small in such discharges and ionization processes is not by the drift velocity along the field but by high random velocities which obtained as a result of numerous elastic collisions in electric field. Electron distribution in these discharges is close to maxwellian with temperatures, usually, up to several electronvolts (1 - 10 eV). Dielectric walls restrict discharge and ion flow reflected from the walls equals zero.

SPT as the discharge device (Fig.1) has many features similar to classic discharge: there are a cathode (electron source), an anode, dielectric chamber which restricted discharge. But magnetic field transversal to electric field exists in SPT. This circumstance changes the situation in principle. The applied magnetic field increases from the anode to the cathode and is maximal near system outlet. Its magnitude is chosen so that electrons in the region where magnetic field is near maximum electrons are magnetized and ions are not magnetized (the Larmour radius of latters is much greater than system size). The characteristic feature of electric potential distribution in such a system is a presence of overthermal electric field which magnitude is determined by dynamics of electron component

$$\vec{E} = -\frac{\nabla p_e}{en} - [\vec{v}_e \vec{B}].$$

Projection of this equation on the magnetic field direction gives

$$-e \frac{\partial \phi}{\partial l} + \frac{kT_e}{n} \frac{\partial n}{\partial l} = 0$$

which means

$$\phi - \frac{kT_e(\gamma)}{n} \ln \frac{n}{n_0} = \phi^*(\gamma).$$

Here  $n_0$  is arbitrary constant. We call  $\phi^*(\gamma)$  as "thermalized" potential. It remains constant along magnetic force line  $\gamma = \text{const}$ . That is, magnetic force lines are equipotential and the change of  $\phi^*$  due to

displacement from one magnetic surface to another is set by either special electrodes or by the conductivity of plasma flow. This conductivity can be "classic" (collisions of electrons with heavy particles, ions and atoms), "anomalous" (electron scattering on fluctuations and oscillations) and "near-wall" (diffusive scattering of electrons on accelerating channel walls). Experiments revealed that electron scattering transfer due to oscillations is  $\sim 10\%$ . In the region where electrons are maximally magnetized the transfer is realized by collisions. But from ionization zone to near-anode zone the transfer is realized by near-wall conductivity. The mechanism of near-wall conductivity forecasted by A.I. Morozov [1] may be considered as classic stipulated by diffusive collisions with "big molecule", that is with wall. Such collisions lead to the loss of electron drift velocity. When electrons restore their drift velocity they move opposite electric field and increase their kinetic energy, that is are accelerated. Electrons move inside plasma volume along cycloida-like trajectories. As a result, plasma volume is divided into layers having alternated directions of electric current. Since electron flow falling on the walls is nonmonochromatic the distribution of electric current is oscillating (Fig. 2).

Electron distribution in SPT is nonmaxwellian. Its characteristic shape (Fig.3) is determined by the presence of dielectric walls and volume electric field. Mainly, near-wall fields separate the group of long living electrons rotating azimuthally as a solid body, at first approximation. The second group of electrons is so called "runaway" electrons which take part in near-wall conductivity. These electrons move opposite electric field increase their energy proportionally with passed voltage. The third, intermediate, group exists between these two main groups. Intermediate electrons collide inelastically with the wall and pass continuously from one group to another.

The change of main plasma parameters ( $n_e$ ,  $T_e$ ,  $\phi$ ) in the channel is nonmonotonous but has maximum near maximum of magnetic field. Maximum of electron temperature is nearer to the anode than density maximum which can be explained so that the main flow on ionization placed in the zone of magnetic field maximum. It is characteristically that maximum of  $T_e$  is determined by the value of first threshold of multiplication in energy dependence of secondary electron emission coefficient for wall dielectric. For dielectrics used in SPT this threshold is about 20 eV. Such high energy of electrons stimulates some unexpected phenomena: disruption of Debye layers from dielectric walls and anomalous erosion. The first phenomenon leads to oscillations of electron temperature in the discharge with maximal value  $\sim$



# One-dimensional Models of Stationary Plasma Thruster

L. Garrigues, J.P. Boeuf and L.C. Pitchford

Centre de Physique des Plasmas et Applications de Toulouse (E.S.A. 5002), UPS,  
118 route de Narbonne, 31062 Toulouse Cedex, France

## 1. Introduction

A stationary plasma thruster (SPT, or Hall Thruster) is an electromagnetic thruster whose properties make it especially suitable for applications such as satellite station-keeping. Fig. 1 represents schematically the geometry of the SPT. Xenon is injected from the anode (rate on the order of 5mg/s), at the end of the dielectric cylinders and on the cathode side, outside the cylinders. We are mainly interested here in the plasma column which is located between the coaxial cylinders (internal radius: 3 cm, external radius: 5 cm). Since the device must work under conditions of relatively low gas density (the xenon density is on the order of a few  $10^{13} \text{ cm}^{-3}$  close to the anode), and the length of the column is on the order of a few cm (typically 4 cm), the electrons undergo very few collisions from the cylinder entrance, on the cathode side, to the anode and it would not be possible to sustain a plasma in the column without enhancing the confinement of the electrons. This confinement is provided by a magnetic field created by coils which are located on the external surface of the cylinder. The magnetic field is radial in the exhaust region (cathode side of the cylinders), and on the order of 200 G at the exhaust and ten times less at the anode). The potential drop in the plasma column can be as large as 200 to 300 V in standard conditions.

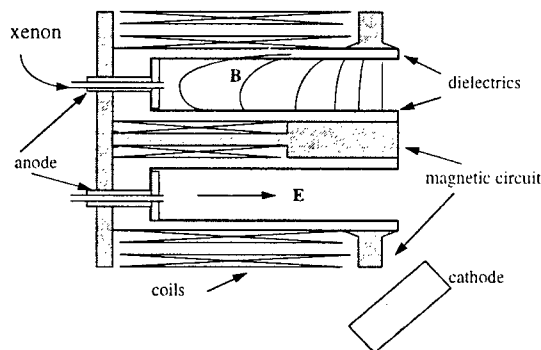


Figure 1: Schematic of the SPT geometry.

## 2. Physical description

Several features of the SPT are not well understood. One of them is the conductivity of the column which is much higher than what could be expected from the classical collisional conductivity in a transverse magnetic field. The collisional electron mobility perpendicular to a magnetic field line is given by:

$$\mu_c = \frac{e}{mv} \frac{1}{1 + \frac{\omega_B^2}{v^2}} \quad (1)$$

where  $v$  is the electron collision frequency and  $\omega_B$  the electron cyclotron frequency  $\omega_B = eB/m$ .

Assuming an electron mobility of this form, the order of magnitude of the current flowing through the device can be estimated by  $J_T \approx en\mu_e E$  where  $n$  is the plasma density and  $E$  the electric field in the column. The Plasma density and electric field in the column can be estimated from experimental measurements and are on the order of  $10^{12} \text{ cm}^{-3}$  and 50 V/cm, respectively. Calculating the current from this estimation of the plasma parameters and mobility gives the results represented in Fig. 2.

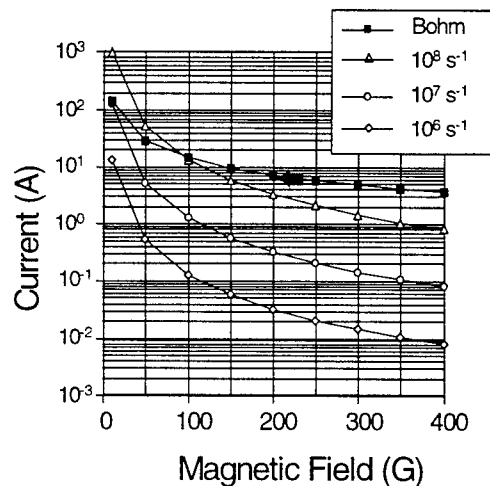


Figure 2: Estimated current in a SPT for typical conditions and different values of the electron collision frequencies using a classical mobility (open symbols - Eq. 1), and assuming anomalous Bohm conductivity (full symbols). The arrow represents a typical current measurement under these conditions.

The typical electron-neutral collision frequency in the SPT is in the  $10^6$ - $10^7 \text{ s}^{-1}$  range and is much too small to be responsible for the large measured conductivity. Assuming [1] anomalous Bohm conductivity (i.e. conductivity due to field fluctuations, with an electron mobility of the form  $\mu_c \approx \frac{1}{16B}$ ) gives a current in better agreement with experimental measurements. However it has not been clearly established that Bohm diffusion plays an important role in this device and the Russian

school of Morozov *et al.* have proposed another interpretation of the observed anomalous conductivity [2]. They point out that electron collisions with the dielectric walls and secondary electron emission by electron impact could be responsible for the observed conductivity. The collisions frequency of electrons with the walls is on the order of  $10^8$  cm/s, which gives an electron mobility in the correct range - see Fig. 2. Other features of the SPT are far from being clearly understood. For example it seems that under standard operating conditions, the current through the plasma and voltage across the column undergo oscillations at frequencies from kHz to MHz with those in the kHz range being of large amplitude.

### 3. One-dimensional models

We have developed a simple 1D quasi-neutral hybrid model of the column. In this model the plasma is supposed to be quasi-neutral, i.e. the electric field distribution is not obtained from Poisson's equation but from a current equation. Ions are supposed to be collisionless and are described by a 1DIV (one dimensional in position and one dimensional in velocity) Vlasov equation with an ionization source term due to electron-neutral collisions. Electrons are supposed to be collisional and are simply described by a mobility limited current density, the mobility being the classical collisional mobility (taking into account collisions with walls) or a Bohm mobility. The electron energy distribution function is supposed to be Maxwellian and the electron temperature is given by a semi-empirical energy equation. The neutral atoms are all supposed to have the same velocity  $v_0$  and to be lost in electron impact ionization events. A Monte Carlo simulation of the electron trajectories has been developed and can also be used to obtain a better estimation of the electron energy and ionization frequency [3].

The equations were solved for a steady state situation. Since this system is strongly non-linear the system was solved iteratively, using an underrelaxation method. Shown in Fig. 3 are the axial variations of the neutral and plasma densities for typical conditions of the SPT.

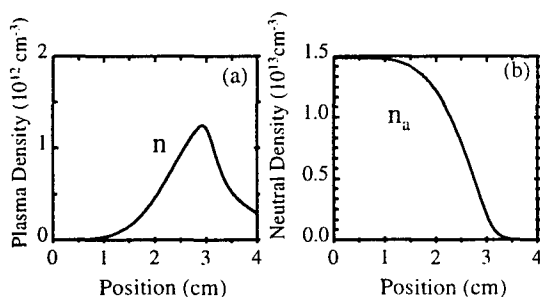


**Figure 3:** Axial variation of (a) plasma density, (b) neutral density.

The physical quantities obtained from the model are in good qualitative agreement with the measurements [4].

As mentioned above there is experimental evidence that large amplitude oscillations (20 kHz) of the current and voltage across the plasma column exist in the SPT even under normal operating conditions [5].

We have therefore looked for transient solutions of the set of equations described above. These transient solutions exhibit systematic oscillations at a frequency on the order of 100 kHz. The ion current displayed in Fig. 4 exhibits large amplitude oscillations in typical conditions.

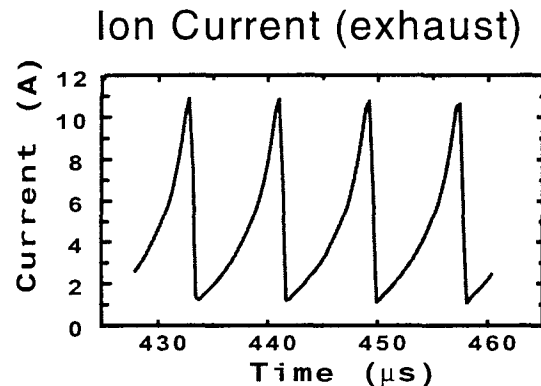


**Figure 4:** Time evolution of the ion current at the exhaust showing strong oscillations at a frequency on the order of 100 kHz.

### 4. Conclusion

Although more work is still needed to improve our understanding of the intricate physical mechanisms involved in a Stationary Plasma Thruster, some of the properties and characteristics of this device have been successfully (qualitatively) reproduced with simple models. Detailed comparisons with experiments will help us adjust and improve the assumptions of the models.

### 5. Acknowledgments

This work is supported by the GDR CNES-CNRS « Propulsion Plasma pour Vols Spatiaux ».

### 6. References

- [1] H.R. Kaufman, R.S. Robinson, J. Spacecraft, **18** (1981) 470.
- [2] A.I. Morozov, Yu.V. Esipchuk, A.M. Kapulkin, V.A. Nevroskii, V.A. Smirnov, Sov. Phys. Tech. Phys., **18** (1973) 615.
- [3] L. Garrigues, J.P. Boeuf, L.C. Pitchford, XXIII ICOPS Conf. Proceedings, Boston, (1996) 160.
- [4] G. Guerrini, A.N. Vesselovzorov, M. Bacal, I.B. Pokrovsky, Rev. Sci. Instrum., **67** (1996) 990.
- [5] GDR « Propulsion Plasma pour Vols Spatiaux » research reports, (1996), unpublished results.

# Argon metastable density in Ar-O<sub>2</sub> and Ar-TEOS helicon plasmas.

L. Le Brizoual, A. Granier, Ph. Briaud

Laboratoire des Plasmas et des Couches Minces, IMN, CNRS-Université de Nantes

2 rue de la Houssinière, BP 32229, 44322 Nantes cedex 3, France

E-mail : Laurent.LeBrizoual@cnsr-immn.fr

## 1. Introduction

The deposition of thin films by plasma generally involves mixtures of gases, which often contain an important fraction of argon. The important role of argon 1s<sub>5</sub> and 1s<sub>3</sub> metastable states which energy is 11.5 eV was demonstrated in different low pressure deposition processes [1,2]. Indeed they are able to dissociate or ionize the deposition precursors. Different experimental and modelling determinations of their density were recently developed. This study is devoted to the measurement of their density [Ar<sup>M</sup>] in a low pressure helicon diffusion plasma created in Ar/O<sub>2</sub> and Ar/TEOS (tetraethoxysilane) mixtures. The variations of [Ar<sup>M</sup>] as functions of the rf power and the oxygen fraction in Ar/O<sub>2</sub> mixtures will be investigated. Moreover we will try to measure if there is an efficient reaction between TEOS molecules and argon metastable states, or in other words if Ar<sup>M</sup> are able to dissociate the TEOS molecule.

## 2. Experimental setup

The helicon reactor used for deposition of thin films from organosilicon vapor precursor is made of the helicon source and the diffusion chamber where the substrate is positioned and where most diagnostics of the plasma are carried out. A more complete description of the reactor can be found in [3]. In this study, plasmas are created in Ar/O<sub>2</sub> and Ar/TEOS mixtures. The total pressure and gas flow rate are fixed at 5 mTorr and 18 sccm respectively. The rf power is varied up to 400 W. The light emitted by the plasma is collected by an optical fiber at mid height of the diffusion chamber and analyzed by a HR 460 monochromator equipped with a 1200/mm grating and a Hamamatsu 928S photomultiplier.

## 3. Self absorption technique

The self absorption method [4] consists of measuring the ratio of two emission lines, which are self absorbed. There are two possibilities to choose the couple of spectral lines : either they decay on the same metastable state from upper levels with very different oscillator strength or they originate from the same upper level, one of them arriving on a radiative state, the other one on the metastable state. We have chosen the second approach, using the 800.6 nm (2p<sub>6</sub> → 1s<sub>4</sub>) and 763.5 nm (2p<sub>6</sub> → 1s<sub>5</sub>) Ar lines, where the 763.5 line is self absorbed. This choice allows us eliminate some populating effect when the plasma conditions change, because the two lines come from the same level.

This simple method can be used as long as the 800.6 nm line is not self absorbed, e.g. the density of the 1s<sub>4</sub> level can be neglected. Then the intensity ratio I<sub>763.5</sub>/I<sub>800.6</sub> is a function of K<sub>0</sub>ℓ where ℓ is the optical depth in the plasma and K<sub>0</sub> is the absorption coefficient of the 763.5 line for a gaussian profile in a homogeneous medium. Finally the metastable density is given (in SI units) by :

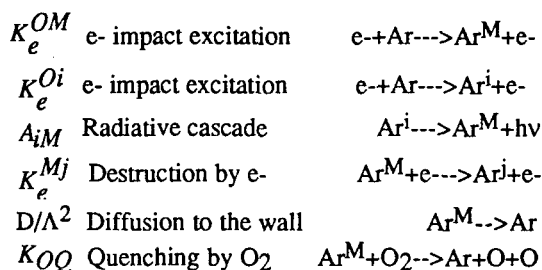
$$[Ar^M] = 1.363 \cdot 10^7 \frac{K_0 \sqrt{T}}{f \lambda}$$

where T = 300 K is the gas temperature, λ = 763.5 nm, and f denotes the oscillator strength.

## 4. Experimental results and discussion

In figure 1, the metastable density measured in pure Ar and different Ar-O<sub>2</sub> mixtures is plotted as a function of the rf power. As expected, whatever the rf power, the metastable density decreases as the O<sub>2</sub> fraction increases. This can be the consequence of different processes : the quenching of Ar<sup>M</sup> by oxygen molecules, the decrease of Ar partial pressure, variations of the electron density. To circumvent the variations due to Ar partial pressure the metastable to ground state argon concentration ratio has been plotted in figure 2.

In order to further interpret these results we consider the following kinetics for Ar<sup>M</sup> :



which yields the following relation :

$$[Ar^M] = [Ar] \frac{n_e (K_e^{OM} + \sum \frac{A_{iM}}{\sum A_{ij}} K_e^{Oi})}{n_e \sum K_e^{Mj} + [O_2] K_{OQ} + D/\Lambda^2}$$

First of all, let us note that the electron density increases with the rf power, typically ranging from a few 10<sup>9</sup> cm<sup>-3</sup> at 50 W to a few 10<sup>10</sup> cm<sup>-3</sup> at 400 W. Moreover, n<sub>e</sub> is two times higher in Ar than in O<sub>2</sub> [3].



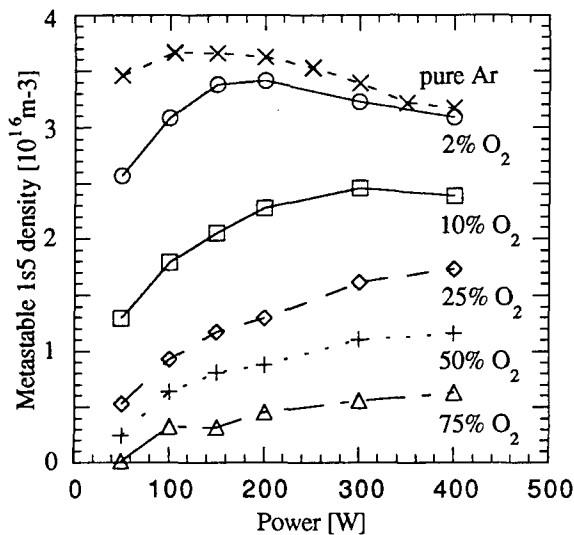


Fig. 1 : Metastable density as a function of the rf power.

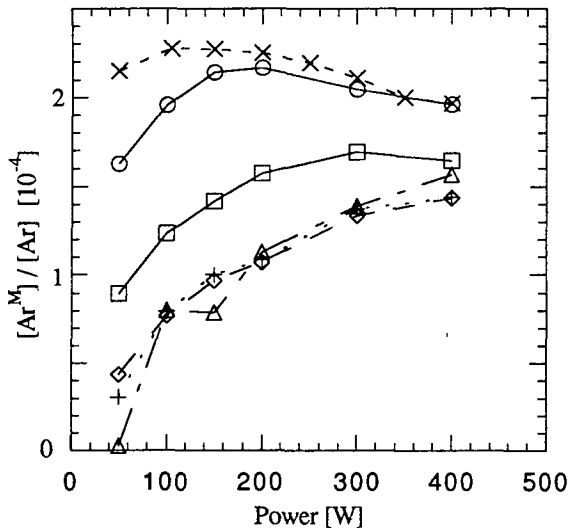


Fig 2 : Metastable density normalised to argon density (calculated at 300K) : same symbols as in Fig. 1

The first information given by figure 1 is that  $[Ar^M]$  and  $n_e$  are of comparable magnitude. Second, from the above expression of  $[Ar^M]/[Ar]$  two limit behaviours can be expected :

- (i) at low electron density (i.e. low rf power), as far as  $Ar^M$  is mainly lost by diffusion and/or quenching by  $O_2$ , it is expected to be proportional to  $n_e$ .
- (ii) at high rf power it saturates at a limit value equal to the ratio of metastable production and destruction terms by electron collisions.

As can be seen in Fig. 2, the variations of  $[Ar^M]/[Ar]$  are quite different according to the composition of the  $Ar/O_2$  mixture. In pure argon the saturation limit is obtained from low rf powers. In contrast, in oxygen rich mixtures  $[Ar^M]/[Ar]$  increases with  $n_e$  without reaching the saturation limit at 400 W.

This can be explained by the increase of the  $Ar^M$  loss by  $O_2$  quenching which is never negligible as compared to the electron destruction term under our rf power range.

On the other hand, in the case of pure Ar, above 150 W, the metastable density decreases slowly as the rf power increases. Several interpretations are possible : an increase in the gas temperature with the rf power, a variation of the electron temperature or some error inherent to the simple absorption method used.

To investigate this latter point, the self absorption of the 800.6 nm Ar line was estimated. In fact if the density of  $1s_4$  level becomes greater than  $2 \cdot 10^{15} m^{-3}$ , the 800.6 nm self-absorption can no longer be neglected. To take it into account the intensities of other Ar lines were measured. Three ratios are considered :  $I_{7635}/I_{8006}$ ,  $I_{8014}/I_{8424}$ ,  $I_{7067}/I_{7383}$  where the 763.5, 801.4, 706.7 nm lines arrive on the metastable  $1s_5$  level and the 800.6, 842.4, 738.3 nm lines arrive on the radiative level. We just have to find a couple  $([Ar^M], [Ar1s_4])$  consistent with the three line ratios. The highest density of  $1s_4$  radiative level is about  $2 \cdot 10^{15} m^{-3}$ , which validates the use of the simple method. Neglecting the 800.6 nm self-absorption only yields slightly underestimated metastable densities.

The other possible explanation of this decrease is that the EEDF changes above 150W, and loss processes with cold electron become greater. This might be consistent with the evolution of  $T_e$  measured by langmuir probes [3].

To conclude, the experimental variations of the Ar metastable density in  $Ar/O_2$  mixtures are well described by a simple kinetic model. Further developments of this kinetic scheme are in progress.

In  $Ar/TEOS$  mixtures preliminary experiments exhibit a decrease in  $[Ar^M]$  as a few per cent TEOS is added to argon. The drops in  $[Ar^M]/[Ar]$  measured in  $Ar/O_2$  and  $Ar/TEOS$  are of comparable magnitude. Further experiments and simulations are in progress in order to estimate the quenching rate of  $Ar^M$  by TEOS.

## Conclusion

The argon metastable density has been measured in  $Ar-O_2$  and  $Ar/TEOS$  helicon reactors for different rf powers. By adding  $O_2$  to Ar, a decrease in  $[Ar^M]$  occurs due to their quenching by  $O_2$  especially at low rf power. At high rf power their quenching by electrons seems to be higher than their quenching by  $O_2$ .

## References

- [1] Trennepohl W. Jr., Bretagne J., Gousset G., Pagnon D. and Touzeau M. : Plasma Sources Sci. Technol., 5 (1996) 607-621
- [2] Etemadi R., Godet C. and Perrin J. : Le vide : science, technique et applications, 275 (1995) 77-80
- [3] Granier A. et al. submitted to Plasma Sources Sci. Technol.
- [4] Jolly J, Touzeau M : J. Quant. Spectrosc. Radiat. Transfer., 15 (1975) 863-872

# Emission spectra of O<sub>2</sub>/TEOS plasmas used for SiO<sub>x</sub>C<sub>y</sub>H<sub>z</sub> deposition

A. Granier, L. Mage, F. Nicolazo, P. Raynaud, Y. Segui, G. Turban, C. Vallée, M. Vervloet

GDR 1136 Procédés de dépôts de couches minces par plasmas d'organosiliciés  
2 rue de la Houssinière, BP 32229, 44322 Nantes Cedex 3, France  
e-mail : Agnes.Granier@cnrs-imn.fr

## 1. Introduction

Plasmas of oxygen/tetraethoxysilane mixtures (O<sub>2</sub>/TEOS) are widely used for the deposition of thin SiO<sub>x</sub>C<sub>y</sub>H<sub>z</sub> films which are utilized as insulating, optical or barrier films. Although the properties of the deposited films have been investigated in the literature, very few studies were devoted to the plasma phase. Here we present the optical emission spectra of O<sub>2</sub>/TEOS plasmas recorded in the 180-850 nm range. First of all the emission spectra recorded in a low pressure helicon diffusion plasma are studied as a function of the oxygen fraction in the O<sub>2</sub>/TEOS mixture. Second, they are compared to the emission spectra from a DECR plasma.

## 2. Experimental

The low pressure rf helicon reactor used to create plasmas in mixtures of oxygen and vapour of tetraethoxysilane (Si-(O-C<sub>2</sub>H<sub>5</sub>)<sub>4</sub>) is described in detail in [1]. It is operated at 2 mTorr, 300 W with a fixed total gas flow rate of 16 sccm. The light emitted by the plasma is transmitted to a 46 cm focal length monochromator (JY HR460) by an optical fibre positioned at mid height of the diffusion chamber. The monochromator is equipped with two gratings (a 2400 g/mm grating used in the 180-420 nm spectral bandwidth and a 1200 g/mm one used in the 420-850 nm spectral range), and a 928S Hamamatsu photomultiplier. The acquisition of spectra is monitored by a PC computer and the SpectraMax software. Under standard acquisition conditions the resolution was 0.3

nm, but resolution of 0.1 nm was achieved in order to identify unambiguously the multiple structures present in the emission spectra.

## 3. Emission spectrum

The spectra are dominated by the emissions of a few strong atomic lines or molecular systems but below these dominating features very complex structures can be observed. A typical spectrum of an O<sub>2</sub>/TEOS plasma in the UV range which was seldom investigated, is shown in figure 1. Almost all the measurable features have been identified using the Pearse and Gaydon tables [2]. The emitting species depend on the oxygen content in the O<sub>2</sub>/TEOS mixture. The main results are the followings :

(i) in an oxygen rich mixture, typically for an oxygen percent higher than 50 % all the identified structures can be attributed to CO, CO<sup>+</sup>, CO<sub>2</sub><sup>+</sup>, OH, O, H and C. Details on the corresponding transitions are given in table 1. Although relatively weak, seven systems of CO are unambiguously identified, most of them appearing in the UV range.

(ii) as the TEOS fraction is increased, the emission from oxygen atoms decrease, while new systems from CH, C<sub>2</sub> and H<sub>2</sub> appear.

(iii) in pure TEOS plasmas, the emission from oxygen atoms completely vanishes. The emission from H<sub>2</sub> is identified by a spectrum of isolated lines (denoted the secondary spectrum) in all the visible range, which

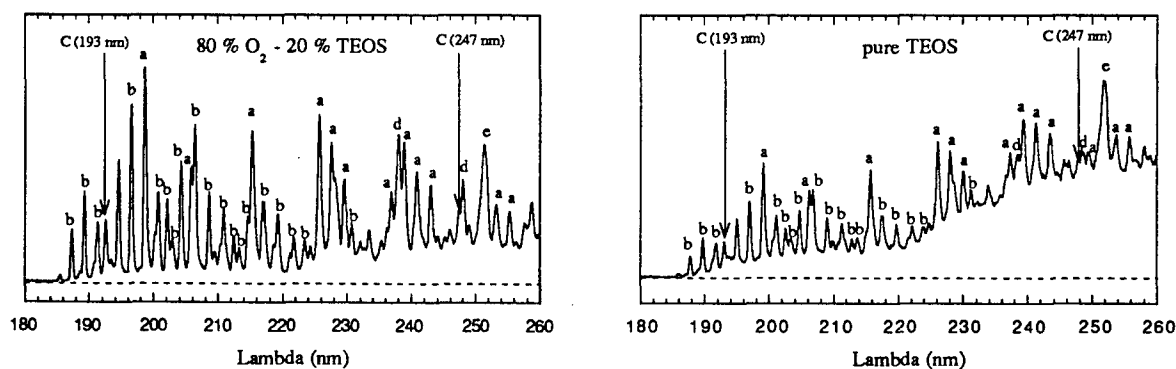


**Figure 1 :** UV Optical Emission Spectra (180-260 nm) of O<sub>2</sub>/TEOS helicon plasmas created at 2 mTorr - 300 W  
letters a,b,c,e denotes the following systems of CO : a : Cameron bands, b : fourth positive system,  
d : 3A bands, e : Kaplan bands

	Transition	System name	Spectral range (nm)
CO	$A^1\Pi \rightarrow X^1\Sigma$	4 <sup>th</sup> positive syst.	180-255
	$a^3\Pi \rightarrow X^1\Sigma$	Cameron bands	206-258
	$b^3\Sigma \rightarrow a^3\Pi$	5B system	266-383
	$b^3\Sigma \rightarrow a^3\Pi$	3 <sup>rd</sup> positive syst.	283-370
	$c^3\Pi \rightarrow a^3\Pi$	3A bands	271-230
	$d^3\Delta \rightarrow a^3\Pi$	Triplet bands	401-647
		Kaplan Bands	275-252
	$B^1\Sigma \rightarrow A^1\Pi$	Ångstrom syst.	451-608
	$a^3\Sigma \rightarrow a^3\Pi$	Asundi bands	575-800
CO <sup>+</sup>	$B^2\Sigma \rightarrow X^2\Sigma$	1 <sup>st</sup> negative syst.	219-255
	$A^2\Pi \rightarrow X^2\Sigma$	Comet-tail syst.	309-640
CO <sub>2</sub> <sup>+</sup>	$A^2\Sigma^+ \rightarrow X^2\Pi$	Bands $\lambda\lambda 2883$ and 2896	288.3 289.6
OH	$A^2\Sigma^+ \rightarrow X^2\Pi$	3064 Å syst.	281-309
CH	$A^2\Delta \rightarrow X^2\Pi$	4300 Å syst.	431.4
C <sub>2</sub>	$A^3\Pi \rightarrow X^3\Pi$	Swan syst.	516.5
H <sub>2</sub>		Secondary spect.	406-835

Table 1 : List of the molecular systems identified in the helicon O<sub>2</sub>/TEOS plasma

are the strongest lines from the opened rotational structure of H<sub>2</sub>. The most intense and isolated one appears at 752 nm. Moreover, as can be seen in figure 1-b some continuous emission appears between 200 and 300 nm, under the emission of the different systems of CO. This continuous emission is attributed to H<sub>2</sub> [3].

(iv) whatever the O<sub>2</sub>/TEOS mixture and rf power, no emission from Si, SiO, SiH (which main lines or systems are expected at 288, 229.9 and 414.2 nm respectively) was seen. Similar observations were previously reported in different O<sub>2</sub>/TEOS plasmas by several authors [4-6]. To our knowledge, Tochitani [7] was the only one to observe the silicon atomic lines at 288.1 and 254 nm in a low frequency discharge.

(v) although most of the structures are unambiguously identified, some of them could not be assigned to any emitting species : an example is a structure lying between 460 and 470 nm which appears whatever the TEOS fraction.

#### 4. Comparison to the spectra emitted in a O<sub>2</sub>/TEOS DECR plasma

The emission spectra of O<sub>2</sub>/TEOS helicon and DECR plasmas are compared. In the DECR reactor the

emission spectra were recorded in the 240-500 nm range using a 32 cm focal length monochromator and a 1200 g/mm grating. Optical emission spectrometry was performed in pure TEOS and different O<sub>2</sub>/TEOS DECR plasmas created at 1 mTorr, 200 W [4], e.g. under pressure and power conditions close to those of the helicon plasma.

The same species emitting in this reduced spectral range were identified in both spectra. The general trends relative to O, CH emission as a function of the oxygen content are quite similar. Nevertheless, the importance difference lies in the emission of CO<sup>+</sup> ions : the CO<sup>+</sup> Comet tail system is very intense in the DECR spectrum, whereas it remains very weak and mixed to neutral CO triplet bands in the helicon plasma. This difference certainly traduces the fact that the electron density in the DECR plasma is about 10 times higher in the DECR than in the helicon diffusion plasma (typically a few 10<sup>11</sup> cm<sup>-3</sup> against a few 10<sup>10</sup> cm<sup>-3</sup> in pure oxygen plasmas).

#### 5. Conclusion

In both reactors, the emission from CO and/or CO<sup>+</sup> in pure TEOS plasmas suggests that CO is directly created by fragmentation of the TEOS molecule by electron collision. This is in pretty good agreement with the measurements by infrared absorption spectroscopy carried out in the DECR plasma, which prove the presence of stable CO and CO<sub>2</sub> molecules in TEOS plasmas [8]. In O<sub>2</sub>/TEOS mixtures, CO and CO<sub>2</sub> are also formed from oxidation of the growing film by oxygen atoms. The absence of emission from any Si containing species is attributed to the fact that the Si-(O-C<sub>2</sub>H<sub>5</sub>)<sub>n</sub> (n<4) fragments are incorporated into the growing film before all the Si-O bonds are broken.

#### References

- [1] A. Granier, F. Nicolazo, C. Vallée, A. Goullet, G. Turban and B. Grolleau, submitted to Plasma Sources Sci. and Technol.
- [2] R.W.B. Pearse and A.G. Gaydon, The identification of molecular spectra, 4<sup>th</sup> edition (Chapman and Hall, London, 1984)
- [3] M. Shimozuma, G. Tochitani and H. Tagashira, J. Appl. Phys. **70** (1991), 645
- [4] M. Latreche, Y. Segui, R. Delsol and P. Raynaud, Proceedings of 11th ISPC Loughborough UK, (1993), 1284
- [5] F. Fracassi, R. d'Agostino and P. Favia, J. Electrochem. Soc. **2636** (1992), 139
- [6] S. Wickramanayaka, A. Matsumoto, Y. Nakanishi, N. Hosokawa and Yoshinori Hatanaka, Jpn. J. Appl. Phys. **33** (1994) 3520
- [7] G. Tochitani, M. Shimozuma and H. Tagashira, J. Vac. Sci. Technol. A **11** (1993), 400
- [8] P. Raynaud, C. Marlière, Y. Segui and G. Durand, this conference

## Helicon plasmas in various magnetic field configurations.

O.V. Braginskiy, A.S. Kovalev, D.V. Lopaev, A.N. Vasilieva.

Inst of Nuclear Physics, Moscow State University, Moscow, 119899, Russia.

### 1. Introduction.

The helicon radio-frequency sources provide the generation of high-density plasma at low pressure and relatively weak magnetic field. They have good perspective for application in plasma processing in submicron technology. Many experimental [1,2] and theoretical [3,4] studies have been devoted to the mechanism of high ionization efficiency and helicon wave absorption, but this mechanism still remains inconclusive. According to the theoretical investigations of helicon discharge the plasma density have to be sensitive to the magnetic field configuration. In the present paper we study the change over plasma characteristics at the formation of helicon waves for various configurations of magnetic field.

### 2. Experiment.

The plasma source consist of 15 cm in diameter and 40 cm long glass tube surrounded by two loops helicon antenna 17 cm long. Both are surrounded by two coils creating dc magnetic field. The diameter of coils is 24 cm, distance between them 25 cm. The tube is attached to the stainless steel chamber 26 cm in diameter and 25 cm in length. The chamber is surrounded by additional magnetic coil to reduce the divergence of magnetic field on the distance from the source. The rf (13.56 MHz) power is delivered by a 700 W generator and matching network.

The multy-grids electrostatic ion energy analyzer is used to measure the ion current and ion energy. Lengmuir probe is used for determination of plasma potential and electron density. Both are placed on the axis of diffusion chamber at the distance 30 cm from center of plasma.

Two configurations of magnetic field have been studied in our experiments. First-"uniform"-the magnetic fields of both coils are identically directed and create the axial and uniform magnetic field in discharge volume. Second-"trap"- the magnetic fields of two coils are contrary directed and create the configuration like to magnetic trap. The currents of magnetic coils in both magnetic field configurations are equal.

### 3. Experimental results.

The values of positive ion current  $I_p$  obtained in an Argon plasma at the pressure 3 mTorr are presented in figure 1. The curve 1 corresponds to capacitive mode of discharge in absence of magnetic field. The curves 2 and 3 represent behavior of  $I_p$  for "uniform" and "trap" configurations at the magnetic field value  $H=30$  Gs. The curves 4 and 5 are the same at 60 Gs. One can see the passage from the capacitive to helicon discharge modes occur between 150 and 400 W of rf power. It depends

on value and configuration of magnetic field. This passage is indicated by the sharp increasing of  $I_p$ . One can see the values  $I_p$  for the "trap" configuration of magnetic field essentially exceed values  $I_p$  for the "uniform" configurations at the same values of rf power.

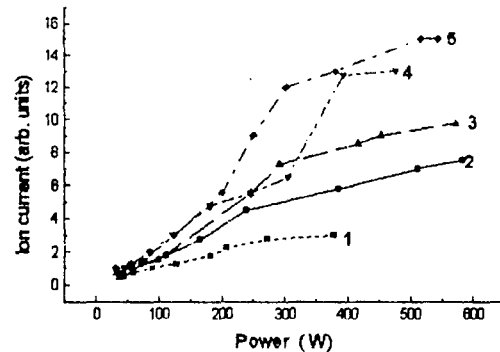


Fig.1 Ion current as a function of rf power: 1-  $H=0$ ; 2,4-"uniform" configuration, 2- $H=30$  Gs, 4-  $H=60$  Gs 3, 5- "trap" configuration, 3-  $H=30$  Gs, 5-  $H=60$  Gs

Fig.2 shows the decrease of plasma potentials at the transition between capacitive and helicon discharges. It is clear the plasma potentials are the same for both magnetic field configurations after transition to the helicon discharge.

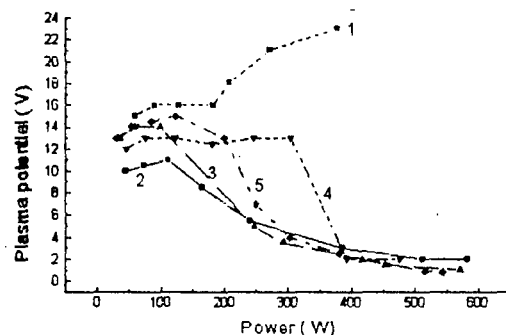


Fig.2 Plasma potential as a function of rf power. 1-  $H=0$  2, 4- "uniform" configuration, 2-  $H=30$  Gs, 4-  $H=60$  Gs 3, 5- "trap" configuration, 3-  $H=30$  Gs, 5-  $H=60$  Gs

Fig. 3 shows the variations of mean ion energy for both magnetic field configurations at  $H=30$  Gs and  $H=60$  Gs. One can see the ion energy increases sharply at the transition between capacitive and helicon discharge. After transition the ion energy at the "trap" configuration exceeds the ion energy at the "uniform" configuration of magnetic field.

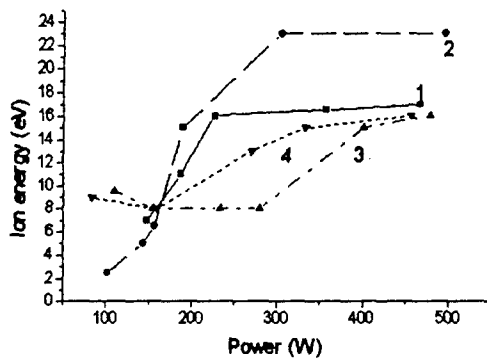


Fig. 3 Ion energy as a function of rf power.

1, 3- "uniform" configuration, 1-  $H=30$  Gs, 3-  $H=60$  Gs  
2, 4- "trap" configuration, 2-  $H=30$  Gs, 4-  $H=60$  Gs

The electron concentrations as a function of applied rf power is presented on figure 4. Electron concentrations increases at the transition between the capacitive and helicon discharge for both magnetic field configurations. After transition the increase of electron concentration terminates for "uniform" configuration, but keeps on for "trap" configuration.

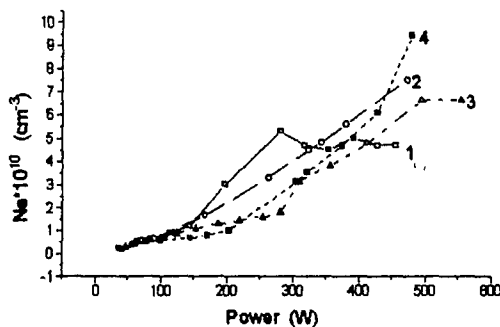


Fig. 4 Electron density as a function of rf power.

1, 3- "uniform" configuration, 1-  $H=30$  Gs, 3-  $H=60$  Gs  
2, 4- "trap" configuration, 2-  $H=30$  Gs, 4-  $H=60$  Gs

Radial distributions of ion current have been investigated for both magnetic field configurations and radial uniformity was similar in both cases.

#### 4. Conclusion.

We have investigated the plasma parameters of helicon discharge in two essentially different magnetic field configurations. In "uniform" (axial and uniform magnetic field) the plasma parameters behavior is in agreement with the results of other investigators [1]. For example the sharp grows of plasma density at the transition between capacitive and helicon discharge terminates on some  $N_e$  (Fig. 4, curve 1,3). This  $N_e$  is approximately within the gap between  $N_{min}$  and  $N_{max}$ .

where the helicon waves at our magnetic field value and antenna length can exist [4].

In contrast for the "trap" (magnetic fields of coils are opposite directed) configurations the existence of helicon waves is doubtful at all. Nevertheless one can see the plasma parameters are the same ones in "uniform" configuration. However there is no termination of electron density growth after transition between capacitive and helicon discharge.

Notice that the ion current value and electron density in "trap" configuration exceed the ones in "uniform" configuration. So the "trap" configuration can be sometime preferable.

#### 4. References.

- [1] A.J. Perry, D. Vender, R.W. Boswell: J. Vac. Sci. Technol., **B9** (2), (1991), 310.
- [2] K. Nakamura, K. Suzuki, H. Sugai: Aust. J. Phys., **48**, (1995), 461.
- [3] F.F. Chen: Plasma Phys. Control. Fusion, **33**, (1991), 339.
- [4] K.P. Shamrai, V.B. Taranov: Plasma Sources Sci. Technol. **5**, (1996), 471

## Investigation of small, closed electron drift, SPT-50.

G. Guerrini, C. Michaut, A.N. Vesselovzorov\*, M. Dudeck and M. Bacal

*Laboratoire de Physique des Milieux Ionisés, Laboratoire du C.N.R.S  
Ecole Polytechnique, 91128 Palaiseau Cedex, France*

### I. INTRODUCTION

Recent work<sup>1,2</sup> indicates interest in light controlled satellites, equipped with a low power electric thrusters. This work suggests that one of the most promising thrusters for these satellites can be the Hall-type thruster, which is widely used at present on satellites with 1 kW power on board<sup>3</sup>. The main advantages of the Hall-type thruster are the high thrust and energetic characteristics, an acceptable lifetime, simplicity and reliability of its design. In the meantime the first experiments with Hall-type (or stationary plasma thruster, SPT) of small power and also small size have shown that with the reduction of size the thrust and energetic characteristics go down considerably<sup>1</sup>. The purpose of this work is to study the essential mechanisms in small size SPT in order to identify the main processes lowering the level of SPT characteristics when the thruster size is reduced, and optimize small SPT design. In an earlier work, we have studied a very small thruster SPT-20<sup>4</sup>.

### II. THE TEST FACILITIES AND THE EXPERIMENTAL THRUSTER.

The SPT-50 thruster is studied in a test facility consisting of a horizontal, cylindrical stainless steel chamber (0.8 meter in diameter and 2 meters long). This facility is equipped with a cryogenic pumping system. Its pumping speed is 8000 l/s for air (with a residual gas pressure of  $3 \times 10^{-7}$  mbar). For a mass flow rate of 1 mg/s of the working gas (Xenon), the pressure in the chamber is  $5 \times 10^{-5}$  mbar.

Figure 1 shows schematically the experimental Hall-type thruster SPT-50 studied at Ecole Polytechnique. A coaxial discharge chamber is located in a magnetic field generated by the four outer and one inner coils. The main dimensions of the discharge chamber are: the outer diameter is 50 mm, the inner diameter is 28 mm and the distance between the anode and the channel exit is 25 mm. The magnetic system to produce an essentially radial magnetic field includes a soft iron magnetic circuit made of a back flange, and the two poles: the inner pole (a rod) and the outer, ring-shaped, pole. The gas, Xenon, is injected from the back end of the channel via a ring-shaped dispenser. The ring-shaped anode was fixed on the external ceramic wall of the channel. The cathode-neutralizer was a hollow cathode using LaB<sub>6</sub>.

The structure of magnetic field has been studied using a Hall probe<sup>5</sup>. In the region of acceleration the obtained magnetic field has the typical for SPT lens-type structure. The magnetic field lines are not exactly

perpendicular to the axis, therefore the magnetic field is not purely radial, but has an axial component  $B_z$ . The maximum magnetic field  $B_r^{\max}$  is located just before the channel exit.

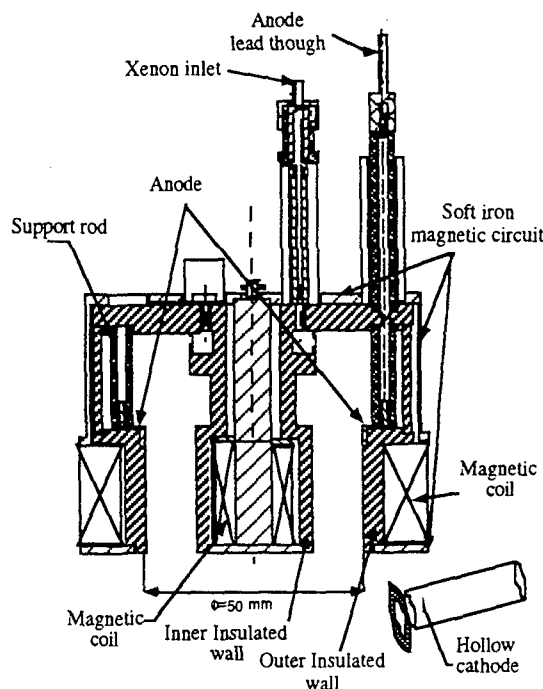


FIG 1 : Description of the SPT-50 thruster studied at Ecole Polytechnique.

The thrust was measured at RRC Kurchatov Institute, using a thrust scale, designed on the principle of a torsion scale with reaction. This scheme ensures a fixed position of the thruster in space during the measurement of thrust, which eliminates the effect of the rigidity of current and gas leads on the accuracy of the thrust measurement. The ion current was measured, at Ecole Polytechnique, on a metal target: 30 cm in diameter biased to -30 V located at a distance of 35 cm from the exit of the thruster.

### III. ENERGETIC EFFICIENCY AND THRUST.

Figure 2 presents the variation with the gas flow of the thrust and the thrust efficiency. Note that at constant discharge voltage and magnetic field, the thrust dependence is linear for values  $V_d = 300$  V and  $B_r^{\max} \approx 170$  Gauss. The thrust efficiency increases

until the flow rate attains 1 mg/s and then saturates at 0.44.

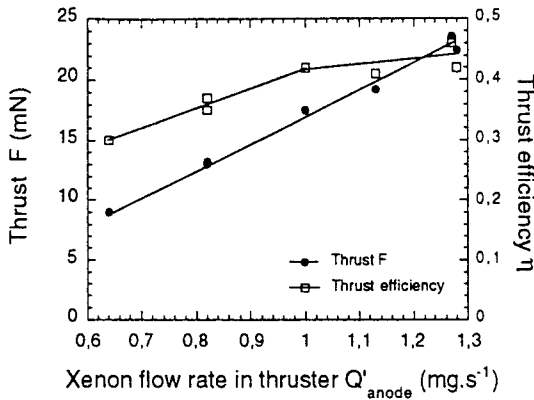


FIG 2 : Dependence on the gas flow of the thrust and thrust efficiency. The discharge voltage was 300 V and the optimal radial magnetic field value is 170 Gauss.

Figure 3 shows the variation with the discharge voltage of the thrust and the thrust efficiency. The mass flow rate was 1 mg/s and  $B_r^{\max} = 170$  Gauss. For comparison, we also plotted the thrust efficiency of SPT-20<sup>4</sup>.

The thrust increases with the discharge voltage and reaches 19 mN at a discharge voltage of 350 V. The thrust efficiency also increases with the discharge voltage from 0.18 to 0.44 when the discharge voltage varies from 110 to 350 V. It seems that the thrust efficiency saturates at a discharge voltage of 300 V. The thrust efficiency of SPT-50 is higher than the thrust efficiency of SPT-20 but their behavior on the discharge voltage is similar. Thus, the gas flow rate and the discharge voltage are important parameters in the discharge of SPT-50. Nevertheless, for SPT-50, the thrust efficiency is acceptable for spatial applications.

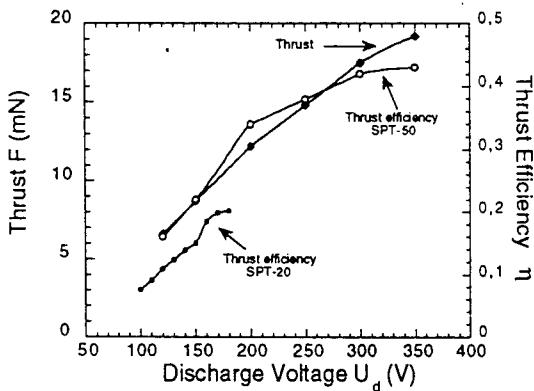


FIG 3 : Dependence on the discharge voltage of the thrust and thrust efficiency. The gas flow rate was 1 mg.s<sup>-1</sup> and the optimal radial magnetic field value is 170 Gauss.

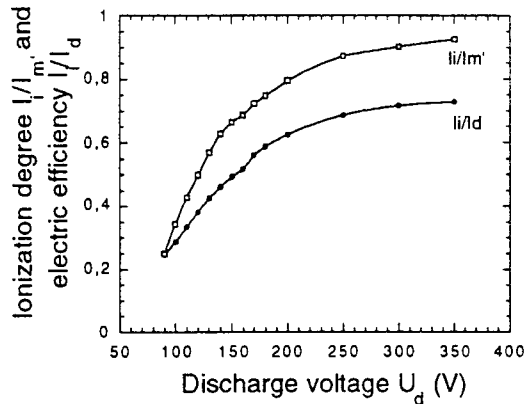


FIG 4 : Dependence on the discharge voltage of the degree of ionization and the energetic efficiency. The gas flow rate was 1 mg/s and the optimal radial magnetic field value is 170 Gauss.

Fig. 4 shows the variation of the ratios  $I_i / I_d$  and  $I_i / I_m$  with the discharge voltage. The ratio  $I_i / I_d$  characterizes the energetic efficiency of the thruster, while the ratio  $I_i / I_m$  is the degree of gas ionization ( $I_m$  is the current equivalent of the gas flow, assuming a total single ionization). When the discharge voltage is enhanced from 90 to 350 V the degree of ionization goes up from  $I_i / I_m = 0.12$  to 0.85, while the ratio  $I_i / I_d$  varies in the range 0.28 to 0.73.

**Acknowledgements.** This work was performed within Groupement de Recherche CNRS/CNES/SEP/ONERA n°1184 "Propulsion à Plasma pour Systèmes Orbitaux".

We acknowledge the support of C.N.E.S. (France).

\* Permanent address : RRC "Kurchatov Institute", Moscow, Russia.

<sup>1</sup>T.S. Colbert, V.M. Gravyshin, S.A. Khartov, V. Kim, G.A. Popov, R.K. Tchuyan, Colloque International "Propulsion des véhicules spatiaux", 8-10 Nov. 1994, Toulouse, France.

<sup>2</sup>L. Bussolino, G.B. Amata and al, Paper IAA-94-IAA.L.1.2.766

<sup>3</sup>A.I. Morozov, Yu.V. Esinchuk, G.N. Tilinin, A.V. Trofimov, Yu.A. Sharov, G.Ya. Schepkin, Soviet Physics - Technical Physics, **17**, 38 (1972).

<sup>4</sup>G. Guerrini, A.N. Vesselovzorov, M. Bacal, I.B. Pokrovsky, Rev. Sci. Instrum., **67**, 3, 990 (1996).

<sup>5</sup>G. Guerrini, C. Michaut, A.N. Vesselovzorov, A.G. Nikitin, M. Bacal and M. Dudeck, 33<sup>rd</sup> AIAA/ASME/SAE/ASEE Joint Propulsion Conference and Exhibit, July 6-9, 1997, Seattle, WA (USA).

# PIC-MC Modelling of a RF Magnetron Discharge

T.M. Minea, J. Bretagne and G. Gousset

Laboratoire de Physique des Gaz et Plasmas, Unité Associée au CNRS  
Université Paris XI 91405 ORSAY Cedex, FRANCE

## 1. Introduction

Magnetron discharges are widely used as plasma devices for etching, sputtering or thin film deposition. Initially designed to work with DC power, the need for dielectric or semiconductor surface modification applications require high-frequency excitation.

In spite of their wide industrial utilisation, the understanding of the main phenomena occurring in magnetron discharges is far from being complete. The difficulty comes from the strong non-uniform electric and magnetic fields which act on the charged particles in front of the cathode.

The widely accepted contribution of ions to secondary electron emission in DC magnetron discharges is reduced in low-pressure RF (13.56 MHz) ones in which the volume production of charged particles by the RF heating of bulk electrons becomes non-negligible.

Previous dimensional models for the magnetron discharges have been developed. Some MC simulations [1,2] were accomplished for the DC case, and a kinetic model for an 1D ideal RF magnetron model was proposed by Lieberman [3].

The present model, based on a Particle-in-Cell Monte Carlo (PIC-MC) simulation, similar to Birdsall model [4], was carried out with the aim to simulate the plasma behaviour in the RF magnetron discharge and to get information on charged particle densities, electric field and ionisation source distributions during the RF period.

## 2. Model

### 2.1 Theoretical background

All computations were done for a circular planar magnetron and, due to the symmetry with respect to the central axis, the problem was reduced for the PIC to a rectangular domain (2D) bounded by this axis and by the vessel walls. The static magnetic field map, close to the target, was obtained by fitting the experimental data recorded on our device. The 2D electric field map was obtained by solving Poisson's equation at each time-step. Between two successive collisions, the plasma charged particles, represented in PIC models by macro-particles, move according to Lorenz force:

$$\ddot{\vec{x}} = \frac{q}{m} (\vec{E} + \dot{\vec{x}} \times \vec{B}) \quad (1)$$

where  $\vec{x}$ ,  $\dot{\vec{x}}$  denote the space and velocity co-ordinates (or a point in phase-space),  $q$  represents one elementary signed charge and  $m$  denotes the mass of concerned particle. Practically, ions are not sensitively affected by the presence of the magnetic field (typical  $\vec{B}$  values are of some hundred Gauss).

### 2.2 Numerical implementation

The boundary conditions necessary to solve the potential equation were imposed from the experimental electric circuit and device geometry. The anode is constituted by the chamber walls for which the potential is zero while the powered cathode is assumed as biased to RF voltage shifted down from zero by a DC negative voltage ( $V_{DC}$ ). This bias is due to: i) the capacitive coupling between the RF supply and discharge electrodes throughout cathode dielectric, ii) to a very large ratio of the two electrode areas and iii) to the presence of magnetic field close to the target electrode. According to Lieberman [3] the peak-to-peak RF voltage ( $V_{pp}$ ) can be approximated by the double of  $|V_{DC}|$  bias. Above Dirichlet conditions are completed by a zero Neumann boundary condition on the central axis.

Actual model assumes a constant value for the potential all along the target radius. This means that the charge distribution on insulating target surface created by ion collection is perfectly neutralised by electrons for each moment and position on the surface.

Due to the cylindrical symmetry of the discharge device, the azimuthal component of electric and magnetic fields are zero. Thus, only the radial distance from the central axis and the axial distance from the target surface are stored for the calculation of macroscopic discharge parameters. The contribution of each macro-particle to the closer mesh nodes was weighted as indicated in [4].

High expected gradients of electric fields in front of the cathode compel us to work with a variable step on the two axis. With above boundary conditions and every step recalculated source term, the 2D potential map was numerically obtained by the over-relaxation



method. The axial and radial components of the electric field are easy to compute from potential map.

In these fields, the particle orbits are calculated integrating the motion equation (1) by using a quality control Runge-Kutta routine [5]. The time-step was taken so that the corresponding displacement of electrons was smaller than the mesh cell length. The concept of virtual collision frequency, detailed in [6], was used for higher computation speed.

### 2.3 Physical aspects.

Present simulation was performed with Xenon as buffer gas. Collision cross-sections for momentum transfer were taken from [7], for total excitation from [7] and for single ionisation from [8]. For the various involved collision process, differential cross sections were assumed as having almost the same angular dependence for a given incident electron energy. According to McDaniel [9], this approximation is reasonable in the case of noble gases. Energy dependence of electron deflection by Xenon atoms in elastic and inelastic collisions was taken from [10,11]. The anisotropy becomes non-negligible for energy higher than 5eV. Data are available up to 500eV.

The electric circuit is closed by the electrons which escape from magnetic field and reach the anode. At the beginning of simulation only secondary photoelectrons release the cathode due to the photoelectric effect of UV resonant radiation emitted by excited plasma atoms. Photoelectron emission is considered only if the photon falls on the cathode surface, and the corresponding solid angle leads to a probability of 0.3. Excitation processes were regarded as corresponding to an overall energy level for which an average lifetime of 10ns was assumed. The de-excitation of this state was randomly produced according to an exponential decay law and the self-absorption phenomenon was neglected. The relative importance of this process is weakened after some periods in favour of secondary electron emission due to ion bombardment of the cathode characterised by  $\gamma$  coefficient. For a BN cathode material considered here and ion energy below 1keV, the value of  $\gamma$  is about 0.1.

We completely neglect the Coulomb scattering of charged particles (electron-electron or electron-ion collisions) and also the production of doubly charged and excited ions. According to the small sheath thickness, even for long ion time of flight the resonant charge transfer from ions to neutrals could be neglected as a first order approximation, nevertheless it will be taken into account.

### 3. Expected results and discussions

The present model was developed for the study of the sputtering of boron nitride (BN) and the plasma

behaviour in a RF magnetron discharge. For this reason it is important to control the energy and the flux of ions which arrive on the BN target and control the sputtering yield and the secondary emission. The model provides also the temporal evolution and spatial distribution of excitation and ionisation events. This permits to compare the production of new electrons by bulk plasma heating or by secondary emission due to ion bombardment on the target.

Results of the model are planned to be compared to experimental ones, in particular for spatial distributions of the line intensities observed by optical emission spectroscopy for Xenon and also for sputtered materials. Experimental results indicate that the RF magnetron discharge regime changes for a critical pressure value of a few mTorr. It is also interesting to test the model against this experimental observation and eventually to explain it.

In order to explain the differences in the transport of charged particles into the DC and RF magnetrons the results of proposed model can be directly compared with previous DC MC model [1] or with 1D analytical one [3] for an ideal magnetron.

### 4. References

- [1] T.E. Sheridan, M.J. Goeckner and J. Goree: *J. Vac. Sci. Technol.* **A8** (1990) 30
- [2] S. Ido and K. Nakamura: *Jpn. J. Appl. Phys.* **35** (1996) 2302
- [3] M.A. Lieberman, A.J. Lichtenberg and S.E. Savas: *IEEE Trans. Plasma Sci.* **19** (1991) 189
- [4] C.K. Birdsall: *IEEE Trans. Plasma Sci.* **19** (1991) 65
- [5] W.H. Press, B.P. Flannery, S.A. Teukolsky and W.T. Vetterling: *Numerical Recipes*, Cambridge University Press, 2nd edition, (1989) p. 554
- [6] M.J. Brennan: *IEEE Trans. Plasma Sci.* **19** (1991) 257
- [7] M. Hayashi: *J. Phys. D: Appl. Phys.* **16** (1983) 581
- [8] E.J. McGuire: *Phys. Rev.* **A16** (1977) 62
- [9] E.W. McDaniel: *Collision Phenomena in Ionized Gases*, Wiley, New York (1964)
- [10] D. Filipovic, B. Marinkovic, V. Pejcev and L. Vuskovic: *Phys. Rev.* **A37** (1988) 356
- [11] T.Y. Suzuki, Y. Sakai, B.S. Min, T. Takayanagi, K. Wakiya and H. Suzuki: *Phys. Rev.* **A43** (1991) 5867

# Distribution of Surface Discharge for Ozone Generation

T. Murata, Y. Okita and K. Terai  
Toshiba Corporation

## 1. Introduction

Surface discharge shows high performance for industrial uses such as ozonizers, flue gas treatments, UV sources and other non-equilibrium plasma processes[1]. Some workers have studied the fundamental mechanisms with respect to the influences of the surface charges on discharge channel extensions, the polarity effect of an applied voltage and the diffusion processes of generated ozone [2].

In this report, we present the distribution of discharge channels in surface discharge and the electrode design method in the case of narrow mutual pitch of surface electrodes for high concentration ozone generation.

## 2. Experimental setup

The electrode arrangement consists of the surface high voltage electrodes on a dielectric plate and the rear earth electrode as shown in Figure 1. We prepared two types of surface electrodes with wide and narrow mutual pitch for electrical and optical measurements. For a wide mutual pitch of 5mm, the metal wires with a 0.3 mm diameter were fixed on a 1.8 mm thick glass plate. For a narrow mutual pitch under 1 mm, metal stripes were printed on a ceramic plate or glass coated metal plate. The distribution of discharge channels in surface discharge was observed by using high speed CCD camera system (Princeton Instruments, ST130).

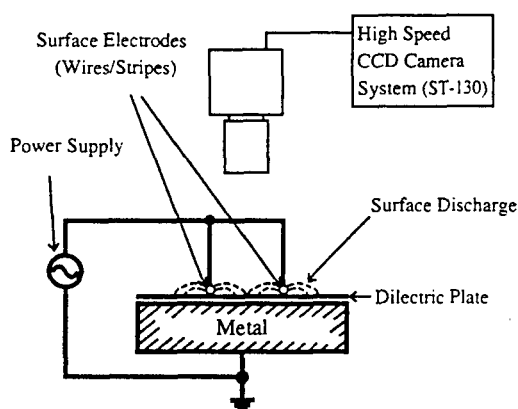


Fig.1 Electrode configuration for optical and electrical measurements

## 3. Results and discussions

### 3.1 Wide pitch surface electrodes

In the case of mutual surface electrode pitch of 5mm, the distributions of discharge channels were observed as shown in Figure 2. Gas is dry air whose pressure is 1.7

bar and the dew point is below -60 degree.

Figure 2 shows the light emission from surface discharge observed at the exposure time of 100  $\mu$ s for both polarities of an applied voltage (6kV). At the negative polarity, the strong light emission occurred in the neighborhood of the wire electrodes, and at the opposite positive polarity, it occurred in an extensive region. The half width at half maximum of light intensity is 1.3 mm at a positive polarity and 0.7 mm at a negative polarity; the former is about twice the length of the latter.

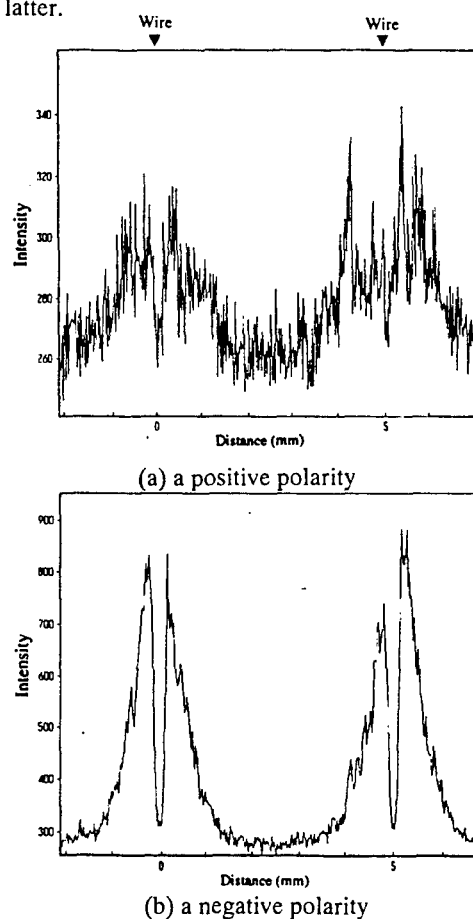


Fig. 2 Collective distributions of discharge channels for both polarities in the case of mutual pitch of surface electrodes of 5 mm(exposure time;100  $\mu$ s)

To observe the individual discharge channel at a positive polarity, the exposure time is reduced to 20 ns and 6 ns as shown in Figure 3. The discharge channel length at the exposure time of 6 ns is shorter than that at 20 ns. In some cases, it can be seen that the luminous parts of discharge channel are apart from wire electrodes, as shown in Figure 3 (b). We think the active region of surface discharge is the discharge channel head.

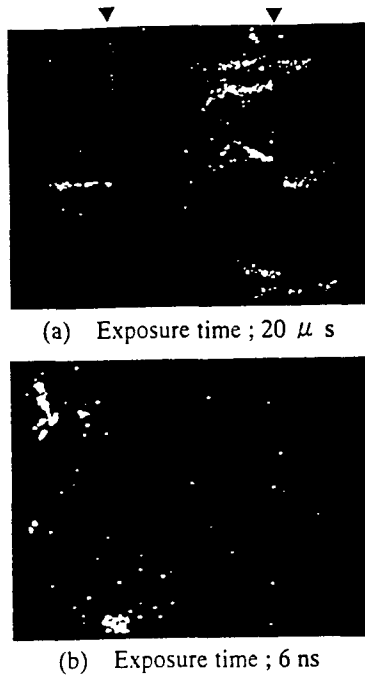


Fig. 3 Distribution of individual discharge channels at a positive polarity in the case of mutual pitch of surface electrodes of 5 mm.

### 3.2 Narrow pitch surface electrodes

For a narrow mutual pitch of 0.25 mm, the distribution of discharge channels was observed as shown in Figure 4, where dielectric material and surface electrode is made of AlN and wolfram, respectively. The thickness of AlN is 0.25 mm. The bright part of surface discharge is the center of mutual pitch of surface electrodes. This result is the same as reference [1] and is caused by discharge channel being no longer perpendicular to surface electrode.



Fig. 4 Collective distribution of discharge channels in the case of mutual pitch of surface electrodes of 0.25 mm

The narrow pitch of stripe electrodes decreases the electric field along the dielectric surface and increases breakdown voltage. The electric field analysis by using the high speed surface charge simulation method (HSSSM) was carried out. Figure 5 shows the results of calculated electric field on dielectric surface, when the applied voltage is 3 kV. The increment of dielectric thickness causes the decrement of electric field regardless of dielectric constant. It is considered

that the electric field near surface electrodes is so high that the breakdown occurs from the Paschen minimum distance of about 5  $\mu$  m.

The measured breakdown voltage was compared with the calculated electric field at 5  $\mu$  m from surface electrode. The experimental setup consisted of stripe surface electrode and glass coated metal plate electrode, whose dielectric thickness is 0.2 mm. Table 1 shows the measured breakdown voltage and the calculated electric field in the case of a constant applied voltage of 4 kV. At the pitch of 0.5 mm, the calculated electric field decreases with the pitch, and so the breakdown voltage increment was verified. As a result, we found that the aspect ratio of the strip electrode pitch to the dielectric thickness should be more than 1 regardless of dielectric constant.

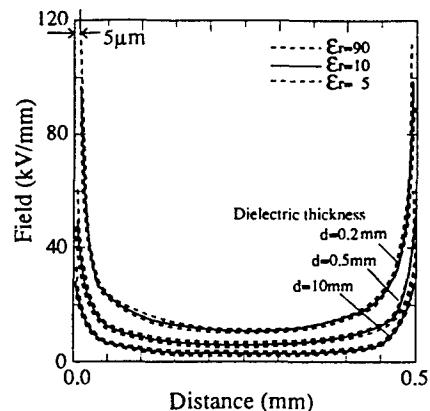


Fig. 5 The calculated electric field on dielectric surface

Table 1 The measured breakdown voltage and the calculated electric field in the case of 4 kV

Surface Electrode Pitch, mm	0.2	0.5	1.0
Breakdown Voltage, kV	3.2	2.1	2.0
Electric Field, kV/mm	67	82	88

## 4. Conclusions

At a negative polarity, the light intensity from surface discharge increases steeply in the neighborhood of the surface electrodes, and at a positive polarity its distribution is twice as extensive. The extension speed of discharge channel is observed in the time range of some ns for a positive polarity. The narrow pitch of surface electrodes decreases the electric field along the dielectric surface and increases breakdown voltage. It was found that the aspect ratio of the strip electrode pitch to the dielectric thickness should be more than 1.

- [1] S. Masuda et al., IEEE Trans. Ind. Appl., 24, 2 (1988) 223
- [2] Pietch and R. Richter, Proc. of 12th Ozone World Congress, (1995) 17

## Comparative behaviour of DC positive point-to-plane discharges in Nitrogen and dry Air for pressures around 50 Torr

A.E. Ercilbengoa, J.F. Loiseau, R. Peyrous, N. Spyrou\*, N. Soulem and B. Held

Laboratoire d'Électronique des Gaz et des Plasmas - Université de Pau, 64000 PAU, FRANCE

\*Electrotechnic Materials Laboratory - Patras University, 26500 PATRAS, GREECE

### 1. Introduction

A lot of work has been performed concerning corona discharge in ambient air, but only a few studies are dealing with the intermediate (50 - 400 Torr) pressure range for DC discharges with inhomogeneous field [1,2], and no systematic drawing of V-I characteristics and recording of related current impulses were published.

The aim of the present work is to contribute to a better knowledge of the discharge in the lower part of this pressure range, comparing pure Nitrogen, with Dry Air (cylindred) which presents electronegative properties. It is a development of studies initiated for lower pressures in the frame of a franco-hellenic collaboration [3,4] and recently pursued [5-7].

### 2. Experimental procedure

A rhodium point electrode with 100  $\mu\text{m}$  tip curvature radius is positively stressed with a 0-30 kV DC power supply, whereas the grounded electrode is a stainless steel plane. In order to access to the steepest parts of the characteristics, a 200 M $\Omega$  load resistor is used in the external circuit. Current impulses as well as the DC component are visualized on a digital oscilloscope and recorded by a printer or a plotter.

Measurements are performed with pressure  $p$  in the 50-70 Torr range and gap length  $d$  in the 1.0-1.4 cm range, in such a way that the same values of  $p \cdot d$  can be obtained with different values of  $p$  and  $d$ .

### 3. Comparison between $\text{N}_2$ and Dry Air for $p = 50$ Torr and $d = 1$ cm

In this pressure range, for the given load resistor and within the limits of the power supply, three distinct regimes successively occur in Nitrogen with increasing applied voltage [6,7]; they can be followed either visually or along the V-I characteristic curve (figure 1). As the applied voltage is increased, the discharge inception occurs with a thin luminous anodic layer on the point surface, becoming brighter as the gap voltage  $V$  increases. This region, hereafter designed as "Luminous Point" (LP), presents similarities with the dark self-sustained discharge [5]. For increasing values of the applied voltage,  $V$  drops suddenly (for average current about 10  $\mu\text{A}$ ) and remains quasi-constant. The

visual aspect is globally cylindrical with decreasing light intensity from the point to the plane and presents a bright cathodic sheath. This regime is called "Glow-Like" (GL). When the applied voltage is further increased, a sudden growth of  $V$  is observed, followed by a second decrease as the current rapidly increases (and would lead to arc if allowed by the external impedance). To avoid hazardous interpretations, this regime is simply called "Total Discharge" (TD).

For Dry air, the LP regime is identical, except that the anodic layer is more diffuse and tends to spread up along the conical part of the rod. But the V-I characteristic (figure 1) appears different after the first voltage drop. The discharge seems to stay in the GL regime for much higher values of the applied voltage. An increase of  $V$  is observed, but less important than in the case of Nitrogen. The transition to TD, if any, occurs at much higher current values.

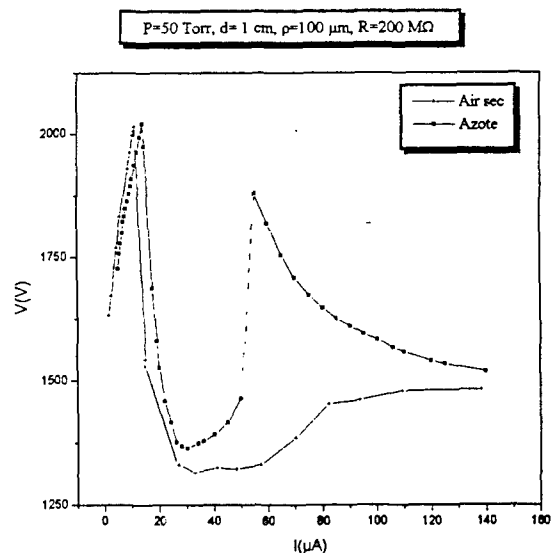


Fig. 1. V-I characteristics at  $p = 50$  Torr for Nitrogen (•) and Dry Air (+).

In Nitrogen, space charge in the vicinity of the point consists in positive ions, the accumulation of which may be equivalent to a virtual anode with a more important curvature radius as the real one. In Air, the presence of negative ions in the gap modifies the local space charge field. The LP regime is controlled by the applied voltage, and GL by the current flow, so that the difference between the curves concerning Nitrogen and

Dry Air, which mainly occurs in this last regime, is probably due to the different nature of space charge. Each of the three above mentioned regimes is characterized by typical shapes of current impulses superimposed to the DC component of the discharge current [6.7] which may be recognized for both gases.

#### 4. Variation of gap length and pressure

The gap length has been varied for Nitrogen and Dry Air, keeping constant the pressure (figures 2 and 3). A translation of the gap voltage to higher values is observed when  $d$  is increased. But in the case of Nitrogen, the extension in current of the GL regime correlatively decreases.

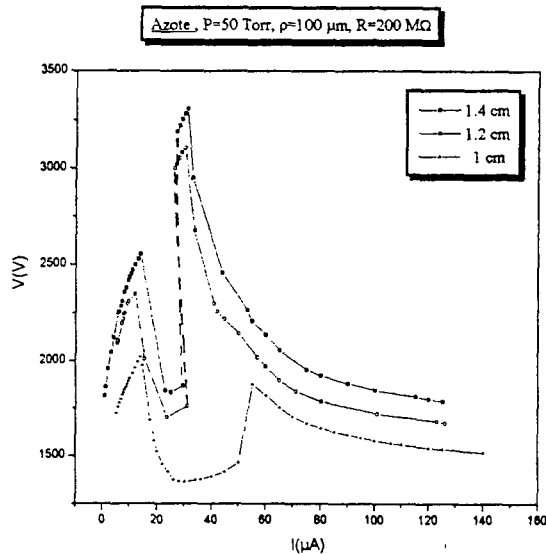


Fig. 2. V-I characteristics at  $p = 50$  Torr for Nitrogen with varying gap length.

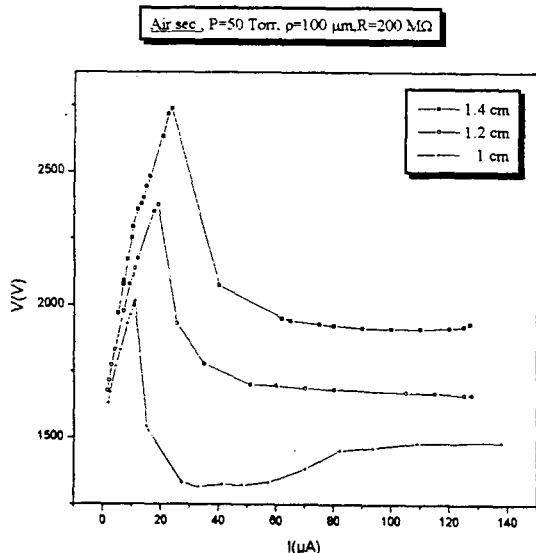


Fig. 3. V-I characteristics at  $p = 50$  Torr for Dry Air with varying gap length.

Measurements performed for  $p = 60$  and  $70$  Torr and compared with the above results show that the evolution of phenomena with the product  $p.d$  is different when either  $p$  or  $d$  is varied, the other one being kept constant. As a consequence,  $p.d$  does not appear to be a similarity parameter.

#### 5. Concluding remarks

Even if the visual aspect of the discharge is similar for both gases, the observation of the V-I characteristic curves and of the related current impulses show that the behaviour of discharges in Nitrogen and Dry Air are quite different, especially when the influence of space charge is predominant, i.e. in the GL regime, this latter covering a more extended current range in Air.

#### 6. References

- [1] R.C. Davidson, B.R. Lynch and O. Farish - Proc. 4th Int. Conf. on Gas Discharges and their Applications, Swansea (G.B.), (1976) 242-245
- [2] J. Dupuy and A. Gibert - J. Phys. D: Appl. Phys. **15** (1982) 655-664
- [3] R. Peyrous, N. Spyrou, P. Pignolet and B. Held - Proc. 9th Int. Conf. on Gas Discharges and their Applications, Venezia (Italy), (1988) 205-208
- [4] N. Spyrou, R. Peyrous, N. Soulem and B. Held - J. Phys. D: Appl. Phys. **28** (1995) 701-710
- [5] N. Soulem - Thèse de Doctorat, Université d'Orléans, oct. 1996
- [6] A. Ercilbengoa, J.F. Loiseau, N. Soulem and B. Held - Proc. 13th ESCAMPIG, Poprad (Slovakia), Europhysics Conf. Abstr. **20E**, part A (1996) 165-166
- [7] A. Ercilbengoa, J.F. Loiseau, N. Soulem and B. Held - Acta Physica Universitatis Comenianae (Bratislava, Slovakia), (accepted for publication, 1997)

## Effect of sample-cathode shape in DC glow discharge ion source for mass spectrometric analysis.

S. Baude\*, S Lorthioir\*, G. Blaise\*\*, A. Fiala\*\*\* and L.C. Pitchford\*\*\*

\*CEA, Centre d'Etudes de Bruyères-le-Châtel BP12, 91680 Bruyères-le-Châtel, France

\*\*Laboratoire de Physique du Solide, Univ. Paris Sud, Orsay, France

\*\*\*CPAT, Univ. Paul Sabatier, Toulouse, France

Glow discharge sources have been widely used in analytical chemistry, essentially as sources for optical emission or atomic absorption spectrometry and more recently for mass spectrometry. The successful application of glow discharge in mass spectrometry has shown up excellent capabilities for the characterization of solids [1]. Because the elemental (and isotopic) composition of a material defines its chemical and physical properties and *in fine* its quality, more sensitivity and reliability in analytical measurements are needed to qualify recent materials. To improve the figures of merit in GDMS, a better understanding of the physical processes that occur in the ion source is required. In this paper, we describe the effect of the cathode (sample) geometry on the argon plasma and the consequences on analytical capabilities.

### 1. Instrumentation

All measurements were done using the VG9000 high resolution glow discharge mass spectrometer (FISONS Elemental, UK) with the so-called MegaCell source for pin samples. In direct current GDMS the sample functions as the cathode and the plasma cell as the anode of the discharge chamber. Typical conducting samples are cylindrical shaped : 15-20 mm length, 1-3 mm diameter and penetrate 5-10 mm into the plasma. A low pressure (0.5-1.5 torr) of high purity argon is introduced. The potential difference around 1kV leads to a discharge current of some mA. The cathode material is sputtered by argon ions and fast neutrals and the atoms ionized in the plasma enter the mass spectrometer to be measured. These conditions usually give good analytical results but some of the operating parameters must be kept constant to ensure low deviation in measurements. More often the ion source parameters are fixed according to empirical or practical considerations. Thus, the discharge cell was modeled to study the influence of the different parameters.

### 2. Simulation of the glow discharge

A self-consistent, two-dimensional hybrid fluid-particle model is used to study the plasma produced in the MegaCell ion source of the spectrometer [2-3]. Calculations of the properties of steady-state glow discharge in pure argon are performed for two different shapes of the cathode.

In a pin-sample configuration (length 9mm ; diameter 3mm, referred as A) we first studied the formation of the plasma region by increasing the pressure from 0 to 1 torr, the voltage being fixed at 1kV. From 0.5 torr, a plasma forms in a ring around the cathode as shown by the ion density profiles in figure 1-a.

The existence of an electric field inversion in the plasma can be seen from the calculated equipotential contours. With such a field reversal, ions which can reach the anode are those created in ionization events on the anode side of the potential maximum. None of the ions created on the cathode side of this maximum can be drawn into the mass spectrometer.

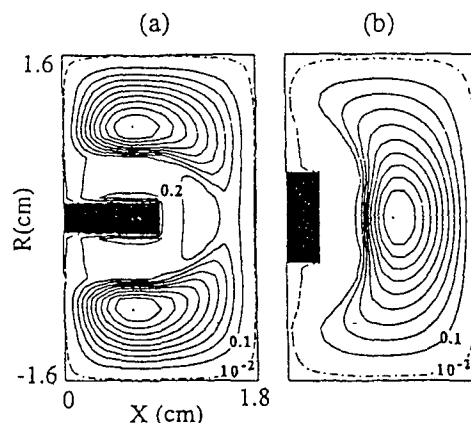


FIG. 1. Contours of constant ion density calculated in 0.5 torr Ar for (a) A and (b) B shaped cathodes (see text).

The calculated argon ion current density is maximum along the side walls and not in the extraction plane. See figure 2-a for current density in the extraction plane.

By changing the cathode geometry (length 3mm ; diameter 9mm, B shape) we point out that the plasma region is in front of the cathode. A maximum in the ion density distribution is observed on the axis of the cell (figure 1-b) with an increase of a factor 4 compared with the baseline geometry (A). Again, a field reversal exists but is now centered on-axis, generating an increase in the  $\text{Ar}^+$  density on the extraction plane by a factor of 10 (figure 2-b).

These results suggest that the analytical performance and especially sensitivity of glow discharge mass spectrometric analysis can be enhanced by suitably choosing the sample geometry.

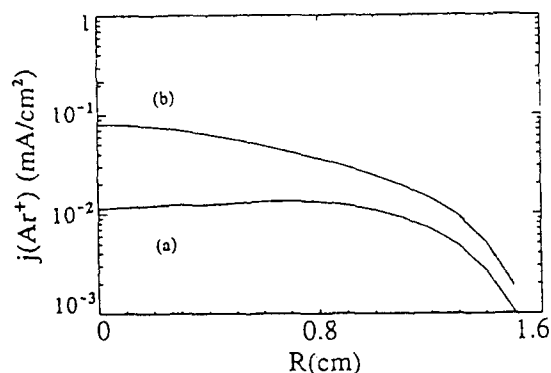


FIG. 2. Ion current density distribution along the extraction plane as a function of the distance from axis for (a) A and (b) B cathode shapes and 0.5 torr argon pressure.

### 3. Experimental results

In order to define the experimental operating conditions of the ion plasma-source, the voltage-current characteristics for a high purity copper cathodes have been measured. The data for 0.5, 0.9 and 1.4 torr argon pressure are reported in figure 3 for the two cathode shapes discussed above. As expected, the discharge current increases with the pressure and the voltage. Though there is a small difference in the surface areas of the cathodes (respectively 0.9 and 1.5 cm<sup>2</sup> for A and B shaped cathodes), the electrical current for the large diameter cathode is higher.

In these experiences, the cell was cryocooled with liquid nitrogen and the discharge voltage was regulated. The pressure was measured using an additional system that we have to develop because no reliable measurement can be done with the spectrometer in its standard configuration. Standard deviation in measurements did not exceed 0.1 torr.

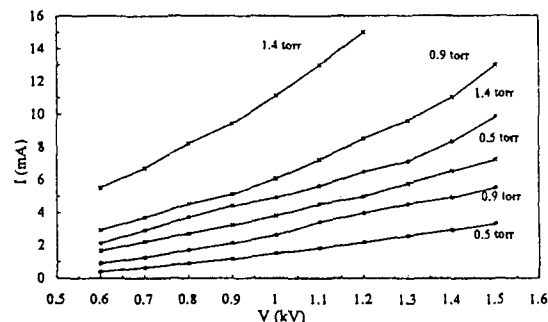


FIG. 3. Experimental voltage-current characteristics for 0.5 ; 0.9 and 1.4 torr argon pressure. Circles are for the A geometry and crosses for B.

The ion beam intensities collected in the mass spectrometer of each isotope of argon, copper and some trace impurities are measured for each running point of the V-I characteristics presented just before. Integrated peak areas for <sup>63</sup>Cu<sup>+</sup> and <sup>40</sup>Ar<sup>+</sup> ions (major abundance isotopes) are reported in figure 4 for A and B cases. As predicted by the calculations, the ion signals increase by changing the sample geometry from pin to quasi-disk shape.

A one order increase in the ion intensities is confirmed by the experience.

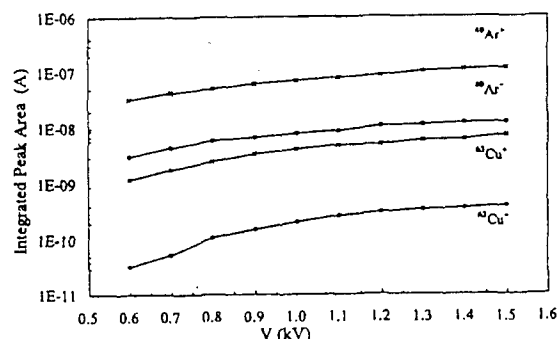


FIG. 4. Integrated peak areas for argon and copper ions as a function of the voltage measured for 0.5 torr. Circles are for the A geometry and crosses for B.

### 4. Summary

Calculations of the properties of the ion plasma-source of the VG9000 spectrometer have been performed for pin and disk cathode geometries in pure argon discharge. Results are consistent with calculations for such ion sources using a one-dimensional model [4]. Experimental data validate the model and its predictions regarding the ion fluxes arriving in the extraction plane. From this, we have simulated an increase of a factor 10 in the sensitivity of the analytical technique considering principally the field reversal in the negative glow of the discharge. Thus, analytical performances can be improved by a suitable adjustment of the cathode shape.

Moreover, the distance from the cathode top to the exit slit, a typically empirical parameter usually carefully adjusted by users have been shown to have a little influence. This result was obtained by reducing the anode length [3].

Further, the controlling quantities for the sputtering rate of the cathode due to Ar<sup>+</sup> bombardment, that means the argon ion fluxes to the cathode and the energy of these ions, can be obtained by the model. First results indicate that the predicted erosion profile shapes are in good agreement with experiment. However, as pointed out in reference [5] sputtering by fast neutrals is also important.

### 5. References

- [1] R. K. Marcus : Glow Discharge Spectroscopies Plenum Press, New York, 1993
- [2] A. Fiala, L.C. Pitchford and J.P. Boeuf : Phys. Rev., E49 (1994) 5607
- [3] A. Fiala, L.C. Pitchford, J.P. Boeuf, S. Baude : Spectrochim. Acta B, to be published
- [4] A. Bogaerts, R. Gijbels and W.J. Goedheer : J. Appl. Phys., 78 (1995) 2233
- [5] A. Bogaerts, R. Gijbels : Fresenius J. Anal. Chem., 355 (1996) 853

## CHARACTERISTICS OF LOW POWER HF 10-CM TECHNOLOGICAL ION SOURCE

S.G. Kondranin\*, E.A. Kralkina\*, S.K. Koh\*, H.G. Jang\*, W.K. Choi\*, H.-J. Jung\*,  
T.B. Antonova\*\*, G.E. Bougrov\*\*, V.B. Pavlov\*\*, A.A. Rukhadze', A.F. Alexandrov'

\* Korea Institute of Science and Technology, Cheongryang P.O. Box 134, Seoul, Korea

\*\*RIAME MAI, Russia, 125871, GSP, Moscow A-80, Volokolamskoe shosse, 4.

Physical Faculty of Moscow State University, Russia, Moscow, Vorobiev Gory

In [1] the low power HF ion source was represented, which operational principle was based on the excitation of electrostatic waves. A.F. Alexandrov et.al. [2] showed that contrary to helicons, electrostatic waves excitation in plasma, located in the external magnetic field, is independent on plasma density and can occur at low HF power input. Under conditions of electrostatic waves excitation, HF fields penetrate into plasma volume and electrons are effectively heated due to Landau damping mechanism [2]. The presence of external magnetic field in addition helps to confine electrons in the discharge and decrease the power losses for the discharge sustaining. The construction of the HF ion source is described in details in [1]. The present paper represents the test results of the HF ion source models with magnetic systems based on one, two and three magnetic rings. The increase of the number of magnetic rings was followed by the increase of the magnetic field at the source axis from 180 to 350 Gs. Models of HF ion source with convex and concave grids of ion optic system (IOS) were tested.

### 1. Results of Technological HF Ion source experimental tests.

Fig.1 shows the extracted ion currents of different gases, obtained at fixed HF power input to the ion sources with different magnetic systems. One can see that introduction of magnetic field leads to significant (about 3 times) increase of the ion current but the multiplication of the magnetic rings number results only in 20-30% increase of the ion current. That means that in construction of technological ion source it is reasonable to utilize magnetic system, based on one or two magnetic rings.

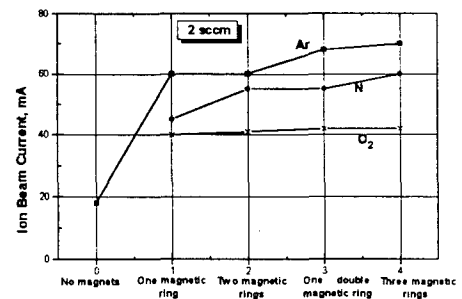


Fig.1. The extracted ion currents of different gases, obtained at fixed HF power input to the ion sources with different magnetic systems.

Ion beam profile at a given distance from the ion source is controlled by three parameters:

- 1) ion beam profile at the exit of IOS;
- 2) divergence of the elementary ion beam, extracted from the single hole of IOS;
- 3) shape of the grids of the IOS.

At small distances from the IOS the first and the third factor play essential role, while at the large distances from IOS two last factors are much more important because in this case every hole of IOS contributes nearly to any point within the ion current profile. Fig.2 shows the ion beam profiles, measured close to the exit of IOS. One can see

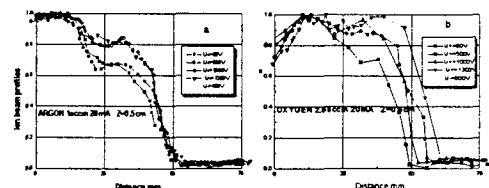


Fig.2. Ion beam profiles, measured close to the exit of IOS.

that the homogeneity of the ion beam is high, especially at large accelerating potentials. One can also observe not-pronounced but



nevertheless existing structure of the ion beam profile. Most probably it can be related to the spatial distribution of electrical field in the excited electrostatic wave. This idea is confirmed by the measurements of current distribution near the IOS at zero acceleration and deceleration potentials, i.e. in the case when electrons and ions can go out of the ion source only due to their velocities, obtained in plasma volume and near emission electrode sheath. One can see from Fig.3 that in this case electrons are emitted from the ring, situated close to the center of gas discharge chamber. The position of electron ring correlates with the structure of the ion current, observed in case of applied voltage to the electrodes of IOS.

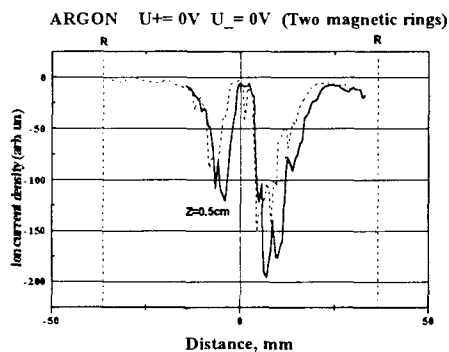


Fig.3. Current distribution near the IOS at zero acceleration and deceleration potentials. Solid and dashed lines represent currents measured at zero and -12V potentials of the Faraday cup.

Fig.4 represents the ion beam profiles, measured at the distances 5 and 22 cm from the HF ion source with concave IOS and different magnetic systems. One can see that ion beam profiles, obtained with different magnetic systems at the distance 22cm, are close to each other in spite of the fact that ion beam profiles, measured at the distance 5cm have remarkably different shape. This is the result of the influence of the divergence of the elementary ion beams, produced by every hole of the IOS.

Ion beam current density measurements, carried out at different distances from IOS showed that the divergence of the ion beam, extracted from the HF ion source with installed magnetic system and used shape of concave type IOS is about 13-15°.

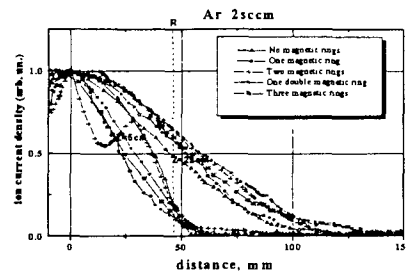


Fig.4. Ion beam profiles obtained with different magnetic systems and concave type IOS.

Results of ion beam current density measurements at the distance 40cm from IOS for different working gases: Ar, O<sub>2</sub>, N<sub>2</sub> and air showed that the working gas change does not influence the shape of ion current density spatial distribution. In order to find the conditions, when the most uniform ion current density distribution can be obtained with concave grids, the dependence of Ar ion beam density on acceleration potential in the range from -300 V to -900 V at a constant ion beam energy was studied. Experiments showed that the best uniformity of the beam profile was at the potential of acceleration electrode about -500 V. The diameter of spot with 90 % uniformity reaches about 16 cm. The change of the uniform spot dimensions with the change of ion beam energy is negligible. But significantly higher uniformity of the ion beam can be achieved with convex grids, this fact can be brilliantly illustrated by Fig.5.

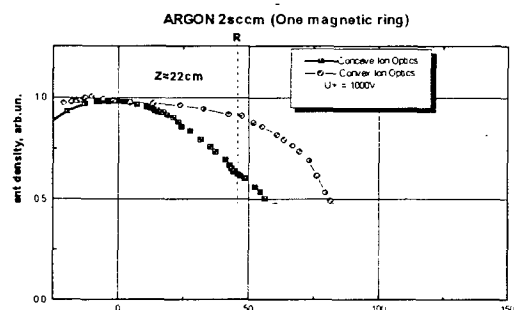


Fig.5. Ion beam profiles obtained with concave and convex grids.

#### References

- [1] A.V.Alexandrov et al Proc. of 22 ICPIG, vol.4, (1995).
- [2] A.F.Alexandrov et al Appl. phys. (Russia) 1, (1995), 3-22.

# Mass spectrometric study of SF<sub>6</sub> plasma beam extracted from an ECR ion source

T. Chevolleau, P.Y. Tessier, C. Cardinaud and G. Turban

Laboratoire des Plasmas et des Couches Minces.

Institut des Matériaux de Nantes. UMR 110 - CNRS

2, rue de la Houssinière. 44 072 Nantes cedex 03 - France.

## 1. Introduction

A SF<sub>6</sub> reactive ion beam etching (RIBE) system has been developed using an ECR ion source with a 3 grids beam extraction system. A better understanding and control of this etching process requires a knowledge of the composition of the ion beam and the neutral species extracted from the plasma through the grids. Therefore, a mass spectrometric study of the SF<sub>6</sub> plasma beam (ions + neutral species) has been carried out. The effects of the microwave power and the SF<sub>6</sub> gas pressure have been studied. Application to the RIBE of silicon is discussed.

## 2. Experimental arrangement

The experimental system is shown in figure 1. The sample to be etched is clamped on a moveable holder. In RIBE configuration, the surface of the sample is normal to the beam and located at near 25 mm away from the outer grid of the ion source. In mass spectrometric analysis, the substrate holder is removed and the plasma beam can reach the aperture of the spectrometer located at 100 mm opposite to the outer grid. The description of the ECR ion source is given elsewhere [1]. The diameter of the beam is 10 mm at the output of the source. Extracted current density of the beam is a few mA.cm<sup>-2</sup>. The energy of the beam can be controlled between 60 eV and 2000 eV.

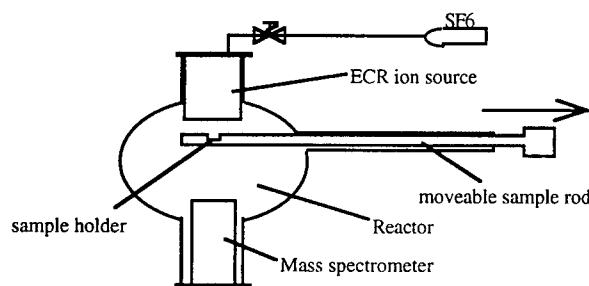


Figure 1 - Schematic drawing of the experimental setup

Reactor chamber is pumped down  $4.10^{-7}$  mbar. This pressure is measured with a Bayard-Alpert ionization gauge calibrated for nitrogen. When the SF<sub>6</sub> plasma is generated, the pressure is between  $3.10^{-5}$  and  $5.10^{-4}$  mbar according to the SF<sub>6</sub> gas flow injected in the source. This pressure is lower than the pressure in the plasma source because of the low conductance of the grids. The spectrometer, differentially pumped down  $10^{-7}$  mbar, consists of an electrostatic energy analyzer (0 to 500 eV) coupled with a quadrupole mass filter (0 to 500 u.m.a).

## 3. Results

### 3.1 Analysis of the ion beam

To limit the ion current coming into the spectrometer, the diameter of the aperture is reduced to 100  $\mu$ m. A correct fit of the parameters of the spectrometer allows to get a transmission factor independent of the ion mass. So the proportion of the different ions species is proportional to the intensity of each peak. Results are given in figure 2 and figure 3.

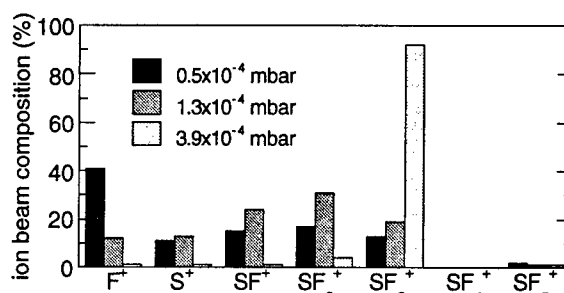


Figure 2 - Ion beam composition at 150 W microwave power for 3 SF<sub>6</sub> gas pressures.

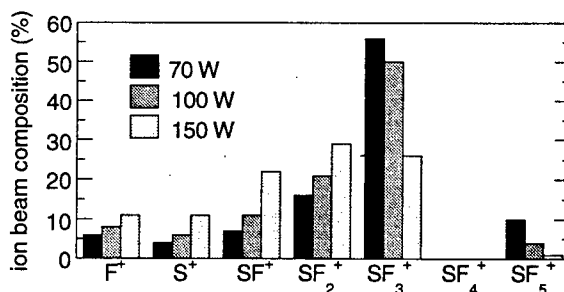


Figure 3 - Ion beam composition at  $1.3 \times 10^{-4}$  mbar for 3 microwave powers.

At low pressure, F<sup>+</sup> is the dominant ion (40%) whereas at higher pressure the fragmentation is less important and the proportion of SF<sub>3</sub><sup>+</sup> is the highest. The increase in the microwave power allows to get a higher proportion of low mass ions. These results are qualitatively consistent with those given by ref. [2]. The FWHM is lower than 10 eV for each peak.

### 3.2 Analysis of the neutral species

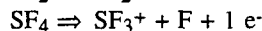
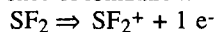
To avoid the penetration of the ions into the spectrometer, its aperture is biased positively and the conditions of beam extraction are chosen in the way to increase the broadening of the ion beam. The diameter of the aperture is 1 mm to achieve a high enough concentration of neutral species in the ionization chamber of the spectrometer. These neutral particles are partially ionized by electron impact. The energy of the

electrons can be adjusted between 10 eV and 70 eV. At 70 eV, the  $SF_5^+$ ,  $SF_4^+$ ,  $SF_3^+$ ,  $SF_2^+$ ,  $SF^+$ ,  $S^+$  and  $F^+$  ions are detected. The appearance potentials of the main ionic species created in the spectrometer have been measured (table 1) when no plasma is generated (plasma off) and when a plasma is generated in the ECR ion source (plasma on).

	$SF_5^+$	$SF_4^+$	$SF_3^+$	$SF_2^+$
plasma off	16	20	20.5	28
plasma on	15.5	20	13	11

Table 1 - Appearance potential in eV of  $SF_x^+$  ( $2 \leq x \leq 5$ ) under plasma on and off

In plasma off condition, the experimental values are in agreement with the measurements given by ref. [3] for the appearance potential of ions produced by electron impact dissociative ionization of  $SF_6$ . For  $SF_3^+$  and  $SF_2^+$ , differences appear between plasma on and plasma off. They are attributed to the existence of  $SF_2$  and  $SF_4$  radicals when the plasma is on according the following sequence of ionization:



Ionization energy of the first reaction is measured at 11 eV and is in agreement with the value of 10.1 eV calculated by ref. [4]. Dissociative ionization energy of the second reaction is measured at 13 eV. Theoretical estimation of this value can be obtained by summing the calculated values [4] of the  $SF_3$ -F bond energy (4.2 eV) and  $SF_3^+$  ionization energy (8.4 eV) which gives 12.6 eV. This value is close to our experimental value in plasma on. The rate of dissociation of  $SF_6$  in the ion source is calculated by:

$$R = \frac{H_{127}^{off} - H_{127}^{on}}{H_{127}^{off}}$$

With,  $H_{127}^{on}$  ( $H_{127}^{off}$ ) height of the  $SF_5^+$  peak in plasma on (plasma off) which is attributed to only  $SF_6$  gas and is proportional to  $SF_6$  pressure. High value of R (80%) is observed at low pressure and high microwave power (fig. 4) because the mean free path of electrons in the source is higher and thus the ECR effect is more efficient.

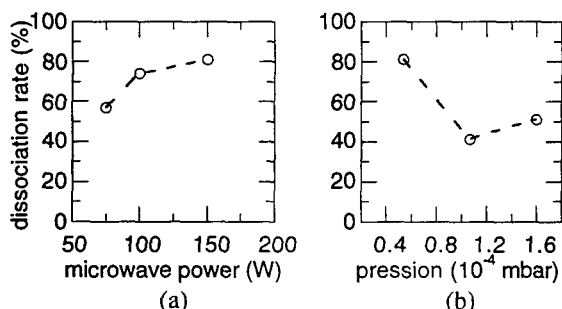


Figure 4 - Dissociation rate of  $SF_6$ :

- (a) for 3 microwave powers at  $1.3 \cdot 10^{-4}$  mbar  
(b) for 3 pressures at 150 W

This condition of operation corresponds to high value of the extracted beam current with a large proportion of  $F^+$  ions in the beam (fig. 2 and 3).

Concentration of  $SF_4$  and  $SF_2$  radicals has been estimated using:

- the mass spectrum of fragmentation of  $SF_6$  obtained in plasma off condition,
- the mass spectrum of fragmentation of  $SF_4$  given by ref. [5],
- the ratio of the cross section of dissociative ionization of  $SF_4$  ( $\Rightarrow SF_3^+$ ) over the cross section of dissociative ionization of  $SF_6$  ( $\Rightarrow SF_5^+$ ) estimated at 3.

The concentration of atomic fluorine is deduced from the difference between the total concentration of fluorine injected in the source (determined in plasma off) and the concentration of fluorine coming from  $SF_6$  in plasma on and coming from  $SF_4$  and  $SF_2$  radicals.

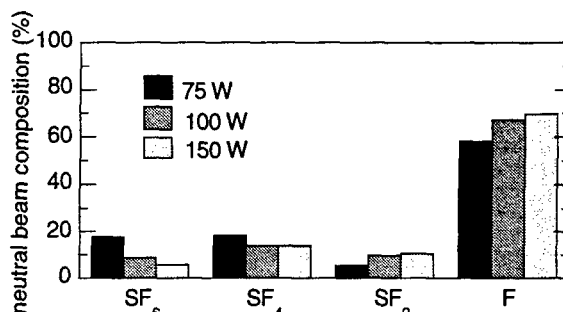


Figure 5 - composition of the neutral species

High proportion of fluorine is observed at  $5.3 \cdot 10^{-5}$  mbar and 150 W (fig. 5). This behavior is correlated with high rate of dissociation and high proportion of  $F^+$  in the beam. These conditions of operation have been chosen to study the RIBE of silicon [6]. The neutral flux of fluorine is roughly estimated at  $2 \cdot 10^{17} \text{ cm}^{-2} \text{ s}^{-1}$  using the measurement of the  $SF_6$  flow injected in the ion source and the knowledge of the dissociation of  $SF_6$  in the plasma (in our RIBE conditions, each  $SF_6$  molecules gives 2.3 F atoms on average). Since the current density of the beam is about  $5 \text{ mA} \cdot \text{cm}^{-2}$  [6], the ratio of the neutral flux of fluorine over the ion flux is evaluated at about 10. This result indicates the importance of the active neutral flux of fluorine in RIBE using  $SF_6$  gas.

### 3. References

- [1] F. Boukari et al., Nucl. Instr. and Meth. in Phys. Res. B101 (1995) 459
- [2] F. Boukari et al., "Le vide: science, technique et applications" 275 (1995) 329
- [3] B.P. Pullen and J.A.D. Stockdale, Int. J. Mass Spectrom. Ion Phys., 19 (1976) 35
- [4] K.K. Irikura, J. Chem. Phys. 102 (1995) 5357
- [5] W.H. Beattie, Applied Spectroscopy 29 (1975) 334
- [6] T. Chevolleau et al., Submitted to J. Vac. Sci. Technol. A

Special topic at the XXIII ICPIG :  
**High pressure, non-thermal plasmas.**

# Détermination of electron density and temperature of an E.C.R. plasma by V.U.V. spectroscopy

R. Berreby, D. Hitz, M. Druetta\*

Département de Recherche Fondamentale sur la Matière Condensée  
Service des Ions, Atomes et Agrégats/C.E.A. Grenoble  
17, rue des Martyrs  
38054 Grenoble cedex 9, France

\* Laboratoire du Traitement du Signal et Instrumentations  
Université Jean Monnet URA CNRS 842  
42054 St Etienne cedex, France

## Introduction

In Electron Cyclotron Resonance Ion Source, electrons are magnetically confined in a minimum-B structure. By interaction with a high frequency wave, they acquire energy enough to overcome the ionization potentials of neutral atoms and ions of the element injected in the source [1]. For a better understanding of E.C.R. plasma, it is important to determine the parameters that are responsible for the production of multicharged ions such as electron density and temperature. It is an acknowledged fact that E.C.R. plasmas always have cold electronic population. A V.U.V. spectrometer has been used to diagnose this population. After a presentation of the experimental set-up, we give some results in which electron density and temperature are determined according to a collisional radiative model [2].

## Experimental set-up

A 3 m grazing incidence spectrometer is connected perpendicularly to the plasma chamber of the Quadrumafios source [3], where most of the multicharged ions confined in the resonance zone could be observed, as shown in Fig 1.

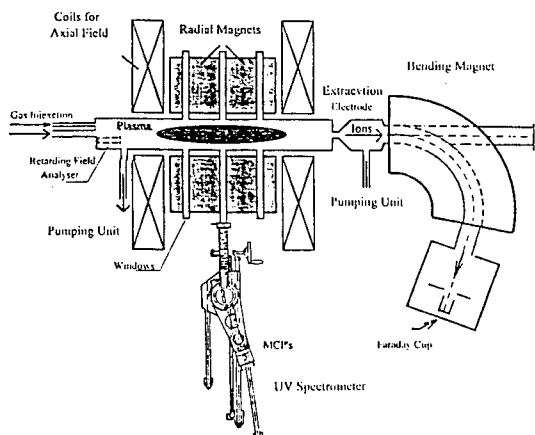


Fig 1. Quadrumafios source and V.U.V. spectrometer.

The spectrometer is equipped with a 600 grooves/mm grating blazed at 25.6 nm. The photons are detected by MCP's coated with  $MgF_2$ .

The relative calibration curve has been determined by the branching ratio method which is directly applied to the plasma of the source. The part of the curve below 30 nm has not been yet obtained because of very weak line intensities emitted by highly charged ions in this source. This to be realized soon with a more powerful multicharged ion source. The relative intensity calibration curve has the profile indicated in Fig 2.

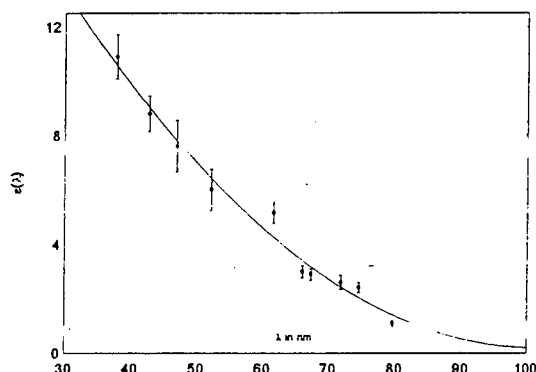


Fig 2. Relative intensity calibration curve for the 600 grooves/mm and MCP's.

## Results and Discussion

The intensity line ratios method applied to the O V ion, gives us an estimation of electron density and temperature according to the coronal hypothesis. The V.U.V. spectroscopy only analyses a low energy electron population that is responsible for the first excited levels of O V. Indeed, the photon energies detected by our system are from 15 to 120 eV.

We firstly present the line intensity ratios which have a dependance on electron temperature and density as a function of the injected R.F. power and the gas pressure inside the plasma chamber.

As shown in Fig 3, the intensity ratios depending on temperature increase with R.F. power, whereas, those depending on density are decreasing. These curves are not corrected by the efficiency calibration

but they give the evolution of electron temperature and density. The evolution of the  $O^{4+}$  extracted current intensity from the Quadrumafios source is also plotted on the graph.

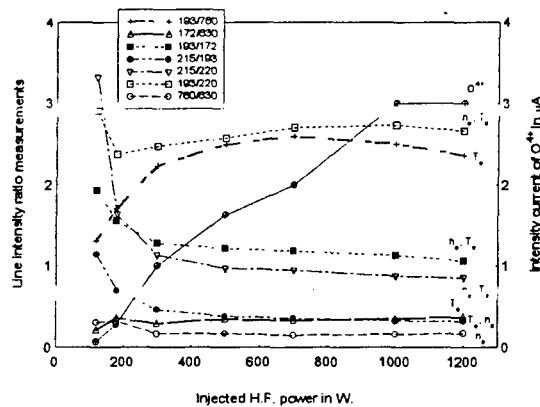


Fig 3. Line intensity ratio of O V in function injected H.F. power

The line intensity ratios that are only depending on  $T_e$  are 17.2/63.0 and 19.3/76.0 nm. These two ratios are a linear growing function of temperature. They increase by a factor 2 between 120 and 400 Watts then remain constant, while the  $O^{4+}$  beam current intensity is growing by a factor of about 50 from the ignition to 1200 W. When R.F. power is increasing the electron temperature should also grow up. This is observed at low power. The electron density is decreasing at low injected R.F. power and then remains constant. This electron density behavior was also observed on previous measurements made in our lab on Caprice source [4]. The 76.0/63.0 ratio is used to estimate the electron density because of the available part of the calibration curve. It varies from  $5 \cdot 10^{11}$  to about  $1.2 \cdot 10^{11} \text{ cm}^{-3}$  in the studied energy range.

Fig 4. shows the evolution of the same line intensity ratios, electron temperature and density dependant, as a function of  $O_2$  gas pressure into the plasma chamber.

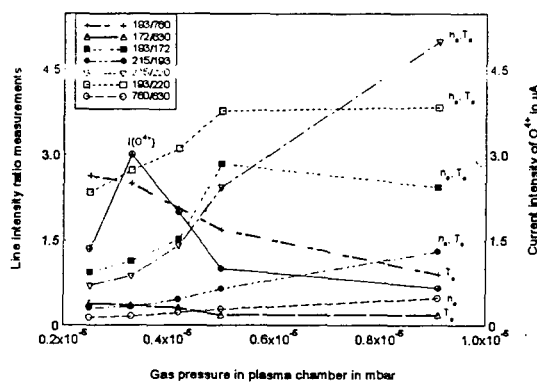


Fig 4. Line intensity ratio of O V versus gas pressure inside the plasma chamber

We note that the line intensity ratios which depend on electron density increase with the pressure and those which depend on electron temperature decrease with neutral pressure inside the plasma chamber. Among the line intensity ratios, some depend both on density and temperature. So we have taken into account the strongest dependency on these two parameters. The classical point of view generally adopted to explain the behavior of these curves, is that when gas pressure increases, collisions between electrons and other plasma particles also increase. Thus electrons loose their energy by collision processes. The electron temperature varies with gas pressure from 50 to 15 eV. The increasing electron density with the pressure can be explained by the higher production of low charged ions. We thus can imagine that cold electrons pulled out from neutral and monocharged ions are contributing to the electrons density which varies from  $3.5 \cdot 10^{10}$  to  $4 \cdot 10^{11} \text{ cm}^{-3}$ .

Microwave interferometer was also installed on the Quadrumafios source providing a total electron density which is increasing with R.F. power from  $2 \cdot 10^{11}$  to  $4.5 \cdot 10^{11} \text{ cm}^{-3}$ . This observed discrepancy relative to our results may come from the Maxwellian Electron Distribution Function used in the model. Therefore the excitation and ionisation rate coefficients calculated by theoretical method are no more valid. A recent paper by Sasaki et al. [5] shows effects of a hot electron tail on the line intensity ratios, applied to a heated R.F. helium plasma.

## Conclusion

V.U.V. spectroscopy is a non invasive powerful tool used in the investigation of E.C.R. plasma parameters. In the future work, we will be able to give the ionic densities for an oxygen plasma as a function of R.F. power and gas pressure. Consequently these results should provide an estimation of the ion confinement times and thus more insights about transport phenomena which occur in the plasma of E.C.R. Ion Source.

## References

- [1] R. Geller: IEEE Trans. Nucl. Sci. NS, 26, (1979), 2120.
- [2] T. Kato, J. Lang, K.E. Berrington: Atomic Data and Nuclear Data Tables, 44, (1990), 133
- [3] A. Girard et al. Review of Scientific Instruments 5, (1994), 65
- [4] M. Druetta, D. Hitz: J. Optics, (1992), 23, n°6, 259
- [5] S. Sasaki et al. Private communication

# Effect of partial discharges on sulfur hexafluoride (SF<sub>6</sub>) by-products

Clavreul. R, Hoang The Giam\*, Essolbi. R\*

Electricité de France, DER, Moret sur Loing, France

\* Laboratoire Genie Electrique. Université P. Sabatier, Toulouse. France

## 1. Introduction

SF<sub>6</sub> is the most commonly used gas for electrical insulation. In order to have the alternative for gaseous electrical insulation, we have compared sulfur hexafluoride (SF<sub>6</sub>) with the following gases : nitrogen (N<sub>2</sub>) and the mixture SF<sub>6</sub>/N<sub>2</sub> with 10 % SF<sub>6</sub>; traces of oxygen (O<sub>2</sub>) were systematically added to these gases. Partial discharges (P.D) have been produced in the test gases in order to determine precisely by analytical methods the nature of SF<sub>6</sub> and N<sub>2</sub> by-products and their quantity, and to deduce the real effects of toxic products. Experiments on SF<sub>6</sub>/N<sub>2</sub> mixtures by-products have already been carried out by M.C. Siddagangappa and R.J. Van Brunt [1] : the absolute production of SO<sub>2</sub>, SOF<sub>4</sub>, SOF<sub>2</sub>, SO<sub>2</sub>F<sub>2</sub> and NO, N<sub>2</sub>O was determined versus percent-by-volume concentrations of nitrogen between 0 and 100 %. In our study were introduced new parameters : temperature, pressure, partial discharges production time, traces of oxygen.

## 2. Production of partial discharges

A cell for the production of partial discharges with point-plane electrodes has been worked out by LGET : the combined effects of temperature, pressure and high A.C voltage have been taken into account (Figure 1).

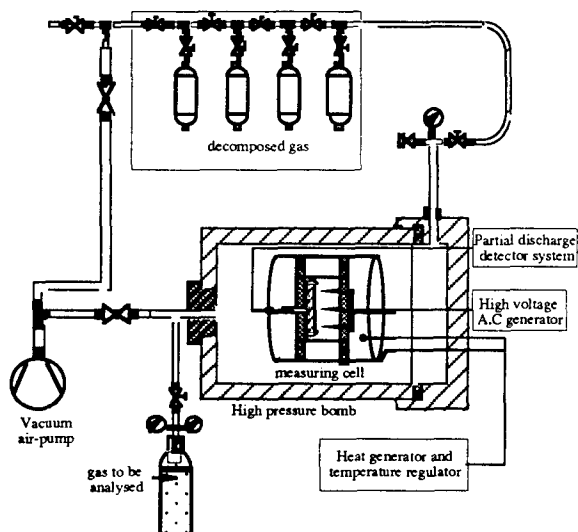


Figure 1. Apparatus for the production of partial discharges under pressure.

All the experiments have been done with point-plane electrodes and 2 mm air gap. Before filling up the cell with gas, a primary vacuum was obtained. A high A.C

voltage of 22 kV was then applied to 8 point electrodes of a mean radius about 10 µm in SF<sub>6</sub>, N<sub>2</sub> and SF<sub>6</sub>/N<sub>2</sub> mixture with oxygen traces pressurized at 6 bar absolute. The voltage across the discharge gap was continuously monitored and the current maintained at 100 µA. The variable parameters were the following : nature of the gas (nitrogen, SF<sub>6</sub>, SF<sub>6</sub>/nitrogen mixture with 10 % SF<sub>6</sub>), temperature (20 °C, 60 °C), partial discharges formation time (10h to 40 h), percent-by-volume of oxygen (300 ppmv, 3000 ppmv).

## 3. Analysis of SF<sub>6</sub>/N<sub>2</sub> mixture by-products

After the production of partial discharges in electrical insulation gases, we have proceeded to quantitative measurements of SF<sub>6</sub> and N<sub>2</sub> by-products with a precision of 5 % :

-The SF<sub>6</sub> by-products (SO<sub>2</sub>, SOF<sub>2</sub>, SO<sub>2</sub>F<sub>2</sub>...) have been analysed by gas chromatography with a detection threshold of about 10 ppmv;

The nitrogen by-products have been dosed by chemiluminescence with a detection threshold of 1 ppmv.

## 4. Experimental results

### 4.1 Effect of the partial discharges formation time in SF<sub>6</sub>/N<sub>2</sub> mixture with 10 % SF<sub>6</sub> and 3000 ppmv Oxygen

The concentration of the Oxifluoride SO<sub>2</sub>F<sub>2</sub> increase with partial discharges formation time from 10 to 40 hours. The total amount of toxic products is as more important as the P. D. formation time is long (Figure 2).

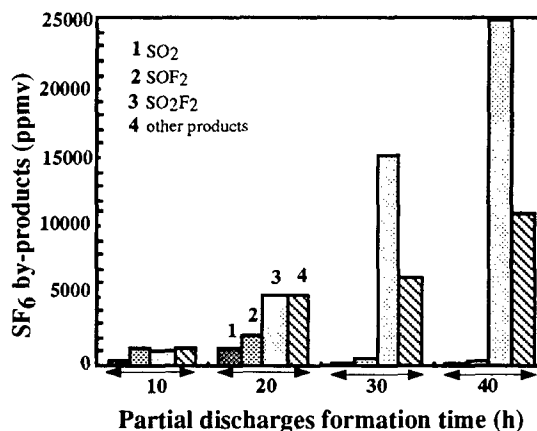


Figure 2. Effect of the P.D formation time in SF<sub>6</sub>/N<sub>2</sub> mixture

#### 4.2 Effect of the percent-by-volume concentration of oxygen in SF<sub>6</sub>/N<sub>2</sub> mixture with 10 % SF<sub>6</sub>

The percent-by-volume of oxygen from 300 ppmv to 3000 ppmv in SF<sub>6</sub>/N<sub>2</sub> mixture with 10 % SF<sub>6</sub> seems to have some significant effects on the formation of SF<sub>6</sub> by-products (Figure 3). We can notice that the total amount of oxygen in oxifluorides is more important than the concentration of oxygen we added in the SF<sub>6</sub>/N<sub>2</sub> mixture before the P.D. formation : traces of water may also contribute to the oxifluorides formation.

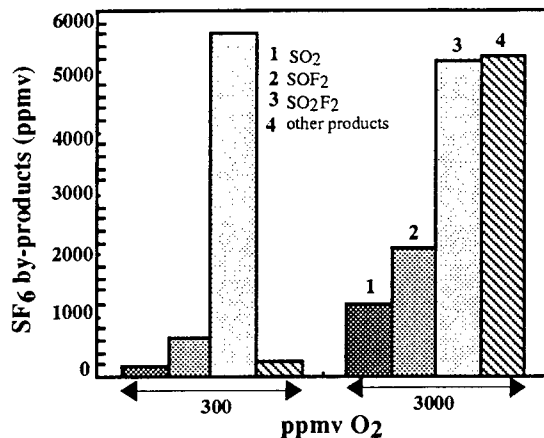


Figure 3. Percent-by-volume of SF<sub>6</sub> by-products in SF<sub>6</sub>/N<sub>2</sub> mixture with 300 and 3000 ppmv O<sub>2</sub>

#### 4.3 Effect of temperature in SF<sub>6</sub>/N<sub>2</sub> mixture with 10 % SF<sub>6</sub> and 3000 ppmv oxygen

The temperature between 20 °C and 60 °C in SF<sub>6</sub>/N<sub>2</sub> mixture with 10 % SF<sub>6</sub> and 3000 ppmv oxygen seems to have significant effect on the SF<sub>6</sub> by-products (Figure 4).

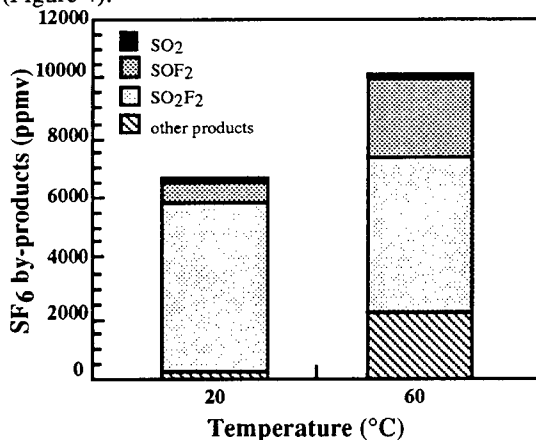


Figure 4. Percent-by-volume of SF<sub>6</sub> by-products in SF<sub>6</sub>/N<sub>2</sub> mixture at ambient temperature and 60°C.

#### 4.4 Effect of the nature of electrical insulation gas

Two gases have been studied : SF<sub>6</sub>/N<sub>2</sub> mixture with 10% SF<sub>6</sub> and 3000 ppmv oxygen, nitrogen with 3000 ppmv oxygen. The P.D. formation has been done during

20 hours at 60 °C. The following results have been obtained :

-N<sub>2</sub> : about 70 ppmv of toxic products (NO, NO<sub>2</sub>);

-N<sub>2</sub>/SF<sub>6</sub> : about 4000 ppmv of toxic products.

We can notice that the total amount of SF<sub>6</sub> toxic by-products is about 50 times the N<sub>2</sub> toxic by-products. We can also mention that SF<sub>6</sub> can lead to the formation of a very toxic product : S<sub>2</sub>F<sub>10</sub>. The very low quantity of this last product did not allow us to detect it by gas chromatography.

## 5. Conclusion

The experiments on partial discharges formation in SF<sub>6</sub>/N<sub>2</sub> mixture with traces of oxygen have showed that the predominant by-products are the oxifluorides SOF<sub>2</sub>, SO<sub>2</sub>F<sub>2</sub> and SO<sub>2</sub>. These by-products tend to increase with the partial discharges formation time and are stable. So, they induce a toxicity that is as more important as the P.D formation time is long. We could recommend to limit the formation of partial discharges in SF<sub>6</sub> gaseous insulated electrical equipments because several SF<sub>6</sub> by-products are very toxic.

## 6. References

- [1] M.C. Siddagangappa, R.J. van Brunt, "Decomposition products from corona in SF<sub>6</sub>/N<sub>2</sub> and SF<sub>6</sub>/O<sub>2</sub> mixtures", IEEE 1995.



# The Experimental Study of the Relaxation Processes in He with Admixture of O<sub>2</sub>

J. Glosík, G. Bánó, P. Zakouřil

Department of Electronics and Vacuum Physics, Mathematics and Physics Faculty, Charles University, V Holešovičkách 2, Prague 8, Czech Republic

## Introduction and experiment

Very effective tool for study of elementary processes in low temperature plasma is flowing afterglow (FA) technique. The flowing afterglow Langmuir probe (FALP) apparatus can be used to study kinetics of elementary processes where electrons take place. The High Pressure Flowing Afterglow (HPFA) apparatus used in presented experimental study is of the FALP type and was constructed to operate with buffer gas pressure up to 20 Torr. The apparatus consists of a glass discharge tube with microwave cavity discharge, adjacent metallic flow tube (30 cm long, 16 mm internal diameter) with axially movable Langmuir probe and mass spectrometer. The carrier gas, He in the present experiments, is purified by liquid nitrogen cooled molecular sieve trap. The plasma which is created in the microwave discharge is then carried down the flow tube with velocity 50m/s. 5cm along the flow tube corresponds to 1 ms of the decay time of the plasma. Immediately downstream from the discharge region Ar is added to the flow tube in order to remove metastable atoms and molecular He<sub>2</sub><sup>+</sup> ions (for details see ref. [1]). At the beginning of the "reaction region" He<sup>+</sup>/Ar<sup>+</sup> plasma is created. Via the entry port, situated 10 cm down stream from the discharge region, oxygen is added to the decaying plasma. The position of the reactant port is below referred as L=0. Typical electron temperature T<sub>e</sub>(L=0) ≈ 0.04 eV and electron number density N<sub>e</sub>(L=0) ≈ 1·10<sup>10</sup> cm<sup>-3</sup>. The principal diagnostic tool in HPFA is the Langmuir probe (14 micron in diameter and 4 mm long), which is used to measure N<sub>e</sub>, T<sub>e</sub>, and to determine electron energy distribution function f<sub>e</sub>(E) along the length of the column of the decaying plasma. The N<sub>e</sub> is determined from the slope of a plot of the square of the probe current versus the probe voltage. The f<sub>e</sub>(E) are calculated from the measured second derivative of the probe current, i, against probe potential, U, i.e. d<sup>2</sup>i/dU<sup>2</sup>. A linear plot of log of d<sup>2</sup>i/dU<sup>2</sup> against U is indicative of a Maxwellian f<sub>e</sub>(E); more generally the form of the plot indicates the actual f<sub>e</sub>(E). If f<sub>e</sub>(E) is not Maxwellian we use "effective" temperature, denoted as T<sub>eff</sub>, to characterize the body of the distribution. T<sub>eff</sub> is determined from the slope of the linear part of the semilogarithmic plot of measured second derivative (indicated by lines in the upper panel of Fig. 3).

## Results and discussion

When O<sub>2</sub> is added to the flow tube (at L=0) He<sup>+</sup> ions are rapidly converted to O<sub>2</sub><sup>+</sup> and O<sup>+</sup> ions. In the fast secondary reactions O<sup>+</sup> ions are converted also to O<sub>2</sub><sup>+</sup>. The reaction of Ar<sup>+</sup> with O<sub>2</sub> is slow. The formed O<sub>2</sub><sup>+</sup> ions recombine with electrons. This recombination is fast because the electron

density is high, N<sub>e</sub>(L=0) ≈ 1·10<sup>10</sup> cm<sup>-3</sup>. In Fig. 1 is plotted N<sub>e</sub> against the flow rate of O<sub>2</sub> for three fixed positions of the Langmuir probe (positions 6, 10, and 14 cm corresponds to 1.2, 2, and 2.8 milliseconds of the reaction-decay time, respectively).

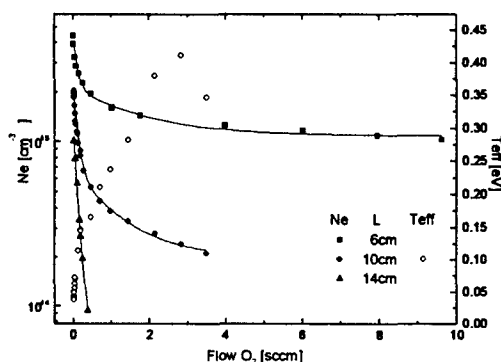


Fig. 1: The decay curves - decrease of the plasma concentration due to addition of O<sub>2</sub> (p<sub>He</sub>=11.7 Torr, flow rate Φ<sub>He</sub>=4550 sccm).

The rate of the observed rapid decrease of N<sub>e</sub> is determined by the rate of the reaction of Ar<sup>+</sup> with O<sub>2</sub>. The obtained reaction rate k = 5·10<sup>-11</sup> cm<sup>3</sup>s<sup>-1</sup>, this value is in good agreement with previous data (see compilation in ref. [2]). Only the fast decrease at the beginning of the decay curves, was considered in the determination of k, slow decrease at higher flow rate of O<sub>2</sub> is influenced by several processes and analyses of the data is more complicated. The measured T<sub>eff</sub> is also included in the Fig. 1, note fast increase of T<sub>eff</sub> with increasing flow rate of O<sub>2</sub>. The recombination preferentially removes slow electrons from the plasma and the average energy of the electrons is increasing, indicating that relaxation processes are not enough effective in order to cool down plasma. The measurements of the plasma parameters along the flow tube, at constant flow of O<sub>2</sub>, give further information about processes involved. In the upper panel of the Fig. 2 are plotted the plasma potential, V<sub>pl</sub>, and the floating potential, V<sub>f</sub>, as a function of the location - distance, L, from the reactant port.

In the lower panel of Fig. 2 is plotted the measured N<sub>e</sub> against L. Rapid decrease of N<sub>e</sub> due to the recombination corresponds with the rapid increase of V<sub>pl</sub>, and T<sub>eff</sub>. The exponential decay at L ≥ 2.5 cm (linear part in semilog plot, lower panel of Fig. 2) indicates that the dominant loss process is diffusion.

More detailed information concerning role of the energy of electrons in this "chemically active He-O<sub>2</sub> plasma" is given in Fig. 3, where measured d<sup>2</sup>i/dU<sup>2</sup> and f(E) are plotted. Note

that the obtained electron energy distribution functions are not Maxwellian.  $f_e(E)$  is close to Maxwellian for  $L \geq 2.5$  cm where diffusion is the dominant process.  $f_e(E)$  measured at  $L=3.25$  cm has local maximum at  $E=0.8$  eV, we assume that it is due to production of electrons in associative Penning ionization of remaining Ar metastables.

The presented experimental results will be used for verification of the model describing processes in He-O<sub>2</sub> plasma.

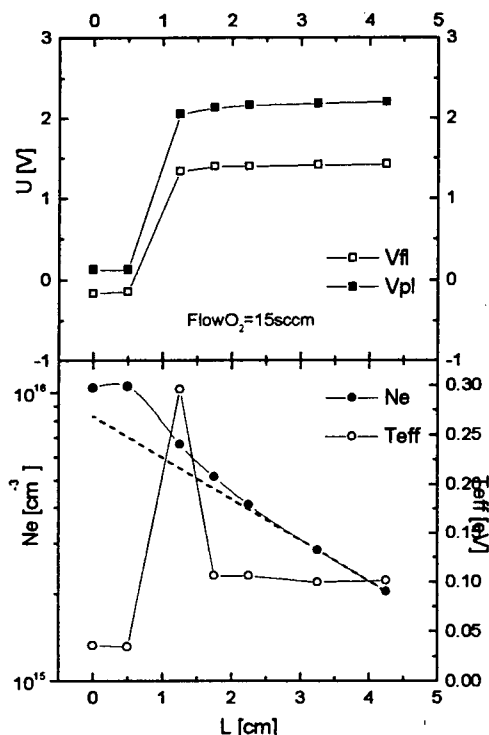


Fig. 2 Evolution of the plasma parameters along the flow tube ( $p_{He}=11.7$  Torr, flow rate  $\Phi_{He}=4550$  sccm).

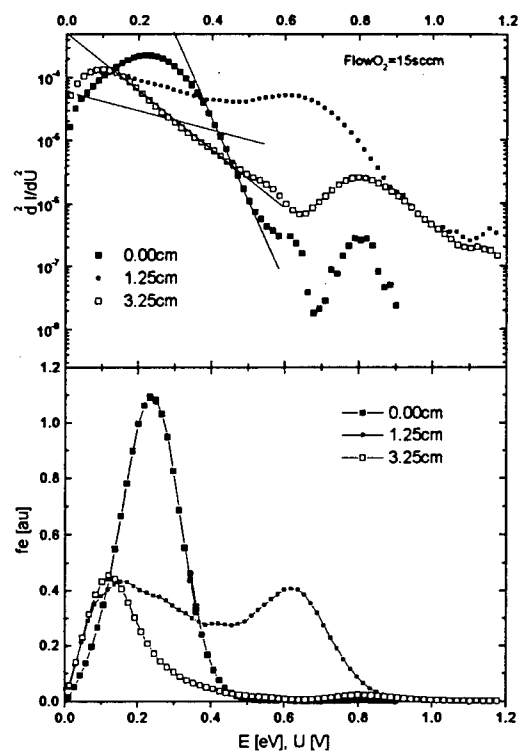


Fig. 3 Upper panel: The second derivative of the probe current,  $d^2i/dU^2$ , against probe potential,  $U$  in different positions along the flow tube.

Lower panel: The evolution of the electron energy distribution function,  $f_e(E)$ , along the flow tube, normalized to electron number density,  $N_e$ .

### Acknowledgement

This work was supported in part by the European Community through the COPERNICUS Grant No. CIPA-CT-94-0183, and in part by Charles University Prague under project No. GA UK 179/96

### References

- [1] J. Glosík, P. Zakouřil, V. Hanzal, V. Skalský, *Int. J. Mass Spec. Ion Proc.*, **149/150**, 187 (1995)
- [2] Y. Ikezoe, S. Matsuoka, M. Takebe, and A. Viggiano: *Gas Phase Ion-Molecule Reaction Rate Constants*, The Mass Spectroscopy Society of Japan, Tokyo (1987)

## OZONE PRODUCTION IN CYLINDER-TO-CYLINDER PROXIMITY BARRIER DISCHARGES IN OXYGEN.

P. Veis<sup>#</sup>, M. Goldman<sup>+</sup>, A. Goldman<sup>+</sup>, R. Haug<sup>+</sup> and L. Petit<sup>°</sup>

<sup>+</sup> Laboratoire de Phys. des Gaz et des Plasmas, URA 073 CNRS, SUPELEC, 91192 Gif-sur-Yvette, France

<sup>#</sup> Dept. of Plasma Physics, Comenius University, 84215 Bratislava, Slovakia

<sup>°</sup> Electricité de France, Centre des Renardières, 77250 Moret-sur-Loing, France

**Abstract:** Ozone production is studied in cylinder-to-cylinder proximity discharges in oxygen at atmospheric pressure. Up to 5-6 W/cm<sup>3</sup> of injected power density, the ozone yield increases with voltage amplitude and frequency to 180 g/kWh. Ozone concentration increases proportionally to the frequency up to 4 kHz.

### 1. Introduction

Different types of dielectric barrier discharges in various geometrical configurations (e.g. coaxial cylindrical or planar ones) are successfully used for ozone production. The role of the dielectric barrier is to prevent the streamer-to-arc transition and so to keep the plasma in low temperature conditions. Its presence implies the use of alternating voltages, with frequencies which have been varied from 50 Hz to 5 kHz [1]. To reduce the operating voltages, surface discharges [2] and dielectric pellets [3] were also used and investigations on a planar dielectric barrier discharge with minimised gaps performed [4]. An increase in ozone yield from 107 g/kWh to 150 g/kWh was found in the last case when decreasing the gap from 1.35 mm to 0.2 mm. Corresponding concentrations were not reported; it was only mentioned that a saturation appeared at 2.3 % vol. ozone for a gap of 0.2 mm [4].

A few years ago [5], dielectric barrier discharges in a cylinder-to-cylinder configuration with an insignificant discharge gap were developed in our laboratory. These discharges, called «proximity discharges», were at first studied at 50 Hz and then at higher frequencies, up to 2000 Hz [6]. The main advantage of proximity discharges, compared with other types of barrier discharges, is their low onset voltage.

### 2. Experiment

A dielectric barrier discharge between two Cu wire electrodes (respectively 1 and 2 mm diam., 40 cm length and put side by side in contact) covered with a polymer layer (20 µm thickness) was used as the ozonizer unit. The discharge gap was thus as small as possible on their line of contact and laterally increasing with the distance from this line outwards. These electrodes were placed inside a Teflon tube under flowing technical grade oxygen (99.9% purity). No additional drying was used. The reactor walls, the injected gas and one of the electrodes were cooled; gas temperature at the exit of the reactor before switching on the discharge was 7 °C. Gas flow was 0.49 Ndm<sup>3</sup>/min and gas pressure 10<sup>5</sup> Pa.

A digital memory storage oscilloscope type TDS 544 A from Tektronix was used for the determination of the

discharge power consumption, by means of the area of the Lissajous' figure, using the relation :

$$P [W] = \langle \text{area } U_x U_y \rangle [V^2] R_{HV} C_0 [F] f [Hz]$$

where  $f$  is the frequency of the applied voltage,  $R_{HV}$  the dividing ratio of the high voltage probe,  $C_0$  the capacity used for current integration. The results were compared in our previous work [6] with those provided by multiplication of the discharge current by the voltage in instantaneous values. Values obtained are within an error range of  $\pm 10\%$ . The electrodes were supplied with an AC voltage of different frequencies between 50 Hz and 4 kHz. The high voltage generator was described in [6]. After onset (peak-to-peak applied voltage  $U_{ppo} \approx 2.32$  kV), the discharge appears between the wires along their whole length. Coming out from the oscilloscopic measurements, the discharges are dominated by streamers, taking place in both half-periods of the applied voltage, according to which wire electrode is playing a role of anode. An intense capacitive current was observed, but no current synchronous with the voltage. Hence the measured power is mainly due to the streamer current and the power measurements can be used to evaluate the RMS streamer current by simply dividing the mean power by the RMS voltage.

Ozone concentration was measured by means of UV absorption using the 253.7 nm wavelength radiation with a Perkin-Elmer Lambda 15 UV-VIS spectrophotometer; two different gas cells (10 cm and 1 mm length) were used for low and high ozone concentration measurements respectively. These measurements were verified by IR absorption spectroscopy [6]; values were within an error range of  $\pm 5\%$ .

### 3. Results

With our electrode configuration and operating conditions, ozone production was seen to increase with the injected power up to a critical production limit of 0.15 g/h (corresponding power length density  $\approx 2.5$  W/m and concentration  $\approx 0.3\%$  vol.), and only then the gas temperature starts to increase and the yield to decrease subsequently. Fig. 1 shows ozone concentration as a function of injected power (with variable applied voltage amplitudes and frequencies, that gives a large explored field). This ozone concentration proportionally increases with the

injected power :

$$[O_3]/[O_2] \cong \text{const} (U_{PP}, f) * P[W]^{(1.077 \pm 0.03)}$$

Below the critical production limit, gas temperature remains quite constant and the ozone energetic yield increases from 100 g/kWh up to 180 g/kWh with power density (fig. 2 presents the yield increase with voltage and frequency). Fig. 3 shows the ozone concentration vs. the mean streamer current for constant values of the applied maximal voltage  $U_{PP}$  (variable frequency  $f$ ,  $U_{PP}=\text{const.}$ ). The ozone concentration is seen to increase with the mean streamer current as:

$$[O_3]/[O_2] \cong \text{const} (U_{PP}) * I_{RMS}(f)^{(1.04 \pm 0.03)}$$

On the contrary, if the frequency  $f$  is kept constant (variable peak-to-peak applied voltage  $U_{PP}$ ), the ozone concentration vs. the mean streamer current (fig. 4) can be expressed as :

$$[O_3]/[O_2] \cong \text{const} (f) * I_{RMS}(U_{PP})^{(1.45 \pm 0.1)}$$

#### 4. Concluding discussion

Cylinder-to-cylinder proximity barrier discharges are produced in a variable gap, which varies from practically zero (during the discharge ignition) up to a length equal to several times the radius of the wires. With the increase of the applied voltage during half-periods, the discharge can expand to the whole inter-electrodes volume, the first streamers produced on the line of contact of the wires providing seeds for longer streamers to develop, between the wire electrodes farther out of this line. This is illustrated by figs. 3-4, which show that the ozone concentration increases more rapidly with the applied voltage than with the frequency.

The increase of ozone yield with the applied voltage amplitude (fig. 2), should be explained by the decrease of the power volume density with the lateral expansion of the discharge. Inversely, the critical limit in the ozone production (fig. 1) should be due to the high power volume density which reaches about 4 W/cm<sup>3</sup> at this limit.

**Acknowledgements** The authors gratefully acknowledge help received from Electricité de France with a financial support.

#### 5. References

- [1] B.Eliasson, M.Hirth and U.Kogelschatz; J.Phys.D 20 (1987) 1421
- [2] C.Yamabe,N.Katsuki,S.Ihara,M.Ishimine,S.Satoh; 11<sup>th</sup> Conf.Gas Disch., Tokyo (1995) II-312
- [3] K. Schmidt-Szalowski, S. Jodzis; 4<sup>th</sup> Int. Symp. High Press. Low Temp. Plasma Chem. - HAKONE, Bratislava (1993) 37
- [4] K.V.Kozlov, T.Opalinska; 9<sup>th</sup> Int. Symp. Plasma Chem., Pugnoliuso (1989) 202
- [5] M.Lécuiller, M.Goldman, A.Goldman, R.Haug K.Amara; 3<sup>th</sup> HAKONE, Strasbourg (1991) 73
- [6] P.Veis,M.Goldman,A.Goldman,R.Haug,L.Parissi, L.Petit, 5<sup>th</sup> HAKONE, Milovy (1996) 320

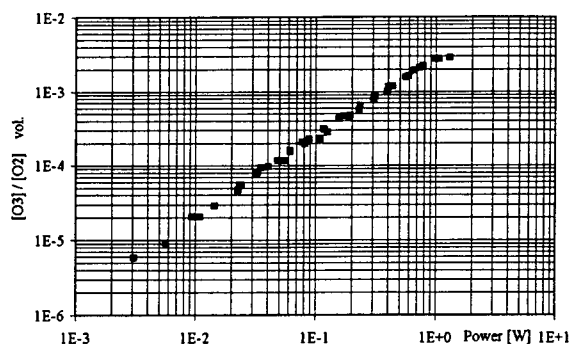


Fig. 1. Ozone concentration versus injected power.

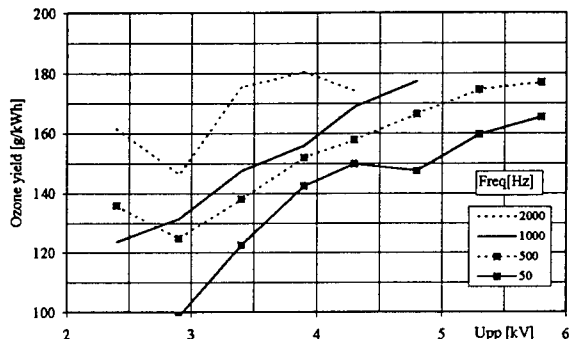


Fig. 2. Ozone energetic yield vs. applied maximal voltage  $U_{PP}$  and frequency  $f$ .

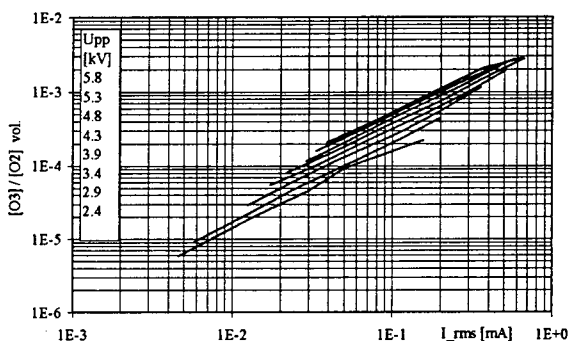


Fig. 3.  $O_3$  concentration vs.  $I_{RMS}$  by varying  $f$ .

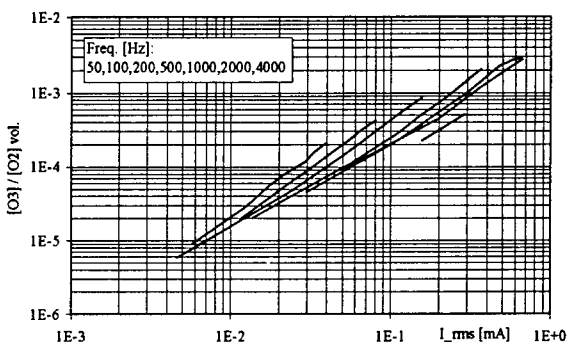


Fig. 4.  $O_3$  concentration vs.  $I_{RMS}$  by varying  $U_{PP}$ .

# Diagnostic of a plasma display panel cell : Spectroscopic and kinetic study. Electric study of light efficiency.

A. Hirech, V. Destombes

Ph. Guillot, J. Galy and H. Brunet

Centre de Physique des Plasmas et Application de Toulouse (E.S.A. 5002), UPS,

118 Rte de Narbonne 31062 Toulouse Cedex, France

Email: hamid@cpa01.ups-tlse.fr

## Abstract

This work presents an experimental study of color AC plasma display panel cell. After the description of some flat display devices, we present a first study of spectroscopic and kinetic properties of the UV-Visible light. A second study deals with the influence of the composition of Ne-Xe and Ne-Kr-Xe mixture on light efficiency.

## 1. Introduction

Plasma display panels are flat display devices where the light of each picture element is emitted from plasma created by an electric discharge. The dimensions of the discharge can be in the 100  $\mu\text{m}$  range at a pressure of a few hundred Torr. The performances of plasma displays have been constantly improved during three decades, and they are now serious competitors in the race of market of large size hanging high definition monitors.

Plasma displays [1,2] consist of two glass plates, each with parallel electrodes deposited on their surfaces. The plates are sealed together with their electrodes at right angles, and the gap between the plates is filled with rare gas mixture. Each picture element, at the intersection between a line and a column electrode, can be illuminated independently when a voltage pulse is applied between two electrodes. The voltage pulse leads to the electrical breakdown of the gas and to the formation of a weakly ionized plasma which emits UV light. This light is used to excite phosphors in the three fundamental colors. Rare gas mixture used are generally based on xenon, where photons emitted by  $\text{Xe}^*(^3\text{P}_1)$  at 147 nm, upper vibrational levels of  $\text{Xe}_2^*(^1,3\Sigma_u^+)$  at 173 nm are used to excite the phosphors.

## 2. Experiment

While applying the appropriate electric signal to the electrodes, the energetic electrons excite gas mixture atoms giving rise to an emission of UV photons lying in the [150-200 nm] range. This range of wavelength is covered by a monochromator in vacuum. Photons are detected using a photomultiplier working under low illumination conditions (single photoelectron method).

## 3. Study of the neon-xenon mixture

While the discharge occurs, an integrator allows the measurement of the discharge inherent current. Time evolution of the current pulse, for a given plasma display, is illustrated in Fig. 1. The pulse is very intense and very short (about ten nanoseconds).

Figure 2 presents the variation of luminescence for a Ne-Xe mixture. The UV light is emitted by xenon. The intensity of this light increases with the ratio of xenon. Figure 3 shows the influence of the ratio of xenon in the mixture on the light efficiency.

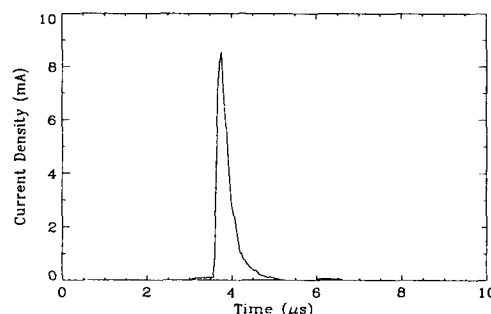


Fig.1. Discharge current density of hundred cells, as a function of time for a discharge in a Ne-(10%)Xe mixture. Conditions: total gas pressure 560 Torr.

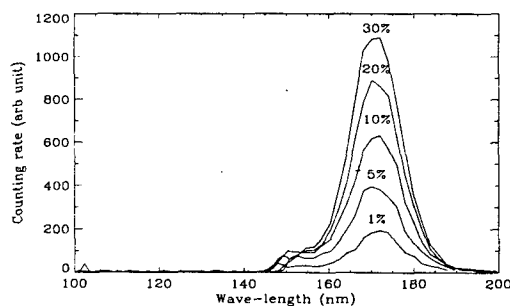


Fig. 2. Emissions spectra as a function of the ratio of xenon (same Conditions: as in Fig. 1).

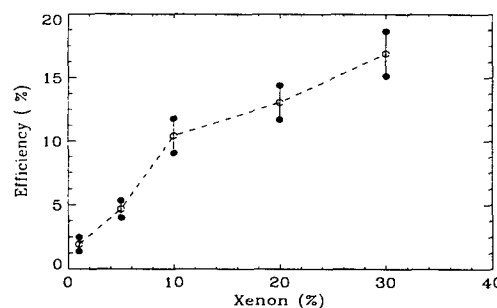


Fig. 3. Efficiency of the discharge in producing UV photons, as a function of ratio of xenon (same Conditions: as in Fig. 1).

Increasing the ratio of xenon improves the light efficiency but involves high electrical breakdown, leading to damages on the magnesium monoxide layer.

#### 4. Study of Ne-Kr-Xe mixture

In order to improve the performances of the plasma display and to preserve the MgO layer from ionic bombardment, we study the effect of adding some krypton to Ne-Xe mixture on the electric and emission characteristics. Fig.4 presents the ternary mixture emissions spectra for various ratio of krypton.

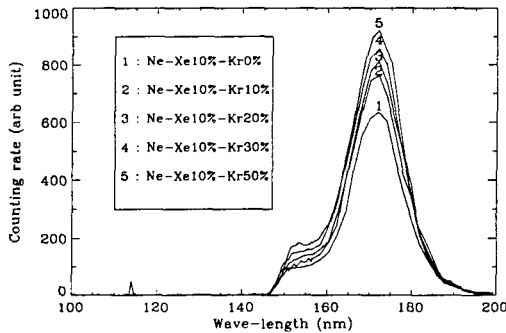


Fig. 4. Emissions spectra as a function of the percentage of krypton in Ne-Kr-Xe(10%) mixture; total gas pressure 560 Torr.

The observed emissions still correspond to xenon as a result of a transfert from the lighter gas to the heavier. Fig. 5. illustrates the influence of adding some krypton to a binary mixture, on light efficiency. Krypton improves light efficiency for 20 to 30%.

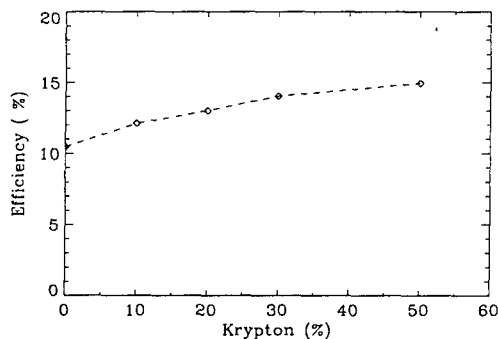


Fig. 5. Efficiency of the discharge in producing UV photons, as a function of percentage of krypton in Ne-Kr-(10%)Xe mixture; total gas pressure 560 Torr.

#### 5. Study of Ne-Kr mixture

The study of the ternary mixture enlightens the fact that krypton improves the plasma display performances. The first stage consists in a study of the kinetic and spectroscopic properties of the Ne-Kr mixture. Then we focus on the ternary mixture, to finally end up with the modelisation of the middle. From the kinetic study, we derive a kinetic model for the involved reactions. Spectra of the Ne-Kr mixture are presented in Fig. 6. This time, the excitation source is radioactive (alpha) [Fig.6(a)].

The resulting spectra only show krypton emissions. The increase in krypton ratio leads to an enhancement of radiations. Similar results are obtained for an excitation of the middle by a plasma display [Fig.6(b)]. We conclude that luminescence and mode of excitation are independant.

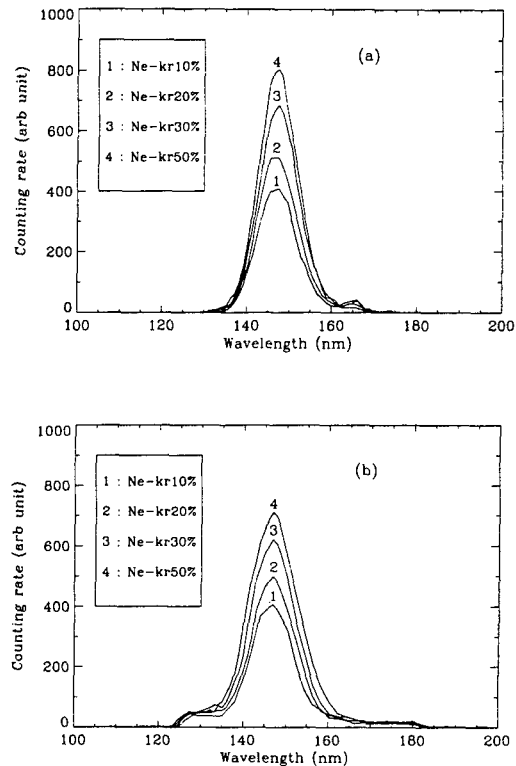


Fig. 6. Emissions spectra as a function of the percentage of krypton in Ne-Kr mixture; gaz pressure 560 Torr, excitation source (a) alpha particles (b) plasma display.

#### 6. Conclusion

We have studied the electric and emission properties of the Ne-Xe mixture. Light efficiency increases with the ratio of xenon. In order to increase the lifetime of the plasma display, we have studied the influence of adding some krypton on the discharge. The kinetic study of the Ne-Kr mixture allows a modelisation of the ternary mixture. We are still carrying the study of the ternary mixture.

#### 7. References

- [1] L.F Weber, in Flat Panel Displays and CRT's, edited by L.E Tannas, Jr. (Van Nostrand Reinhold, New York, 1985), p. 322.
- [2] A. Sobel, IEEE Trans. Plasma Sci. **PS-19**, 1032 (1991).

# The One Atmosphere Glow Discharge As A Sterilization Agent

M. Laroussi & I. Alexeff

Microwave & Plasma Laboratory  
University of Tennessee  
Knoxville, TN 37996, U.S.A.

K. Gillispie & Gary S. Saylor

Center for Environmental Biotechnology  
University of Tennessee  
Knoxville, TN 37932, U.S.A.

## 1. Introduction

This paper describes the generation of a uniform glow discharge at atmospheric pressure [1], and its use to effectively destroy microorganisms. The fact that no vacuum system is used to generate the discharge makes the apparatus very practical and inexpensive to build. Among the various potential industrial applications of this kind of plasma, investigations of its capability to sterilize contaminated matter, have been recently conducted [2]-[5].

## 2. Using the Discharge as a Sterilization Agent

Corona discharges and R.F. discharges have already been tested as sterilization means. However most R.F. discharges are operated at pressures below one atmosphere, and corona discharges have a small reactive volume, which renders them not suitable for large industrial applications. The One Atmosphere Glow Discharge, developed at the University of Tennessee Plasma Laboratory [1], combines the advantages of a large reactive volume, a relatively low input power, and the absence of a vacuum system.

The plasma in the One Atmosphere Glow Discharge (see Fig. 1) is generated between two plate electrodes, at least one of which is insulated by a dielectric material. The two electrodes are powered by a low frequency R.F. source (1 to 100 KHz). It is found that when the source frequency is within a narrow range, a uniform glow discharge fills up the gap between the electrodes. The frequency range is set by the gap distance between the electrodes, the applied RMS voltage, and the type of gas used. Outside this frequency range, the discharge becomes filamentary, or unstable. The typical input power is in the 50-150 W range, and the plasma power density, which is a function of the frequency and the RMS voltage, is in the 10-80 mW/cm<sup>3</sup> range. Usually, the electrodes setup is contained within an enclosure with a gas inlet port and an exhaust port. The discharge can be

operated in air, or a mixture of air and another gas such as helium, argon, etc... The gap between the electrodes is adjustable so as to accommodate the medium to be treated.

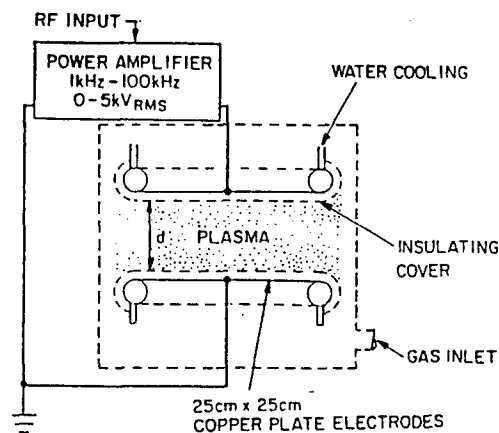


Fig. 1 One Atmosphere Glow Discharge Reactor

The plasma generated by the One Atmosphere Glow Discharge is a source of reactive free radicals, charged particles, and radiation. The free radicals interact with microbial cells at the molecular and atomic levels, inducing lethal changes to the chemical composition of the cells. Also, serious lesions and complete fragmentation of the cells have been observed. Hence, the discharge constitutes a very destructive environment for microorganisms with which it comes in contact. Laroussi et al. [2]-[4], and Ku et al. [5] have exposed various media contaminated by various types of bacteria. Sterilization was

achieved in less than 10 minutes in most cases, and in as low as 15 seconds in some cases.

The results obtained so far, indicate that the One Atmosphere Glow Discharge can be used as a sterilization apparatus. The absence of a vacuum system makes it practical and inexpensive, and the short treatment times makes it more versatile, more effective, and more practical than most presently used methods. Finally, this new method poses no environmental drawbacks, since no toxic byproducts or residues are generated in the process.

### 3. References

- [1] J. R. Roth, M. Laroussi, and C. Liu: Proc. IEEE Int. Conf. Plasma Sci., (1992), 170-171.
- [2] M. Laroussi: Bull. Amer. Phys. Soc. **40**, (1995), 1685-1626.
- [3] M. Laroussi: IEEE Trans. Plasma Sci. **24**, (1996) 1188-1191.
- [4] M. Laroussi, et al.: Bull. Amer. Phys. Soc. **41**, (1996), 1539-1540.
- [5] Y. Ku, et al.: Proc. IEEE Int. Conf. Plasma Sci. (1996), 175.

---

Work supported in part by the United States Air Force Office of Scientific Research.



# Theoretical and experimental investigation of a discharge with liquid nonmetallic electrodes in air at atmospheric pressure.

V.P.Afanas'ev<sup>2</sup>, P.Andre<sup>1</sup>, Yu.A.Barinov<sup>2</sup>, G.Faure<sup>1</sup>, V.B.Kaplan<sup>2</sup>, A.Lefort<sup>1</sup>, S.M.Shkol'nik<sup>2</sup>.

1. LAEPT, CNRS URA 828, University Blaise Pascal, 24, Avenue des Landais, F 63177 Aubière cedex, France.

2. A.F.Ioffe Phys.-Techn. Inst. Rus. Acad. Sci., Politechnicheskaya 26, Petersburg 194021, Russia.

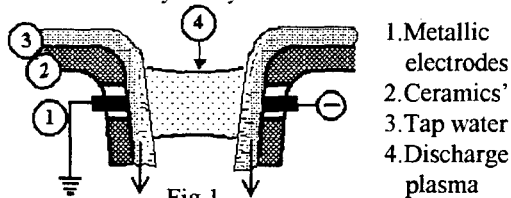
## 1. Introduction

The discharge with liquid nonmetallic electrodes (DLNME) has unique properties. It is self-maintaining discharge, which even at atmospheric pressure in air keeps the volumetric (diffuse) form of burning. DLNME till now is scanty investigated. The published results concern to discharge with one liquid electrode, as a rule with the liquid cathode [1]. The integral characteristics of discharge are measured mainly. The interest to researches of discharge is stimulated by opportunities of technical use [2] and in particular by prospect of use for the solving of such ecological problems, as monitoring of technical and waste waters composition, analysis and clearing of waste gas flows [3].

The present work aims at investigation of plasma parameters of discharge in the most simple for the analysis case - DLNME with electrodes from tap water.

## 2. Experimental technique

Discharge between two flows of tap water (fig.1) was investigated at d.c.  $I \approx 50\text{mA}$  in air at atmospheric pressure. The metal anode was grounded. On the cathode there was the voltage  $U \approx 3\text{kV}$ . The ballast resistor  $10\text{k}\Omega$  was used in series. The metal electrodes were covered by a layer of water of thickness 3mm.



Interelectrode gap (distance between water surfaces) was  $L \approx 8\text{mm}$ . The emission spectrum of discharge was registered with the spectral resolution  $\approx 0.15\text{nm}$ . Into discharge cylindrical probe  $d=2a=0.3\text{mm}$  in diameter and  $1\text{mm}$  length was short-term entered.

## 3. Experimental results and discussion

The discharge burns in volumetric (diffuse) form, diameter of the luminous channel is about 6mm. The axial dependence of probe floating potential  $V_f$  is shown on fig.2. We notice that discharge is non-uniform in an axial direction. Measured in a central

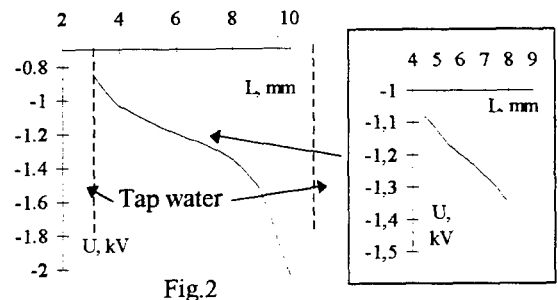


Fig.2

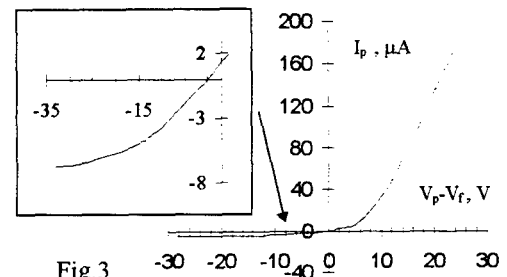


Fig.3

region of discharge volt-ampere probe characteristic is shown on fig.3.

Analysis of probe characteristic shows that current transfer in discharge is provided by electrons. The same result gives the calculation of plasma composition (see 4 Theory), according to which the concentration of negative ions is negligible, carriers of negative charge are electrons, and positive - ions  $\text{NO}^+$ . The estimation of recombination length of  $\text{NO}^+$  gives:  $L_r \approx 10^{-3}\text{cm} \ll a$  ( $a$  - probe radius). Therefore at a collection of an electronic current the main contribution to a difference between potential of plasma  $V_{pl}$  and probe  $V_p$  is made by nonperturbed plasma area, in which current transfer has a drift character, in contrast with near probe layer, in which nonquasineutrality of plasma and diffusion of charges is essential. In this case probe volt-ampere characteristic at  $V_p > V_f$  should be linear, as is observed in experiment. The theory [4] allows to determine from a linear plot conductivity of plasma and potential of plasma:  $V_{pl} \approx V_f$ . Thus it is possible to consider, that on fig.2 distribution of potential of plasma is shown and to determine an electrical field in the gap. The positive ion concentration was estimated from an ion current at  $V_p < V_f$ . The theory of probe ion current which accounts for ion generation in a probe layer was used [5].

The emission spectrum was measured in an interval (250-900)nm. In a spectrum the molecular bands of  $\text{N}_2$  (2+system),  $\text{N}_2^+$  and  $\text{OH}$ , and also spectral lines of atoms H, O and metal impurity contained in water were

observed. The second positive system of  $N_2$  was used for determination of rotation  $T_{rot}$  and vibration  $T_{vib}$  temperatures, and relative intensity of lines  $H_\alpha$  and  $H_\beta$  for an estimation of  $T_{at.ex.}$ -atomic excitation temperature  $T_{at.ex.}$  was determined in assumption of Boltzmann distribution on exited levels. Treatment of molecular spectra was carried out by comparing the recorded spectra with those calculated [6]. At all estimations we supposed, that the electron distribution function was Maxwellian,  $T_{vib}$  of a electronically-excited level  $C^3\Pi_u$  of a  $N_2$  was close to  $T_{vib}$  of the ground level. Lacks of such assumptions are obvious. The further work will be directed on derivation of the approach more adequate to examined conditions.

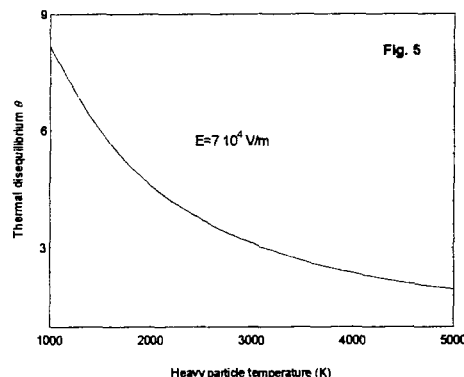
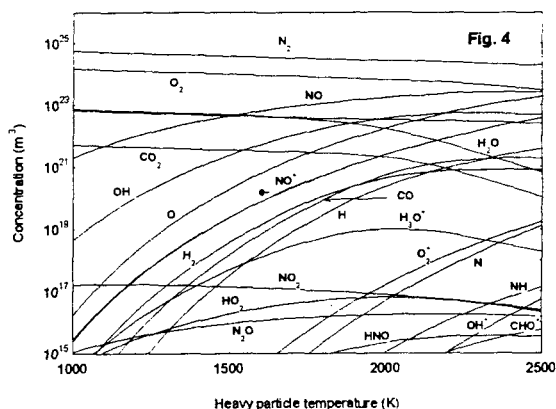
Results of measurements: DLNME consists of three approximately equal extent areas: cathode ( $E \approx 4 \text{ kV/cm}$ ) and anode ( $E \approx 2 \text{ kV/cm}$ ), the electrical field in which is variable along an axis, and column of discharge with approximately constant  $E \approx 0.7 \text{ kV/cm}$ . Concentration of charged particles in a column from an electronic branch of probe characteristic  $n \approx (4 \div 6) \cdot 10^{11} \text{ cm}^{-3}$ , from an ionic branch  $n \approx (1 \div 2) \cdot 10^{12} \text{ cm}^{-3}$ . The estimation from measured  $E/p$  and  $j$  gives  $n \approx 10^{12} \text{ cm}^{-3}$ . Temperature  $T_{rot} \approx 1000\text{-}1500 \text{ K}$ ,  $T_{vib} \approx 3000 \text{ K}$ ,  $T_{ex.at.} \approx 4200 \text{ K}$ .

#### 4. Theory

If the pressure and the temperatures are maintained constant, the chemical equilibrium is reached when the Gibbs free energy is minimum. The Gibbs free energy depends on the concentration of the species. So with two other equations: Dalton law and electrical neutrality, we can determine the concentration versus the heavy particle temperature [7]. We can introduce a parameter  $\theta$  that is the ratio between the temperature of free electron  $T_{tr.e-}$  and the heavy particle translation temperature  $T_{tr.h.}$  this parameter characterised the thermal disequilibrium. As regard the internal temperature we have made the following hypothesis:  $T_{ex}^{diat} = T_{ex}^{at} = T_{tr.e-}$ ;  $T_{rot} = T_{tr.h}$  and  $T_{vib} = 2.5 \cdot T_{tr.h}$ .

The figure 4 shows the composition for a thermal disequilibrium of 3.5 and for a mixture of 1 % water and 99 % of atmospheric air. We note that the electrical neutrality with the electron is done with  $NO^+$ .

In a purpose to evaluate the thermal disequilibrium, we have equalized the energy gained in the electrical field by the electrons with the energy delivered during the collision of the electrons with the heavy particles [8]. We show the results in figure 5 for an electric field of  $7 \cdot 10^4 \text{ V/m}$ . The thermal disequilibrium takes a value included between 8.5 to 6 for a heavy particle temperature of 1000 to 1500 K.



#### 5. Conclusion

The study of discharge with liquid nonmetallic electrodes is very complex. The first experimental results show that the electrical field is high ( $\geq 0.7 \text{ kV/cm}$ ) and that the plasma is out of thermal equilibrium ( $\theta \geq 3.5$ ). The composition calculation seems to give results in accordance with those experimentally obtained but this is not the case of thermal disequilibrium calculation. So this calculation have to be upgrade.

#### 6. References

- [1] F.M. Gaysin, E.E. Son, Sverdlovsk, Russia, Ural Univ. Publ., (1989) 432p.
- [2] R.G. Khakimov: The characteristic of plasma electro-heat unit with liquid electrodes. Thesis, St. Petersburg Tech. Univer, Russie (1993) (in Russian)
- [3] Yu.A. Barinov, I.O. Blinov, G.A. Dyuzhev, S.M. Shkol'nik: Proc. Conf. Physics and Technology of Plasma, Minsk, Belarussia, 1 (1994) 123 (in Russian)
- [4] M.S. Benilov: High Temperature, 26 (1988) 993
- [5] F.G. Baksht, G.A. Dyuzhev, N.K. Mitrofanov, S.M. Shkol'nik, V.G. Yur'ev: Sov. Phys.-Tech. Phys., 18 (1974) 1617
- [6] G. Faure, H Coitout, Spectroscopy Letters, 29 (1996) 1201
- [7] P. André, IEEE Trans. Plas. Sci., 23 (1995) 453
- [8] Finkelunburg W, Maecker H, Handbuch der Physik, 32 (1956) 306

## Electrical behavior of a Dielectric Barrier controlled Atmospheric Pressure Glow Discharge

Philippe Decomps, Françoise Massines and Christian Mayoux.

Laboratoire de Genie Electrique, Universite Paul Sabatier 118 route de Narbonne 31062 Toulouse cedex, France

The objective of the present study is to better define the behavior of a glow discharge controlled by a dielectric barrier and obtained at atmospheric pressure [2, 5]. The intended application is for a homogeneous treatment of polypropylene films in view of increasing its wettability and its adhesion.

### 1. Experimental conditions :

In a discharge cell, [1, 4], the glow discharge is obtained between two dielectric-covered plane electrodes.

Before filling the discharge cell with helium (Air liquide, type C), a primary vacuum is created. The residual pressure is 0.1 Pa. A generator coupled to a transformer delivers a voltage having a maximum r.m.s. value of 1640 V. In addition, as shown in figure (1) a capacitor " $C_p$ " is connected in parallel with the transformer.

In this configuration, assuming that the discharge is homogeneous and that the section is equal to the surface area of the metalization, one can consider that there exists a capacitor on either side of the ionized gas column. Their plates are represented on the one hand by the metalization of the dielectric placed on the electrodes and on the others by the surface on which the charges are deposited.

Six parameters have been studied. They concern the electrode configuration (gas gap " $d$ " and the capacitance of the solid dielectrics between electrodes " $C_{ds}$ ") or the excitation and the electrical circuit (voltage applied " $V_a$ ", excitation frequency " $f$ ", series resistance " $R_s$ " and parallel capacitance " $C_p$ ") [Fig. 1].

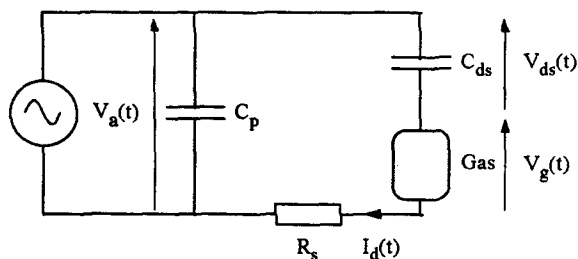


Fig. 1 : Electrical circuit diagram.

The effect of each of these parameters has been studied keeping the rest as constant at the following values ( $f = 10$  kHz,  $d = 5$  mm,  $V_a = 800$  V,  $C_{ds} = 70$  pF,  $C_p = 350$  pF,  $R_s = 47 \Omega$  et  $P_r = 0.1$  Pa). The entire set of these values, so called "standard", have been defined beforehand with the help of criteria which are the

wettability of the polypropylene surface and the homogeneity of the treatment.

### 2. Measurements and electrical equations:

The electrical characterization of this discharge consist of the measurements of two variables : the discharge current " $I_d(t)$ " and the applied voltage on the entire set composed of the dielectrics and the gas " $V_a(t)$ " [3, 1].

The current is measured with a resistance. Current and voltage measurements are performed with the help of an oscilloscope H.P. 54601A-100 MHz. From these two measurements performed over one time period, the voltages applied to the dielectrics " $V_{ds}(t)$ " and to the gas " $V_g(t)$ " are calculated according to the equation below :

$$V_a(t) = V_g(t) + V_{ds}(t) \quad (\text{Eq. 1})$$

$$V_{ds}(t) = Q(t)/C_{ds} + V_{ds}(t_0) \quad (\text{Eq. 2})$$

$$Q_d(t) = \int_{t_0}^{t+t_0} I_d(t) \cdot dt \quad (\text{Eq. 3})$$

$V_{ds}(t_0)$  : Solid dielectric voltage at the time  $t = t_0$ .

$$V_g^*(t) = V_g(t) + V_{ds}(t_0) \quad (\text{Eq. 4})$$

$$\overline{V_g^*} = 1/T \int_{t_0}^{T+t_0} V_g^*(t) dt = V_{ds}(t_0) \quad (\text{Eq. 5})$$

### 3. Results and discussion :

When the discharge is of a glow type, a single current pulse is observed on each half period. The discharge current is periodic and a small current peak is observed when the voltage applied to the gas is reversed [3]. In addition, even if the electrode configuration is symmetrical, which is the case of the results given here, a current desymmetry is observed between the positive and the negative alternations. The amplitude of the difference between two successive alternations is limited. Indeed, when the desymmetry becomes important, a reversal of the properties of the positive and negative alternations is observed. The correlations have been brought into evidence when the current amplitude before initiation is high, the maximum current amplitude and the ignition voltage are high too while the minimum voltage is small [Fig. 2].

Under standard experimental conditions, the average values and the difference measured between the positive and the negative alternations are : a current density of the order of  $(2.5 \pm 1.6)$  mA.cm<sup>-2</sup>, a density of

the charges displaced per period of  $(23 \pm 0.5) \text{ nC/cm}^2$ , a geometrical field at ignition of  $(2.5 \pm 0.4) \text{ kV.cm}^{-1}$ , a minimum voltage of  $(150 \pm 150) \text{ V}$ .

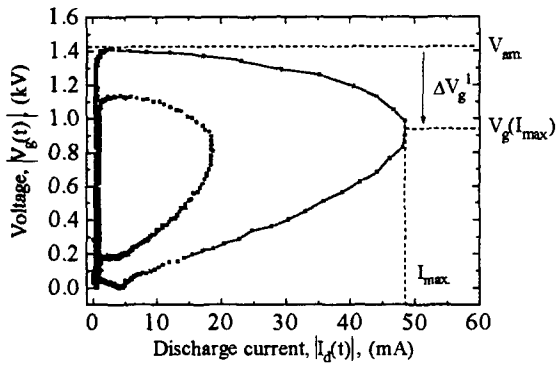


Fig. 2 : Absolute value of the gas voltage as a function of the absolute value of the discharge current ( $f = 10 \text{ kHz}$ ,  $d = 5 \text{ mm}$ ,  $V_a = 800 \text{ V}$ ,  $C_{ds} = 70 \text{ pF}$ ).

We have shown earlier [3], the importance of the residual charge density before ignition. They are the charges which explain the desymmetry. If this density is high, the number of ionizing collisions under a weak field increases and the breakdown voltage is small. The discharge develops slowly and the maximum-current has a small amplitude. The charge deposited on the dielectrics is, in this case, relatively low and it induces a small drop of the gas voltage in such a way the voltage minimum remains high. The charges are then effectively drained towards the electrodes, this effect together with the small number of charges generated leads to a small residual charge density during the next ignition. In those conditions the following ignition requires a higher breakdown voltage which results, at the same time, in a current peak of higher amplitude, a rapid fall in gas voltage, a small minimum voltage and a small flow of charges after the current peak. When the residual charge density remains important, an ignition under a weak field is then observed during the next alternation.

The charge density remaining during the initiation of a discharge depends, at the same time, on the density of the charges generated during the preceding discharge and the manner in which the charges are drained, as well as on the time separating the reversal of the gas voltage from the initiation of the discharge. This last point permits to explain the property reversals of positive and negative alternations for an important desymmetry. This is observed when the polarity reversal of the electrodes occurs too soon. As a matter of fact, an intense current peak helps maintain an important charge density in the gas, between two current impulses. However, if after the discharge the gas voltage is small, the polarity changes as soon as the applied voltage starts to fall. At this instant, the current being small, the variation of the gas voltage is equal to the variation of the applied voltage. If the latter varies

slowly, the gas voltage varies slowly, this being the case near the peak values of the sinusoid. In this case, the time between the reversal of the gas voltage and the discharge initiation is greater than in the case where the gas voltage changes sign as the applied polarity starts to fall. Hence, if the gas voltage changes polarity as soon as the applied voltage starts to fall, the electrons will have more time to flow before the initiation of the discharge. This leads to a decrease of the electron germ density in the gas during the next initiation and thus, to an intense current peak in the alternation which corresponded to a small amplitude current.

We have drawn in figure (3) the evolution of the average value of the gas voltage obtained at maximum current " $V_g(I_{\max})$ ", as a function of the average value of maximum-current over one period " $I_{\max}$ ", for different parameters under study.

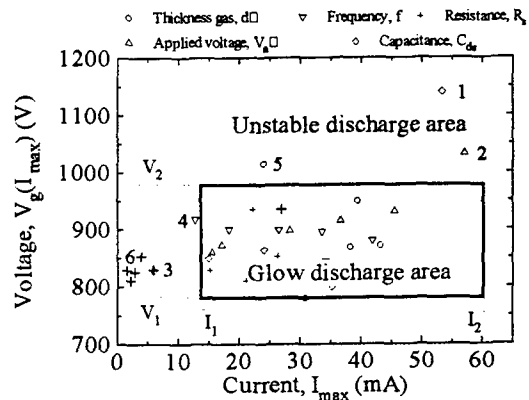


Fig. 3 : Evolution of the average gas voltage at maximum current as a function of the average maximum-current amplitude.

In addition, we have reported the maximum ( $V_2$ ,  $I_2$ ) and minimum ( $V_1$ ,  $I_1$ ) values observed for positive and negative alternations, obtained under standard conditions. These values demarcate a rectangle. We note that by varying the parameters we can not alter the characteristics of the gas beyond what could be observed under standard condition, without modifying the diameter and the discharge régime. When this experimental conditions furthers from the optimal condition, the discharge becomes symmetrical.

- [1] Decomps P., Massines F., Mayoux C., Acta Phys. Universitatis Comenianae, 35(1), (1994), 47.
- [2] Kogoma M., Okazaki S., J. Phys. D: Appl. Phys., 27, (1994), 1985.
- [3] Massines F., Ben Gadri R., Decomps P., Rabehi A., Segur P., Mayoux C., ICPIG-Hoboken-USA, published in "Phenomena in ionized gases", AIP Conference Proceedings 363, (1995), 306.
- [4] Massines F., Decomps P., Mayoux C., 4th Inter. Symp. on High Pressure Low Temp. Plasma Chem., Hakone 4, Bratislava, (1993), 141.
- [5] Okazaki S., Kogoma M., Uehara M., Kimura Y., J. Phys. D: Appl. Phys., 26, (1993), 889.

## The influence of the surrounding atmosphere on plasmas sustained by the "Torche à Injection Axiale"

J. Jonkers, L.J.M. Selen, A. Hartgers, J.A.M. van der Mullen and D.C. Schram

Department of Applied Physics, Eindhoven University of Technology,  
PO Box 513, 5600 MB Eindhoven, The Netherlands

### 1. Introduction

The microwave torch named "Torche à Injection Axiale" (TIA), i.e. torch with axial gas injection, was developed by the group of Moisan in 1993 [1]. A schematic of the TIA is depicted in Figure 1. This plasma torch can, depending on the geometry of the nozzle (cf. Figure 2), excite many kinds of gases or mixtures, such as air, CO<sub>2</sub> and noble gases. Therefore, it is a very promising plasma source for spectrochemical purposes [2]. The plasmas sustained by the TIA normally expand in the open air and are typically 10 cm long and 2 mm in diameter. Microwave powers up to 2 kW can be used without the need for external cooling. In a previous paper we presented the electron density and temperature determined by Thomson scattering [3]. In a plasma with helium as main gas  $n_e$  ranges between  $0.64$  and  $5.1 \times 10^{20} \text{ m}^{-3}$  and  $T_e$  is around 25000 K. In an argon plasma the electron temperature is lower and the electron density is higher: 17000 K and around  $10^{21} \text{ m}^{-3}$  respectively. In both cases the original nozzle is used.

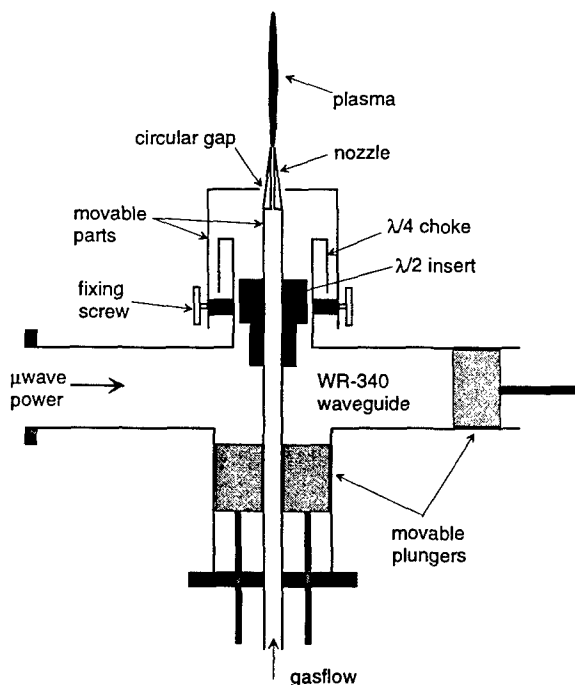


Figure 1: The TIA consists of a coaxial waveguide perpendicular to a standard rectangular waveguide. Due to its specific design the matching is very insensitive for changes in plasma parameters like applied power and gas flow [1].

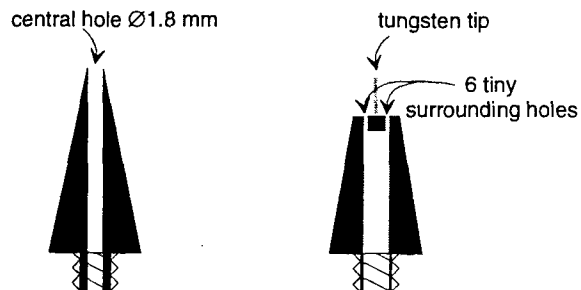


Figure 2: Two possible nozzle geometries of the TIA. On the left the original nozzle proposed by Moisan et al. [1] is depicted; on the right the one by Ricard et al. [4].

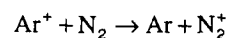
Using these Thomson scattering results, it can be established that the ionisation rates of both plasmas are much larger than the recombination rates, which means that the plasmas are far from Saha equilibrium. However, the production of new ions and free electrons outranges by two orders the estimated "classical" losses due to flow and diffusion [5].

Radially resolved Thomson scattering measurements on this small plasma show that it has a hollow structure [5]. This means that the diffusion losses were originally underestimated, since the steep outer gradients enhance the losses due to diffusion. Taking these losses into account the high electron temperatures in the helium plasma can be explained. But in the argon plasma the higher diffusion rate can not balance the ionisation rate, which remains one order of magnitude higher [5].

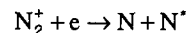
This means that there is a fourth process (besides diffusion, flow and recombination) which can not be neglected. This contribution deals with one possible process: mixing with the surrounding air.

### 2. Theory

If the surrounding air is mixed with the argon plasma an extra destruction channel for the ions and free electrons is created, i.e. charge transfer with nitrogen



followed by dissociative recombination



The charge transfer reaction is resonant since the ionisation energies of argon and molecular nitrogen are almost equal (15.76 and 15.58 eV respectively). The second reaction is fast due to the attractive Coulomb interaction between the positively charged molecule

and the electron. The presence of this mechanism is supported by the fact that in these plasmas the First Negative system of  $N_2^+$  and many atomic nitrogen lines can be observed [2,4]. Moreover, a significant entrainment of air into an ICP, which is also expanding in the open air, was measured by de Regt et al. [6]. If we assume that 1% of the heavy particles in the plasma are nitrogen molecules this destruction channel can be fast enough to balance the ionisation. However, the remaining excited atom can be easily ionised again. Therefore the significance of such kinds of mechanisms has to be investigated by controlling the atmosphere in which the plasma expands.

### 3. Experimental

A special vessel is constructed around the coaxial top of the TIA and on top of the rectangular waveguide. The coaxial structure itself is sealed using a teflon ring. The vessel is flushed with either argon or nitrogen. Using the same high resolution Thomson scattering setup [5], the electron density and temperature are measured as function of the radius and the height above the nozzle. A typical result is depicted in Figure 3. The plasma which is sustained in a nitrogen atmosphere is more or less the same as the one expanding in the open air. However in case the nitrogen is replaced by argon, the plasma becomes much larger (cf. Figure 3). This confirms that mixing with the surrounding gas is an important mechanism.

Using vibrational Raman scattering [6] the density of nitrogen molecules in the plasma is measured as function of the radius. Using these densities the destruction rate via the processes discussed in Section 2 can be determined and compared to the other loss processes. In this way quantitative information on the significance of the entrainment of air can be obtained. In case the tungsten tip nozzle (cf. Figure 2) is used to sustain the plasma, the electron density appears to be much lower than in a similar plasma using the original nozzle [4]. This might be due to a more turbulent plasma which enhances the mixing with surrounding air. This is supported by the fact that the change between a nitrogen and an argon atmosphere is clearly visible with the naked eye.

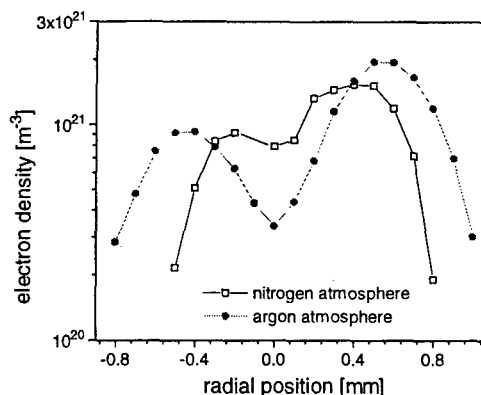


Figure 3: The influence of the surrounding atmosphere on an argon plasma created by the original nozzle.

### 4. References

1. M. Moisan, G. Sauvé, Z. Zakrzewski and J. Hubert: Plasma Sources, Sci. and Technol. **3** (1994) 584.
2. E.A.H. Timmermans, K. Letourneur, F.P.J. de Groote, J. Jonkers and J.A.M. van der Mullen: Proceedings of the European Winter Conference on Plasma Spectrochemistry, Gent Belgium (1997) 134.
3. J. Jonkers, J.M. de Regt, J.A.M. van der Mullen, H.P.C. Vos, F.P.J. de Groote and E.A.H. Timmermans: Spectrochim. Acta B. **51** (1996) 1385.
4. A. Ricard, L. St-Onge, H. Malvos, A. Gicquel, J. Hubert et M. Moisan: J. Phys. III France **5** (1995) 1269.
5. J. Jonkers, L.J.M. Selen, J.A.M. van der Mullen, J. van Dijk, E.A.H. Timmermans and D.C. Schram: "Characterisation of Plasmas produced by the Torche à Injection Axiale", submitted to Phys. Rev. E.
6. J.M. de Regt, F.P.J. de Groote, J.A.M. van der Mullen and D.C. Schram: Spectrochim. Acta B. **51** (1996) 1527.

## The role of He<sub>2</sub> molecules in plasma kinetics of high pressure helium fast discharges.

A. Treshchalov<sup>a</sup>, H. Korge<sup>b</sup>, A. Chizhik<sup>b</sup> and A. Vill<sup>a</sup>

<sup>a</sup> Institute of Physics, Riia 142, EE 2400 Tartu, Estonia (e-mail: atr@fi.tartu.ee)

<sup>b</sup> University of Tartu, Ülikooli 18, EE 2400 Tartu, Estonia

Pulsed high-pressure discharges in noble-gas mixtures are of interest for a variety of technological applications which need ionization sources of samples in gas chromatography or efficient radiation in the VUV range. Well-known broad-band continuum emission of noble-gas excimers is caused by bound-free  $B, A \ ^1,3\Sigma_u^+ \rightarrow X \ ^1\Sigma_g^+$  transitions. These transitions have perspectives for high-power VUV lasing media as well.

For the most of noble gases (Ne, Ar, Kr, Xe) the formation of excited dimer molecules in high pressure conditions is connected with relatively slow three-body association reaction (excited atom + two ground state atoms). Excited atoms are produced mainly after the fast dissociation recombination reaction of rare gas dimer ions and cold electrons in the early afterglow. The situation for helium plasmas, however, is far from being well understood up to now. Manifold of strongly bounded electronically excited molecular He<sub>2</sub><sup>+</sup> states may play significant role in the excitation-recombination processes in high pressure conditions.

A serious applied problem for the long-term operation of VUV lasers and excimer lamps is contaminants created in a gas mixture due to discharge-induced chemical reactions between trace impurities and main gas components. Accumulated contaminants not only absorb VUV radiation but change significantly the excitation energy-flow kinetics and destroy the spatial homogeneity of the discharge. Development of new generation of "sealed-off" high-pressure gas lasers and excimer lamps with qualitative improvement of gas lifetime stimulates spectroscopic investigations of trace contaminants in noble-gas discharge plasmas.

The aim of this work is on-line monitoring of excited atomic and molecular helium species in high pressure helium discharge, investigation of key plasm-chemical reactions for their creation kinetics and influence of accumulated contaminants on these kinetics.

The object of our investigation is helium discharge plasma in commercially available miniature excimer laser PSX-100 (MPB Technologies Inc.). This laser operating as F<sub>2</sub> laser (gas mixture He/F<sub>2</sub>, 6 bar / 5 mbar) gives pulse energy of about 1 mJ at 157.6 nm with repetition rate up to 100 Hz and gas lifetime of

10<sup>6</sup> pulses. This laser operating as ArF excimer laser gives the output energy of 5 mJ at 193 nm.

In this work we report temporal and spectral emission (absorption) data from the discharge and afterglow stages of a high-pressure (3 - 9 bar) helium discharge plasma under the fast (~10 ns) high deposition power (~20 MW/cm<sup>3</sup>) excitation. Kinetics of spontaneous emission were measured through the monochromator by fast PMT and transient digitizer, while absorption kinetics were detected by pulsed (5 ns) tunable dye laser absorption probing technique. Dye laser was pumped by XeCl laser which was electronically synchronized with the investigated discharge. The computer-control delay generator triggered both lasers with an adjustable time-shift up to several microseconds.

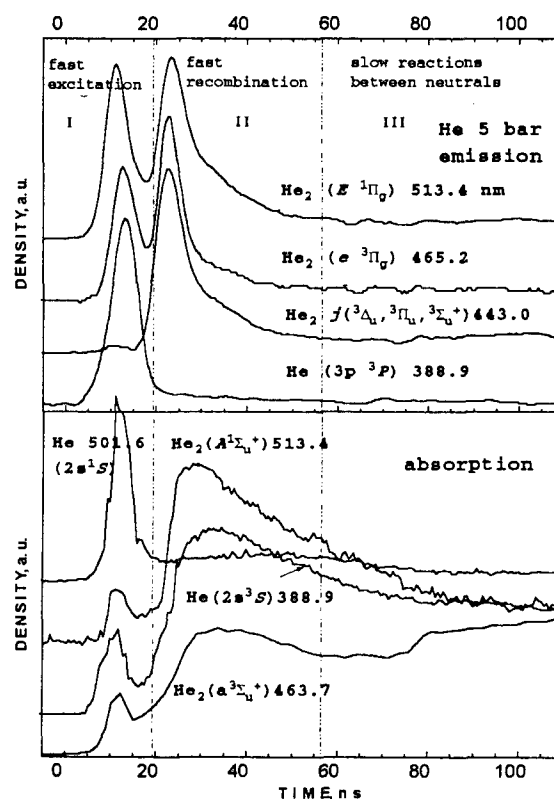


Figure shows temporal behaviors of the densities of some excited atomic He<sup>+</sup> and molecular He<sub>2</sub><sup>+</sup> species measured from spontaneous emission and

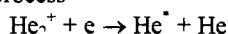
absorption kinetics in the discharge of pure helium at 5 bar pressure. The intensity of He atomic emission lines (the most intense is 388.9 nm line) decreases continuously with the growth of He pressure from 3 to 9 bar, while the intensity of  $\text{He}_2^+$  emission lines increases up to optimum pressure 6 bar and then declines depending on the impedance mismatching of the discharge plasma and the pumping circuit.

It is possible to identify three different stages in these kinetics:

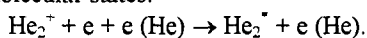
- I - the stage of fast discharge excitation,
- II - the stage of fast electron recombination,
- III - the stage of slow reactions between excited neutral species.

Atomic helium emission is observed only during the stage I when the temperature of electrons is high enough to excite He electronic states.  $\text{He}_2^+$  molecular electronic low-energy states ( $E^1\Pi_g$ ,  $e^3\Pi_g$ ) are excited very effectively during the first stage by the direct electron impact excitation of quasibounded helium molecules (the pairs of helium atoms which are distributed on the repulsive He-He interaction  $X^1\Sigma_g^+$  curve). The fraction of such helium atomic pairs grows as the square of helium gas density. In the pure helium gas the  $\text{He}_2$  molecules play the role of additives which have lower excitation (ionization) potential compared with the atomic helium.

As concerning high-energy  $\text{He}_2^+$  molecular electronic states  $j$  ( $^1\Delta_u$ ,  $^3\Pi_u$ ,  $^3\Sigma_u^+$ ) there is only small emission maximum in the first stage caused by the direct electron impact excitation of helium molecules. However, the emission maxima in the recombination stage II of the discharge are nearly the same for all measured  $\text{He}_2^+$  emission bands. This shows that together with well-known for noble gases dissociative recombination process

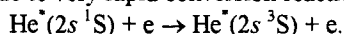


significant recombination flow is realized through the helium molecular states:



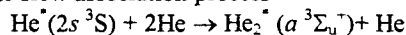
This recombination is very fast in our high pressure and high electron density conditions. We estimate the recombination rate of 2 - 20 ns (this estimation depends strongly on the temperature and density of electrons).

The maximum density of  $\text{He}^+(2s^1S)$  metastables is about  $3 \times 10^{14} \text{ cm}^{-3}$  and is observed in the first (excitation) stage of the discharge. However, the density of  $\text{He}^+(2s^3S)$  metastables achieves its maximum about  $2 \times 10^{15} \text{ cm}^{-3}$  during the second (recombination) stage of the discharge. The density of  $\text{He}^+(2s^1S)$  metastables in the recombination stage is very low due to very rapid conversion reaction:



The long tail in the absorption kinetics of He ( $2s^3S$ ) metastables (stage III) reflects their destruction

in rather slow association process



with the rate constant in our conditions of  $3.5 \times 10^6 \text{ s}^{-1}$ .

The longest decay kinetics ( $\tau \approx 400 \text{ ns}$ ) in our discharge have  $\text{He}_2^+(a^3\Sigma_u^+)$  metastable molecules. Unfortunately oscillator strengths are unknown for molecular  $\text{He}_2^+$  transitions, so we can not calculate absolute densities of  $\text{He}_2^+$  species. Their lifetime is very sensitive to the presence of contaminants in helium gas. The following impurity radicals ( $\text{CN}^+$ ,  $\text{CH}^+$ ,  $\text{C}_2^+$ ,  $\text{OH}^+$ ), atoms ( $\text{O}^+$ ,  $\text{C}^+$ ,  $\text{N}^+$ ,  $\text{H}^+$ ), molecules ( $\text{CO}^+$ ,  $\text{N}_2^+$ ) and molecular ions ( $\text{CO}^{++}$ ,  $\text{N}_2^{++}$ ) are identified from time-resolved spontaneous emission spectra in the aged helium gas mixture [1]. Carbon radicals and carbon atoms show rather long emission decay kinetics which reflect chemical reactions between trace stable carbon-containing contaminants and high-energetic  $\text{He}_2^+$  molecular excimers in long-lived triplet electronic states.

The measured absorption spectra of  $e^3\Pi_u \leftarrow a^3\Sigma_u^+$  and  $E^1\Pi_g \leftarrow A^1\Sigma_u^+$   $\text{He}_2$  transitions were used to determine the rotational temperature during the stages II and III. The calculations show that the lower  $\text{He}_2$  rotational levels ( $J \leq 7$ ) are considerably colder ( $T_{\text{rot}} = 400 \text{ K}$ ) than the higher rotational levels ( $J > 7$ ) for  $a^3\Sigma_u^+$  state ( $T_{\text{rot}} = 4000 \text{ K}$ ) and for  $A^1\Sigma_u^+$  state ( $T_{\text{rot}} = 1500 \text{ K}$ ) if we suppose Boltzmann-like distribution with different rotational temperatures in these two groups of levels. Generally it means the prevailing population of high rotational levels by some reaction which is clearly demonstrated by the different temporal behaviors in absorption lines with low and high rotational quantum numbers  $J$ .

[1] A.B.Treshchalov, A.S.Chizhik and A.A. Vill: J.Anal. At. Spectrom. 10, (1996) 649.



## Authors Index

### A

Abbaoui M. I-4  
 Abdelli S. IV-264  
 Abdullin I.Sh. IV-72  
 Ablitzer D. IV-200  
 Abramzon N. I-62  
 Adachi K. I-246  
 Adler H.G. III-22  
 Afanas'ev V.P. III-104  
 Ahedo E. I-2  
     I-204  
 Akaishi K. IV-156  
 Akhmedzhanov R.A. I-272  
     I-274  
 Alcaide I. II-2  
 Aldea E. IV-254  
 Alekseeva L.M. I-206  
     II-156  
 Alexandrov A.F. I-44  
     I-108  
     III-88  
 Alexandrov L.S. I-208  
 Alexandrovich B. IV-76  
 Alexeff I. III-102  
 Al-Hussany A. II-216  
     II-218  
 Alkaa A. II-260  
 Allen J.E. I-116  
     I-132  
     I-192  
     I-194  
 Almi A. I-254  
 Alnot P. IV-244  
 Alvarez I. I-18  
 Alves L. I-120  
 Amakawa T. I-246  
 Amemiya H. I-110  
     IV-60  
     IV-62  
 Amirov A.H. IV-262  
 Ammelt E. II-182  
 Amorim J. IV-232  
 Andre P. I-4  
     III-104  
 Andreatza P. IV-252  
 Andreatza-Vignolles C. IV-252  
 Andrieux M. IV-192  
 Anikin N.B. IV-48  
 Annaratone B.M. I-116  
     I-132  
     I-192  
     I-194

Anschutz B. II-204  
 Anschutz F.B. II-202  
 Antoni V. II-262  
     IV-134  
 Antonova T.B. III-88  
 Arai T. IV-86  
     IV-88  
     IV-90  
 Arnal Y. IV-230  
 Arnas-Capeau C. I-202  
     II-164  
 Arriaga C. I-18  
 Asselman A. III-24  
 Atipo A. II-170  
 Aubes M. III-16  
     IV-64  
 Aubrecht V. II-78  
     II-80  
     II-82  
 Aubreton J. I-4  
     IV-102  
     IV-220  
 Auday G. I-58  
 Averyanov V.P. I-188  
 Awakowicz P. I-60  
     II-202  
     II-204

### B

Babaeva N.Yu. II-246  
 Babaritskiy A. IV-224  
 Babich I.L. II-154  
 Babich L.P. I-6  
     I-8  
     I-10  
     IV-2  
 Babich M.L. I-10  
 Babicky V. I-248  
     IV-14  
 Bacal M. I-12  
     III-78  
 Bachev K. I-160  
     I-162  
 Baclawski A. II-110  
 Badie J.M. IV-192  
 Bagatin M. II-262  
     IV-134  
 Bagautdinov A. IV-222  
 Baksht F.G. I-12  
     IV-138  
     IV-194  
 Baldwin M. IV-194  
 Baltog A. I-94

Bano G. III-96  
     IV-212  
 Baranov I.E. IV-224  
 Baravian G. IV-232  
 Barinov Yu.A. III-104  
 Barj M. IV-142  
 Bartlova M. II-80  
 Bashutin O.A. IV-112  
 Basner R. IV-196  
 Basurto E. I-18  
 Batanov G.M. I-138  
 Bauchire J.M. II-120  
     II-136  
     II-206  
 Baude S. III-86  
 Bayle P. I-252  
     II-220  
     IV-154  
 Becker K. I-62  
     I-64  
     IV-196  
 Behnke J. IV-226  
     II-4  
 Behnke J.F. II-4  
     II-6  
     II-8  
 Beilis I.I. I-14  
     II-84  
 Belenguer Ph. I-100  
 Belhaouari J.B. II-86  
 Belmonte T. IV-66  
     IV-198  
 Ben Gadri R. IV-44  
 Benabdessadok M.D. I-252  
 Bernard J.F. IV-130  
 Berreby R. III-92  
 Berthomieu D. I-148  
 Bezborodko P. IV-68  
 Bezemer J. II-224  
 Bhattacharjee S. I-110  
 Biborosch L. II-190  
 Biel W. II-226  
 Bilikmen S. I-172  
 Bindemann Th. II-6  
 Birau M. III-46  
 Bisch C. IV-192  
 Blaise G. III-86  
 Blanc E. III-10  
 Blois D. IV-142  
 Blundell R.E. II-150  
 Bobrov Yu.K. II-166  
     II-168

Bobrov Yu.K.	II-208 II-210 IV-4 IV-6	Busov B.	II-78	Choi W.K.	III-88
Bobrova L.N.	IV-6	Buzzi J.M.	III-46	Chorazy J.	I-82
Bockel S.	IV-200	Bykanov A.N.	IV-72	Christophorou L.G.	I-68
Boeuf J.P.	I-112 II-56 II-228 II-252 II-254 III-42 III-70	<b>C</b>		Chuaqui H.	II-12 III-28
Bogaerts A.	II-10	Cachoncinlle C.	III-30 III-32 III-44	Chumak G.M.	IV-206
Bonhomme G.	II-16 II-170	Cahoreau M.	IV-220	Cicconi G.	II-176
Bonifaci N.	IV-10 IV-12	Caillez Y.	III-46	Cicman P.	IV-250
Booth J.P.	IV-70 IV-202	Cajal D.	II-92 IV-74	Cinelli M.J.	IV-102 IV-220
Borcia C.	II-172	Calderon M.A.G.	II-112	Ciobanu S.S.	II-100 II-102 IV-150
Bordage M.C.	IV-44	Capitelli M.	I-24 I-26 I-66 II-116 II-242	Cisneros C.	I-18
Borisenko A.G.	I-38 IV-248	Cardinaud C.	III-90	Clavreul R.	III-94
Borodin V.	III-18	Carman R.J.	II-258	Clenet F.	II-212
Bouaziz M.	II-88	Cartry G.	II-70 II-72	Clupek M.	I-248 IV-14
Boubert P.	IV-152	Catherinot A.	IV-102 IV-220	Coitout H.	II-96 IV-78
Boucher I.	III-2	Cenian A.	I-16 III-18	Collins G.	IV-194
Bouchoule A.	I-200 III-66	Censor D.	I-234	Colombo V.	II-214
Boudjella A.	IV-16	Cercek M.	IV-162	Conde L.	I-70 II-2
Boufendi L.	IV-204	Cernak M.	I-248 IV-8	Coppa G.G.M.	II-214
Bougdira J.	IV-244	Cernogora G.	I-102 II-70 II-72	Cormier J.M.	II-122
Bougrov G.E.	III-88	Chabert P.	IV-202	Coste C.	I-268
Boxman R.L.	II-84	Chaker M.	I-166 I-168	Coulombe S.	II-98
Bozin J.V.	I-98	Champaign H.	IV-94	Courtois L.	II-42
Brablec A.	I-128 IV-226	Chapelle J.	II-122	Csambal C.	II-8
Bragin V.E.	IV-72	Chapput A.	IV-142	Cunge G.	IV-202
Braginskiy O.V.	III-76	Charles C.	IV-252	Czerwec T.	IV-66 IV-198
Brasile J.P.	II-42	Chatei H.	IV-244		
Bratescu M.A.	I-92	Chebotarev A.V.	IV-110	<b>D</b>	
Brault P.	IV-252	Chenevier M.	IV-70	D'yachkov L.	I-188 I-190
Bretagne J.	III-80 IV-184 IV-210	Cheredarchuk A.I.	II-154	Damelincoirt J.J.	III-16 III-24
Brethes S.	I-268	Chernukho A.	III-18	Darnon F.	III-66
Briaud Ph.	II-212 III-72	Chernyshev A.V.	I-176	Dauchot J.P.	IV-210
Bruhn B.	II-200	Cheron B.G.	II-90	David M.	II-226
Brunet H.	I-58 III-100	Chervy B.	II-104	Davies A.J.	II-216 II-218
Bruno D.	II-242	Chevolleau T.	III-90	De Benedictis S.	I-72 IV-14 IV-80
Bugrova A.I.	II-76 III-68	Chevrier P.	II-100 II-102	De Graaf A.	IV-254
Bultel A.	II-90	Chinnov V.F.	II-94	De Hoog F.J.	I-152 IV-246
Burke R.	IV-230	Chirkin M.V.	IV-262	De Souza A.R.	IV-46
Burm K.T.A.L.	II-108	Chizhik A.	I-208 II-174	De Urquijo J.	I-18
Bursikova V.	IV-260	Choi P.	III-110 II-12 III-28	Debal F.	IV-210
				Decomps Ph.	III-106
				Deegan C.M.	I-114
				Degond P.	III-64
				Deha I.	IV-116

Delaporte Ph.C.	I-48 III-26 IV-52	Dussoubs B.	II-158	Filippov A.A.	II-142
Delhaes P.	IV-236	Dyatko N.A.	I-24 I-66 II-116	Fitaire M.	IV-28
Denat A.	IV-10 IV-12	Dyomkin S.A.	IV-224	Fitzgerald T.J.	III-10
Derouard J.	I-150 IV-202	Dyson A.E.	I-116	Flamant G.	II-124
Deschamps N.	IV-46	Dzermanova N.	II-192	Flazi S.	IV-16
Desideri D.	II-262 IV-134	<b>E</b>		Fleddermann C.B.	IV-214
Desoppere E.	I-20 I-106 III-38	Eby S.D.	I-50	Fleurier C.	II-100 II-102 III-44 IV-150
Despax B.	IV-208	Egli W.	II-236	Flieser J.	IV-124
Dessaux O.	IV-142	Ehrich H.	II-118	Fliesser W.	IV-122 IV-126
Destombes V	III-100	Eichwald O.	I-252 II-220 IV-154	Fodrek P.	IV-128
Deutsch H.	II-4 II-6 II-74 II-200 IV-188	El Bezzari M.	I-190	Foest R.	IV-196
Devyatov A.M.	I-44	El Shaer M.	I-118	Fontaine B.	III-26
Dewald E.	II-50 II-52	Elchinger M.F.	I-4	Fortov V.	I-212
Diamy A.M.	IV-218	Eldevik T.	I-32	Fortov V.E.	I-176 I-178
Dias F.M.	I-122	Elloumi H.	IV-64	Frank K.	II-52
Dilecce G.	I-72 IV-14 IV-80	Entlicher M.	II-232	Franke St.	II-74
Dinescu G.	IV-254	Epifanie A.	II-160	Franklin R.N.	II-14
Dinklage A.	II-200 IV-188	Ercilbengoa A.E.	III-84	Frost R.M.	I-60
Djakov A.F.	II-166 II-168 II-208 II-210 IV-4 IV-6 IV-94 II-162 II-238 I-18 II-64 IV-210 II-146 I-210 I-250 IV-216 I-202 I-120 I-30 III-92 IV-192 III-78 III-28 IV-208 I-148 III-44	Eremenko Yu.	IV-222	Fujioka H.	IV-88 IV-90
		Erraki A.	II-106	Fukuchi Y.	I-74
		Ershov A.P.	II-60	Fukuda M.	IV-168
		Escarguel A.	I-174	Fulcheri L.	II-124
		Essolbi R.	III-94	Funato Y.	IV-156
		Etievant C.	IV-224	<b>G</b>	
		Etoh A.	IV-104	Gajic D.Z.	I-222 I-224
		Ezubchenko A.N.	II-162	Galofaro J.T.	II-146
		<b>F</b>		Galy J.	I-58 III-100
		Fabry F.	II-124	Ganciu M.	II-50 II-52
		Fanack C.	III-2	Garanin S.F.	IV-158
		Fang M.T.C.	II-148 II-150	Gardou J.	I-104
		Fauchais P.	I-4 II-158	Garrigues L.	III-70
		Fauconneau J.	IV-68	Gary F.	II-92 IV-74
		Faure G.	III-104 IV-78	Gasteiger S.	III-36
		Favre M.	II-12 III-28	Gavrilenko V.P.	IV-82
		Fedorovich O.A.	IV-240	Gavrilov N.V.	II-32
		Fergusson E.E.	I-84	Gavrilova T.	I-188
		Ferguson D.C.	II-146	Gerova E.	IV-120
		Fernsler R.	II-30	Gerteisen E.	II-238
		Ferreira C.M.	I-120 I-122 I-124	Gherman C.	II-172
		Fetisov I.K.	II-24	Gicquel A.	IV-70
		Fewell M.	IV-194	Gigant L.	IV-114
		Fiala A.	III-86	Gijbels R.	II-10
		Fiermans V.	I-20	Gillispie K.	III-102
		Fievet C.	II-102 IV-150	Giordano D.	I-26
				Girard A.	I-140 II-256
				Glanschnig M.	I-84

Gleizes A.	II-86	Gross B.	II-82	Henrion G.	II-16
	II-88	Grosswendt B.	I-78	Herben P.G.J.M.	III-63
	II-104	Grozev D.	I-156	Hertl M.	IV-216
	II-106		II-192	Heuraux S.	III-2
	II-126	Grozeva M.	II-130	Higaki H.	I-230
	II-136	Gryaznov V.	I-212	Hipp M.	IV-122
	II-140	Gubsch S.	II-200		IV-126
Glisic S.	IV-42	Guerra V.	IV-160	Hirech A.	II-230
Glosik J.	III-96	Guerrini G.	III-78		III-100
	IV-212	Guiberteau E.	II-16	Hirota A.	I-228
Godyak V.	IV-76	Guillot Ph.	I-58	Hitz D.	III-92
Goedheer W.J.	II-108		III-100	Hoang T.G	III-94
	II-222	Gyergyek T.	IV-162	Hoffmann D.H.H.	I-212
	II-224				II-52
Goldman A.	III-98	<b>H</b>		Hoffmann V.	I-146
Goldman M.	III-98	Hacquin S.	III-2	Holzinger R.	I-260
Goldsmith S.	II-84	Hadi H.	IV-16	Hong D.	III-44
Golly A.	II-110	Hadjadj A.	IV-204		IV-150
Golosnoy I.O.	IV-84	Hajek V.	IV-258	Hopkins M.B.	I-114
Golubev A.	I-212	Hallil A.	IV-62	Horikoshi K.	IV-88
Golubovskii Yu.B.	I-36	Hamada T.	IV-118		IV-90
Golubovskii Yu.B.	II-4	Hamers E.A.G.	II-224	Horvath M.	II-232
	II-6	Hanacek P.	II-78	Hosokawa T.	IV-16
	II-54	Hangai N.	I-144		IV-168
	II-62	Hanitz F.	I-266	Houska A.	II-82
Gombert M.M.	I-22	Hansel A.	I-84	Hrach R.	II-230
Gomes A.M.	I-254		I-260		II-232
	II-160	Harendt A.	I-126		IV-128
Gonzalez J.J.	II-86	Hartgers A.	III-108	Hrachova V.	IV-218
	II-120	Hartmann G.	IV-94		II-18
	II-136		IV-96		II-20
	II-140	Hartmann W.	IV-164		IV-218
	II-206	Hassouni K.	II-116	Hubicka Z.	I-130
Gonzalez-Aguilar J.A.	II-112		IV-70		IV-228
Gorbachev A.M.	I-272	Hatano Y.	I-74	Huet S.	IV-204
	I-274	Haug R.	III-98	Hugon R.	II-16
Gorbunov N.A.	I-80		IV-96	Hure L.	III-44
	I-82		IV-166		
Gordeev O.A.	IV-136	Hava O.	II-18	<b>I</b>	
Gordiets B.F.	I-124	Hayashi N.	I-216	Ieda Y.	II-22
Gorse C.	I-26		II-198	Ignatov A.M.	I-180
	II-116	Haydon S.	IV-194	Inagaki K.	IV-140
Gortchakov S.	III-58	Hbid T.	I-152	Inomata T.	IV-26
Goto M.	I-96		IV-246	Ion L.	IV-236
	IV-86	Hebner G.A.	IV-214		IV-238
	IV-88	Hecq M.	IV-210	Isakaev E.H.	II-94
	IV-90	Helbig V.	II-8	Iserov A.D.	II-94
Goudmand P.	IV-142	Held-B.	I-268	Ishida A.	IV-118
Goulet J.C.	I-218		III-84	Ivanov M.S.	II-242
Gousset G.	I-120		IV-180	Ivanov O.A.	I-272
	III-80		IV-236		I-274
	IV-92		IV-238	Ivanov V.G.	I-12
	IV-184	Heldt J.	III-50	Ivanov V.V.	I-86
Grabowski D.	III-50	Hemmati M.	I-214		I-182
Graham W.G.	IV-151	Hemmers D.	II-226		II-28
Granier A.	III-72	Hempel F.	IV-196		II-234
	III-74	Henneberger K.	I-40		III-40
Gregor J.	II-30	Hennig A.	II-8		
Gresser L.	IV-180				

**J**

Jacobsen L.M.	III-4
Jager H.	IV-122
	IV-124
	IV-126
Janca J.	I-256
	IV-98
	IV-100
	IV-260
Jang H.G.	III-88
Jastrabik L.	IV-226
	IV-228
Jauberteau I.	IV-102
	IV-220
Jauberteau J.L.	IV-102
	IV-220
Jelenkovic B.M.	I-98
Jivotov V.K.	IV-222
	IV-224
Johnston C.	III-62
Jolly J.	IV-190
	IV-216
Jones J.E.	IV-18
	IV-20
	IV-22
Jonkers J.	III-62
	III-63
	III-108
Jordan A.	I-260
Jugroot M.	II-220
	IV-154
Jung H.J.	III-88

**K**

Kalachov I.	IV-222
Kalinin A.V.	II-60
Kameta K.	I-74
Kandah M.	IV-176
Kando M.	IV-104
Kaneda T.	IV-168
Kanka A.	II-18
	II-20
Kapicka V.	I-128
	IV-226
	IV-228
Kaplan V.B.	III-104
Kapoun K.	I-130
	IV-228
Karchevsky A.I.	II-162
	IV-106
Karderinis S.N	I-132
Katkalo A.A.	IV-234
Kawaguchi M.	I-134
	II-34
	IV-132
Kawai Y.	I-136
	I-216
	I-244

Kawakami R.	II-198
Kawamura K.	IV-266
	IV-144
	IV-186
Keidar M.	I-14
Kempkens H.	II-226
Kerdja T.	IV-264
Kettlitz M.	II-114
	IV-108
Khacef A.	III-30
	III-32
Khadka D.B.	I-74
Kharchevnickov V.K.	II-76
Khodachenko G.V.	II-24
Khodataev K.V.	IV-24
Khodja H.	I-140
Kidalov S.V.	III-54
	III-56
Kimura T.	I-76
	II-22
Kindel E.	III-34
	IV-108
Kinoh Y.	IV-104
Kirillin A.	I-184
Kirnev G.S.	II-26
Kirov K.	I-156
	II-192
Kiyooka C.	IV-156
Klima M.	I-128
	IV-226
Kling R.	III-36
Klopovskiy K.S.	I-86
	I-88
	II-28
	II-234
	III-40
Kobayashi Y.	I-164
	IV-144
Koch A.W.	IV-54
	IV-56
Koch B.P.	II-200
Kocik M.	III-50
Kof L.M.	IV-58
Koga K.	I-216
	I-244
Kogelschatz U.	II-236
Kogoma M.	IV-26
Koh S.K	III-88
Kolenic F.	IV-128
Kolisko A.L.	I-272
	I-274
Kolosov V.Yu.	IV-170
	IV-172
Kondranin S.G.	III-88
Konjevic N.	IV-146
Konstantinov E.	IV-222
Kopytin A.A.	III-40
Korbel A.	II-132
Korge H.	III-110

Korolev Yu.D.	IV-174
Korshunov O.V.	IV-262
Kosbagarov A.	IV-222
Kosecek A.M.	IV-128
Kossyi I.A.	I-138
	IV-110
Kouchi N.	I-74
Kovalev A.S.	III-76
Kozyrev A.V.	III-54
	III-56
	IV-174
Krajcar-Bronic I.	I-78
Kralkina E.A.	III-88
Krasa J.	IV-272
Krasilnikov M.A.	III-46
Krcma F.	IV-100
Krenek P.	II-104
Kriha V.	I-266
Kroesen G.M.W.	I-152
	IV-246
Ksiazek I.	II-110
Kuba P.	IV-128
Kubota Y.	IV-156
Kudelcik J.	IV-8
Kudrle V.	IV-28
Kudryavtsev A.Yu.	I-6
	I-10
	IV-2
Kudu K.	IV-34
Kulikovskiy A.A.	I-258
	IV-30
Kulish M.	I-212
Kumar S.	IV-194
Kuraica M.M.	IV-146
Kurilenkov Yu.K.	I-186
	I-188
	I-190
Kurnaev V.A.	II-24
	II-26
	IV-112
Kurunczi P.	I-64
Kutsyk I.M.	I-6
	I-8
	IV-2
Kuwae H.	II-198
Kuzelev M.V.	III-46
Kuzovnikov A.A.	I-154

**L**

Laan M.	IV-32
Lagstad I.H.	IV-34
Lamoureux M.	I-140
Lancellotti C.	I-210
Lange H.	IV-36
Lapuerta V.	I-204
Laroussi M.	III-102
Lasgorceix P.	IV-102
Laska L.	IV-272

Latocha V.	III-64	Lorthioir S.	III-86	Matsuoka M.	I-134
Latyshev Ph.E.	I-80	Louhibi D.	II-244		II-34
	I-82	Loureiro J.	I-90		IV-132
Laure C.	IV-252		I-102	Matveev A.A.	I-138
Laurent A.	II-92		IV-160	Maury J.	IV-114
	IV-74		IV-232	Maximov A.I.	I-256
Law D.A.	I-192	Louvet G.	I-186	Mayoux C.	III-106
	I-194	Loza O.T.	III-46	McFarland J.	IV-151
Laz'ko V.S.	II-162	Lozneanu E.	II-184	Meger R.	II-30
Le Brizoual L.	III-72		II-186	Melin G.	I-140
Le Guen C.	I-188	Luca A.	IV-212	Melnig V.	II-172
Leborgne L.	I-218	Lungu C.P.	I-94	Melnikov A.S.	I-80
Leclert G.	III-2	Lyapin A.I.	IV-234	Mentel J.	II-130
Le Coeur F.	IV-230	Lyszyk M.	III-66		II-132
Lecot C.	II-256				III-48
Le Duc E.	IV-28	<b>M</b>			III-50
Lee Z.H.	IV-112	Machala Z.	I-262	Merad A.	I-112
Lefort A.	I-4	Maftoul J.	IV-74	Mercier M.	II-92
	III-104	Mage L.	III-74		IV-74
Legrand J.C.	IV-218	Magne L.	II-70	Merel P.	I-168
Lemaire P.	IV-114		II-72	Mesyats G.A.	II-32
Lemeur F.	II-90	Maheu B.	II-90	Meunier J.L.	II-98
Lemperiere G.	II-214	Mahony C.M.O.	IV-151		IV-176
Leon L.	I-70	Makasheva K.	I-156	Mezhiba A.	I-212
Leprince P.	I-120	Malek S.	IV-264	Michaut C.	III-78
	IV-92	Malinowsky G.Y.	I-48	Michel H.	IV-66
Leroux A.	II-238	Malovic G.N.	I-98		IV-198
Leroy O.	IV-216	Malykh N.I.	I-138		IV-200
Lesage A.	I-174	Mandache N.B.	II-50	Michishita T.	I-230
Leu F.	II-118		II-52	Mikheev L.D.	I-48
	II-188	Manheimer W.	II-30		IV-52
Leu G.	II-184	Mankelevich Yu.A.	II-234	Mikikian M.	I-202
	II-186	Maouhoub E.	II-96	Milenin V.M.	III-54
Levchenko V.D.	I-220	Marchal F.	I-104		III-56
	II-240	Margot J.	I-166	Milic B.S.	I-28
Leys C.	III-38	Mark T.D.	IV-250		I-222
Li Bo	I-52	Markovic V.Lj.	II-46		I-224
Li Y.M.	III-20		IV-178		I-226
Lindinger W.	I-84	Marliere C.	I-148	Millet P.	I-104
	I-260	Marode E.	IV-46	Mimura M.	IV-118
	IV-212	Martines E.	IV-134	Minami K.	I-144
Lino J.	IV-232	Martus K.	I-64		I-228
Lipaev A.M.	I-178	Marty-Dessus D.	IV-236	Minea T.M.	III-80
Lipatov A.S.	II-76		IV-238	Mintsev V.B.	I-212
Lister G.G.	III-22				
Loffhagen D.	III-34	Masek J.	II-78	Mitrofanov N.K.	II-134
	III-58		II-82		IV-138
Loiseau J.F.	III-84	Masek K.	IV-272	Mize:aczyk J.	I-250
Lomakin B.N.	IV-262	Mashino S.	IV-88		II-130
Londer J.I.	II-144		IV-90		III-50
Longo S.	I-24	Massines F.	III-106	Mobasher M.	I-118
	I-26		IV-44	Modreanu G.	II-50
	II-116	Matejcik S.	IV-250	Mohri A.	I-230
	II-242	Matheron P.	IV-116	Moisan M.	I-168
Lopaev D.V.	I-86	Mathew J.	II-30	Mokhtari A.E.	II-244
	I-88	Matsui T.	I-142	Molotkov V.I.	I-178
	II-28	Matsumoto M.	I-238	Mond M.	I-236
	III-40		II-58	Monin M.P.	I-270
	III-76				

Moreno J.	II-12	Neuilly F.	IV-202	Pauna O.	I-166
	III-28	Nichipor G.V.	I-250	Pavlenko V.N.	I-232
Mori A.	II-34	Nicolazo F.	III-74		II-178
Mori I.	IV-266	Nienhuis G.J.	II-224		II-180
Morimoto T.	IV-266	Niessen W.	I-264		IV-240
Morozov A.	IV-124	Nikulin S.P.	II-36		IV-248
Morozov A.I.	II-76	Nishioka T.	II-58	Pavlik J.	IV-128
	III-68	Nistor M.	II-50	Pavlik M.	IV-250
Morozov D.A.	I-208		II-52	Pavlov V.B.	III-88
Morrow R.	II-258	Nogaki M.	IV-40	Pawelec E.	II-122
	IV-38	Novak M.	IV-226	Pealat M.	IV-216
Morvova M.	I-262		IV-228	Pechacek R.	II-30
Mouadili A.	III-24	Novak S.	II-248	Pedoussat C.	II-252
Movtchan I.A.	I-80		IV-128	Pejovic M.M.	II-46
Mozgovoï A.L.	I-6	Novakovic N.V.	I-28		IV-178
Mozgrin D.V.	II-24	Nunomura S.	I-196	Pekarek S.	I-266
Muller H.J.	IV-54	Nur M.	IV-10	Pellerin S.	II-122
Muller I.	II-182		IV-12	Pelletier J.	IV-230
Muller S.	IV-120			Peres G.	II-254
Murata T.	III-82			Perret C.	II-256
Muromkin Yu. A.	II-162			Perrin J.	IV-190
Murphy D.	II-30			Peska L.	II-78
Musa G.	I-92				II-82
	I-94			Petit L.	III-98
	II-118			Petrov G.	II-266
	II-188			Petrov O.F.	I-176
Mushiaki M.	IV-156	Ohno N.	I-196		I-178
Musikowski H.D.	II-128	Ohtani K.	IV-86	Petrov T.	II-130
Musinov S.	IV-222	Oien A.H.	I-32	Petrovic Z.Lj.	I-34
Musiol K.	II-122		III-4		I-98
Mustata I.	II-118	Oishi H.	I-230		II-44
	II-188	Okada T.	I-96		II-46
Myamoto K.	I-92	Okazaki S.	IV-26		IV-42
		Okita Y.	III-82		IV-178
		Olthoff J.K.	I-68	Peyrous R.	I-268
		Ono M.	IV-186		III-84
		Onoda H.	II-68		IV-180
		Onose H.	I-144	Pfau S.	II-38
		Otorbaev D.K.	IV-110		II-40
		Otte M.	II-38	Phelps A.V.	II-48
			II-40	Piejak R.	IV-76
		Overchuk K.	IV-222	Pierre Th.	II-164
					II-170
				Pierson J.F.	IV-198
				Pignolet P.	II-42
				Pinheiro M.J.	IV-232
					I-124
				Pintassilgo C.D.	I-102
				Pitchford L.C.	I-100
					II-56
					II-252
					III-42
					III-70
					III-86
				Placinta G.	IV-242
				Pogora V.	II-138
				Pointu A.M.	II-50
					II-52
				Pokrzywka B.	II-122

Ponomarev N.S.	I-36	Revel I.	II-56	Sadeghi N.	I-150
	II-54	Riad H.	II-106		I-152
Popa G.	II-66	Ricard A.	I-168		IV-202
	IV-242		IV-66		IV-246
Popescu A.	II-118		IV-198	Saenko V.A.	I-38
	II-188		IV-200		IV-182
Popescu I.I.	II-50		IV-210		IV-248
	II-52	Richou J.	I-174	Saidane K.	II-126
Popov A.M.	II-28		IV-116	Sakai T.	IV-16
Popov N.A.	I-88	Rivaletto M.	II-42	Sakai Y.	I-92
Poppe F.	III-38	Robert E.	III-30	Sakamoto S.	IV-186
Porokhova I.A.	II-4		III-32	Salabas A.	II-118
	II-6	Robin L.	IV-152	Salamero Y.	I-104
	II-62	Robson R.E.	I-52	Samaritan A.	I-184
	III-60		I-54	Sando K.	I-164
Porras D.	I-270	Roca i Cabarrocas P.	IV-204	Sanduloviciu M.	II-172
Postel C.	IV-106	Rodriguez-Yunta A.	II-112		II-184
Potantin E.P.	IV-224	Rohlens K.	IV-272		II-186
Potapkin B.V.	II-126	Rohmann J.	II-38		II-188
Pousse J.	III-30		II-40		II-190
Pouvesle J.M.	III-32	Romeas P.	I-186	Sapozhnikov A.V.	I-138
	III-44	Rosatelli C.	II-176	Sarrette J.P.	I-254
Praessler F.	I-146	Rosenfeld W.	III-44		II-160
Prazeller P.	I-260	Rosenkranz J.	I-266	Sarroukh H.	III-24
Proshina O.V.	I-88	Rosum I.N.	II-178	Sarytchev D.V.	II-26
	II-234		II-180	Sasada T.	IV-132
Protuc I.	II-138	Roth M.	I-212	Sato K.	IV-118
Proulx P.	II-206	Rousseau A.	IV-92	Sato S.	I-242
Puech V.	I-270	Roussel J.	IV-130	Sato T.	I-164
Punset C.	III-42	Roussel-Dupre R.T.	III-6	Satoh H.	I-238
Purwins H.G.	II-182		III-8		II-58
			III-10	Satoh K.	II-260
<b>R</b>			III-12	Saulle C.	III-46
Rabehi A.	IV-44		III-52	Savinov V.P.	I-108
Rahal H.	I-22	Rovtar J.	IV-162	Savjolov A.S.	II-24
Rahel J.	IV-250	Rozoy M.	I-270		II-26
Rakhimov A.T.	I-86	Rozsa K.	II-64		IV-112
	I-88	Rudakowski S.	IV-148	Säyler G.S.	III-102
Rakhimov A.T.	II-28	Rudnitsky V.A.	I-38	Scheibe H.J.	II-128
	II-234	Rukhadze A.A.	I-172	Scheibner H.	IV-188
	III-40		III-46	Schein J.	II-132
Rakhimova T.V.	I-86		III-88	Scheiring Ch.	I-84
	I-88	Rulev G.B.	I-86	Scherbakov Yu.V.	II-210
	I-182	Rusanov V.	IV-222	Schepe R.	I-40
	II-28	Rusanov V.D.	IV-224	Scheubert P.	II-202
	II-234	Rusnak K.	IV-258		II-204
	III-40	Rutkevich I.	I-234	Schimke C.	III-34
	II-124		I-236		IV-108
Ravary B.	I-148	Ryazantsev E.I.	IV-224	Schmidt E.	III-48
Raynaud P.	III-74	Rybakov A.B.	IV-138	Schmidt M.	IV-196
	II-88	Rybakov V.V.	I-240	Schmoll R.	IV-164
Razafinimanana M.	II-120			Schopp H.	II-114
	II-126	<b>S</b>			IV-108
	II-136	Sa P.A.	I-90	Schram D.C.	II-108
Redon R.	IV-116	Sabonnadiere M.P.	I-48		III-62
Reess T.	II-250	Sabotinov N.	II-130		III-63
Remscheid A.	IV-148				III-108
Remy M.	IV-244				IV-254
				Schruft R.	I-264



Schulze J.	II-130 III-48 III-50	Simek M.	I-72 IV-14 IV-80	Stoykova E.	I-160 I-162 III-46
Schumann J.	II-118	Simko T.	II-64	Strinic A.I.	IV-42
Schumann M.	II-132		IV-184	Suchaneck G	I-146
Schwarzenbach W.	I-150 IV-202	Simonet F.	III-16	Sugawara M.	I-96 I-164 II-68
Segui Y.	I-148 III-74	Singaevsky I.F.	I-108		
Segur P.	I-148 III-74	Singh D.P.	I-44 I-154	Suginuma Y.	IV-40
	II-260 IV-44		II-60	Sukhinin G.I.	I-46 I-198
Selen L.J.M.	III-108	Singh N.	II-136	Sukhomlinov V.S.	IV-170
Sentis M.L.	I-48 III-26 IV-52	Sirghi L.	II-66		IV-172
	II-196	Si-Serir F.	II-244	Sultan G.	IV-232
Sergeichev K.F.	II-196	Skalny J.D.	IV-250	Sunarchin A.A.	IV-262
Serianni G.	II-262 IV-134	Skowronek M.	I-186	Sunka P.	I-248 IV-14
	II-92	Skrynnikov A.V.	IV-256	Supiot P.	IV-142
Servant S.	II-92	Skvortsov V.A.	III-14 IV-270	Surda V.	IV-8
Sery M.	I-130 IV-228	Slavicek P.	I-128 IV-226	Sychov I.A.	II-194 II-196
	I-104	Smakhtin A.P.	I-240		III-8
Sewraj N.	I-104	Smirnov V.V.	I-42 IV-136	Symbalisty E.	III-10 III-12 III-52
Shakhatov V.A.	I-16 I-42 IV-136	Smurov I.	I-80		
	IV-256	Snell J.	II-14		
Sharafutdinov R.G.	IV-256	Snyder D.B.	II-146		
Sharkov B.	I-212	Solntsev I.A.	II-208	T	
Shibamoto M.	IV-186	Solonin V.V.	II-174	Tabbal M.	I-166 I-168
Shibkov V.M.	I-44 I-154 II-60	Sonnenschein E.	I-234	Taddei F.	II-214
	I-154 II-60	Sorokin A.V.	II-166 II-168	Takamura S.	I-196
Shibkova L.V.	I-44 I-154 II-60	Soukup L.	IV-226 IV-228	Takayama K.	IV-144 IV-186
	IV-62	Soulem N.	III-84	Talsky A.	IV-160
Shimizu K.	I-144	Spector N.O.	II-94	Tamme D.	I-40
Shiozaki A.	IV-190	Spyrou N.	III-84 IV-180	Tanaka H.	I-230
Shiratani M.				Tanaka K.	I-228
		Stacewicz T.	I-82	Taniguchi K.	II-198
Shivarova A.	I-156 I-158 II-192	Stamate E.	IV-140	Taranenko Y.	III-8 III-12 III-52
	I-12	Stan C.	II-188		
Shkol'nik S.M.	II-134 III-104 IV-138	Stanciu T.	II-138	Tarnev Kh.	I-158
	III-46	Stanojevic M.	IV-162	Tatarova E	I-122 I-160 I-162
Shkvarunets A.G.	IV-194	Starikovskaia S.M.	IV-48 IV-50 IV-58		
Short K.	IV-264	Starikovskii A.Yu.	IV-48 IV-50 IV-58	Tcheremiskine V.I.	I-48 IV-52
Si-Bachir M.	I-130			Tchuyan R.K.	II-268
Sicha M.	IV-226 IV-228	Stark R.	II-52	Teboul E.	IV-92
	I-62	Steel W.H.	I-192 I-194	Telbizov P.	II-130
Siegel R.	II-62	Stefanovic I.	II-44	Telegov K.V.	II-240
Sigeneger F.	IV-34	Stefka J.	II-78	Tendys J.	IV-194
Sigmund R.S.	I-220	Stepanov V.A.	I-208	Terai K.	III-82
Sigov Y.S.	I-138 IV-110		II-174	Tereshkin S.A.	II-94
Silakov V.P.		Stockl C.	I-212	Tesar C.	IV-98
		Stojanovic V.D.	I-34	Tessier P.Y.	III-90
		Stojilkovic S.M.	I-28	Teuner D.	II-130 III-48

Theroude C. II-254  
 Thomann A.L. IV-252  
 Thomaz J. IV-232  
 Tichonov M.G. IV-262  
 Tichy M. IV-226  
 Tiirik A. IV-32  
 Timofeev N.A. III-54  
 III-56  
 Tioursi M. IV-96  
 IV-166  
 Toader E.I. IV-151  
 Toedter O. IV-54  
 IV-56  
 Tokumasu H. I-228  
 Toma M. II-190  
 Tominaga K. IV-266  
 Tonegawa A. IV-144  
 IV-186  
 Torchinskii V.M. I-178  
 Tous M. IV-226  
 Touzeau M. II-70  
 II-72  
 IV-46  
 IV-160  
 Tramontin L. II-262  
 Trepanier J.Y. I-50  
 Treshchalov A. III-110  
 Trinecoste M. IV-236  
 Trusca A. II-140  
 Tsuda N. IV-268  
 Tsuda S. I-142  
 Tsukabayashi I. I-242  
 Tsvetkov T.S. II-192  
 Turban G. II-212  
 III-74  
 III-90

## U

Udrea M. II-50  
 Ueda Y. I-136  
 Uhlenbusch J. II-226  
 Uhrlandt D. II-74  
 Ukai M. I-74  
 Ulyanov D.K. III-46  
 Ulyanov K.N. II-142  
 II-144  
 Uneyama T. IV-118  
 Ustalov V.V. IV-240  
 Ustinov A.L. II-162  
 Uteza O. III-26

## V

Vacquie S. II-120  
 II-126  
 Valentini H.B. II-202  
 Vallee C. III-74  
 Vallone F. IV-134  
 Van Bever T. I-106

Van de Grift M. I-152  
 IV-246  
 Van de Sanden M.C.M. IV-254  
 Van der Mullen J.A.M. II-108  
 III-62  
 III-63  
 III-108  
 Van Dijk J. III-63  
 Van Egmond C. III-38  
 Van Ootegem B. I-218  
 Vardelle A. II-158  
 Vardelle M. II-158  
 Vaselli M. I-44  
 I-154  
 II-60  
 Vasenkov A.V. I-56  
 IV-256  
 Vasilieva A.N. III-76  
 Vaulina O. I-184  
 Vayner B.V. II-146  
 Veis P. III-98  
 Veklich A.N. II-154  
 Velleaud G. II-92  
 IV-74  
 Verdes D. IV-242  
 Vereshchagin K.A. I-42  
 IV-136  
 Vervisch P. I-218  
 II-238  
 IV-152  
 Vervloet M. III-74  
 Vesselovzorov A.N. III-78  
 Vialle M. II-70  
 II-72  
 Videlot H. IV-190  
 Videnovic I.R. IV-146  
 Viel V. IV-130  
 Vikharev A.L. I-272  
 I-274  
 Viladrosa R. III-30  
 III-32  
 III-44  
 Vill A. III-110  
 Vitel Y. I-188  
 I-190  
 I-200  
 Vivet F. I-200  
 Vizgalov I.V. II-26  
 Vlcek J. IV-258  
 Vogel N.I. III-14  
 IV-270  
 Voitik M. III-26  
 Vovchenko E.D. IV-112  
 Vrba P. II-264  
 Vrhovac S.B. II-44  
 Vul A.Ya. III-54  
 III-56

## W

Wachutka G. II-204  
 Wakabayashi Y. II-58  
 Wang Yicheng I-68  
 Watanabe T. I-244  
 Watanabe Y. I-170  
 Wautelet M. IV-210  
 Wendt R. IV-36  
 Wetzig K. I-146  
 White R.D. I-52  
 I-54  
 Wieme W. I-20  
 Wiesemann K. IV-148  
 Wilke C. II-74  
 II-200  
 Winkler R. IV-188  
 II-62  
 II-266  
 III-58  
 Wiolland R. III-46  
 Wolf O. I-264  
 Wolowski J. IV-272  
 Woryna E. IV-272  
 Wujec T. II-110  
 Wuttmann M. I-118  
 Wyndham E. II-12  
 III-28

## Y

Yagi Y. IV-134  
 Yamada J. IV-268  
 Yamada K. I-74  
 I-142  
 Yamazawa Y. I-230  
 Yan J.D. II-148  
 II-150  
 Yasuda M. I-170  
 Yasui S. I-246  
 Yatsu M. II-68  
 Yilmaz A. I-172  
 Yoshida M. I-134  
 Yoshimura S. I-244  
 Yousfi M. I-252  
 II-220  
 IV-154  
 Yukhimuk V. III-6  
 III-8  
 III-12  
 III-52  
 Yumoto M. IV-16  
 Yurghelenas Yu.V. II-208  
 II-210  
 Yuyama T. I-230

## Z

Zahoranova A. IV-8  
 Zahraoui A. II-260

Zajickova L.	IV-260
Zakouril P.	III-96
Zambra M.	II-12
	III-28
Zaretsky E	I-236
Zatsepin D.V.	IV-50
Zhelyazkov I.	I-160
	I-162
Zheng X.	I-228
Zhovtyansky V.A.	II-152
	II-154
Zicha J.	II-18
Zigman V.J.	I-226
Zissis G.	III-60
Zivkovic J.V.	IV-42
Zobnin A.V.	II-94
Zoller V.	IV-222
Zuev V.S.	IV-52
Zvonicek V.	IV-160